ABSTRACT

Title of Document: STATE-RESOLVED QUENCHING DYNAMICS IN COLLISIONS OF VIBRATIONALLY EXCITED MOLECULES

Juan Du, Doctor of Philosophy, 2010

Directed By: Professor Amy S. Mullin, Department of Chemistry and Biochemistry

The collisional relaxation of highly excited molecules plays a very important role in many chemistry processes. The work presented in this thesis studies the collisional quenching dynamics of highly vibrationally excited molecules using high-resolution transient IR absorption spectroscopy. This work investigates "weak" (small energy transfer) and "strong" (large energy transfer) collisions between donor and bath molecules. The experimental results illustrate how the properties of donor molecules influence the collisional energy transfer. These properties include the molecular structure, internal energy, state density. In several weak collision studies, this thesis studies the vibration-rotation/translation pathway for pyrazine/DCl, pyrazine/CO_2 with different internal energies and for three excited alkylated pyridine molecules/CO_2 systems. A single-exponential rotational distribution and J-dependent translational energy distributions of scattered DCl molecules are observed. For CO_2 collisions, the scattered CO_2 has a biexponential rotational distribution and J-dependent translational energy distributions for all collision pairs. Recoil velocities scale with product angular momenta.

The observed collision rates for these collision pairs match Lennard-Jones rates. The full energy transfer distribution for these pairs is determined by combining data for weak and strong collisions. Lowering the internal energy of donor molecules reduces the amount of rotational and translational energy transfer to CO_2. Reducing the internal energy of pyrazine decreases the probabilities of strong collision and increases the probabilities of weak collision. The average energy transfer reduces by ~ 50% when the internal energy is decreased by only 15%. The collision rates are independent on the internal energy for these systems. Methylation of donor molecules decreases the magnitude of V−RT energy transfer. The collision results are affected by the number of methyl-groups, and not by the position of the group. Increasing the number of methyl groups increases the ratio of the measured collision rate to the Lennard-Jones collision rate. In the strong collision studies, the effects of alkylation and internal energy are studied. In collisions with alkylated pyridine donors with E ~ 39000 cm^{-1}, CO_2 molecules gain less energy from alkylpyridine than from pyridine. The alkylated donors undergo strong collisions with CO_2 via a less repulsive part of the intermolecular potential compared to pyridine. For azulene/CO_2 collisions with two different internal energies, scattered CO_2 molecules gain double the amount of rotational and translational energy when the azulene energy is doubled. The rate of strong collisions increases four times when the internal energy is doubled.

STATE-RESOLVED OF COLLISIONAL QUENCHING DYNAMICS OF VIBRATIONALLY EXCITED MOLECULES

By

Juan Du

Dissertation submitted to the Faculty of the Graduate School of the
University of Maryland, College Park, in partial fulfillment
of the requirements for the degree of
Doctor of Philosophy
2010

Advisory Committee:
Professor Amy S. Mullin, Chair
Professor Millard H. Alexander
Professor Daniel Falvey
Professor John T. Fourkas
Professor Christopher Monroe

Acknowledgements

At the completion of my graduation thesis, I wish to express my sincere appreciation to all those who have offered me invaluable help during the last several years of my graduate study in University of Maryland, College Park.

Firstly, I would like to express my heartfelt gratitude to my advisor, Professor Amy S. Mullin, for her constant encouragement and guidance. Her enthusiasm and creativity in problem solving are inspirational. Without her valuable suggestions and constant support over the last several years, this doctoral thesis cannot be finished forever. All knowledge and experiences in this lab will benefit the rest of my career and life.

Secondly, I should give my hearty thanks to Dr. Ziman Li, Dr. Liwei Yuan, Dr. Daniel K. Havey, Dr. Qingnan Liu, Dr. Nicolas A. Sassin, and Professor Shizuka Hsieh. Dr. Ziman Li and Dr. Qingnan Liu helped me set up the experimental system and taught me so much when I just joined this group. I got a lot of help from Dr. Qingnan Liu in my first three years in the lab. Dr. Liwei Yuan and I investigated two strong collision dynamics projects and one weak collision project for DCl system in Chapter 3, Chapter 7 and Chapter 8. Dr. Daniel K. Havey and I worked together for three weak collision projects in Chapter 4 to Chapter 6. Dr. Nicolas A. Sassin and I studied the effect of internal energy in Chapter 5. With Professor Shizuka Hsieh's help, we finished our DCl project smoothly. I also learned much theoretical physical chemistry knowledge from her. They are all fantastic science mentors to me.

I would also like to express my thanks to all Mullin Group members, Samuel Teitelbaum, Junmei Chao, Allision Robinson, Geraldine O. Echebiri, Matthew D. Smarte and Felix Lin. I got a lot help from them in the lab.

I want to express my thanks to all teachers in my last several years in Boston University and University of Maryland, College Park.

Lastly, my thanks would go to my beloved family for their loving considerations and great confidence in me all through these years. Their love supports me to face all difficulties bravely in my life and to realize my dreams. Their affection and support enable me to finish this work successfully.

Table of Contents

List of Tables

List of Figures

Abbreviations

A	rotational constant
α	absorption strength
AC	alternating current
B	rotational constant
c	speed of light
C	rotational constant
cm	centimeter
cm^{-1}	wavenumber
CO	carbon monoxide
CO_2	carbon dioxide
cw	continuous wave
DC	direct current
DCl	deuterium chloride
ΔE	energy change
E_{rot}	rotational energy
E_{trans}	translational energy
E_{vib}	vibrational energy
ε	Lennard-Jones well depth
F-center	F-center laser
FWHM	full width at half maximum
HCl	hydrogen chloride
H_2O	water
HOD	hydrogen deuterium oxide
InSb	indium antimonide
IR	infrared
J	total angular momentum quantum number
K	Kelvin
k_{int}	integrated energy transfer rate constant

k_{app}^{J}	appearance rate constant
k_B	Boltzmann constant
k_{LJ}	Lennard-Jones collision rate constant
ℓ	path length
LJ	Lennard-Jones
λ	wavelength
m	meter
mol	mole
μs	microsecond
μm	micrometer
MW	megawatt
ν	vibrational frequency
Nd	Neodymium
ns	nanosecond
p	pressure
P	probability
pop	population
R	ideal gas constant
RT	rotation and translation
ρ	vibrational state density
S_0	electronic ground state
S_1	first excited singlet electronic state
S_2	second excited singlet electronic state
S_4	forth excited singlet electronic state
σ	Lennard-Jones diameter
s	second
t	time
T_0	initial temperature
T_1	first excited triplet electronic state
T_{rot}	rotational temperature

T_{trans}	translational temperature
UV	ultraviolet
v	velocity
V→V	vibration to vibration
V→RT	vibration to rotation and translation

Chapter 1: Introduction of Collisional Quenching Dynamics

1.1 Significance of Collision Energy Transfer

Collisional energy transfer is a key step in many chemical reactions.[1-5] When molecules have energies near their reaction thresholds, collisions between these excited molecules and cold bath molecules determine the fate of the reactions of the activated molecules.[6] Therefore, understanding the mechanisms of the collisional relaxation of highly excited molecules is of both fundamental interest and practical value for the modeling of combustion and atmospheric chemistry. Knowledge of the collisional energy transfer dynamics between molecules can help us to predict the rates of reactions in combustion and atmospheric chemistry.[5,7,8]

A general theory for thermal unimolecular reactions was developed by Lindemann in 1922 and later improved upon by Hinshelwood in 1927.[9-11] The Lindemann-Hinshelwood Model incorporates collisional energy transfer to explain the pressure dependence of unimolecular reaction rates.[12] This model shows that inelastic collisions play a key role in the mechanism of unimolecular reactions. The mechanism for the unimolecular reaction in the presence of collisions is described by three steps:

$$A + M \xrightarrow{k_1} A^* + M \qquad \text{(collisional activation)} \qquad (1.1)$$

$$A^* + M \xrightarrow{k_{-1}} A + M \qquad \text{(collisional deactivation)} \qquad (1.2)$$

$$A^* \xrightarrow{k_2} B \qquad \text{(unimolecular reaction)} \qquad (1.3)$$

Here, A is the reactant molecule, M is an inert collision partner, A^* is the excited species with high internal energy and B is the product of dissociation of A^*. Eq 1.1 shows that the reactant A becomes excited to A^* through collisions with M and the rate of appearance of A^* from this step is shown as Eq 1.4:

$$\frac{d[A^*]}{dt} = k_1[A][M] \tag{1.4}$$

Eq 1.2 tells us that excited A* can be deactivated following collisions with M with a rate given as Eq 1.5:

$$\frac{d[A^*]}{dt} = -k_{-1}[A^*][M] \tag{1.5}$$

The Lindemann-Hinschelwood Model assumes that every collision is effective at removing enough energy from A* so that it is not reactive. This assumption is known as the strong collision assumption. Excited A* can also dissociate to product B. The rate for the reaction is shown by Eq 1.6:

$$\frac{d[A^*]}{dt} = -k_2[A^*] \tag{1.6}$$

Applying the steady-state approximation to A* yields an overall reaction rate given by Eq 1.7:

$$\text{Reaction rate} = \frac{k_1 k_2 [A][M]}{k_{-1}[M] + k_2} \qquad (1.7)$$

At low pressures, Eq 1.1 is the rate determining step and the reaction rate has 2nd order kinetics. At high pressures, the collisional activation and deactivation establish a rapid equilibrium, and Eq 1.3 becomes the rate determining step. In this case, the observed rate for the reaction has 1st order kinetics.

After the Lindemann-Hinshelwood Model, other theories were developed, such as the Statistical Adiabatic Channel Model (SACM), to describe unimolecular reactions. Most of these theories use the strong collision assumption, so understanding collisional dynamics and the role of collisions on the fate of excited molecules is an important goal.

Many important questions about the collisional dynamics of highly excited molecules remain unanswered: How does energy transfer between two molecules occur through collisions? Which pathways are the predominant channels of energy transfer in collisions of two molecules? What properties of highly excited molecules are important in the collisional activation and deactivation? How does the internal energy of the excited molecules affect the energy transfer?

The work presented in this thesis seeks to find the answers for these questions. Using high resolution transient IR absorption spectroscopy, my doctoral research illustrates how excited molecules transfer energy to cold bath molecules through collisions. This work provides a detailed picture of the collisional quenching of high energy molecules and will serve as a benchmark for future models of molecular energy transfer.

1.2 "Weak" and "Strong" Collisions

Lindeman recognized that collisions are often the means by which molecules gain sufficient energy to react. Without detailed knowledge of energy transfer mechanisms, Hinschelwood introduced the "strong" collision assumption to account for collisional deactivation by equating the deactivation rate (Eq 1.2) with the collision rate. He assumed that every collision would remove enough energy to deactivate a reactive molecule. Since collisions actually involve a distribution of energy transfer values, the strong collision assumption greatly overestimates the effect of deactivating collisions.

Strong collisions, by definition, involve large amounts of energy. On the other extreme, collisions that induce small energy changes are known as weak collisions. Troe introduced the concept of "weak" collisions to account for the discrepancy between observed and calculated rates for unimolecular reactions in the presence of collisions.[13,14] Some studies on unimolecular reactions have illustrated this phenomenon, such as in Figure 1.1.[13,15,16]

This thesis uses the terms "strong" and "weak" as relative descriptors for collisions that induce large and small changes of energy, respectively. A representative energy transfer distribution function for the relaxation of a highly excited molecule is shown in Figure 1.2, where we see that weak collisions occur far more often than strong collisions. In this thesis, the dynamics of energy transfer for strong and weak collisions are investigated. Projects described in Chapters 3–6 measure the complete energy transfer distribution from both weak and strong collisions. Work in Chapter 7 and 8 focuses on studying the strong collisions for different highly excited molecules.

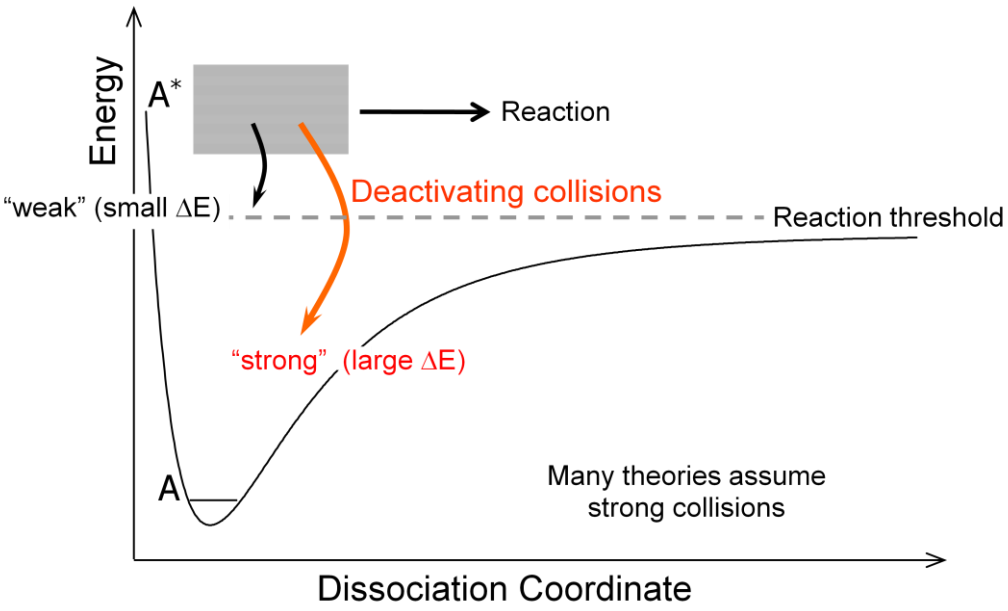

Figure 1.1 Schematic illustrating collisional deactivation by strong and weak collisions.

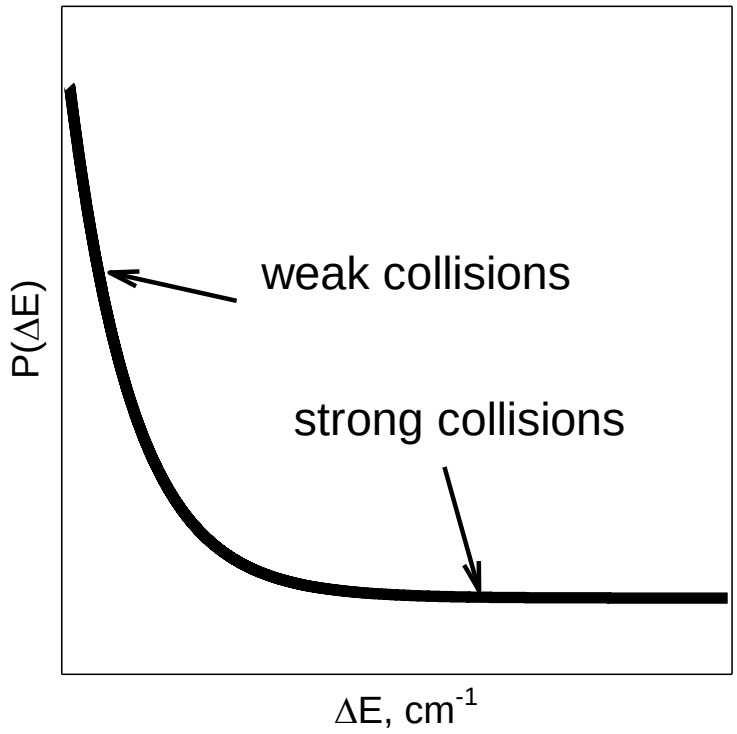

Figure 1.2 Energy transfer distribution function shows that weak collisions of excited molecules (small ΔE) occur more often than strong collisions (large ΔE).

1.3 Methods for Studying the Collisional Relaxation of Highly Vibrationally Excited Donors

A number of theoretical studies have investigated the collisional quenching of highly excited large molecules. In the 1970's, Troe and Rabinovitch independently developed semiempirical master equation theories using microcanonical transition state theory to describe collisional relaxation.[14,17-20] Since the exact nature of the distribution function was not known at that time, they introduced different model functions such as stepladder, exponential and Gaussian forms for the distribution function. Due to the unknown functional form of the distribution, a consistent picture of how collisional relaxation depends on fundamental molecular properties did not emerge. Schlag and co-workers developed a statistical model wherein a collision complex is formed and energy randomization occurs among all degrees of freedom.[21-23] Nordholm and coworkers proposed that the energy of the colliding molecules is redistributed microcanonically, as it would be in a quasibound collision complex. Based on this idea, they developed the ergodic collision theory (ECT).[24-26] This theory correctly predicts observed collision trends but overestimates average collision energy transfer values $\langle \Delta E \rangle$. Recently, Nordholm and coworkers have developed a semiempirical extension of ECT, called the partially ergodic collision theory (PECT), which describes energy redistribution using a variable subset of donor and bath degrees of freedom that are involved in the energy redistribution.[27-30]

Developing a detailed physical picture of energy transfer in molecular collisions is challenging because of the high dimensionality of the available phase space. Classical and semiclassical trajectories are powerful tools for providing insight into molecular

collisions, particularly when coupled with experimental results. Trajectory calculations have been performed on collisions that quench high energy molecules by a number of investigators, including Lendvay and Schatz,[31,32] Gilbert and co-workers,[33,34] Lim,[35,36] Bernshtein and Oref,[37,38] Luther and co-workers,[39-41] Yoder and Barker,[42] Chapman and co-workers,[43,44] and Li *et al*.[45] Most studies have focused on atomic collision partners. These studies show that most of the energy transfer involves the low-frequency donor modes, that chattering collisions are involved in both large- and small-ΔE collisions (particularly when the collision partner is a molecule), and that large-ΔE collisions occur through repulsive interactions.

A number of experimental methods such as UV absorption (UVA),[46-52] IR fluorescence (IRF),[53-60] and time-resolved FTIR emission[61-63] have been used to measure the collisional deactivation of high-energy molecules. The experimental data from these studies have been fit using various model distribution functions such as single-, double-, and extended-parameter exponentials. Luther and co-workers have used kinetically controlled selective ionization (KCSI) and fluorescence (KCSF) techniques to measure relaxation distributions of highly excited molecules.[27,29,64-68] These approaches measure the complete energy transfer distribution function P(E,E') using two-color, two-photon ionization to monitor the highly excited molecules as they relax by collisions. Distributions of highly excited molecules with initial energy E are monitored as the molecules pass through experimentally determined energy windows at the energy E'. KCSI experiments are "self-calibrating" and do not require an empirical calibration curve. Their results are best described using a parameterized mono-exponential distribution. There is good agreement between their results and the predictions of Nilsson and

Nordholm's partially ergodic collision theory (PECT).[27] Recently, a new technique used molecular beam ion imaging to determine the energy transfer distribution functions for highly excited molecules with atomic collision partners.[69-73]

Our group has investigated the collision dynamics for a number of collision pairs using high-resolution transient IR absorption spectroscopy.[74-88] This approach measures energy gain of the energy-accepting molecules after collisions with highly excited molecules. This technique tells us directly about the bath molecule's energy gain in the vibrational, rotational and translational degrees of freedom resulting from collisions with high energy molecules. In addition, the energy transfer probability distribution function $P(\Delta E)$, the collision rate, and the average transfer energy ΔE rate for the single collisions are measured experimentally.

The work in this thesis uses pulsed optical excitation to generate a highly excited molecule and monitors energy gain in small bath molecules using high-resolution transient IR spectroscopy. State-resolved product distributions yield a detailed picture of the collision dynamics. Energy transfer distribution functions are determined from the perspective of the bath molecules. Michaels and Flynn developed the formalism for converting rotational state-specific energy gain distributions and rate constants into an overall probability distribution function.[89] Flynn and coworkers studied the strong collision dynamics for a number of excited molecules (E) with CO_2 system firstly using transient IR absorption.[74,90-100] Sevy and co-workers have studied the interplay of photodissociation dynamics with collisional deactivation for several donor molecules with CO_2 using a similar IR probe technique.[96,101-103]

1.4 High Resolution Transient IR Absorption Spectroscopy

This thesis presents studies of the collisional relaxation of highly vibrationally excited molecules using high resolution transient IR absorption. The experiments can be described by three processes.

Highly vibrationally excited donor molecules are prepared by pulsed visible or UV light.

(1) Donor + $h\nu$ (UV or vis) $\rightarrow$ Donor (E)

Collisions with small bath molecules induce energy losses in the high energy molecules and energy gain in the bath molecule. The scattered bath molecule will have energy in vibration (v), rotation (J), and/or translation (V).

(2) Donor (E) + Bath $\rightarrow$ Donor (E$-\Delta$E) + Bath (v, J, V)

The nascent scattered bath molecules are measured with high resolution transient IR absorption.

(3) Bath (v, J, V) + hν ($\lambda \sim 2.7–4.3$ μm) $\rightarrow$ Bath (v', J', V')

where, v is the vibrational state of bath molecule, J is the rotational angular momentum quantum number of bath molecule and V denotes the component of the recoil velocity

along the IR probe axis. The details of the experimental method will be described in Chapter 2.

1.5 Molecules in this Thesis

1.5.1 Highly Vibrationally Excited for Azabenzene Molecules

This thesis explores how the properties of donor molecules affect collisional energy transfer dynamics. A number of different azabenzene molecules were used as highly vibrationally excited molecules. Figure 1.3 illustrates the azabenzene donor molecules investigated in this thesis.

Most of the highly vibrationally excited donor molecules in this thesis are produced by pulsed UV laser absorption. After being pumped by UV light, azabenzene molecules undergo transitions to electronically excited states, followed by rapid radiationless decay, resulting in vibrationally excited states of the electronic ground state. The lifetimes for radiationless decay of donor molecules range from $\tau = 5$ ps to $\tau = 100$ ns. The fluorescence quantum yields for these azabenzenes are very small (typically on the order of 10^{-5}).

The preparation of the highly vibrationally azabenzene molecules is described in this Section. In each case, preparation of the highly vibrationally excited molecules occurs well before the average collision time in our experiments. In energy-dependent collision projects (Chapters 4, 5 and 8), the donor molecules were prepared with different amounts of internal energy using light wavelengths in the UV or visible. In Chapters 4 and 5, excited pyrazine with E = 32700 or 37900 cm^{-1} was produced by light with λ = 308.75 or 266 nm. Pyrazine is pumped from the ground state S_0 to electronic excited

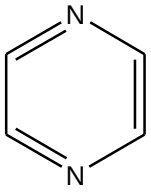

pyrazine

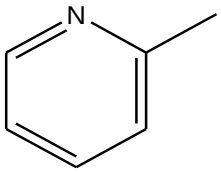

2-methylpyridine
(2MP)

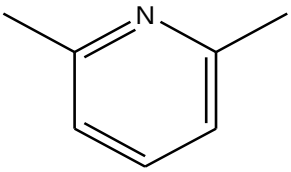

2,6-dimethylpyridine
(2,6MP)

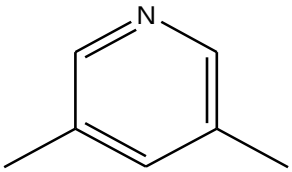

3,5-dimethylpyridine
(3,5MP)

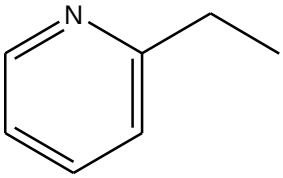

(2-ethylpyridine)
(2EP)

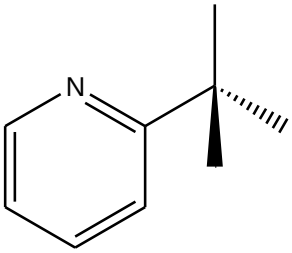

2-t-butylpyridine
(2tBP)

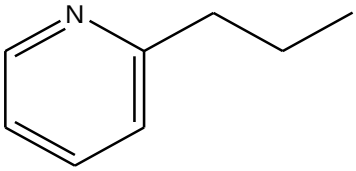

2-propylpyridine
(2PP)

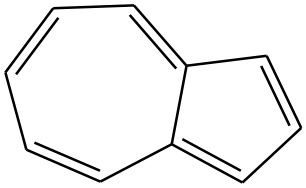

azulene

Figure 1.3 Highly vibrationally excited donor molecules studied in this thesis.

state S_1 by 308.75 nm UV light. Electronically excited pyrazine then transforms a transition to vibrationally excited ground state pyrazine $S_0(E)$ through two paths.[104,105] One process is internal conversion from S_1 to $S_0(E)$ directly and the other process involves two intersystem crossings, $S_1 \rightarrow T_1 \rightarrow S_0(E)$. The first intersystem crossing $S_1 \rightarrow T_1$ is rapid (< 50 ps) and has almost unity quantum yield.[106] The lifetime τ for the second intersystem crossing $T_1 \rightarrow S_0(E)$ is a single-exponential function of the UV laser wavelength with τ = 180 ns for $T_1 \rightarrow S_0(E)$ at 308.75 nm. At λ = 266 nm, pyrazine is pumped from the ground state to the S_2 state, and then converts rapidly to S_1. From S_1, pyrazine intersystem crossing undergoes to T_1 and then to $S_0(E)$ with a life time of $\tau \sim 50$ ns.[95,107] The state-decay information of pyrazine at different pump wavelengths is listed in Table 1.1.

Highly vibrationally excited azulene(E = 20390 or 38580 cm^{-1}) in Chapter 8 is prepared light with λ= 532 or 266 nm. At these wavelengths, azulene molecules are excited to the S_1 and S_4 electronic singlet states, respectively. Internal conversion is the dominant relaxation process from both the S_1 and S_4 states, with near unity quantum yields for forming highly vibrationally excited $S_0(E)$ azulene molecules. The lifetime of the S_1 state is several picoseconds.[108] The S_4 state initially relaxes to S_2 by fast internal conversion and then $S_2 \rightarrow S_0$ internal conversion forms high vibrational levels of the electronic ground state.[65,109] The lifetime of the S_2 state following 266 nm excitation is less than 3.4 ns.[110] The internal energy E includes the photon energy and the thermal vibrational energy. The decay paths and lifetimes for azulene are listed in Table 1.1.

Several vibrationally excited alkylated pyridine molecules are prepared in alkylation-effect projects (Chapter 6 and 7). The excitation processes for these alkylated

Table 1.1 The decay pathways and life times for donor molecules.

Donor	λ, nm	E_{vib}, cm^{-1}	Major Pathway	τ
pyrazine	266	37900	1) $S_2 \rightarrow S_1$	
			2) $S_1 \rightarrow T_1$	
			3) $T_1 \rightarrow S_0(E)$	<50 ns
	308.8	32700	1) $S_1 \rightarrow T_1$	< 50 ps
			2) $T_1 \rightarrow S_0(E)$	180 ns
pyridine	266	37920	1) $S_1 \rightarrow S_0(E)$	60 ps
			2) $S_1 \rightarrow T_1$	50 ps
			3) $T_1 \rightarrow S_0(E)$	<100 ns
azulene	266	38580	1) $S_4 \rightarrow S_2$	
			2) $S_2 \rightarrow S_0(E)$	< 3.4 ns
	532	20390	$S_1 \rightarrow S_0(E)$	< 10 ps

pyridine molecules are similar to those of pyridine and the rates are faster than those for pyridine. Therefore, the preparation of the highly vibrationally excited pyridine is described as a representive sample here. Pyridine molecules are pumped to the single electronic excited state S_1 by 266 nm light. Excited pyridine molecules in the S_1 state undergo relaxation to the vibrationally excited state $S_0(E)$ in two ways. Pyridine(S_1) internally converts to $S_0(E)$ with $\tau \approx 60$ ps. Pyridine molecules also undergo double intersystem crossing of the form $S_1 \rightarrow T_1 \rightarrow S_0(E)$. The life time for the intersystem crossing $S_1 \rightarrow T_1$ is $\tau \approx 50$ ps, while that for the intersystem crossing $T_1 \rightarrow S_0(E)$ is $\tau <$ 100 ns.[111-113] The state-decay information for pyridine molecules are also listed in Table 1.1.

1.5.2 Bath Molecules

Two bath molecules are studied in this thesis: DCl and CO_2. Both species have strong IR absorption and spectral features that are sparse enough so that their energy gain profiles can be measured using transient high-resolution absorption.

High-resolution transient IR absorption was used to measure the rotational and translational energy gain profiles of DCl (v = 0) through collisions with excited pyrazine in Chapter 3. The IR probe is the DCl (v = 1) $\leftarrow$ (v = 0) transition at $\lambda = 4.3$ μm shown in Figure 1.4. In addition to studying the v= 0 state of DCl, this work measured appearance of DCl (v = 1) using the (v = 2) $\leftarrow$ (v = 1) hot band transition. DCl (v = 1) population at 300 K is almost zero and < 1% of the scattered molecules is observed in the v =1 state. The transient signal levels for the DCl (v = 1) state are small compared to those for population changes in the (v = 0) state. Therefore, the population changes for

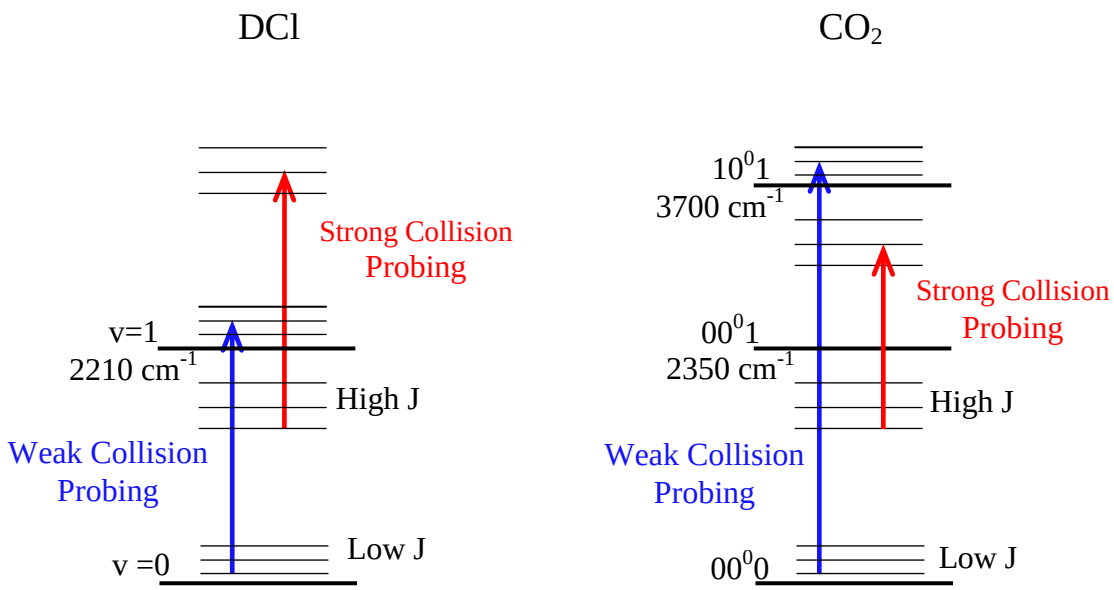

Figure 1.4 IR probing for strong and weak collision for DCl and CO_2 bath molecules.

low and high J states of DCl can be measured using the (v = 1) ← (v = 0) transition without interference from collisions populating the upper state of the probe transition.

After collisions with highly vibrationally excited donor molecules, the population changes for CO_2 in low and high-J states are measured by IR light with λ = 4.3 or 2.7 μm, as shown in Figure 1.4. The number density of scattered CO_2 in high-J states is measured with the single-quantum $(00^01) \leftarrow (00^00)$ transition using a diode laser at λ = 4.3 μm. The outcome of weak collisions involving CO_2 low-J states is probed using combination band CO_2 $(10^01) \leftarrow (00^00)$ transitions near λ = 2.7 μm from a F-center laser. Two factors limit diode laser probing to CO_2 high-J states. The low-J $(00^01) \leftarrow (00^00)$ CO_2 transitions are saturated due to the large oscillator strength and populations of CO_2 in these states.[78,79,114] The oscillator strength of the $(10^01) \leftarrow (00^00)$ transition is small enough that thermally populated CO_2 states do not absorb the probe light completely. In addition, the $(10^01) \leftarrow (00^00)$ combination band is an effective probe of population changes for low-J CO_2 (00^00) states since direct vibration-to-vibration energy transfer into the (10^01) state is negligible and does not interfere with transient absorption measurements within the (00^00) state. It is known that the CO_2 (00^01) state is a product of collisions with highly vibrationally excited molecules.[74]

1.6 Overview of the Work in this Thesis

The research in this thesis is designed to address questions about the collisional relaxation of the highly vibrationally excited molecules. The various projects study how the properties of excited molecules affect the collisional quenching. Chapters 3–6 report the dynamics of weak collisions for a number of collision systems. Combining these data

with prior data for strong collisions yields information about the full distribution of energy transfer. Chapters 7 and 8 consider how molecular structure affects strong collisions.

The organization of this thesis is as follows:

Chapter 2 describes the setup of two types of high resolution transient IR absorption spectrometers: the diode laser spectrometer and the F-center laser spectrometer. These two spectrometers cover the IR probe regions for CO_2 and DCl.

Chapter 3 explores the weak collisions between pyrazine(E = 37900 cm^{-1}) and cold DCl bath molecules. With the results of a previous study of DCl high-J states, the whole vibration-to-rotation/translation (V–RT) pathway energy transfer information is obtained. The rotational distribution of scattered DCl is a single Boltzmann distribution. J-dependent translational distributions are observed. This Chapter provides a direct measurement of the collision rate that is close to the predicted value from the Lennard-Jones collision model. The V–RT pathway is a dominant channel of collision energy transfer. This study has been published in *the Journal of Physical Chemistry A*.[115]

Chapter 4 investigates the weak collisions of pyrazine(E = 37900 cm^{-1}) and CO_2 molecules. In combination with previous data for CO_2 high-J states, the whole distribution for V–RT energy transfer between pyrazine(E = 37900 cm^{-1}) and cold CO_2 bath molecules is presented. The scattered $CO_2(00^00)$ molecules have a biexponential rotational energy distribution. The distribution shows evidence for distinct weak and strong collision pathways. V–RT energy transfer is the dominant pathway through which pyrazine(E) is relaxed by collisions with CO_2. The experimental collision rate is in good agreement with the Lennard-Jones model. The full energy transfer distribution function

P(ΔE) is presented. This study has been published in *the Journal of Physical Chemistry A*.[116]

Chapter 5 investigates the internal energy effect on the collision dynamics of pyrazine(E)/CO_2 pair by comparing the experimental results at E = 32700 cm^{-1} and 37900 cm^{-1}. The distributions of both rotational and translational energy in scattered CO_2 molecules are sensitive to the internal energy of pyrazine. Within experimental error, the observed collision rates are not very sensitive to the internal energy of pyrazine. However, increasing the donor internal energy reduces the probability of weak collision and induces more strong collisions.

Chapter 6 addresses how the structure of vibrationally excited molecules affects the collisions. Scattering dynamics for several donor species are compared: pyrazine, 2-methylpyridine, 2,6-dimethylpyridine, and 3,5-dimethylpyridine. Methyl-group addition has a large impact on the collisional quenching of vibrationally excited molecules. The energy transfer distributions are affected by the number of methyl groups, but not by the positions of the groups in the aromatic ring relative to nitrogen atom in the ring. Biexponential population distributions for the scattered CO_2 are observed in collisions with each of these donors. Donor alkylation also increases the appearance collision rates, which are higher than Lennard-Jones collision rates.

Chapter 7 reports the energy dependence of strong collisions of CO_2 with highly vibrationally excited azulene for two initial energies, E = 20390 and 38580 cm^{-1}. Both the distribution of transferred energy and the energy transfer rates are sensitive to the azulene energy. For strong collisions, the average rotational and translational energies of the scattered CO_2 molecules double when the azulene energy is increased by a factor of 2.

The rate of energy transfer via strong collisions increases by nearly a factor of 4 when the azulene energy is doubled. The energy transfer probability distribution function for $\Delta E >$ 3000 cm^{-1} at each initial energy is an exponential decay with curvature that correlates with the energy dependence of the state density. This result is in excellent agreement with predictions from GRETCHEN, a model that uses Fermi's Golden Rule to describe collisional quenching of highly excited molecules. This study has been published in *the Journal of Chemical Physics*.[117]

Chapter 8 focuses on the strong collisions of a series of alkylated pyridine molecules on strong collisions. The collisions of CO_2 with three alkylated pyridine species (2-ethylpyridine, 2-propylpyridine, and 2-t-butylpyridine) are reported in this Chapter. The alkylated donors impart less rotational and translational energy to CO_2 than does pyridine. Alkyl chains reduce the average energy per mode, and the probability of strong collisions is reduced. Comparison of effective impact parameters shows that the alkylated donors undergo strong collisions with CO_2 via a less repulsive part of the intermolecular potential than does pyridine. Some of this work has been published in *the Journal of Physical Chemistry A*.[118]

Chapter 2: Experimental Methods

2.1 Introduction

The collisional quenching dynamics of high energy molecules was studied using high-resolution transient IR absorption spectroscopy. The spectroscopy was performed using two types of laser systems: a pulsed UV laser to generate highly excited molecules and an IR laser for probing the outcome. This spectroscopy is described in Section 2.2. The high vibrational excitation in the azabenzene donor molecules shown in Figure 1.3 was produced by a pulsed Nd:YAG laser or a dye laser as described in Sections 2.3.1 and 2.3.2. IR light was used to probe scattered CO_2 and DCl bath molecules after collisions with vibrationally hot donor molecules. Two types of IR lasers were utilized to measure the transient absorption spectra of these bath molecules. IR light with $\lambda \sim 4.3–4.5$ μm was produced by lead-salt diode lasers and light at $\lambda \sim 2.7$ μm was produced by an F-center laser.

2.2 High-Resolution Transient IR Laser Absorption Spectrometers

The collisional energy transfer between bath molecules and highly vibrationally excited donor molecules was measured using the transient IR absorption. This technique interrogates the details of collisional energy transfer from vibrationally hot donors to bath molecules. In these experiments, the UV pulse and IR beam were propagated collinearly through a 3 meter flowing-gas Pyrex collision cell as shown in Figure 2.1. A 1:1 mixture of bath and donor vapor was flowed through the collision cell a total pressure near P_{total} = 20 mTorr.

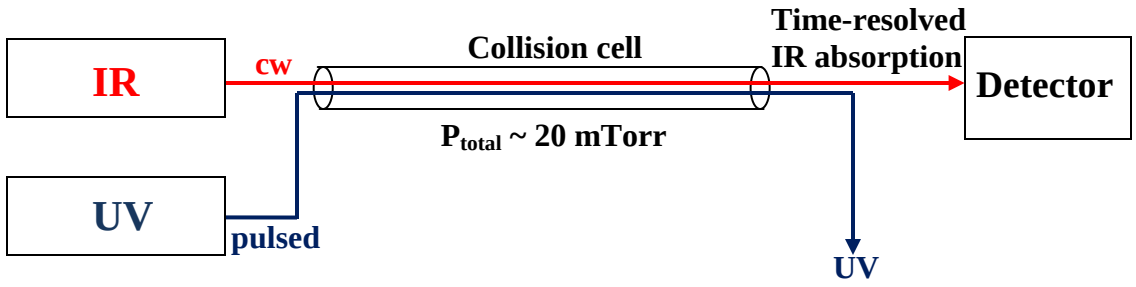

Figure 2.1 High-resolution transient IR absorption spectroscopy uses two laser systems: a pulsed UV laser and a cw IR laser.

2.2.1 Diode Laser Spectrometer

The diode laser spectrometer uses a diode laser as the IR probe and a Nd:YAG laser as the pump laser, as shown in Figure 2.2. The wavelength of the IR output from the diode laser is $\lambda \sim 4.3$ μm and was used to probe CO_2 high-J states and DCl low-J states. After passing through the collision cell, the IR beam goes through a monochromator to ensure that the intensity changes for a single mode of the diode laser are monitored by a liquid-nitrogen-cooled InSb detector with risetime of $\tau = 100$ or 300 ns.

The spectrometer uses a lock-in technique to decrease IR frequency drifts of the diode laser. 10% of IR beam was passed through a reference cell and the signal after the reference cell was collected by a liquid-nitrogen-cooled InSb detector, the output of which was directed into a lock-in amplifier. The lock-in amplifier sends an error signal to the diode laser to correct for drifts in the diode laser current. The reference feedback loop locks the diode laser either to the center of a single rovibrational transition of the bath molecules or to a fringe of a scanning Fabry-Perot etalon.

The translational energy distributions of scattered bath molecules in individual rotational states were measured from nascent Doppler-broadened line profiles at $t = 1$ μs after excitation of donors. This measurement was performed by collecting transient absorption at ~ 40 frequencies over a spectral transition.

A master timer based on the 1 kHz diode laser modulation synchronizes the timing of the diode laser, Nd :YAG laser and a shutter. The frequency of the shutter is set at 1 Hz to ensure that the 3-meter cell is refreshed with new gas prior to the pulsed excitation.

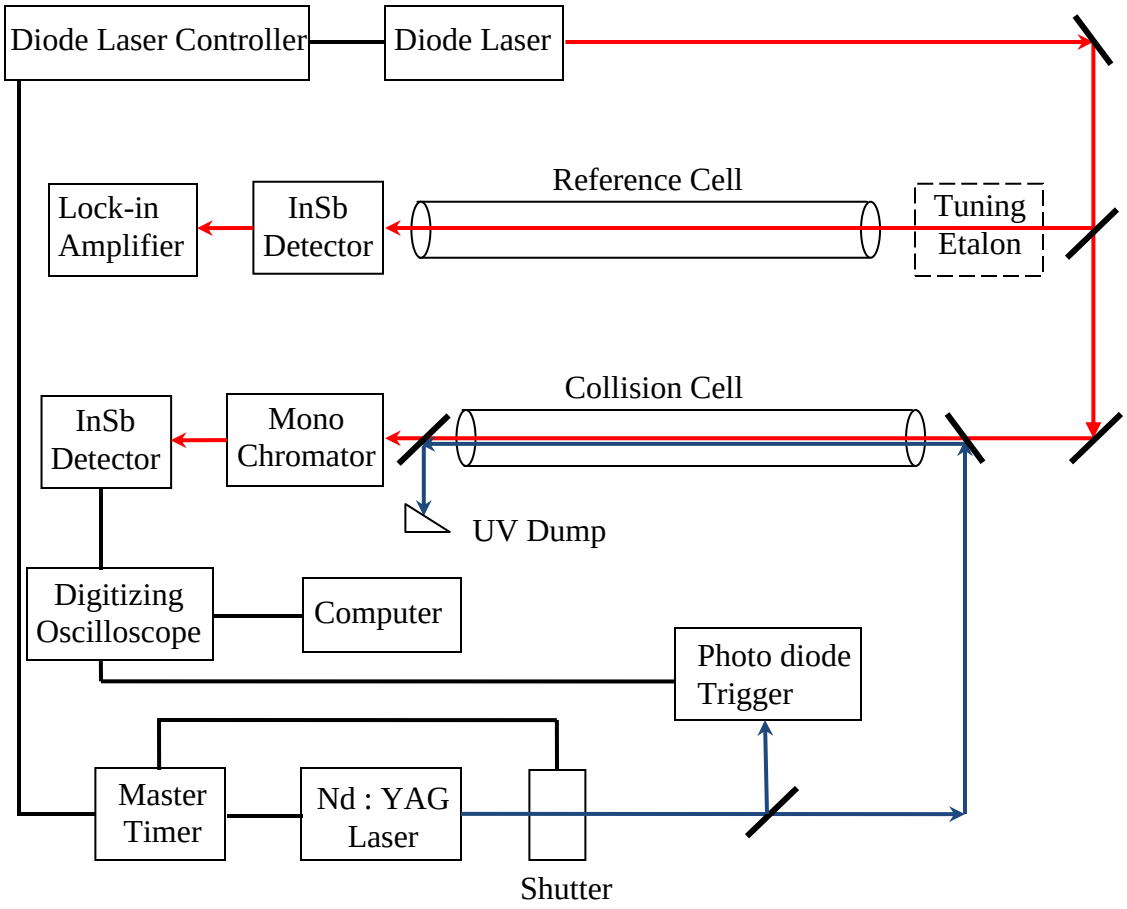

Figure 2.2 Diode Laser Spectrometer

In a diode laser, the surface of a crystal wafer is doped with a very thin layer of semiconductor materials. The top of the doped crystal is an n-type region and the bottom is a p-type region, resulting in a p-n junction or diode. When current goes through the diode, electrons move from the n-type region to the p-type region while the electron holes move from the p-type region to the n-type region. The IR output is provided by the stimulated emission an electron-hole recombination. The energy gaps of electron-hole pairs determine the frequency of emitted photons.

The output power of the diode laser is ~ 200 μW and the frequency resolution is 0.0003 cm^{-1}. For comparison, Doppler-broadened line profiles at 300 K and λ = 4.3 μm have $\Delta\nu_{Dop}$ = 0.004 cm^{-1}. The IR output from a diode laser at λ ~ 4.3 μm was used to probe single quantum transitions CO_2 $(00^01) \leftarrow (00^00)$ and results are presented in Chapters 7 and 8. A different diode laser operating at λ ~ 4.5 μm was used for DCl (v = 1) ← (v = 0) and (v = 2) ← (v =1) transitions at 2100 cm^{-1}, as discussed in Chapter 3.

2.2.2 F-Center Laser Spectrometer

Many aspects of the F-center laser spectrometer are similar to the diode laser spectrometer. In this spectrometer, the IR probe laser is a F-center laser and the pump laser is a Nd:YAG laser or a dye laser, as shown in Figure 2.3. The F-center laser provides a tunable single-mode IR light with λ ~ 2.7 μm. The output wavelength was determined to within 0.1 cm^{-1} by a wavemeter. The intensity of the F-center laser is modulated by low frequency power fluctuations in the Kr pump laser. Therefore, a second InSb detector (τ = 1 μs) was used to measure the IR light and background subtraction techniques were employed to correct for the fluctuations.

A single-mode tunable Burleigh FCL-20 F-center laser was used for studies at $\lambda \sim$ 2.7 μm. The F-center laser uses an alkali halide crystal (RbCl:Li) that contains F_2^+ lattice defects as the gain medium. These F_2^+ lattice defects occur when two adjacent anion vacancies share one electron. Visible light at λ = 647 nm from a Kr^+ laser pumps the F-center crystal to an excited state of the F_2^+ center. A tunable IR beam with $\lambda \sim$ 2.7–3.3 μm was produced following the lattice relaxation of the crystal.

The tuning range of the IR output is relatively broad due to the amount of coupled lattice vibrations of the crystal. The cavity of the F-center laser was designed to obtain tunable and single mode IR light. The design of the F-center laser is shown by Figure 2.4. The laser cavity consists of an end mirror and a diffraction grating. Coarse frequency selection was achieved by scanning the diffraction grating. A piezoelectric air spaced etalon was used to achieve a single cavity mode. Fine adjustment and scanning of the wavelength was performed by rotating a pair of intracavity CaF_2 plates and simultaneously scanning the etalon using active feedback in order to maintain single mode operation.

The output of the F-center was used to measure weak collisions of CO_2 using the $(10^01) \leftarrow (00^00)$ transition near 3700 cm^{-1}.

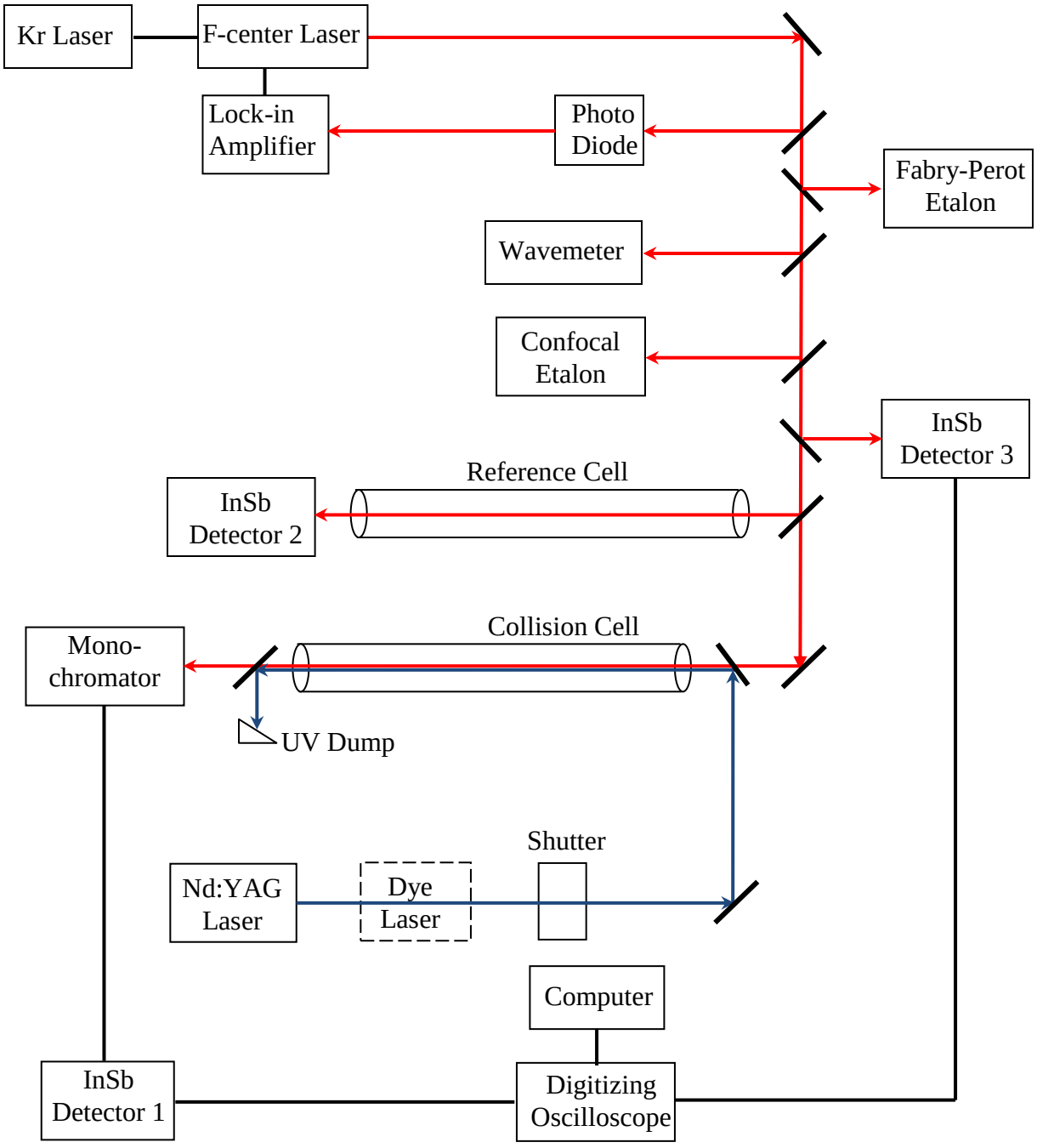

Figure 2.3 F-center Laser Spectrometer.

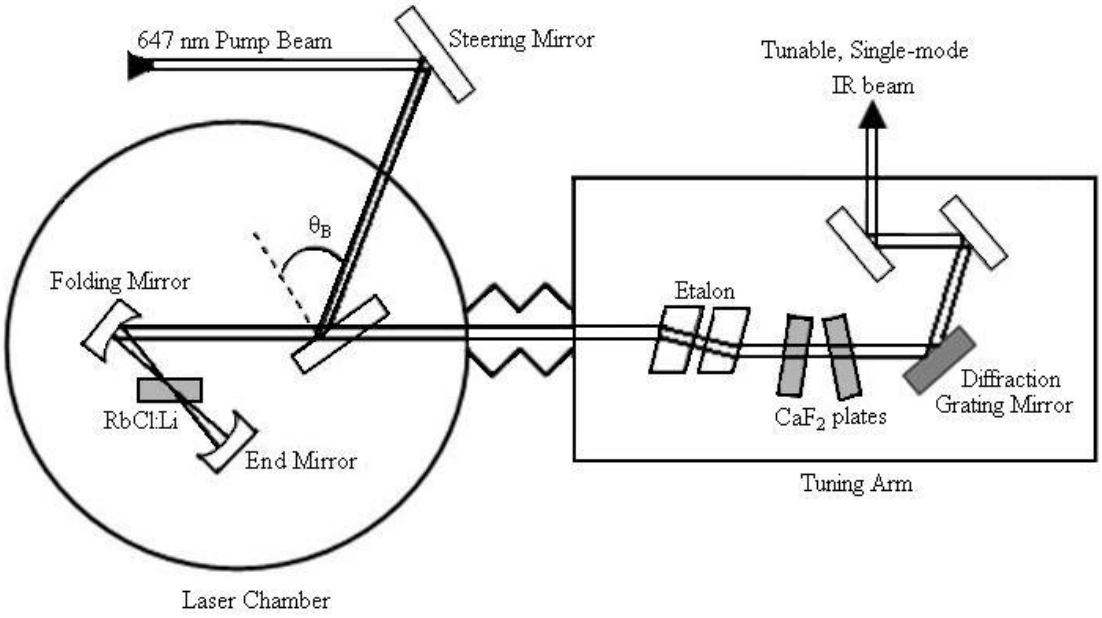

Figure 2.4 Burleigh F-center Laser

2.3 Laser Systems

2.3.1 Nd:YAG Laser

A Nd:YAG laser was used to generate pulsed UV light at λ = 532 or 266 nm. The Nd:YAG laser is a flash lamp-pumped Q-switched oscillator-amplifier system. Nd:YAG (Yittrium aluminum garnet, $Y_3Al_5O_{12}$, doped with Nd ion) is a four-level gain medium. A 6 mm diameter Nd:YAG rod with antireflective coatings on both ends is optically pumped using two linear flash-lamps and generates an IR output beam at a wavelength λ = 1064 nm. The Q-switch in the oscillator cavity generates a pulsed output with a duration of 5 ns by controlling the lasing of the cavity via polarization. By adjusting the Q-switch delay time relative to the flash lamp firing, lasing occurs when the maximum population inversion is reached.

Figure 2.5 illustrates how the Q-switch technique works in the Nd:YAG oscillator cavity. The beam produced from the oscillator cavity makes a double pass through a pockels cell (PC), which has a longitudinal field KD*P ($KH_{2(1-x)}D_{2x}PO_4$) crystal inside. A plate polarizer is highly transparent (> 95%) to horizontal polarization while being highly reflective (> 99%) to vertical polarization. A quarter-wave plate in the cavity adds 45° rotation with each pass. When 3000 V is applied to the PC, another 45° rotation is added for each pass. At last, the returned pass is rotated 180° and its direction remains horizontal. This horizontal beam is transmitted through the plate polarizer. When the PC has 0 V applied, it does not add +45° for each pass. Therefore, the returned pass with total rotation of 90° is changed from horizontal to vertical and is rejected by the polarizer.

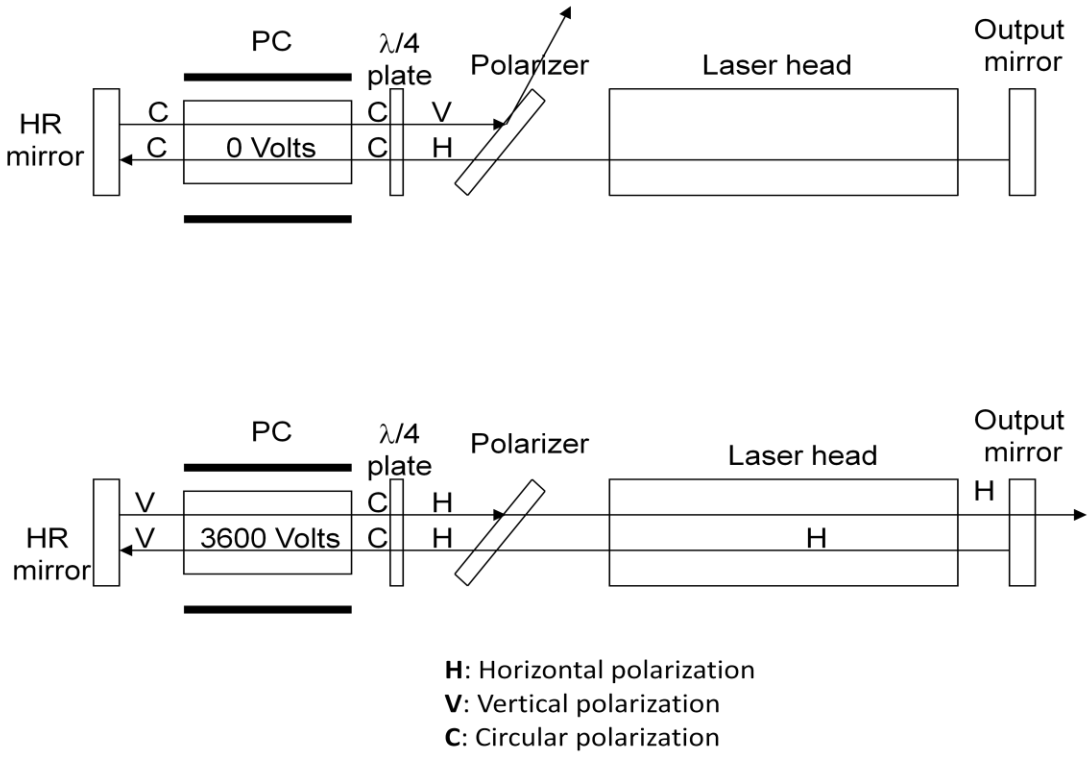

Figure 2.5 The oscillator cavity of Nd:YAG laser.[119]

2.3.2 Dye Laser

In Chapter 5, UV light with λ = 308.75 nm was provided from a ND6000 dye laser using 2nd harmonic generation. The main parts of the ND6000 laser are a dye oscillator and two amplifier cells, which are all pumped by 532 nm light from a Nd:YAG laser. The dye oscillator contains a Moya dye laser cavity, which includes a tuning mirror, a grating, a beam expander, a dye cell and a cavity mirror to generate tunable beams in terms of different dyes. Using different dye solutions, the Moya oscillator provides tunable visible beams with narrow linewidths and low background fluorescence.

The dye laser output beam with λ = 605–630 nm is shown in Figure 2.6. Methanol solutions for the dye Rhodamine 640 were used. A strong solution (214 mg /1) was used for the oscillator cell and a more dilute solution (110 mg/1) was used for the amplifier cell. Harmonic generation of the dye output was obtained by doubling in KD*P. A Pellin-Broca prism separates the doubled dye beam from the fundamental dye beam.

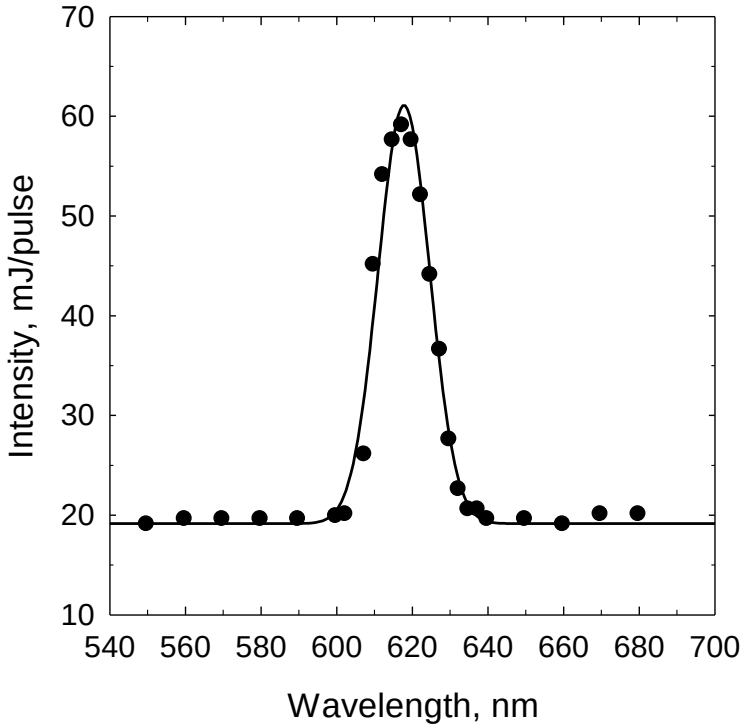

Figure 2.6 The visible output beam of the dye Rhodamine 640 methanol solution in ND6000 dye laser. The peak intensity is at 615.5 nm.

Chapter 3: Dynamics of Weak and Strong Collisions: Highly Vibrationally Excited Pyrazine(E = 37900 cm^{-1}) with DCl

3.1 Introduction

Strong collisions that deactivate highly excited molecules compete with reactive processes when they remove enough energy to put the molecule below a critical reaction threshold energy.[2,6] However, a number of studies on unimolecular reactions illustrate the importance of "weak" collisions that induce small changes in energy.[13,15,16] Energy transfer distribution functions obtained from experiments show that weak collisions occur far more often than strong collisions, but dynamical information on weak collisions is difficult to obtain experimentally. By their very nature, weak collisions induce only small changes to the energies and quantum states of the colliding molecules, making it difficult to distinguish their initial and final energy profiles.

Chapter 1 discusses how weak and strong collisions can be measured by the high-resolution transient IR spectroscopy. This Chapter reports the rotational and translational energy gain profiles of DCl (v=0) molecules in low-J states that are populated by weak collisions with vibrationally excited pyrazine (E = 37900 cm^{-1}). Combined with earlier high-J data,[120] the complete range of weak and strong collisions is characterized.

The dynamics of pyrazine(E)/DCl collisions are reported here. The experimental data show that the low-J states of DCl have recoil velocity distributions near T_{rel} = 700 K for J = 2–15 states. The average recoil velocities increase for higher J-states of DCl. A single rotational distribution with T_{rot} = 880 K describes the scattered DCl (v = 0) molecules with J = 2–21. In addition to V–RT energy transfer measurements, this

Chapter also reports vibration-to-vibration (V–V) energy transfer and finds that V–RT energy transfer is the primary relaxation pathway for highly excited pyrazine(E) through collisions with DCl bath molecules.

Another important aspect of high-resolution IR energy transfer measurements in this Chapter is that absolute rate constants for specific energy transfer pathways are determined. The observed collision rate includes the full distribution of collision outcomes. Since V–RT energy transfer is the primary outcome of pyrazine(E)-DCl collisions, the experimental rate constant for V–RT energy transfer is the lower limit to the inelastic collision rate. Data of this type are extremely useful in testing the quality of model potential that are commonly used to describe molecular collisions, such as the Lennard-Jones potentials, and in establishing guidelines for combining parameters in collision systems that can have hydrogen-bonding interactions.[121] The scattered DCl (v = 0) molecules have an appearance rate constant that is ~85% of the Lennard-Jones collision rate. A small amount of population in DCl (v = 1) is observed as a collision product with an estimated energy transfer rate that is a few percent of the Lennard-Jones collision rate. The energy transfer probability distribution function based on these data is reported. The results are compared with Lennard-Jones collision rates and average energy transfer values from the literature.

3.2 Experimental Methods

The measurements of scattered DCl molecules were performed on a high-resolution transient IR diode laser absorption spectrometer which has been discussed in Chapter 2. The specifics are given here. A 1:1 gas mixture of DCl and pyrazine flowed through a 3 meter collision cell at a total pressure of ~20 mTorr. Highly vibrationally

exited pyrazine was prepared by absorption of 266 nm light from the Nd: YAG laser. 266 nm light excited pyrazine to the S_2 state which undergoes radiationless decay ultimately leading to high vibrational levels in the S_0 state. This process occurs with near unity quantum yield in ~50 ns.[104,105] The UV power density was kept lower than 1.7 MW/cm^2 to avoid multiphoton absorption and to keep the fraction of excited pyrazine molecules at less than 15%.

A liquid-nitrogen-cooled cw IR diode laser at λ = 4.3 μm was passed through the sample cell overlapped with the UV beam. State-specific populations of scattered DCl in the (v = 0) vibrational state were probed by transient IR absorption of DCl (v = 0, J) → (v = 1, J+1) R-branch transitions. The IR light was also used to probe the appearance of scattered DCl molecules in the (v = 1) state by measuring DCl (v = 1, J) → (v = 2, J+1) R-branch transitions.

The average time between collisions in the DCl/pyrazine mixture was $\tau_{col} \approx 4$ μs. Nascent DCl populations resulting from single collisions with hot pyrazine were determined at t = 1 μs after UV pulse using the DCl spectral information listed in Table A.1.[122-124]

Nascent Doppler-broadened line profiles for a number of DCl rotational states with J = 2–12 were obtained by collecting transient absorption signals as a function of IR wavelength. Approximately 10% of the IR light passed through a scanning Fabry-Perot etalon. The IR frequency was locked at the center of an etalon fringe by using a lock-in amplifier. Transient signals were collected at roughly 40 frequency increments across a given line profile.

Pyrazine(Aldrich, 99%+) was degassed by freeze-pump-thawing before use. DCl (Cambridge Isotope Laboratories, chemical purity 98% and deuterium purity 99%) was used directly without purification. The DCl sample contained the natural abundance (3:1 ratio) of Cl isotopes (^{35}Cl:^{37}Cl).

3.3 Results and Discussion

This Chapter shows the energy gain profiles for DCl (v = 0) molecules that are scattered into the J = 2–12 states due to collisions with vibrationally excited pyrazine (E = 37900 cm^{-1}). Doppler-broadened line profiles based on high-resolution transient IR absorption measurements yield nascent J-specific velocity distributions, populations, and energy transfer rates. Results are combined with earlier data on the J = 15–21 states of DCl to consider the full distributions of collisional energy transfer.[120] The following Sections will present and discuss the translational and rotational energy profiles of the scattered DCl molecules in the v = 0 state, the energy transfer rate constant for the V–RT pathway, its connection to the collision rate, and the full energy transfer distribution function for V–RT collisions between pyrazine(E) and DCl. This Chapter also reports on the observation of collisions that lead to vibrationally excited DCl (v = 1).

3.3.1 Transient Line Profiles of Scattered DCl Molecules in (v = 0) and (v= 1)

To measure the outcome of weak collisions using state-resolved IR probing, it is necessary to distinguish the ambient background from molecules that are scattered in the low-J states. Appreciable background absorption is observed for the J = 2–7 states of DCl (v = 0) at 300 K. When highly vibrationally excited pyrazine is generated with 266 nm pulsed light, the transient absorption of the DCl low-J states contains two components.

When the IR laser is tuned to line center ν_0 of a low-J transition, depletion of the initial DCl population is observed as the molecules in this state undergo collisions with pyrazine(E). In Figure 3.1a, the negative-going signal represents net depletion of the DCl J = 5 population at ν_0. The second component corresponds to appearance of collision products and is seen in the Doppler-broadened wings. In Figure 3.1b, the IR laser frequency is tuned 0.003 cm^{-1} away from the transition center, where a positive-going absorption signal indicates the appearance of DCl molecules in the J = 5 state that result from collisions with pyrazine(E).

This Chapter also reports the observation of transient IR absorption that corresponds to appearance of the DCl (v = 1) state from collisions of pyrazine(E) with DCl (v = 0). Linear absorption is directly proportional to the population difference between the lower and the upper states, so measurements of DCl (v = 0) are affected by any population in the DCl (v = 1) state. At 300 K, the DCl (v = 1) population cannot be detected in this experiment, but DCl molecules in the (v = 1) state are formed in small amounts through collisions with pyrazine(E).

The transient signal for appearance of DCl in the (v = 1, J = 6) state is shown in Figure 3.2a. The (v = 1, J = 6) state is the upper state of the (v = 0) R5 probe transition shown in Figure 3.1a, b. Figure 3.2b shows the Doppler-broadened line profile for the (v = 1, J = 6) state measured at t = 1 μs following the UV excitation of pyrazine. This transition is broadened with a full width half-maximum that corresponds to a translational temperature of T ~ 2000 K, suggesting that vibrational energy gain in DCl occurs through impulsive collisions. The population of scattered DCl molecules in the (v = 1, J = 6) state is less than 1% of the transient population in the (v = 0, J = 5) state and has

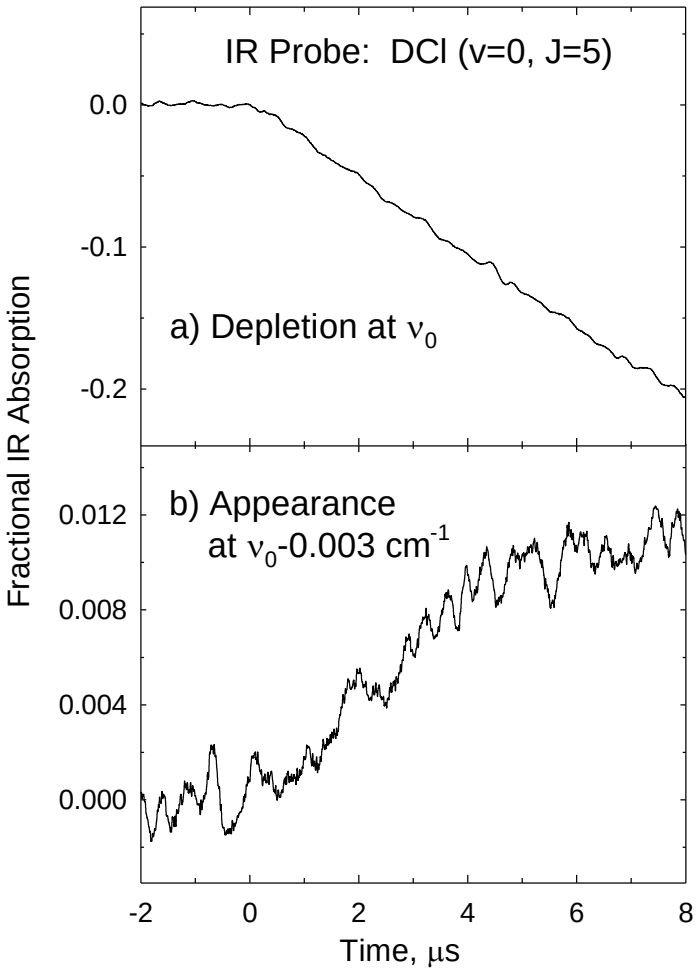

Figure 3.1 Transient absorption signals for the J = 5 state of DCl collisions due to collisions with highly vibrationally excited pyrazine(E = 37900 cm^{-1}) at two different IR frequencies. Panel a shows depletion of initial population at line center ν_0. In Panel b, the IR probe is tuned to the wings of the absorption profile at frequency ν_0–0.003 cm^{-1}. Here, the appearance of DCl molecules that are products of collisional energy transfer is observed.

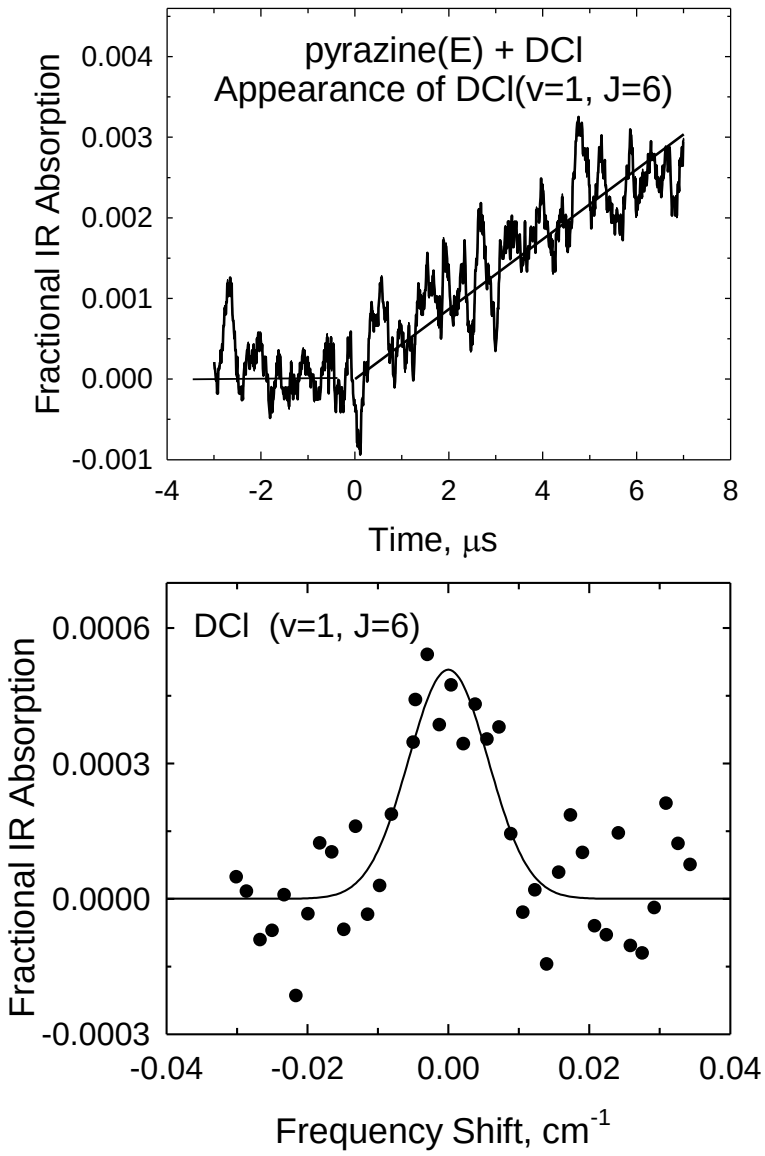

Figure 3.2 (a) Transient IR absorption of appearance of DCl (v = 1, J = 6) that results from collisions of pyrazine(E) and DCl (v = 0), collected at the transition center. (b) Transient absorption line profile for the J = 6 state of DCl (v = 1) measured 1 μs after the UV excitation of pyrazine.

negligible impact on the transient signals for DCl (v = 0). The signal levels for the DCl (v = 1) state in this experiment were too small to characterize the full distribution of rotational states associated with energy gain the (v = 1) state.

Transient absorption signals for the DCl (v = 0) state (such as in Figure 3.1a, b) are linear for the first few microseconds, corresponding to population changes caused by single collisions between DCl and pyrazine(E). IR intensities at t = 1 μs are used to describe the nascent DCl populations. Doppler-broadened line profiles at t = 1 μs were measured for individual rotational states of DCl. Figure 3.3 shows the transient line profile for the v = 0, J = 5 state. Depletion of population dominates the profile at line center, while appearance of scattered DCl molecules is seen in the wings of the profile.

Transient line profiles such as those shown in Figure 3.3 are fit with a six-parameter double-Gaussian function using nonlinear least-squares analysis to account for both appearance and depletion components, as shown in Eq 3.1.

$$F(\nu)=I_{app}\exp\left[-4\ln 2\left(\frac{\nu-\nu_0}{\Delta\nu_{app}}\right)^2\right]-I_{dep}\exp\left[-4\ln 2\left(\frac{\nu-\nu_0}{\Delta\nu_{dep}}\right)^2\right]+F_0 \qquad (3.1)$$

Here, F_0 is a small baseline offset; ν_0 is the center absorption frequency; I_{app} and $\Delta\nu_{app}$ are the intensity and line width for appearance of product DCl molecules; and I_{dep} and $\Delta\nu_{dep}$ are the intensity and line width that correspond to the depletion of initially populated DCl states. Unique fitting results were obtained for all transitions without external constraints. The result of the fit for the (v = 0, J = 5) state is shown in Figure 3.3 as a solid line, and the residuals are shown in the lower section of Figure 3.3. The fitting procedure yields intensity and line width parameters for the appearance and depletion components.

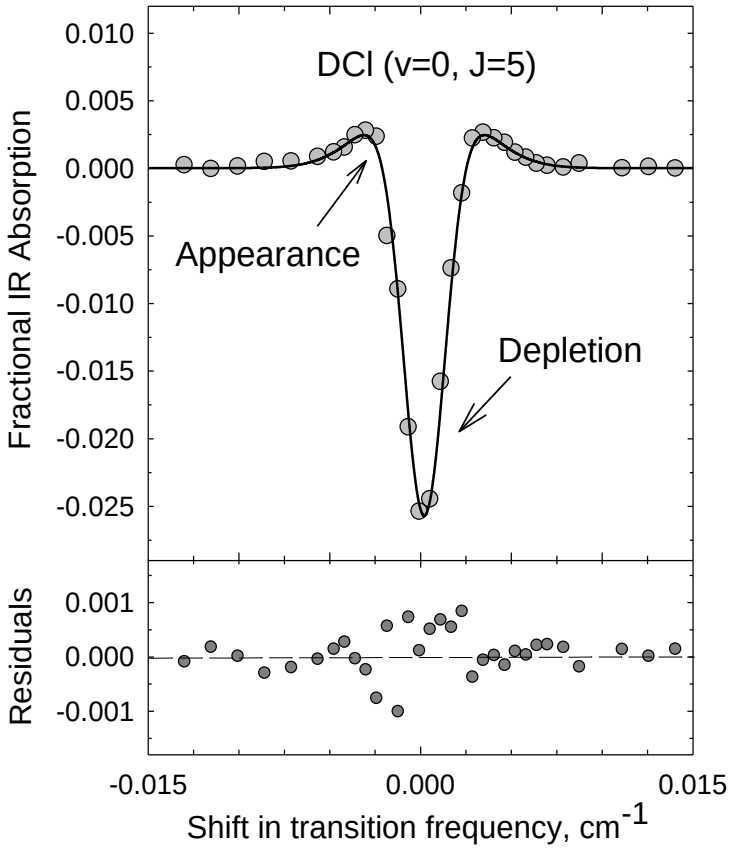

Figure 3.3 (a) Transient absorption line profile for the J = 5 state of DCl (v = 0) measured 1 μs after the UV pulse. The circles are transient IR absorption, and the solid line is the result of fitting with a double-Gaussian function to account for both appearance and depletion of population. (b) Residuals of the fit.

In Figure 3.4, the appearance component is shown in red and that for depletion is shown in blue. The integrated area under the red appearance curve corresponds to the total population of DCl (v = 0) molecules that have scattered into the J = 5 state at t = 1 μs. The integrated area under the blue curve corresponds to the total population of DCl (v = 0) J = 5 molecules that are scattered away by collisions. Similar curves were obtained for each J state investigated. The distribution of recoil velocities in these measurements is expected to be isotropic (with Gaussian line shapes) since collisions do not occur preferentially along a particular laboratory axis. To check for any such preference, we have performed a series of polarization-dependent studies and verified that transient line profiles are invariant to the polarization and crossing orientation of the UV and IR beams.

3.3.2 Energy Profiles of Scattered DCl (v = 0) Molecules

Line widths for appearance Δv_{app} describe the nascent velocity distributions of the scattered DCl molecules in the J = 2–12 states and correspond to laboratory frame translational temperatures of T_{app} = 480–640 K. Values of line widths and translational temperatures are listed in Table 3.1.

The line widths for depletion Δv_{dep} describe the velocity distribution of the DCl molecules prior to collisions with pyrazine(E). The observed depletion line widths are narrower than 300 K line widths, suggesting that collisions of pyrazine(E) with DCl may preferentially involve a subset of slower molecules. This result is somewhat surprising given that molecules with higher relative velocities have higher collision rates. In other studies, our group has found that collisions of pyrazine(E) with other bath molecules, such as HOD[78,79] and CO_2 (Chapter 4) have depletion line widths that correspond to 300K

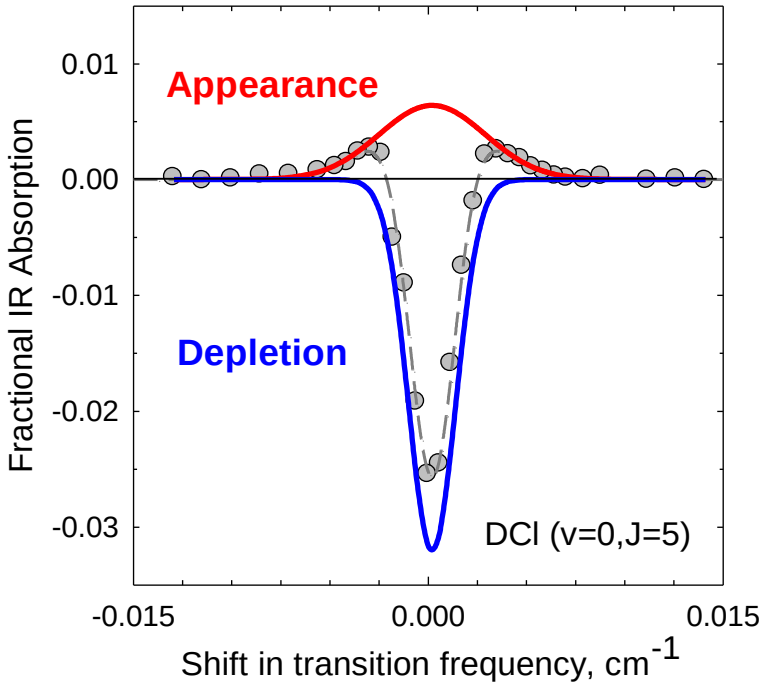

Figure 3.4 Separate appearance and depletion components of the transient line profile for DCl (v = 0) J = 5. The grey circles are transient IR data, and the dashed line is the double-Gaussian fitting curve. The appearance component (red line) is broadened due to collisions, with a line width that corresponds to a translational temperature of T_{app} = 480 ± 130 K. The depletion component (blue line) is caused by population loss of the J = 5 state and has a translational temperature of T_{dep} = 170 ± 80 K.

Table 3.1 Nascent Doppler-broadened line widths and translational temperatures for low-J states of DCl that are populated/depopulated through collisions with vibrationally excited pyrazine(E = 37900 cm^{-1}).

J state	Appearance of scattered DCl(v = 0,J)			Depletion of initial DCl(v = 0, J)	
	$\Delta\nu_{app}$, cm^{-1}[a]	T_{app}, K[b]	T_{rel}, K[c]	$\Delta\nu_{dep,}$ cm^{-1}[a]	$T_{dep,}$ K[d]
2	0.0058	570 ± 140	710 ± 170	0.0034	200 ± 100[f]
3	0.0054	490 ± 130	590 ± 150	0.0028	140 ± 80
4	0.0064	640 ± 140	800 ± 180	0.0031	150 ± 80
5	0.0054	480 ± 130	570 ± 150	0.0033	170 ± 100
7	0.0064	620 ± 140	770 ± 170	0.0033	170 ± 100
12	0.0060	520 ± 120	630 ± 150	—	—

[a]Full width at half-maximum (FWHM) line widths $\Delta\nu_{app}$ and $\Delta\nu_{dep}$ for appearance and depletion components, respectively, of individual states of DCl (v = 0) measured 1 μs after UV excitation of pyrazine. Line widths are reported to ± 0.001 cm^{-1}.

[b]The lab-frame translational temperatures for appearance (T_{app}) and depletion (T_{dep}) are determined from line widths using $T_{trans,lab}=\left(\frac{mc^2}{8Rln2}\right)\left(\frac{\Delta\nu_{obs}}{\nu_0}\right)^2$, where m is the mass of DCl, c is the speed of light, R is the gas constant, the full width at half-maximum widths $\Delta\nu_{obs}$ is $\Delta\nu_{app}$ for appearance and $\Delta\nu_{dep}$ for depletion, and ν_0 is the center frequency of the absorption line.

[c]T_{rel} in K, the center-of-mass frame translational temperature for appearance of scattered DCl, is determined for an isotropic distribution:

$T_{rel}=T_{trans,lab}+(m_{DCl}/m_{pyz})(T_{trans.lab}-T_0)$, where, m_{DCl} and m_{pyz} are the masses of DCl and pyrazine, respectively and T_0 =300 K.

[d]The translational temperatures based on depletion line widths for initial DCl states.

velocity distributions. There is some precedent however for collision cross-section that increase as a function of decreasing velocity. A negative velocity dependence for collision cross-sections has been observed in collisions of Li_2 (v = 1) with Xe, Ar, and Ne that lead to quasi-resonant vibration to rotation energy transfer.[125] It is also known that in cases where collisions are dominated by attractive interactions (such as in thermal atomic beams), the collision cross-section is inversely proportional to the relative velocity. For a purely attractive potential where $V(r) = -C/r^6$, the velocity-dependent collision cross-section $\sigma(v)$ is proportional to $v^{-\frac{2}{5}}$ and a negative temperature dependence is observed.[126] It is not entirely clear why pyrazine(E)-DCl collisions have low initial velocities, while HOD and CO_2 show no such preference.

The distributions of recoil velocities are described by the center-of-mass frame translational temperatures T_{rel}. The distributions of relative recoil velocities for the J = 2–12 states of DCl have values of T_{rel} = 570–800 K. These values are listed in Table 3.2 and are shown in Figure 3.5 along with earlier high-J results. The recoil velocity distributions for the low-J data have values of $T_{rel} \sim 700$ cm^{-1} until J = 15. For J > 15, the translational energy distributions broaden substantially.

Impulsive collisions can impart large changes in both angular momentum and recoil velocity. Figure 3.5 shows that in collisions of pyrazine(E) with DCl, a threshold for the onset of increasing recoil velocities occurs near J = 15. The correlation of angular momentum changes and recoil velocity is consistent with the Angular Momentum Model by McCaffery and co-workers.[127-130] Based on an initial J = 5 state at 300 K, the average change in recoil velocity of the scattered DCl molecules is compared with average changes in angular momentum in Table 3.2.

Table 3.2 Angular momentum and recoil velocities for individual states of DCl J = 2–20 due to collisions with highly vibrationally excited pyrazine(E = 37900 cm^{-1})

final J state	$\langle \Delta J_{bath} \rangle$[a]	$\Delta\nu_{app}$[b]	$\langle v_{lab} \rangle$[c]	$\langle v_{rel} \rangle$[d]	$\langle \Delta v_{rel} \rangle$[e]
2	4.6	0.0058	603	817	285
3	4.0	0.0054	559	744	212
4	3.0	0.0064	659	890	348
5	0	0.0054	554	736	203
7	4.9	0.0064	650	877	335
12	10.9	0.0060	600	800	254
15[f]	14.1	0.0063	619	828	286
16	15.2	0.0064	627	840	298
17	16.2	0.0065	635	853	311
18	17.3	0.0068	663	897	355
19	18.3	0.0069	671	910	368
20	19.4	0.0075	728	998	456

[a]The average angular momentum changes $\langle \Delta J_{bath} \rangle$ in units of $\hbar$ of DCl after collisions with vibrationally excited pyrazine are estimated using $\langle \Delta J_{bath} \rangle^2 = \left| \langle J'_{bath} \rangle^2 - \langle J_{bath} \rangle^2 \right|$. $\langle J'_{bath} \rangle$ is the average final angular momentum vector of DCl determined. The average initial angular momentum vector of DCl at 300 K is $\langle J_{bath} \rangle \sim 5$.

[b]FWHM appearance line widths $\Delta\nu_{app}$ in cm^{-1} for DCl (v = 0) as described in Table 3.1.

[c]The average lab-frame velocity in m (s^{-1}) of individual DCl states following collisions with vibrationally excited pyrazine, determined from

$\langle v_{lab} \rangle = \left(3k_B T_{app}/m_{DCl}\right)^{1/2}$, where, k_B is the Boltzmann constant, T_{app} is listed in Table 3.1, and m_{DCl} is the mass of DCl.

[d]The average center-of-mass frame velocity $\langle v_{rel} \rangle$ in m (s^{-1}) for scattered pyrazine and DCl molecules, determined by $\langle v_{rel} \rangle = \left(M/m_{pyz}\right) \cdot [\langle v_{lab} \rangle^2 - (3k_B T/M)]^{1/2}$, where M is the total mass of pyrazine and DCl, m_{pyz} is the mass of pyrazine, and T = 300 K.

[e]The average change in relative velocity $\langle \Delta v_{rel} \rangle = \langle v_{rel} \rangle - (3k_B T/\mu)^{1/2}$, where μ is the reduced mass for DCl + pyrazine collisions.

[f]Data for the J = 15–20 states are for the $D^{35}Cl$ isotope and are taken from Ref. 87.

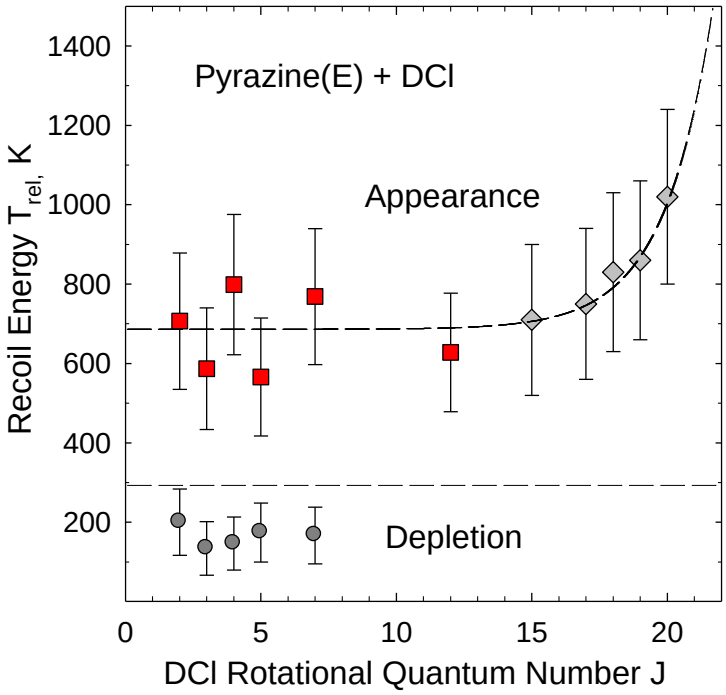

Figure 3.5 Rotational state dependence of the nascent center-of-mass translational temperatures for pyrazine(E)/DCl collisions. Squares show the translational temperatures for appearance of DCl states with J = 2–20 due to collisions with highly vibrationally excited pyrazine(E = 37900 cm^{-1}). Data for the J = 15–20 states are shown as diamonds and are from Ref. 87. Circles are lab-frame temperatures for depletion of DCl via collisions with hot pyrazine.

Our group discussed how the angular momentum changes were determined before this thesis.[120] Measurements of the product translational energies for a large range of CO_2 rotational states gave us the opportunity to consider how the angular momentum of the scattered bath molecules correlates with recoil velocity. Classically, the change in total angular momentum vector $\Delta\vec{J}_{total}$ due to collisions is related to the reduced mass μ, the change in recoil velocity $\Delta\vec{v}_{rel}$ and the impact parameter $\vec{b}$ as shown in Eq 3.2.

$$\Delta\vec{J}_{total}=\Delta\left(\vec{L}+\vec{J}_{rot}\right)=\Delta\left(\vec{L}+\vec{J}_{bath}+\vec{J}_{donor}\right)=\mu\Delta\vec{v}_{rel}\vec{b} \qquad (3.2)$$

For molecules, the change in total angular momentum is the vector sum of changes in orbital angular momentum $\vec{L}$ and rotational angular momentum $\vec{J}_{rot}$ (which includes rotation of both collision partners). Ideally, one would like to have state-resolved data on the rotational changes in both bath and donor molecules. The state-resolved measurements here exactly specify J_{bath} for the scattered CO_2 bath molecules but do not give information about the state-to-state changes in DCl or about the angular momentum changes of the high-energy donor molecules. Lawrence and Waclawik report that angular momentum changes for donor and bath molecules of the type considered here generally have the same sign, so that the final $\vec{J}_{bath}$ is a lower limit to the final $\vec{J}_{rot}$, in cases of small $\Delta\vec{L}$.[131] Changes in orbital angular momentum are zero for scattering in a central force potential, such as used in a Lennard-Jones model. The agreement between the Lennard-Jones collision rate and our measured collision rate therefore suggests that the changes in orbital angular momentum in these collisions are small. On the basis of these considerations, the change in bath rotational angular momentum $\vec{J}_{bath}$ represents a

lower limit to the overall change in angular momentum. Pyrazine(E)-DCl collisions with $\langle \Delta J_{bath} \rangle$ = 0–16 correspond to changes in recoil velocity of $\langle \Delta v_{rel} \rangle$ = 300 $m \cdot s^{-1}$. For the highest angular momentum changes $\langle \Delta J_{bath} \rangle$ = 17–19, the changes in recoil velocity increase to as much as $\langle \Delta v_{rel} \rangle$ = 450 $m \cdot s^{-1}$.

In Chapter 4, a correlation between angular momentum and recoil velocity is also observed in collisions of pyrazine(E = 37900 cm^{-1}) with CO_2, but in this case, values of $\langle \Delta J \rangle$ and $\langle \Delta v_{rel} \rangle$ are substantially greater than when DCl is the bath molecule. Scattered CO_2 molecules are observed in high angular momentum states with J = 60–80 with average velocity changes of $\langle \Delta v_{rel} \rangle$ ~ 1200–2200 $m \cdot s^{-1}$, respectively.[76,91] Rotational states of CO_2 with J = 60–80 have comparable amounts of energy (E_{rot} = 1442 and 2553 cm^{-1}, respectively) as DCl states with J = 16–20 (E_{rot} = 1452 and 2242 cm^{-1}, respectively), but CO_2 molecules in these high-J states are scattered from pyrazine(E) with much more translational energy. This effect may be due in part to the larger angular momentum changes that are observed for CO_2 and in part to differences in the mass distributions of DCl and CO_2. The amount of rotational and translational energy in the scattered molecules (as well as the partitioning of this energy) depends in a nontrivial way on the collision dynamics, the anisotropy of the intermolecular potential, and the kinematics of the collisions, so a direct comparison of energy partitioning for CO_2 and DCl is not possible. However, when similar amounts of rotational energy are imparted to bath molecules in collisions, the experimental data in these Chapters show that bath molecules with more closely spaced rotational states (and higher angular momentum) are scattered with larger recoil velocities. The rotational constant for CO_2 (B = 0.39 cm^{-1}) is relatively small as compared to that for DCl (B = 5.4 cm^{-1}).

In other work, no such J-dependent increases in T_{rel} were observed for collisions of pyrazine(E) with H_2O or HOD.[79] Water has small moments of inertia (A = 27.9 cm^{-1}, B = 14.5 cm^{-1}, and C = 9.3 cm^{-1}), and scattered H_2O molecules are observed with rotational energies up to E_{rot} = 1800 cm^{-1} in states with J = 12. It is not known whether a threshold to the recoil energy distributions exists for higher J states of water, such as seen for DCl and CO_2. Detection of higher J states of water following collisions with pyrazine(E) requires better experimental sensitivity than is currently realized. If the recoil velocities do increase with the higher J states of water, then the onset occurs at J values higher than J = 12. It is possible that the mass distribution of water reduces the likelihood of translational energy gain relative to rotational energy in the scattered molecules. It may also be the case that attractive interactions between pyrazine(E) and water influence the energy gain partitioning between the rotational and the translational degrees of freedom. There is evidence from other measurements in the Mullin labs that preferential interactions of water with the π- and σ-hydrogen bonding sites on pyridine (C_5H_5N) may favor rotational energy gain in water over translational energy gain.[80] Whether these types of interactions play a role in determining energy partitioning from collisions remains to be seen. Computer simulations should be useful in clarifying the importance of this phenomenon.

The rotational distribution of scattered DCl (v = 0) molecules that results from collisions with pyrazine(E) is determined directly from the nascent populations of DCl J = 2–21 states. A semilog plot of the rotationally resolved populations of scattered DCl (v = 0) molecules measured 1 μs following collisions with pyrazine(E) is shown in Figure 3.6. The scattered molecules are well-described by a single Boltzmann distribution with

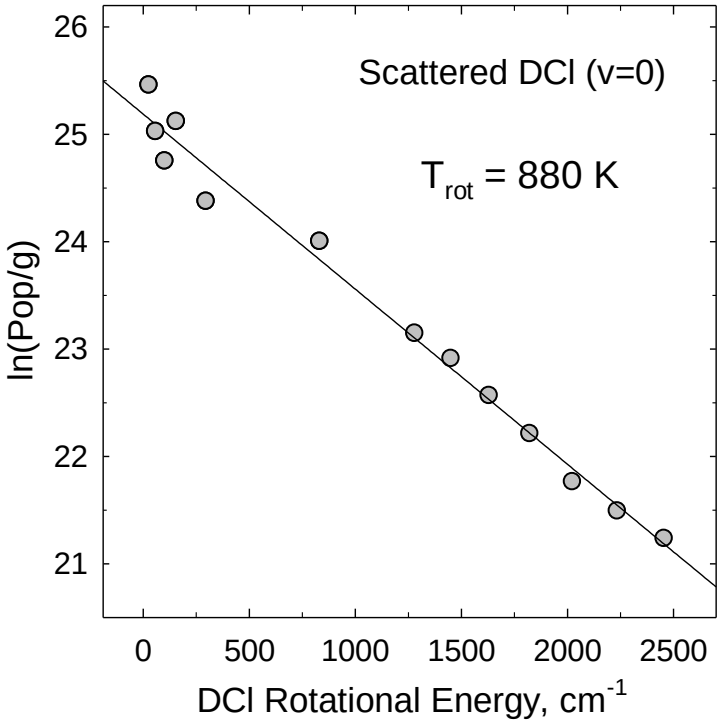

Figure 3.6 Nascent rotational distribution for the J = 2–21 states of DCl that are populated through collisions with vibrationally excited pyrazine. Data for the J = 15–20 states are from Ref. 87. The appearance of DCl molecules due to weak and strong collisions is described by a single Boltzmann distribution with T_{rot} = 880 ± 100 K.

a rotational temperature of T_{rot} = 880 ± 100 K. This result is in good agreement with the previous analysis that considered only the high-J states.[87]

3.3.3 Energy Transfer Rates: Pyrazine(E = 37900 cm^{-1}) + DCl

State-specific rate constants for energy transfer that populates individual rotational states of DCl (v=0) products were determined from J-specific appearance signals (as shown in Figure 3.4). The rate constant k_{app}^{J} describes the rate of appearance of DCl (v = 0, J) population that comes from quenching collisions of pyrazine(E), as shown in Eq 3.2.

$$\text{Pyrazine (E)} + \text{DCl (300 K)} \xrightarrow{k_{app}^{J}} \text{Pyrazine (E')} + \text{DCl (v = 0, J)} \qquad (3.2)$$

The appearance rate of DCl (v = 0, J) is given by Eq 3.3.

$$\frac{d[\text{DCl(J)}]}{dt} = k_{app}^{J}\,[\text{DCl}]_0[\text{Pyrzine (E)}]_0 \qquad (3.3)$$

Based on the method of initial rates, the appearance rate constant k_{app}^{J} is determined using Eq 3.4, where $[DCl]_0$ and $[Pyrazine(E)]_0$ are the concentrations at t = 0.

$$k_{app}^{J} = \frac{\Delta[\text{DCl(J)}]}{\Delta t} \cdot \frac{1}{[\text{DCl}]_0 \cdot [\text{Pyrazine(E)}]_0} \qquad (3.4)$$

The absolute rate constant for energy gain into the J = 3 state was measured using Eq 3.4, and rate contants for the other rotational states of DCl (J = 2–12) were determined using the nascent rotational temperature (Figure 3.6). Values of k_{app}^{J} are listed in Table 3.3 for the J = 2–21 states of DCl (v = 0). These experimental results are in very good agreement with the rates published previously for the J = 15–21 states.[120]

The kinetics of the V–RT energy transfer pathway is described by the rate constants listed in Table 3.3. The total rate constant for V–RT energy transfer based on appearance measurements is obtained by summing over the J states of the scattered DCl molecules as shown in Eq 3.5.

$$k_{app} = \sum_J k_{app}^{J} = (4.6 \pm 1.4) \times 10^{-10} \text{ cm}^3\text{molecule}^{-1}\text{ s}^{-1} \qquad (3.5)$$

V–RT energy transfer is just one pathway for inelastic collisions of pyrazine(E) with DCl. The value of k_{app} represents a lower limit to the collision rate constant and is ~85% of the Lennard-Jones collision rate constant ($k_{LJ} = 5.4 \times 10^{-10}$ cm^3 molecule^{-1} s^{-1} at 300 K). As discussed previously, energy gain into the (v = 1) state of DCl occurs rarely with a rate that is roughly 1% of the Lennard-Jones collision rate, and it is unlikely that higher vibrational states of DCl are populated by collisions. Therefore, k_{app} is essentially the collision rate constant for pyrazine(E)-DCl collisions and is in reasonably good agreement with the Lennard-Jones collision rate.

State-resolved population depletion measurements can also be used to get a lower limit to the collision rate. The depletion component of the Doppler-broadened transient

Table 3.3 State-specific rate constants for appearance of DCl products due to collisions of Pyrazine(E = 37900 cm^{-1}) + DCl → Pyrazine(E−ΔE) + DCl (v = 0, J).

DCl J-State	E_{rot}, cm^{-1}	k^J_{app}, 10^{-12} $cm^3 \cdot molecule^{-1} \cdot s^{-1}$
2	32.2539	26 ± 8
3	64.4979	23 ± 7
4	107.7895	23 ± 7
5	161.1696	40 ± 12
7	301.5287	26 ± 8
12	837.7971	30 ± 9
15[a]	1286.115	19 ± 5
16	1456.389	16 ± 4
17	1636.995	12 ± 3
18	1827.878	8.9 ± 2
19	2028.978	6.0 ± 1
20	2240.233	4.8 ± 1
21	2461.58	3.9 ± 1
$k_{app} = \sum_J k^J_{app}$		$(4.6 \pm 1.4) \times 10^{-10}$ $cm^3 \cdot molecule^{-1} \cdot s^{-1}$[b]
k_{LJ}		5.4×10^{-10} $cm^3 \cdot molecule^{-1} \cdot s^{-1}$[c]

[a]Rate constants for the J = 15–21 states are taken from Ref. 87.

[b]Total appearance rate constant k_{app} for V–RT energy transfer of pyrazine(E)/DCl system, obtained by summing over the J-specific appearance rates k^J_{app}.

[c]The Lennard-Jones collision rate at 300 K for pyrazine/DCl determined in Appendix B. The Lennard-Jones parameters were used:

$\sigma_{DCl}=3.36 \times 10^{-10}$ m,[132] $(\varepsilon/k_B)_{DCl}=328$ K,[133]

$\sigma_{pyz}=5.35 \times 10^{-10}$ m, $(\varepsilon/k_B)_{DCl}=435.5$ K [134].

line profiles consists of DCl molecules that undergo collisions with pyrazine(E). Collisions between highly excited donor molecules and DCl move population out of low-lying J states of DCl that are populated at 300 K as shown in Eq 3.6 and into a distribution of final J′ states that have recoil velocities with component v_{rel} along the IR probe axis.

$$\text{Donor (E)} + \text{DCl (J)} \rightarrow \text{Donor (E')} + \text{DCl (J', } v_{rel}\text{)} \tag{3.6}$$

It is not necessary for J and J′ to have different values to be measured as a scattering event since we measure Doppler-resolved profiles. Depletion of population is observed as long as either the velocity component along the IR probe axis or the rotational quantum number changes during collisions. The depletion rate of population in the J state is given in Eq 3.7.

$$\text{Rate}_{dep}(J) = -\frac{d[DCl(J)]}{dt} = k_{dep} f(J) [DCl]_0 [Donor(E)]_0 \tag{3.7}$$

In Eq 3.7, f(J) is the fractional population in the J state of DCl at 300 K and k_{dep} is the depletion rate constant. It is a reasonable to assume that at 300 K the collision rate does not depend on J. The total depletion rate is a sum of J-specific depletion rates as given by Eq 3.8.

$$\begin{aligned} \text{Rate}_{dep} &= \sum_J \text{Rate}_{dep}(J) = \left(\sum_J k_{dep} f_J [DCl]_0\right) [Donor(E)]_0 \\ &= k_{dep} [DCl]_0 [Donor(E)]_0 \end{aligned} \tag{3.8}$$

The total depletion rate constants are reported in Table 3.4 based on measurements of double Gaussian transient line profiles for low J states of DCl. The population weighted average of the depletion rate constants is $k_{dep}=(4.3 \pm 1.5) \times 10^{-10}$ cm^3 $molecule^{-1}$ s^{-1}. This result is in very good agreement with the total appearance rate constant of $k_{app} = (4.6 \pm 1.4) \times 10^{-10}$ cm^3 $molecule^{-1}$ s^{-1}. The agreement of rates based on depletion and appearance gives us confidence in the consistency of this approach for measuring collision rates experimentally.

The agreement between the observed collision rate and the Lennard-Jones rate for DCl-pyrazine(E) collisions is somewhat surprising. HCl is known to form 1:1 hydrogen-bonded complexes with aromatic molecules.[135-138] Lennard-Jones parameters typically do not account for the effects of hydrogen bonding and often underestimate actual collision rates for molecules that are hydrogen-bonded or have other strong intermolecular interactions. In the case of HOD-pyrazine(E) collisions, the measured collision rate constant is ~70% larger than the Lennard-Jones rate constant.[78,79] The energy minima for interactions of benzene-water and benzene-HCl have similar energies (~1100 cm^{-1}) and intermolecular distances (~3 Å).[136,139] If these interactions played an important role in collisions at 300 K, we might expect the collision rate constants for these two systems to show similar enhancements over the Lennard-Jones estimates. The fact that the Lennard-Jones collision rate for DCl-pyrazine(E) is fairly accurate indicates that hydrogen-bonding forces may not be so important in collisions of these molecules at 300 K.

Table 3.4 Depletion rate constant measurements for collisions of

Pyrazine(E = 37900 cm^{-1}) + DCl (J) → Pyrazine(E−ΔE) + DCl (v', J') at 300K.

DCl J State	E_{rot}, cm^{-1}	k_{dep}, $10^{-10} cm^3 \cdot molecule^{-1} \cdot s^{-1}$
2	32.2539	5.6
3	64.4979	3.6
4	107.7895	4.4
5	161.1696	5.1
7	301.5287	2.1
	$\langle k_{dep} \rangle$	$(4.3 \pm 1.5) \times 10^{-10}$ $cm^3 \cdot molecule^{-1} \cdot s^{-1}$
	k_{LJ}	5.4×10^{-10} $cm^3 \cdot molecule^{-1} \cdot s^{-1}$

3.3.4 Full Energy Transfer Distribution Function P(ΔE)

This study has characterized the complete distribution of DCl molecules that are scattered from vibrationally hot pyrazine and determined the absolute rate constant for collisions, as described in the preceding Section. This Section uses these results to convert J-indexed energy transfer data into an energy transfer probability distribution that is indexed by ΔE, the amount of energy lost from pyrazine(E). The state-resolved probability distributions $P_J(\Delta E)$ are determined for each rotational state of DCl based on the Doppler-broadened line widths, the energy transfer rate constants k_{app}^J and the collision rate.

The full energy transfer probability function P(ΔE) is the sum of the state-specific $P_J(\Delta E)$ over all DCl rotational states, as shown by Eq 3.9.

$$P(\Delta E) = \sum_{all} P_J(\Delta E) \tag{3.9}$$

The initial rotational and translational energy values for DCl and pyrazine were taken to be the average values at 300 K. Currently, it is not known whether there is any correlation between the initial and final J states of DCl. If such a correlation exists, it is likely that our analysis overestimates the rotational energy changes in DCl. This effect will be most pronounced for weak collisions that lead to small changes in rotational angular momentum. Future experiments that identify the initial J-state of DCl would be useful in addressing this issue.

In the upper plot of Figure 3.7 shows the P(ΔE) distribution function for energy transfer in collisions of pyrazine(E) and DCl where the probability is referenced to the

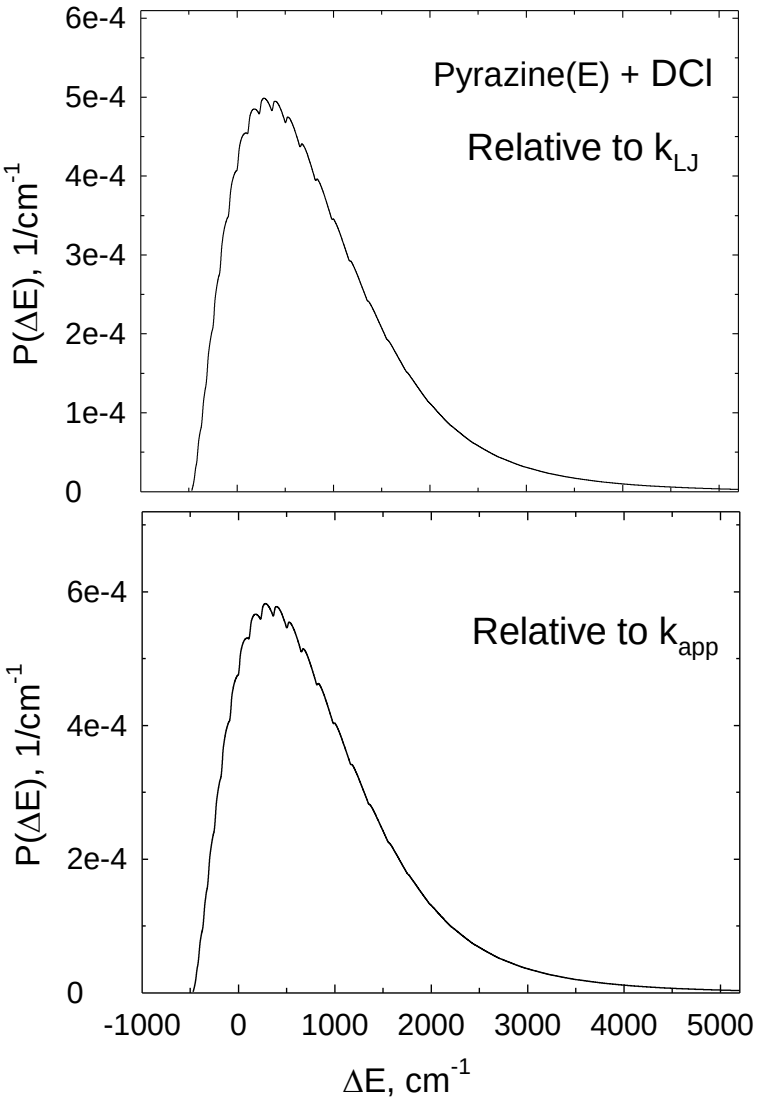

Figure 3.7 The energy transfer distribution function P(ΔE) for collisions of vibrationally excited pyrazine(E = 37900 cm^{-1}) and DCl as determined from state-resolved appearance measurements. P(ΔE) is obtained by the adding state-specific energy transfer distributions $P_J(\Delta E)$ for individual J-states of DCl, such that $P(\Delta E)=\sum_{all} P_J(\Delta E)$. Probabilities are relative to Lennard-Jones collision rate k_{LJ} (upper plot) and relative to appearance collision rate k_{app} (lower plot).

Lennard-Jones collision rate constant. In the lower plot of Figure 3.7, the experimental value of the collision rate k_{app} has been used to reference the overall probability of the distribution function. The P(ΔE) curve accounts for all V–RT energy transfer processes that are observed for pyrazine(E)-DCl collisions. The Lower P(ΔE) curve in Figure 3.7 has an integrated probability of unity.

The redistribution of pyrazine's vibrational energy is the driving force for the energy transfer investigated here. The ΔE index in P(ΔE) accounts for pyrazine internal energy that is lost due to collisions with DCl. ΔE includes the rotational energy gain in DCl and the change in translational energy for DCl and pyrazine(E) based on recoil velocity distribution measurements. It does not account for rotational energy gain in pyrazine(E) that results from collisions with DCl. The measurements in this Chapter clearly identify how energy is partitioned in the scattered DCl molecules, but the rotational and the vibrational energy content in the scattered pyrazine molecules still cannot be distinguished. In Figure 3.7, the P(ΔE) curve has a maximum intensity near $\Delta E = 250\ cm^{-1}$, which may be related to the distribution of rotational energy that is imparted to pyrazine through collisions with DCl. The P(ΔE) curve for pyrazine(E)-DCl collisions is dominated by a major feature at positive ΔE values corresponding to energy loss from pyrazine and a smaller feature for negative ΔE values that correspond to collisional energy gain in pyrazine.

Based on the data in the lower plot of Figure 3.7, the average energy transfer in collisions of pyrazine($E = 37900\ cm^{-1}$) with DCl is $\langle \Delta E \rangle = 888\ cm^{-1}$. Barker and Miller have reported average energy transfer values for pyrazine($E = 30000–33000\ cm^{-1}$) with a number of atomic, diatomic, and polyatomic collision partners.[56] However, HCl or DCl

is not among the bath molecules studied, so a direct comparison cannot be made with their work. Extrapolating their quenching data to E = 38000 cm^{-1} gives the following average energy transfer values: $\langle \Delta E \rangle \sim 50$ cm^{-1} for Ar, $\sim$ 90 cm^{-1} for CO, $\sim$ 290 cm^{-1} for CO_2 and CH_4, and $\sim$ 750 cm^{-1} for NH_3 and SF_6. Our value of $\langle \Delta E \rangle = 888$ cm^{-1} for pyrazine/DCl collisions is larger than expected based on their results but is within the same order of magnitude for small polyatomic species.

3.3.5 Comparison with Pyrazine(E)-HOD Collisions

Full energy transfer distribution functions based on state-resolved IR studies have been determined for three collision systems so far: DCl, HOD and CO_2. The HOD studies have been reported previously[79] and the CO_2 data are reported in the next Chapter. The P(ΔE) curves for collisions of pyrazine(E = 38000 cm^{-1}) with DCl and with HOD[79] are compared in Figure 3.8. Figure 3.8 plots the distribution functions using two different collision rates for defining the probability. The intensity of P(ΔE) curves comes directly from the ratio of observed energy transfer rates to the collision rate. In the upper plot, the Lennard-Jones collision rate is used to define the molecular collision rate for each collision pair. In the lower plot, the experimentally determined collision rate is used to normalize each distribution function.

It is apparent from Figure 3.8 that a comparison of different collision systems depends on the choice of collision rate. From the upper plot, it is clear that water is a more efficient quencher of pyrazine(E) because of the larger area under the HOD curve. The data in the upper plot show that the collision cross-section for pyrazine(E)/HOD at 300 K is $\sigma = 160$ $Å^2$, while that for DCl with pyrazine is $\sigma = 92$ $Å^2$. DCl is a larger collision partner than HOD, but HOD has stronger long-range attractive forces that

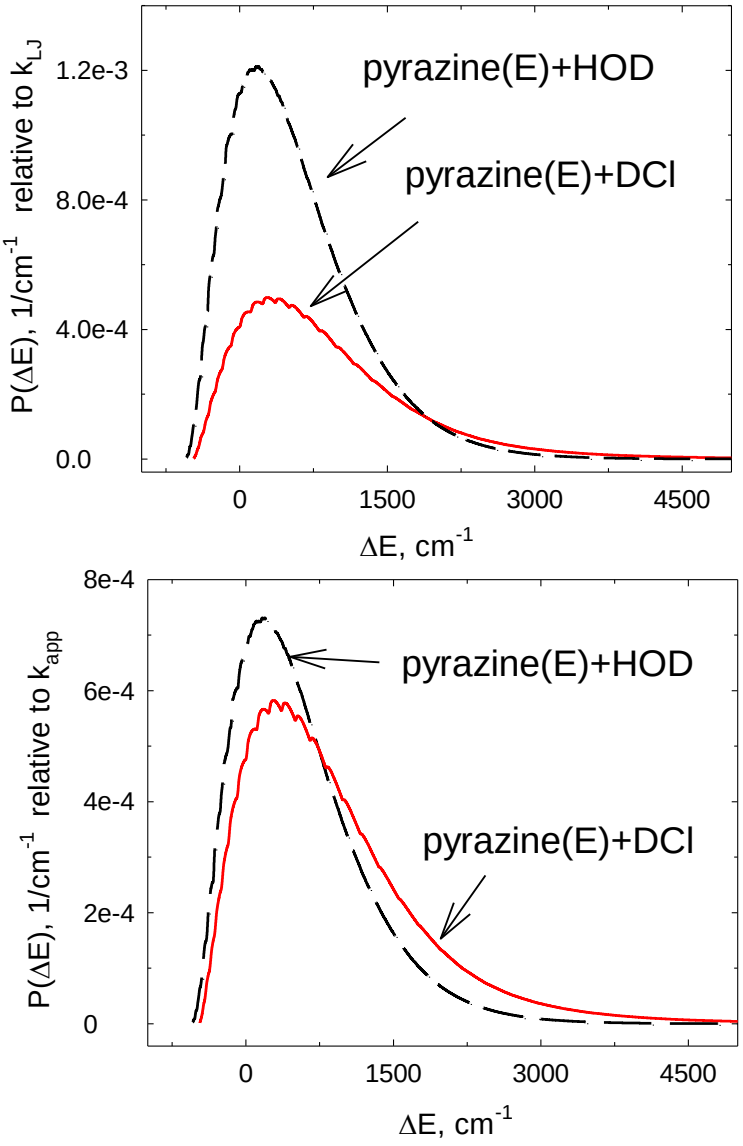

Figure 3.8 Comparison of the full energy transfer distribution function P(ΔE) curves for vibrationally excited pyrazine with HOD (taken from Ref. 79) and DCl. In the upper plot, the energy transfer data are scaled to the Lennard-Jones collision rate, and in the lower plot, the energy transfer data are scaled to the measured collision rate.

enhance the collision cross-section and are underestimated in the Lennard-Jones collision model. The fact that the collision rate for DCl-pyrazine is close to the Lennard-Jones rate suggests that long-range interactions are not very important in the collisional energy transfer between these molecules. It is important to recognize that efficient quenching by water is due in large part to its high collision rate and not from the presence of a prominent large ΔE component in the tail of the distribution function. In fact, the ΔE distribution for HOD is notably narrower than for DCl, as illustrated in the lower plot of Figure 3.8, where the observed collision rates are used to determine probabilities and the area under each curve is unity. Long-range attractive forces between pyrazine and HOD enhance the cross-section for inelastic collisions by effectively extending the range at which collisions are sufficiently strong to cause some energy transfer to take place but, at the same time, decrease the average energy transfer. In the lower plot, there are more strong collisions for quenching with DCl, which lead to DCl molecules scattered into high rotational states with broad velocity distributions. For HOD, it may be that the additional collisions caused by enhanced long-range attraction lead only to relatively weak energy transfer.

It may also be the case that HOD collisions are weaker due to details of the energy transfer involving preferential hydrogen-bonding configurations. There is evidence from other work in our laboratory that the likelihood of large ΔE collisions involving water is affected by preferred geometries of water in collisions with pyridine molecules. While it is unlikely that long-lived complexes form at 300 K, details of the collision dynamics will be sensitive to anisotropy in the intermolecular potential energy surface. One definite conclusion that can be reached from the relatively modest amounts

of energy transferred overall and the low probability of forming DCl in the (v = 1) state is that long-lived complex formation leading to anything even approaching a full statistical redistribution of energy is extremely rare.

3.4 Conclusion

The ability to measure state-resolved energy gain profiles for weak collisions opens up exciting opportunities for understanding the full spectrum of collision dynamics of highly excited molecules. Detailed information about weak collisions and their energy transfer properties complements earlier studies on strong collisions and allows us to profile the entire distribution of energy transfer events from a quantum-resolved perspective. These studies also provide a direct measurement of the collision rate. Comparison of experimental collision rates and Lennard-Jones rates clarifies the role of hydrogen bonding and other specific interactions in energy transfer collisions. The work reported here shows that DCl/pyrazine(E) collisions primarily lead to V–RT energy transfer with an integrated rate that is ~85% of the Lennard-Jones collision rate. Very small amounts of vibrational excitation of DCl in the v = 1 state are observed. A threshold for strong collisions is observed for DCl products near the J = 15 state where the velocity distributions show J-dependent broadening. The energy transfer distribution function contains evidence of a strong collision component and yields an average energy transfer value of $\langle \Delta E \rangle = 888$ cm^{-1}. Studies of this kind provide important guidelines in developing theoretical models of molecular collisions under high temperature conditions.

Chapter 4: Full State-Resolved Energy Gain Profiles of CO_2 (J = 2–80) from Collisions of Highly Vibrationally Excited Pyrazine(E = 37900 cm^{-1})

4.1 Introduction

Collisional energy transfer from highly excited molecules to cold bath molecules involves two types of collisions: weak and strong collisions. Neither of the two can be neglected when studying collisional quenching dynamics. Chapter 3 investigated the complete dynamics of pyrazine(E)/DCl collisions by measuring both types of collisions. This Chapter reports the state-resolved energy gain profiles for "strong" and "weak" collisions of pyrazine(E = 37900 cm^{-1}) and CO_2 molecules.

Several approaches have been used to characterize energy transfer distributions for excited pyrazine(E)-CO_2 collisions, including IRF[56,57] and KCSI.[29,64-68] The experimental data from these studies has been fit using various model distribution functions such as single-, double-, and extended parameter exponentials. The studies quantify energy loss and involve multiple sequential collisions. Here, the nascent state-resolved dynamics of pyrazine(E)/CO_2 collisions are investigated.

This Chapter investigates the collisional energy transfer dynamics for CO_2 in low rotational states through collisions with pyrazine(E = 37900 cm^{-1}) using high-resolution transient IR absorption spectroscopy. Our group already measured the strong collision dynamics for collisions of CO_2 with hot pyrazine(E) that scatter CO_2 molecules in high-J states (J = 58–80). Here IR transient absorption experiments measured the state-resolved energy gain profiles for low rotational states (J = 2–64) of CO_2 (00^00) that come from collisions with highly vibrationally excited pyrazine(E = 37900 cm^{-1}). This experiment

uses rotationally resolved CO_2 ($10^0 1$) ← CO_2 ($00^0 0$) transitions near λ = 2.7 μm to measure the outcome of weak collisions. The low-J state results are combined with the previous data for high-J states to yield the complete state-resolved V–RT energy gain distributions for CO_2 ($00^0 0$) that result from collisions with highly vibrationally excited pyrazine(E).

Rate measurements for both appearance and depletion of population in individual CO_2 states are obtained by this experiment. The data show that the collision rate is well described by the Lennard-Jones model and that the V–RT pathway accounts for ~ 85% of all collisions. Product distributions indicate the presence of two distinct relaxation pathways that scatter CO_2 ($00^0 0$). A two-component model based on the data shows that 78% of collisions are elastic or weakly inelastic and induce only minor changes in CO_2 rotation. The remaining 22% of collisions are highly inelastic and lead to large gains in rotational energy for CO_2. The probability distribution function P(ΔE) based on product energy gain is reported for ΔE values of $-500 < \Delta E < 8000$ cm^{-1} and compared to results from other collision studies.

4.2 Experimental Methods

In this Chapter, state-resolved rotational and translational energy gain of CO_2 molecules at low-J states was measured using the high-resolution F-center laser transient absorption spectrometer. This spectrometer was described in Chapter 2. Additional relevant information is presented here. Highly vibrationally excited pyrazine(E) was prepared by 266 nm UV light from the pulsed Nd:YAG laser. The UV power density was kept below 4.9 MW/cm^2 to minimize multiphoton absorption by pyrazine while <15% of the total pyrazine concentration was excited. A 1:1 mixture of pyrazine and CO_2

vapors with a total pressure of ~ 20 mTorr flowed through a 300 cm collision sample cell. The absolute cell pressure was determined spectroscopically using a low-J CO_2 rotational transition with known absorption strength. The UV and IR beams were propagated collinearly through the cell. Individual rotational states of scattered CO_2 molecules were probed using $(10^0 1, J') \leftarrow (00^0 0, J)$ with the $\lambda = 2.7$ μm output of a single-mode F-center laser.

Pyrazine(Aldrich, 99%+) was degassed by the freeze-pump-thaw method before use and CO_2 (Matheson Tri-gas, 99.995% purity) was used directly.

4.3 Results

4.3.1 Appearance and Depletion Processes of CO_2 $(00^0 0, J)$ Collisions

The outcome of collisions between pyrazine(E) and CO_2 was investigated by measuring nascent population changes for CO_2 $(00^0 0)$ in the J = 2–64 rotational states using high resolution transient absorption. CO_2 states with J < 50 have measurable population at 300 K and transient IR absorption of these states is a measure of the net population changes that include both depletion of initial population and appearance of scattered population caused by collisions. The population changes for appearance and depletion were distinguished by measuring the nascent Doppler-broadened IR line profiles for CO_2.

Figure 4.1 shows transient absorption signals for CO_2 $(00^0 0)$ J = 26 at two different IR wavelengths within the R26 transition centered at $\nu_0 = 3733.4684$ cm^{-1}. In

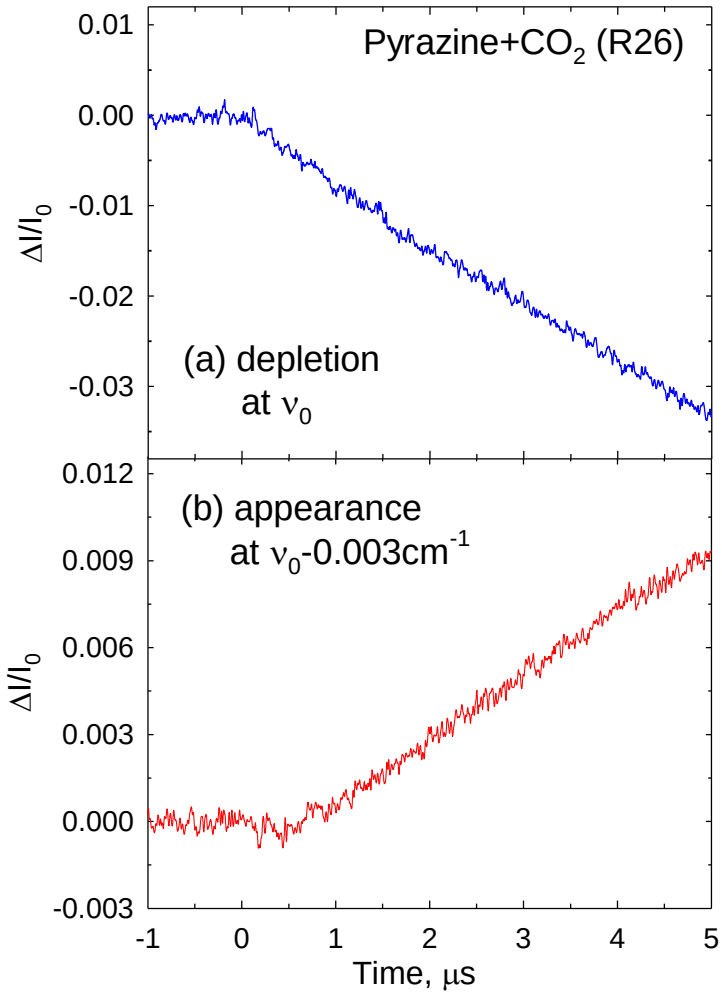

Figure 4.1 Nascent transient IR absorption signals of scattered CO_2 (00^00) at rotational state J = 26 through collisions with vibrationally excited pyrazine(E = 37900 cm^{-1}) at two IR frequencies within the R26 probe transition. The UV pulse happens at probe time t = 0 μs and the signals to t = 0 μs illustrate the initial populations of CO_2 at J = 26 before collisions with excited pyrazine. (a) shows a depletion of initial CO_2 populations at line center ν_0. (b) shows the appearance of scattered CO_2 molecules for J = 26 at by tuning the IR probe of the Doppler-broadened line profile to the frequency $\nu = \nu_0 - 0.003$ cm^{-1}.

Figure 4.1a, negative-going population depletion is observed at the center frequency ν_0. Figure 4.1b shows positive-going appearance in the Doppler-broadened wings at $\nu = \nu_0 - 0.003$ cm^{-1}. Figure 4.2 shows Doppler-broadened transient line profiles for a number of CO_2 states with J = 2 to 54 measured at t = 1 μs following the UV pulse. The positive-going appearance signals increase relative to the negative-going depletion signals as the initial thermal population of the CO_2 state decreases.

CO_2 population initially in state J is depleted by collisions with highly excited pyrazine, Pyz (E), as described by Eq 4.1.

$$\mathrm{Pyz(E)+CO_2}\left(00^00, \mathrm{J}, \mathrm{V}\right) \xrightarrow{k_{dep}} \mathrm{Pyz\ (E')+CO_2(any\ state)} \tag{4.1}$$

Simultaneously, CO_2 molecules are scattered into state J as described by Eq 4.2.

$$\mathrm{Pyz(E)+CO_2} \xrightarrow{k_{app}^{J}} \mathrm{Pyz\ (E')+CO_2}\left(00^00, \mathrm{J}, \mathrm{V}\right) \tag{4.2}$$

In Eq 4.1 and 4.2, V is the velocity component of CO_2 along the IR propagation axis and E and E' are the initial and final pyrazine energies. Population changes associated with depletion or appearance are induced by any collisions that change the initial rotational state and/or velocity component along the IR probe axis. Therefore transient line profiles such as shown in Figure 4.2 include contributions from both elastic and inelastic collisions.

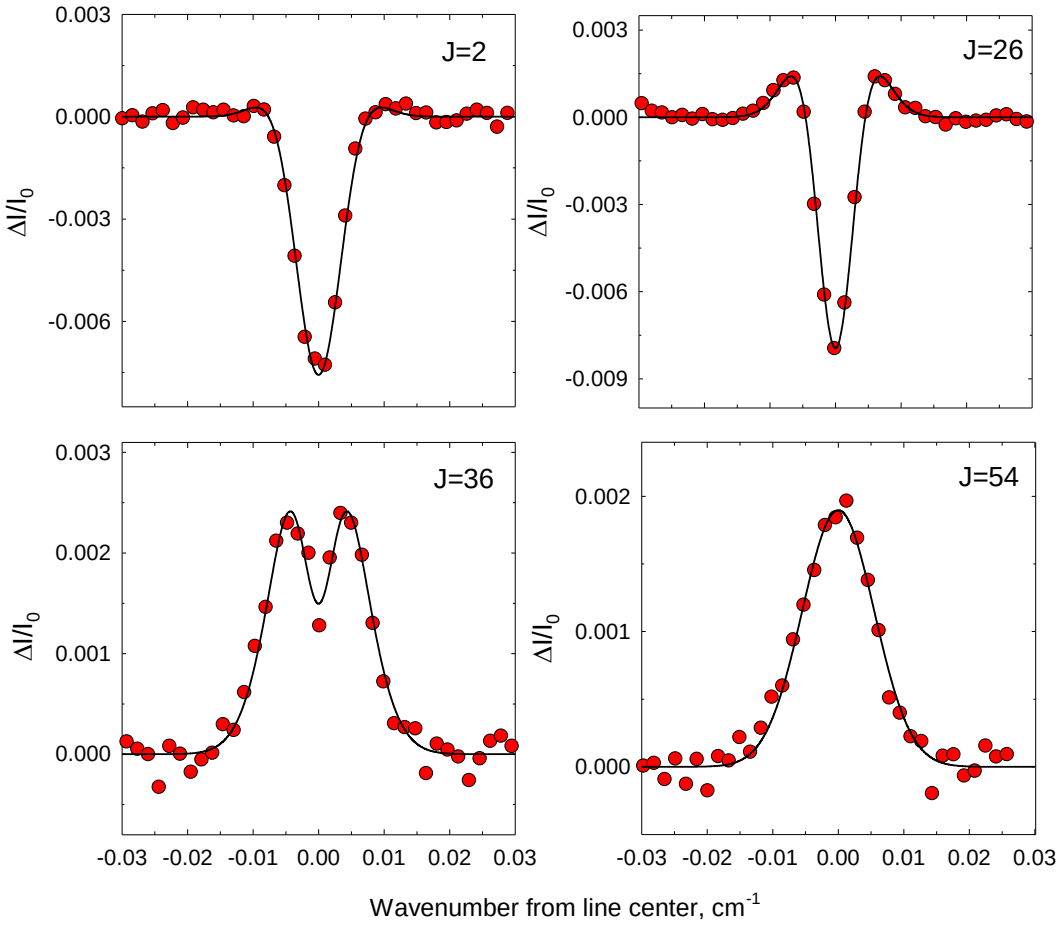

Figure 4.2 The transient absorption line profiles for scattered CO_2 (00^00) at from low to high rotational states (J = 2, 26, 36, and 54). Circles in plots are transient IR absorption data of CO_2 at t = 1 μs through collisions with excited pyrazine(E = 37900 cm^{-1}); the solid curves are the double-Gaussian fitting function for the probe data from two processes, appearance and depletion at CO_2 low states (J < 40) and a single-Gaussian fitting curve fits the data at high rotational states (J > 40) since the contribution from the depletion process approaches zero.

Nascent CO_2 populations are determined from transient IR line profiles measured at short times relative to the time between collisions. Transient absorption measurements at t = 1 μs are made well before the average time between collisions (t_{col} ~ 4 μs) and correspond to populations of scattered CO_2 molecules for which secondary quenching collisions are unlikely.

Each transient line profile is fit with a double Gaussian function (Eq 4.3) to separate the nascent appearance and depletion populations.

$$F(\nu)= I_{app}\exp\left[-4\ln 2\left(\frac{\nu-\nu_0}{\Delta\nu_{app}}\right)^2\right]-I_{dep}\exp\left[-4\ln 2\left(\frac{\nu-\nu_0}{\Delta\nu_{dep}}\right)^2\right]+F_0 \qquad (4.3)$$

Here, I_{app} and I_{dep} are appearance and depletion intensities at ν_0, $\Delta\nu_{app}$ and $\Delta\nu_{dep}$ are the full widths at half maximum (FWHM) for the appearance and depletion components, respectively, and F_0 accounts for small baseline fluctuations from instrumental noise.

Dynamic information about collisions that lead to population appearance and depletion is obtained from the fitting parameters in Eq 4.3. Figure 4.3 shows the separate appearance and depletion components from fitting J = 26 data with Eq 4.3.

The area under each curve in Figure 4.3 corresponds to the nascent sub-population (at t = 1 μs) of molecules (in J = 26) that has either appeared as collision products or been depleted by collisions. J-specific line widths and translational energy distributions (in the lab frame and the center of mass frame) for appearance are listed in Table 4.1. Table 4.2 lists line widths and translational temperatures for depletion. Appearance line widths are all broader than 300 K. Depletion line widths measured for J = 2–38 have values near those for a 300 K distribution.

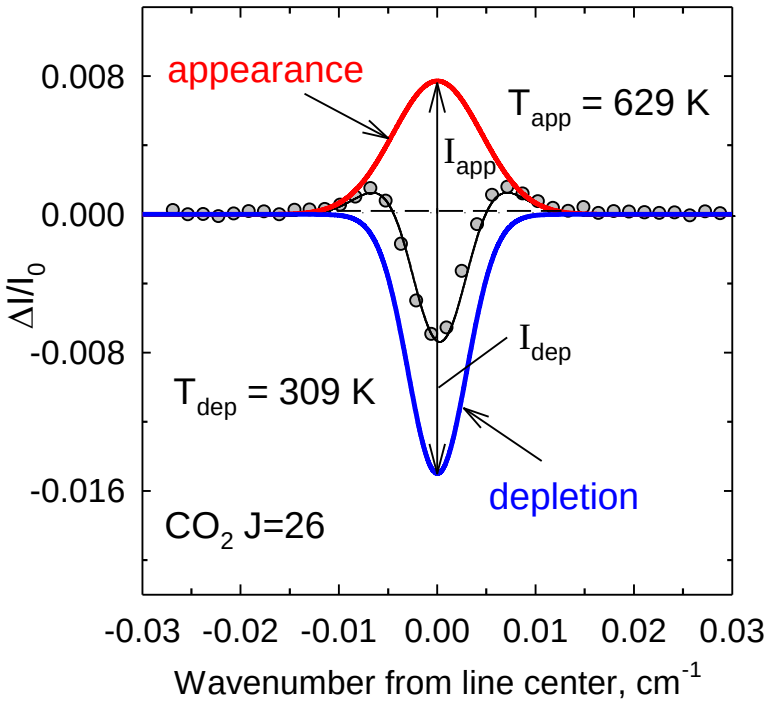

Figure 4.3 The appearance and depletion curves are separated by a double-Gaussian function. Transient absorption line profile for CO_2 (00^00) at J = 26 (open circles) were measured at t = 1 μs after UV pulse. The solid curve is a double-Gaussian function that includes both appearance and depletion processes. Due to the fitting parameters, two processes were measured: the appearance component (red line) is broadened with a translational temperature T_{app} = 629 K and the blue line shows the depletion component with T_{dep} = 309 K through collisions.

Table 4.1 Nascent Doppler-broadened linewidths, translational temperatures and rate constants for appearance of CO_2 (00^00, J) from collisions with vibrationally excited pyrazine(E = 37900 cm^{-1})

CO_2 J	E_{rot}, cm^{-1}	ν_0, cm^{-1}	$\Delta\nu_{app}$, cm^{-1}[a]	T_{app}, K[b]	T_{rel}, K[c]
2	2.3413	3717.0853	0.0103	664 ±91	865 ±119
8	28.0951	3721.5215	0.0104	658 ±89	855 ±116
22	197.4166	3730.9893	0.0097	579 ±85	734 ±107
26	273.868	3733.4684	0.0101	629 ±88	811 ±114
36	519.535	3739.2323	0.0115	820 ±101	1106 ±136
38	578.0115	3740.3115	0.0111	755 ±96	1006 ±128
44	772.1107	3743.4040	0.0126	970 ±109	1339 ±151
52	1074.4305	3747.1946	0.0120	875 ±03	1193 ±141
54	1157.774	3748.0840	0.0131	1052 ±113	1466 ±158
58	1333.7678	3659.4029	0.0118	916 ±110	1255 ±150
64	1621.0035	3652.5720	0.0135	1173 ±123	1654 ±174

[a]Full width at half-maximum (FWHM) linewidth $\Delta\nu_{app}$ for appearance of CO_2 rotational states at 1 μs following UV excitation of pyrazine. Values of $\Delta\nu_{app}$ have an uncertainty of ± 0.001 cm^{-1}.

[b]The lab-frame translational temperature T_{app} for appearance of CO_2 rotational states due to collisions obtained using $T_{app} = (mc^2/(8R\ln 2))^2\left(\Delta\nu_{app}/\nu_0\right)^2$, where m is the mass of CO_2, c is the speed of light, R is the gas constant and ν_0 is the center frequency of the absorption line.

[c]Center-of-mass translational temperature T_{rel} for appearance of scattered CO_2 is determined by assuming an isotropic distribution of collisions and using $T_{rel} = T_{app} + (m_{CO_2}/m_{pyz})(T_{app} - T_0)$, where, m_{CO_2} and m_{pyz} are the masses of CO_2 and pyrazine respectively and $T_0 = 298K$.

Table 4.2 State-resolved depletion linewidths, translational temperatures and rate constants for collisions with vibrationally excited pyrazine(E = 37900 cm^{-1})

$$\text{Pyrazine (E)} + CO_2(00^00, J) \xrightarrow{k_{dep}} \text{Pyrazine (E')} + CO_2(\text{any state})$$

CO_2, J	ν_0, cm^{-1}[a]	$\Delta\nu_{dep}$, cm^{-1}[b]	$T_{dep,lab}$, K[c]	k_{dep}, $\times 10^{-10}$ $cm^3 \cdot molecule^{-1} \cdot s^{-1}$
2	3717.0853	0.0077	364 ± 94	7.4 ± 2.2
8	3721.5215	0.0083	422 ± 102	6.2 ± 1.9
22	3730.9893	0.0082	409 ± 100	8.9 ± 2.7
26	3733.4684	0.0071	309 ± 87	5.1 ± 1.5
36	3739.2323	0.0073	323 ± 88	3.5 ± 1.0
38	3740.3115	0.0064	248 ± 78	2.6 ± 0.8
$\langle k_{dep} \rangle$, $cm^3 \cdot molecule^{-1} \cdot s^{-1}$[d]				$5.6(\pm 2.2) \times 10^{-10}$
k_{LJ}, cm^3 $molecule^{-1}$ s^{-1}[e]				5.6×10^{-10}

[a] ν_0 is the IR transition frequency of probe transition at line center.

[b] Full width at half-maximum (FWHM) line widths and $\Delta\nu_{dep}$ for depletion of individual CO_2 J states. Line widths have uncertainties of ± 0.001 cm^{-1}.

[c] The lab-frame translational temperature T_{dep} for depletion of CO_2 due to collisions with pyrazine(E) are obtained using $T_{dep} = (mc^2/8Rln2)(\Delta\nu_{dep}/\nu_0)^2$, where m is the mass of CO_2, c is the speed of light, R is average the gas constant, and ν_0 is the center frequency of the absorption line.

[d] The average depletion rate constant $\langle k_{dep} \rangle$ is the population-weighted average of k_{dep}

[e] The Lennard-Jones collision rate constant k_{LJ} is determined using the model which is shown in the appendix B with the following Lennard-Jones parameters:

$\sigma_{CO_2} = 4.5 \times 10^{-10}$m, $(\epsilon/k_B)_{CO_2}$ =190 K, and $\sigma_{pyz} = 5.35 \times 10^{-10}$m, $(\epsilon/k_B)_{pyz}$ = 435.5 K.

4.3.2 Rotational and Translational Energy Gained for Scattered CO_2 at J = 2–80 through Collisions with Excited Pyrazine(E).

The nascent CO_2 rotational distribution and the J-specific product translational energy distributions are determined directly from the appearance parameters I_{app} and $\Delta\nu_{app}$. Figure 4.4 shows the rotational distribution of scattered CO_2 molecules (J = 2–80) based on appearance intensities and line widths measured at t = 1 μs. The data for CO_2 J = 2–64 states are shown as red circles. Previous measurements for the J = 58–80 states are shown as white circles.[77] Data for the J = 58 and 64 states of CO_2 are in very good agreement with the earlier high-J measurements. Based on the consistency of the overlapping data, no rescaling of either data set was needed. The distribution is a bi-exponential function of energy with a transition point near E_{rot} = 1100 ± 110 cm^{-1}. Exponential fitting of the data in each region indicates that the lower energy states with J < 50 have a rotational temperature of T_{rot} = 453 ± 50 K and that states with J > 50 have a temperature of T_{rot} = 1164 ± 110 K. The residuals are shown in the lower plot of Figure 4.4. These data show that there are two distinct populations of scattered CO_2 molecules. Given the high state density of pyrazine(E) and the structure of CO_2, it is unlikely that a threshold for enhanced energy transfer occurs at E_{rot} = 1100 cm^{-1}. It is more likely that the two populations of scattered CO_2 molecules each span the full range of J states. This Chapter will use this information to develop a two component model to describe the energy transfer.

The J-specific nascent translational energy distributions (based on T_{rel} in Table 4.1) for scattered CO_2 molecules in J = 2–80 are shown in Figure 4.5. The T_{rel} values for J = 2–64 are shown as red circles and previously reported values for the J = 58–80 states

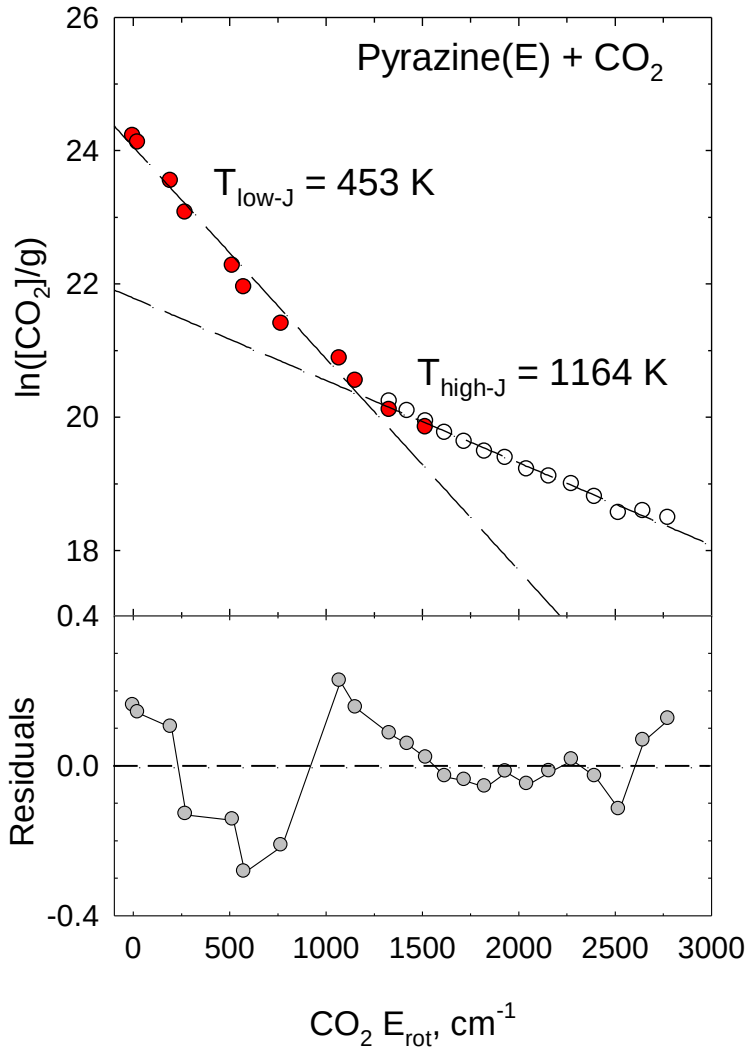

Figure 4.4 Nascent rotational distribution for the J = 2–80 states of CO_2 (00^00) due to collisions with vibrationally excited pyrazine. Measurements of the J = 2–64 states are shown in red circles. Previous data for the J = 58–80 states (from Ref. 77) are shown as open circles. The nascent distribution is a biexponential function of rotational energy with a crossing point at $E_{rot} \sim 1100$ cm^{-1}. Fitting the data for J < 50 yields a low-J distribution with $T_{lowJ} = 453 \pm 50$ K. Fitting the data for J > 50 yields $T_{highJ} = 1164 \pm 110$ K.

are shown as white circles.[75-77] There is good agreement between the two data sets in the overlapping region of J = 58–64. Overall, the data are well described by an exponential increase in T_{rel} as a function of J with an offset of T_{rel} = 780 K at J = 0. The low-J states of CO_2 are scattered with translational energies near T_{rel} ~ 800 K. The J-dependence of T_{rel} becomes stronger for J > 40 where much larger recoil energies are observed.

The data in Figure 4.5 illustrate the impulsive nature of the V–RT collisions between pyrazine(E) and CO_2. It has long been recognized that the scattering of CO_2 in very high J states results from strongly impulsive collisions.[90,91] The measured translational energy profiles for the low-J scattering states presented here are consistent with an impulsive mechanism. The classical physics of impulsive collisions indicates that the smallest recoil velocities result from collisions that have the smallest changes in angular momentum. It is interesting that the smallest value of T_{rel} in Figure 4.5 is for the J = 22 state which is near the peak of the initial CO_2 distribution. Appearance of population in this state is most likely to result from small ΔJ collisions. Given the scatter in the data and the small number of states measured in this region, however, we cannot conclusively identify the presence of a minimum. To address this question, it would be useful to perform scattering experiments where initial J states can be correlated with final states.

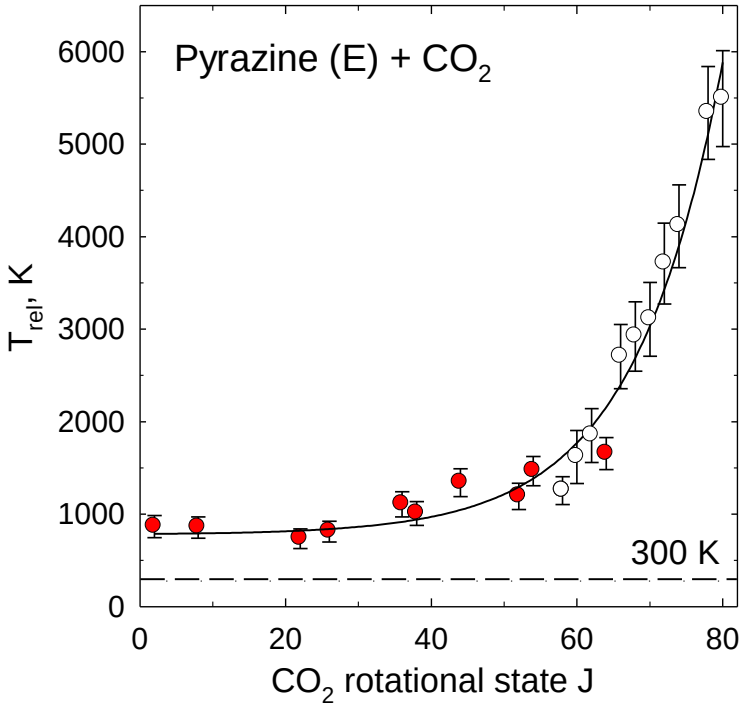

Figure 4.5 The nascent relative translational temperatures T_{rel} for the pyrazine(E)/CO_2 collision system is a function of CO_2 (00^00) rotational state. The red circles are the experimental appearance translational temperatures for CO_2 J = 2–64 while the data for CO_2 high-J states (J = 58–80) from the previous paper[77] are shown as the open circles.

4.3.3 State-Resolved V–RT Energy Transfer Rate Constants and the Total Collision Rate

This Chapter reports appearance and depletion rates of individual CO_2 states using transient IR absorption. Rate constants for depletion and appearance are based on Eqs. 4.1 and 4.2, respectively. The early time population changes associated with depletion are determined using Eq 4.4.

$$\frac{\Delta[CO_2(J)]_{dep}}{\Delta t} = k_{dep}[Pyz(E)]_0[CO_2(J)]_0 \qquad (4.4)$$

In Eq 4.4 the transient population depletion $\Delta[CO_2(J)]_{dep}$ is determined from the integrated depletion line profile at $\Delta t = 1$ μs (as in Figure 4.3). The initial number density of excited pyrazine, $[Pyz(E)]_0$ is determined by measuring UV absorption. The initial CO_2 number density $[CO_2]_0$ is determined by measuring equilibrium IR absorption of a well-populated state.

The initial thermal population of CO_2 is depleted by collisions, and k_{dep} is a measure of the collision rate constant, assuming that the collision rate is independent of J. Depletion rate constants are listed in Table 4.2 for CO_2 J = 2–38 states. The rate constants for these states range from $k_{dep} = 2.6 \times 10^{-10}$ to 8.5×10^{-10} cm^3 $molecule^{-1}$ s^{-1}. The population-weighted average is $\langle k_{dep} \rangle = (5.6 \pm 2.2) \times 10^{-10}$ cm^3 $molecule^{-1}$ s^{-1} which is in excellent agreement with the Lennard-Jones collision rate of $k_{LJ} = 5.6 \times 10^{-10}$ cm^3 $molecule^{-1}$ s^{-1}. The collision cross section based on these data is $\sigma_{col} = k_{dep}/\langle v_{rel} \rangle \sim 120 \pm 50$ $Å^2$.

State-specific rate constants for appearance of CO_2 (00^00) are defined by Eq 4.5.

$$\frac{\Delta[CO_2(J)]_{app}}{\Delta t} = k^J_{app}[Pyz(E)]_0[CO_2(J)]_0 \qquad (4.5)$$

The appearance populations $\Delta[CO_2(J)]_{app}$ are determined from the integrated appearance profiles at Δt = 1 μs (as in Figure 4.3). Values of k^J_{app} for J = 2–64 are listed in Table 4.3 and values for J = 58–80 are taken from Ref. 95. Appearance rate constants for unmeasured CO_2 states (up to J = 100) are determined based on rates for measured states and the T_{rot} values of Figure 4.4. Summing the rate constants for product state appearance yields an overall rate constant for V–RT energy transfer between pyrazine(E) and CO_2 of $k_{app} = \sum k^J_{app} = (4.8 \pm 1.4) \times 10^{-10}$ $cm^3 \cdot molecule^{-1} \cdot s^{-1}$. This overall rate constant corresponds to a cross section for V–RT energy transfer of $\sigma_{V-RT} = k_{app}/\langle v_{rel} \rangle \sim 100 \pm 30$ Å^2.

The V–V energy transfer pathways from pyrazine(E) to CO_2 have been measured for a number of CO_2 vibrational states at a pyrazine energy of E = 40680 cm^{-1}.[74,95] The total rate constant for energy transfer into the (10^00r1), (10^00r2), (02^20) and (00^01) states (2349 cm^{-1}) is $k_v = (3 \pm 1) \times 10^{-11}$ cm^3 $molecule^{-1}$ s^{-1}. The total energy transfer rate constant based on appearance measurements is a sum of the rates for the V–RT and V–V pathways, given by $k_{tot} = k_{app} + k_v = (5.1 \pm 1.8) \times 10^{-11}$ cm^3 $molecule^{-1}$ s^{-1}. The value of k_{tot} is consistent with our measured depletion rate and is in very good agreement with the Lennard-Jones collision rate.

Table 4.3 State-resolved rate constants for appearance of CO_2 (00^00, J) through collisions with highly vibrationally excited pyrazine(E = 37900 cm^{-1}).

$$\text{pyrazine (E)} + CO_2(300\ \text{K}) \xrightarrow{k_{app}^J} \text{pyrazine (E')} + CO_2(00^00, J)$$

CO_2 J	CO_2 E_{rot}, cm^{-1}	$k_{app}^J \times 10^{-12}$ $cm^3 \cdot molecule^{-1} \cdot s^{-1}$[a]
2	2.3413	6.7±2.0
8	28.095	20.5±6.2
22	197.4	33.0±9.9
26	273.9	23.8±7.1
36	519.5	13.9±4.2
38	578.0	10.6±3.2
44	772.1	7.1±2.1
52	1074.4	5.0±1.5
54	1157.8	3.7±1.1
58	1333.8	2.6±0.8
64	1521.0	2.2±0.7
k_{app}, $cm^3 \cdot molecule^{-1} \cdot s^{-1}$[b]		$(4.8 \pm 1.8) \times 10^{-10}$
k_v, $cm^3 \cdot molecule^{-1} \cdot s^{-1}$[c]		$> (3 \pm 1) \times 10^{-11}$
k_{tot}, $cm^3 \cdot molecule^{-1} \cdot s^{-1}$[d]		$> (5.1 \pm 1.8) \times 10^{-10}$
k_{LJ}, $cm^3 \cdot molecule^{-1} \cdot s^{-1}$[e]		5.6×10^{-10}

[a]The state-specific rate constant k_{app}^J for appearance of CO_2 (00^00, J = 2–64) are determined from appearance data at t = 1 μs using

$k^J_{app} = \left([CO_2(J)]_{app}\right)/([Pyz(E)]_0[CO_2]_0\Delta t)$, $[Pyz(E)]_0$ and $[CO_2]_0$ are the number densities of excited pyrazine and 300 K CO_2, respectively, immediately following optical excitation of pyrazine.

[b]The overall rate constant for V–RT energy transfer, k_{app}, is determined by summing appearance rate constants for all CO_2 product states by using the equation $k_{app} = \sum_J k^J_{app}$. Rate constants were measured for the states listed in Table 4.2 and values of k^J_{app} for the remaining products states were determined using the nascent rotational temperature T_{rot} of the scattered CO_2 molecules. The appearance rate constant k_{app} for the V–RT pathway is a lower limit to the total collision rate constant.

[c]The rate constant k_v for appearance of vibrationally excited CO_2 in the (10^00r1), (10^00r2), (02^20) and (00^01) vibrational states following collisions with pyrazine(E), taken from Refs.[74,95].

[d]The total energy transfer rate constant $k_{tot} = k_{app} + k_v$ includes V–RT and V–V channels of energy transfer from pyrazine(E) to CO_2.

[e]The Lennard-Jones collision rate constant k_{LJ} is determined as described in Table 4.2.

The discrepancy between k_{tot} and the actual collision rate constant is likely to be due to the energy transfer into the (01^10) bending state of CO_2 at 667 cm^{-1}. This state is the only low-lying vibrational state that is not included in the V–V rate measurements.[74,95] Because of its relatively small energy gap, the (01^10) state should be readily accessed through collisions with pyrazine(E). It is likely that the rate for energy gain in the bend is greater than that in the stretching modes, based on the rates for the nearly degenerate 10^00 and 02^20 states. Relative to the Lennard-Jones collision rate, the results in this Chapter show that the V–RT pathway accounts for ~ 85% of collisions. The measured V–V pathways account for ~ 6% of collisions, suggesting that the remaining ~ 9% of collisions may involve excitation of the bending mode. This branching ratio is consistent with our current understanding of vibrational excitation in small molecules and provides evidence that the Lennard-Jones collision rate constant is a fairly accurate representation of pyrazine(E)/CO_2 collisions.

4.4 Discussion

The data presented here provide an in-depth description of the dynamics for the full range of collisions by which CO_2 quenches highly excited pyrazine molecules through V–RT energy transfer. The ability to measure the outcome of both weak and strong collisions that scatter CO_2 (00^00) gives us the most complete description to date of this type of collisional relaxation process. These data provide insight into the first set of collisions that lead off the collisional cascade that eventually brings molecules into thermal equilibrium.

4.4.1 Branching Ratio for Inelastic Collisions

The measurements of weak collisions presented in this Chapter confirm that the V–RT pathway is the predominant channel by which highly excited pyrazine molecules are quenched with CO_2. The V–RT pathway includes strong and weak collisions and accounts for ~ 85% of all pyrazine(E)/CO_2 collisions, based on rates measured for appearance of products and depletion of initial states. The V–V pathways for pyrazine(E)/CO_2 account for the remainder of collisions. Similar behavior was seen in classical trajectory calculations of pyrazine(E)/CO_2 collisions, where Luther and coworkers found the V–V energy transfer in pyrazine(E)/CO_2 collisions make an almost negligible contribution to the overall relaxation.[64] State-resolved scattering measurements illustrate that the V–V pathways for the stretching modes of CO_2 occur primarily via long-range near-resonant energy transfer, so it is not surprising that they are not seen in classical trajectories.[74,95]

The agreement between our measured collision rate and that calculated with a Lennard-Jones model indicates that the relaxation is not particularly sensitive to anisotropy in the intermolecular potential between pyrazine(E) and CO_2. Lennard-Jones collision rates are commonly used to model molecular collisions and they should be valid for collisions of weakly interacting species such as CO_2 at 300 K. Caution must be used however for the case of strongly interacting species such as water. In other studies we have measured total appearance rates for scattered HOD molecules that are as much as 3.5 times larger than the Lennard-Jones collision rate.[79,81,118] For these systems, state-resolved scattering data indicate that anisotropy in the intermolecular potential plays an important role in quenching pathways involving water.[118]

4.4.2 The Scattered Population Distributions from Weak and Strong Collisions

The rotational distribution for scattered CO_2 molecules (Figure 4.4) shows clear evidence for the presence of two distinct scattering populations. In Eq 4.6, a two-component model is used to describe the population in each J state as the sum of two Boltzmann distributions,

$$Pop_J = g_J\left(I_a \exp\left(\frac{-E_J}{k_B T_a}\right) + I_b \exp\left(\frac{-E_J}{k_B T_b}\right)\right) \qquad (4.6)$$

where g_J is the rotational degeneracy, E_J is the rotational energy, I_a and I_b are intensity parameters, k_B is the Boltzmann constant, and T_a and T_b are rotational temperatures. Figure 4.6 shows the results of a four-parameter nonlinear least-squares fit of Eq 4.6 to the data with no initial constraints. Modeling the data with the biexponential function in Eq 4.6 yields smaller residuals than the fit shown in Figure 4.6.

The two subpopulations based on the best fit values of I_a, I_b, T_a, and T_b are shown in Figure 4.7. The low-energy rotational states are best described by a cooler distribution with T_a = 329 K while population in the high-energy states comes almost entirely from a hotter rotational distribution with T_b = 1241 K. The value of T_a is very close to the initial 300 K distribution, showing that this subset of collisions is elastic or nearly inelastic and falls into the category of weak collisions. The relatively large value of T_b shows that the second subset of collisions induces large changes in CO_2 rotation, thereby putting this group in the category of strong collisions. The integrated intensity of the weak collision component is 78% of the total population of scattered CO_2 (00^00) molecules, while the high-energy component accounts for 22%. Thus, nearly four out of five collisions involve

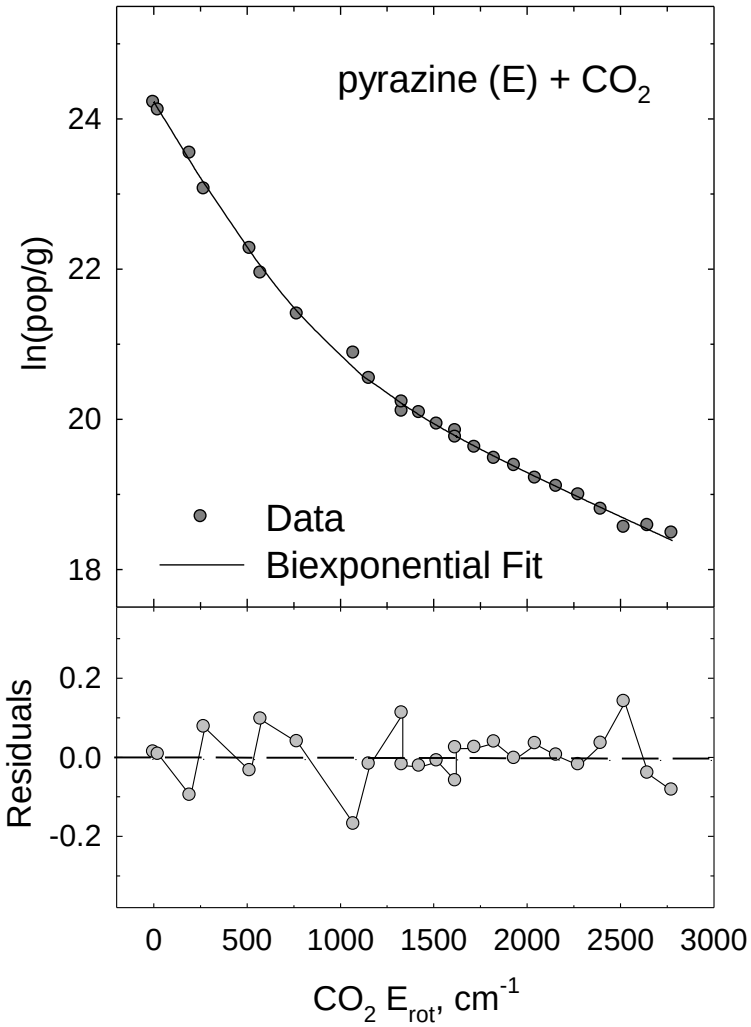

Figure 4.6 A two-component biexponential model fitting the population data of scattered CO_2 molecules with pyrazine(E) in the upper plot. The circles are the measured data and the fitting result is shown as a solid curve. The accuracy for the fitting model is shown as the fractional residuals in the lower plot.

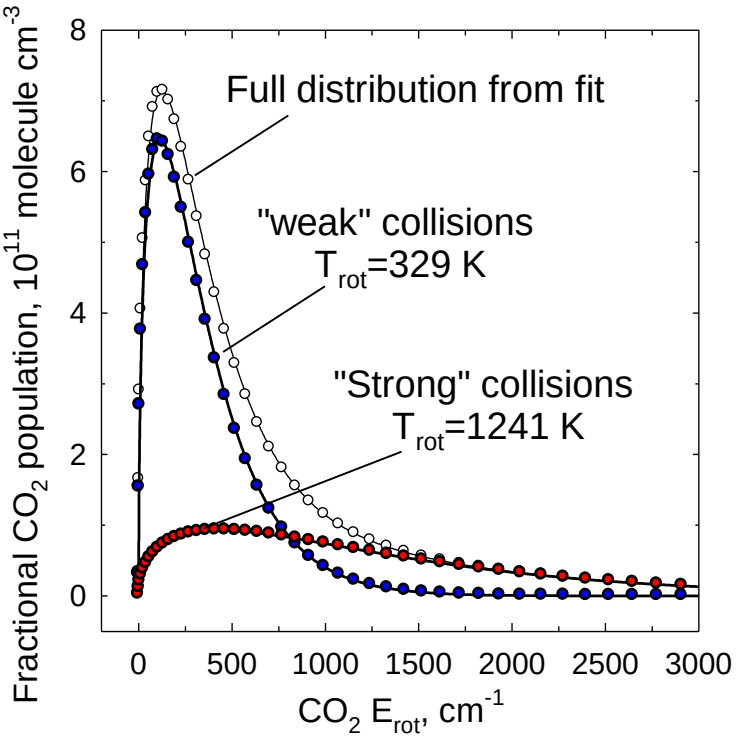

Figure 4.7 Two energy distributions are separated by a two-component model. The low energy distribution is associated with weak collisions and accounts for 78% of V–RT collisions. The high energy distribution is from the strong collision with accounts for 22% of V–RT collisions.

only minor changes to CO_2 rotation, while the remaining one-fifth of collisions induce large changes in rotational energy.

It is interesting that there are two distinct scattering populations for CO_2. Prior to the current measurements of the full distribution for this system, neither the CO_2 rotational distribution nor the collision rate was known. Extrapolating the full distribution based only on high-J data yielded an energy transfer rate that was much smaller than the Lennard-Jones collision rate and was inconsistent with measurements of the V–V energy transfer rates. The data presented here clearly illustrate the predominance of the weak collision pathway and establish the validity of the Lennard-Jones collision rate for quenching collisions of CO_2 and pyrazine(E). In a somewhat related study, Nesbitt and co-workers have measured CO_2 scattering from liquid surfaces and found that the products have a two-component distribution.[140-142] They estimate that about 50% of the scattered molecules undergo desorption trapping, which leads to a cooler distribution of products, while the hotter distribution comes from impulsive scattering.

For gas-phase collisions with high-energy molecules, the presence of a two-component scattering distribution for CO_2 seems to be the norm. Chapters 5 and 6 report other studies on CO_2 collisions with similar scattering behavior. This behavior is not found for collisional quenching in other small bath species such as HOD[79] and DCl (Chapter 3). These bath molecules scatter from highly excited molecules via V–RT collisions with single rotational distributions.

The presence of a strong collisional channel involving large amounts of CO_2 rotation is most likely due to CO_2's length and relatively uniform mass distribution.

Impulsive collisions involving the oxygen atoms on CO_2 are likely to be effective at inducing torque on the molecule. This idea is supported by classical trajectory studies both from our group and from Chapman, Flynn, and co-workers. For the pyrazine(E)/CO_2 collisions in this Chapter, the average recoil energy has little dependence on CO_2 rotational energy until $E_{rot} \sim 750$ cm^{-1} above which the recoil energies increase substantially.[45] Chapman and co-workers found a biexponential rotational distribution for CO following single collisions with pyrazine(E).[43,44] When they doubled the length of the CO molecule to mimic CO_2, while preserving other potential parameters, they found reasonable agreement with the high-energy tail from pyrazine(E)/CO_2 collisions.

4.4.3 The Effect of Angular Momentum Changes for V–RT Energy Transfer

Chapter 3 discussed how the angular momentum changes were determined using the experimental data for pyrazine(E)-DCl collision pair. Table 4.4 lists the average changes in CO_2 angular momentum $\langle \Delta J_{bath} \rangle$ and recoil velocity $\langle \Delta v_{rel} \rangle$ based on the J-specific values of T_{app} (Table 4.1) for J = 2–64. Our calculations are based on an initial J state of J = 22 and an initial average velocity at 300 K, as described in Table 4.4. Figure 4.8a shows $\langle \Delta v_{rel} \rangle$ as a function of $\langle \Delta J_{bath} \rangle$ for the J = 2–80 states of CO_2. Figure 4.8a shows that $\langle \Delta v_{rel} \rangle$ increases monotonically as a function of $\langle \Delta J_{bath} \rangle$. This figure also illustrates that there is a slight minimum in $\langle \Delta v_{rel} \rangle$ at $\langle \Delta J_{bath} \rangle = 0$. Small changes in recoil velocity (~300 m/s) correlate to small $\langle \Delta J_{bath} \rangle$ and more substantial increases in recoil velocity changes for $\langle \Delta J_{bath} \rangle > 40$. This behavior is entirely consistent with the angular momentum model for collisional energy transfer by McCaffery and co-workers.[128-130,143-146]

Table 4.4 The average changes in linear and angular momentum in CO_2 through collisions with highly vibrationally excited pyrazine(E).

CO_2 J	T_{app}, K[a]	$\langle v_{lab} \rangle$, m/s[b]	$\langle v_{rel} \rangle$, m/s[c]	$\langle \Delta v_{rel} \rangle$, m/s[d]	$\langle \Delta J \rangle$, $\hbar$[e]	b_{min}, Å[f]
2	664 ± 91	612 ± 42	869 ± 120	357 ± 49	-21.9	1.36
8	658 ± 89	609 ± 41	864 ± 117	352 ± 48	-20.5	1.27
22	579 ± 85	571 ± 42	800 ± 117	288 ± 42	0	0
26	629 ± 88	595 ± 42	841 ± 118	329 ± 46	13.9	0.92
36	820 ± 101	680 ± 42	983 ± 121	471 ± 58	28.5	1.33
38	755 ± 96	652 ± 42	937 ± 120	425 ± 54	31.0	1.59
44	970 ± 109	739 ± 42	1081 ± 122	569 ± 64	38.1	1.47
52	875 ± 103	702 ± 42	1020 ± 121	508 ± 60	47.1	2.03
54	1052 ± 113	770 ± 41	1131 ± 122	619 ± 67	49.3	1.76
58	916 ± 110	718 ± 43	1046 ± 125	535 ± 64	53.7	2.20
64	1173 ± 123	813 ± 43	1202 ± 126	690 ± 72	60.1	1.91

[a]Nascent translational temperature for appearance of scattered CO_2 molecules in rotational quantum state J.

[b]Average velocity in the lab frame of scattered CO_2 molecules determined using $\langle v_{lab} \rangle = \left(\frac{3 k_B T_{app}}{m_{CO_2}} \right)^{\frac{1}{2}}$, where k_B is the Boltzmann constant, m_{CO_2} is the mass of CO_2 molecule.

[c]$\langle v_{rel} \rangle$, the average velocity in the center-of-mass of pyrazine(E)/CO_2 system is calculated by using $\langle v_{rel} \rangle = \left(\langle v_{lab} \rangle^2 - \frac{3k_B T_{app}}{M} \right)^{\frac{1}{2}} \frac{M}{m_{pyrazine}}$, where the sum of mass $M = m_{pyz} + m_{CO_2}$ and m_{pyz} is the mass of pyrazine.

[d]Average change in center-of-mass velocity $\langle \Delta v_{rel} \rangle$ is calculated by an equation: $\langle \Delta v_{rel} \rangle = \langle v_{rel} \rangle - \left(\frac{3k_B T_0}{\mu} \right)^{\frac{1}{2}}$, where μ is the reduced mass for pyrazine/CO_2 pair and T_0 = 298 K.

[e]$\langle \Delta J \rangle$ is the average change of CO_2 angular momentum which is determined using $\langle \Delta J_{bath} \rangle = \sqrt{J_{final}^2 - J_{initial}^2}$, where $J_{initial} \sim 22$.

[f]b_{min}, minimum impact parameter for pyrazine(E)/CO_2 system is from $\langle \Delta J_{bath} \rangle = \mu \langle \Delta v_{rel} \rangle b_{min}$.

.

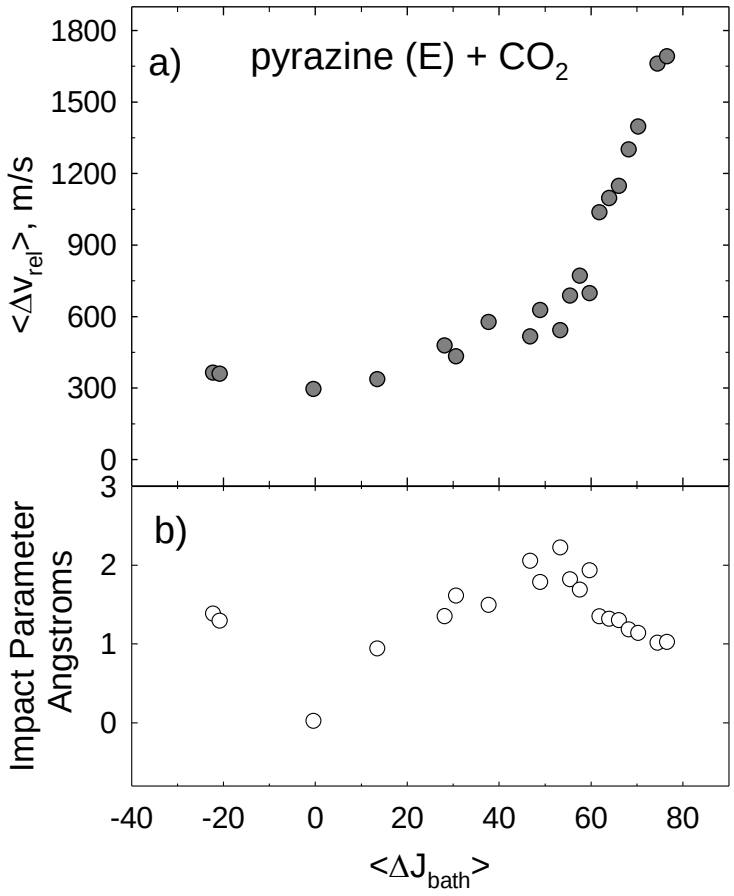

Figure 4.8 (a) Average relative velocity as a function of average change in CO_2 rotational angular momentum collisions between pyrazine(E) and CO_2. (b) Minimum impact parameter b_{min} as a function of average angular momentum changes.

The data in Figure 4.8a further illustrate the impulsive nature of collisions that lead to V–RT energy transfer between pyrazine(E) and CO_2. Increases in recoil velocity are seen even for collisions with small angular momentum changes. On the basis of these data, we estimate that lower limits to the impact parameter have values of b_{min} = 0–2 Å, as shown in Figure 4.8b. These features are consistent with an impulsive mechanism for energy transfer in molecules of the size considered here.

4.4.4 Full Energy Gain Distribution Function P(ΔE)

The nascent product state measurements for CO_2 (J = 2–80) are used to determine the energy transfer probability distribution function P(ΔE). The P(ΔE) distribution function is related to, but not equivalent to, the P(E′,E) distributions from UVA, IRF, and KCSI studies. P(E′,E) curves describe the distribution of vibrational energy loss as high energy molecules initially with energy E undergo collisions to end up at a lower energy E′. The P(ΔE) distribution from transient IR measurements is obtained by converting the J- and velocity-indexed product state data into an energy transfer distribution indexed by ΔE using the method of Michaels and Flynn.[89] The state-specific probability distribution function P_J(ΔE) for energy gain in a single CO_2 product state is based on measurements of the state-resolved appearance rate and the product translational energy distribution (in the center of mass). The ΔE index includes the change in CO_2 rotational energy and the change in relative translational energy of the pyrazine/CO_2 pair. For this calculation we use an estimated initial value of J_0 = 22 based on temperature-dependent measurements and an initial velocity corresponding to the average relative velocity at 300 K.[91]

At present there are not any methods to measure the energy changes associated with rotation of vibrationally excited donor molecules such as pyrazine(E). For this

reason, ΔE_{rot} for pyrazine is not included in ΔE. Therefore the ΔE values in $P(\Delta E)$ are smaller than the amount of vibrational energy lost ($E - E'$) from pyrazine due to collisions. This distinction is particularly important in comparing results from state-resolved transient IR measurements with those from KCSI, IRF, and UVA techniques.

Individual $P_J(\Delta E)$ curves for the J = 0–100 states of CO_2 are shown in Figure 4.9a. The integrated intensity of each $P_J(\Delta E)$ curve is equal to the ratio of k^J_{app}/k_{LJ} and corresponds to the relative population in that product state, based on the measured rotational distribution (Figure 4.4) for the J = 2–80 states. The initial ΔE value for each curve is given by $\Delta E_0 = E(J) - E(J_0 = 22) - \langle \Delta E_{rel} \rangle$, and ΔE_0 is negative for rotational states with $J \leq 32$. Within our assumptions for the initial energies, negative ΔE values correspond to collisions where pyrazine(E) gains energy from CO_2 and positive ΔE values are for collisions where CO_2 gains energy from pyrazine(E). The overall energy gain distribution $P(\Delta E)$ for the V–RT pathway is the sum of $P_J(\Delta E)$ curves and the resulting $P(\Delta E)$ curve extends from $\Delta E = -500$ to 8000 cm^{-1}, as shown in Figure 4.9a. Figure 4.9b illustrates a number of interesting features. Most collisions between pyrazine(E) and CO_2 lead to energy exchanges of $\Delta E < 2000$ cm^{-1}, showing the propensity for small energy transfer in single collisions. Strong collisions that induce larger ΔE values are detectable out to $\Delta E \sim 10000$ cm^{-1}, but the probability for these events is dwarfed by that for the low ΔE collisions. The $P(\Delta E)$ distribution is dominated by the spread of translational energy in the products and is mostly a smoothly varying function of ΔE except near $\Delta E = 0$ where the effect of the CO_2 rotational states structure can be seen as undulations in $P(\Delta E)$.

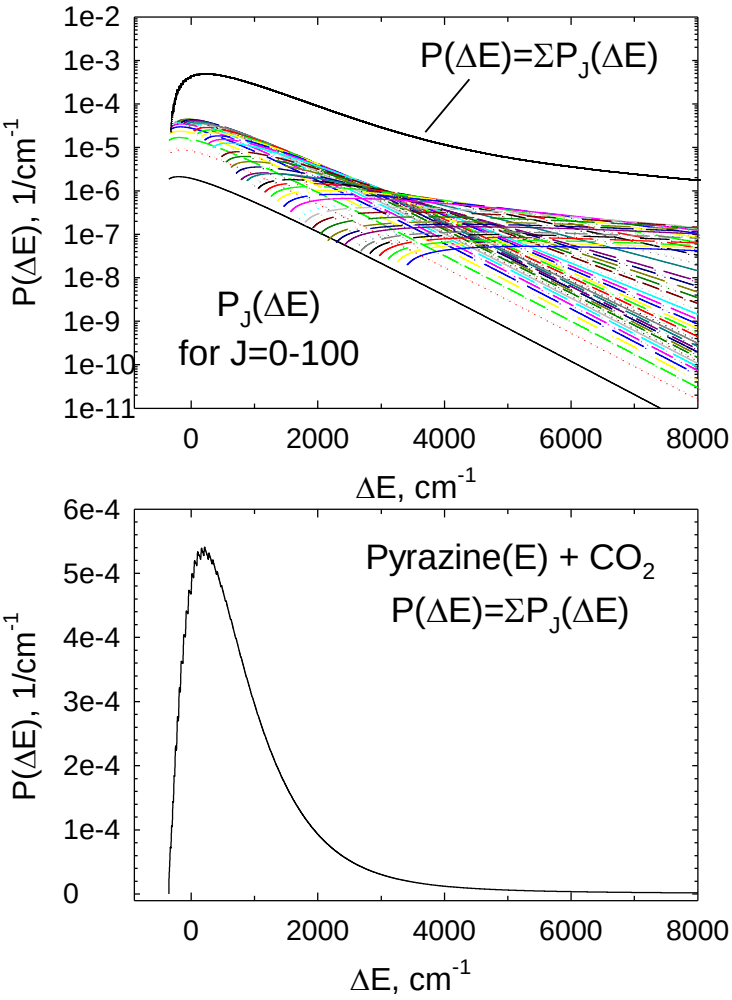

Figure 4.9 (a) The state-specific energy probability distribution $P_J(\Delta E)$ for CO_2 J = 0–100 through collisions with vibrationally excited pyrazine(E). (b) The full energy transfer distribution P(ΔE) curve is the sum of the state-specific energy transfer profiles $P_J(\Delta E)$ (J = 0–100). ΔE is the product energy gain of scattered CO_2 through collisions with highly vibrationally excited pyrazine.

The rotational state structure of both the donor and energy accepting bath molecules will affect the shape of P(ΔE) in the low ΔE region. Rotational degeneracy favors collisions that move population into higher J states, given that there is sufficient energy to populate those states. The availability of a greater number of states at increasing J is balanced by larger energy gaps between states. The impact of the rotational ladders on P(ΔE) will be most apparent for the collision partner with the smaller moment of inertia. For CO_2, the rotational state density levels out at J = 24 to 97% of its ultimate value. This state has an energy of E_{rot} = 236 cm^{-1}. For pyrazine, the rotational states are more closely spaced and the rotational state density becomes uniform at lower energies. Pyrazine reaches 97% of its ultimate rotational state density near J = 11 where $E_{rot} \sim 26$ cm^{-1}. At 300 K, the most populated states of CO_2 have energy gaps on the order of 50 cm^{-1} while for pyrazine the energy gaps are closer than 15 cm^{-1}. This means that in the first set of collisions that quench pyrazine(E), CO_2 will undergo larger energy changes for the same changes in angular momentum, thereby leading to larger gaps between ΔE_0 for sequential $P_J(\Delta E)$ curves. This effect is particularly pronounced for CO_2 since only even J states exist for the (00^00) state. It is likely that bath molecules with more closely spaced rotational states will be scattered with a narrower distribution of rotational energy since there are more states available with small energy gaps. In addition, in cases where the velocity distributions of the scattered molecules are broad, probability density is shifted out to larger ΔE values, leaving the low ΔE region more sensitive to the rotational state density.

The P(ΔE) curve in Figure 4.9b has a maximum value at ΔE = 240 cm^{-1} rather than at ΔE = 0 as expected from P(E,E′) curves reported elsewhere and used in traditional

energy transfer models. There are several reasons for this discrepancy. First of all, there is some uncertainty in the exact values of ΔE associated with the J-specific probability curves. The shape and amplitude of the $P_J(\Delta E)$ curves are well-defined by our measurements, but exactly how they are indexed by ΔE has some uncertainty since our initial values of J and relative velocity are based on guesses. Information about how the initial rotational and translational energy distributions evolve to the final distributions would help pinpoint ΔE more precisely. The contribution of each initial rotational state to the final distribution will depend on its population and possibly its angular velocity. The energy transfer dynamics and the resulting ΔE distribution are also likely to be sensitive to the spread of initial relative velocities. The likelihood of impulsive collisions increases with increasing relative velocity, and distinct dynamics may occur for velocities in which the interaction time becomes short relative the vibrational periods of the highly excited molecules.

An additional source of uncertainty in ΔE comes from the lack of information about the fate of rotational energy in pyrazine. The distribution of final rotational states for pyrazine will likely affect the shape of the $P(\Delta E)$ distribution, but it will not change the integrated intensity of $P(\Delta E)$. Exactly how the distribution is affected will depend on the final rotational distribution of pyrazine and how it correlates with the final CO_2 rotational states. New experimental approaches are needed for making measurements of correlated product states. Since the pyrazine rotational states have relatively close spacing, one might expect small changes in pyrazine rotational energy to be favored based on the propensity for collisions to induce small changes in angular momentum. This situation would have the effect of narrowing the $P(\Delta E)$ distribution by moving

probability density into the low ΔE region. On the other hand, given the large changes in angular momentum seen for CO_2, it appears that there is ample angular momentum available. Furthermore, trajectory studies of pyrazine(E)/CO_2 collisions by Luther and co-workers found that pyrazine(E) and CO_2 each gain substantial amounts of rotational energy through impulsive collisions.[64] This situation would cause P(ΔE) to broaden. It is likely that the second case is closer to the actual situation in the measurements, and therefore, we consider the spread of P(ΔE) in Figure 4.9 as a lower limit to the actual energy transfer distribution.

Numerical integration of the P(ΔE) for the range $-500 < \Delta E < 10000$ cm^{-1} yields a lower limit to the average energy transfer of $\langle \Delta E \rangle_{total} = 879$ cm^{-1}. If only the positive values of ΔE are included, we obtain a lower limit of $\langle \Delta E \rangle_{gain} = 890$ cm^{-1}, where $\langle \Delta E \rangle_{gain}$ is the amount of energy that goes from pyrazine vibration into rotation and translation of the scattered pyrazine and CO_2 molecules. Note that $\langle \Delta E \rangle_{gain}$ here corresponds to the absolute value of $\langle \Delta E \rangle_{down}$ for downward collisions of the vibrationally excited molecule that are often reported from IRF, UVA, and KCSI studies. If we arbitrarily shift ΔE by 240 cm^{-1} so that the peak intensity in P(ΔE) occurs at ΔE = 0, the lower limits for average energy transfer drop to $\langle \Delta E \rangle_{total} = 670$ cm^{-1} and $\langle \Delta E \rangle_{gain} = 716$ cm^{-1}.

Another measure of the average energy transfer is obtained by fitting the P(ΔE) data using a model distribution function. Here we test two different exponential decay models and use P(ΔE) data with ΔE shifted by 240 cm^{-1}. The first fitting function is a two-parameter single exponential function shown in Eq 4.7.

$$P(\Delta E) = A \exp\left(\frac{-\Delta E}{\alpha}\right) \quad \text{for } \Delta E > 0 \tag{4.7}$$

The results are shown in Figure 4.10a. Eq 4.7 is similar to that used by Miller and Barker to fit IRF results on pyrazine(E)/CO_2 collisions.[56] The parameter α is a measure of $-\langle\Delta E\rangle_{down}$. P($\Delta$E) is fit reasonably well with Eq 4.7 and using Barker's notation, we find that $-\langle\Delta E\rangle_{down}$ = 1042 cm^{-1}. For comparison, Miller and Barker report a value of $-\langle\Delta E\rangle_{down}$ = 370 cm^{-1} for pyrazine(E)/CO_2 collisions.

The second model function is a three-parameter monoexponential decay shown in Eq 4.8.

$$P(\Delta E)=A \exp\left[\left(\frac{-\Delta E}{\alpha}\right)^{Y}\right] \quad \text{for } \Delta E > 0 \tag{4.8}$$

Eq 4.8 is similar to one used by Luther and co-workers to fit KCSI data.[29,64] The fitting results are shown in Figure 4.10b and yield α = 1190 cm^{-1} and Y = 1.3. KCSI studies have been performed by Luther and co-workers for a number of collision pairs, but pyrazine(E)/CO_2 is not among the systems studied. However, they do report that for azulene(E)/CO_2 collisions at E = 19776 cm^{-1}, α = 294 cm^{-1} and Y = 0.80.[29] For azulene(E)/Ar collisions, they found that α = 116 cm^{-1} and Y = 0.65. They also report that for pyrazine(E)/Ar collisions at E = 38000 cm^{-1}, α = 258 cm^{-1}, and Y = 0.80.[64] From these results we estimate that $\alpha \sim$ 650 cm^{-1} for pyrazine(E)/CO_2 collisions.

It is informative to contrast the α values for P(ΔE) with those based on IRF and KCSI measurements. The P(ΔE) curve is fit reasonably well by both of the model distributions shown above. The width of P(ΔE) based on either fitting method is noticeably broader than the width reported by the IRF study and the estimated width from

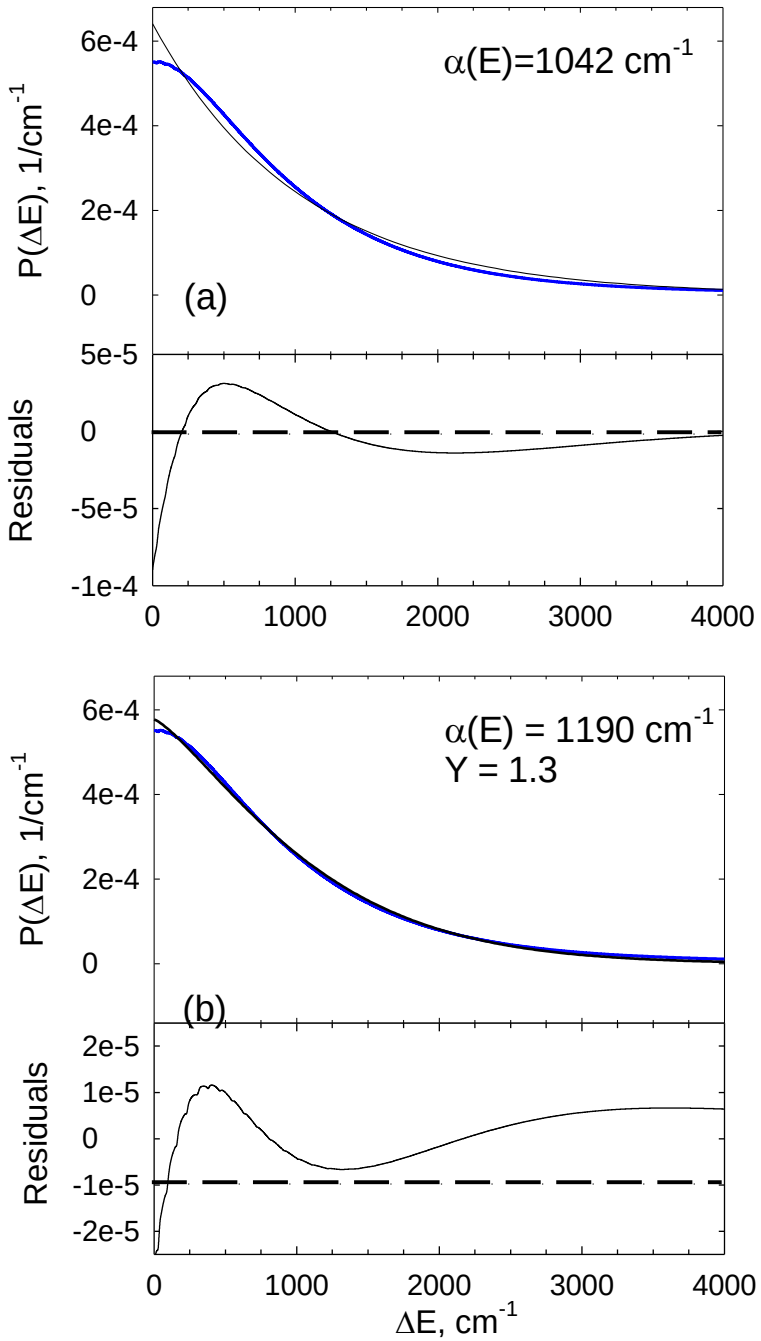

Figure 4.10 (a) A single exponential fit (in black) of the P(ΔE) curve (in blue) for positive ΔE values that correspond to energy loss from pyrazine(E). (b) A parameterized monoexponential fit (in black) of the P(ΔE) curve (in blue) based on the fitting approach taken by Luther and co-workers (Ref. 68 and 120), as described in the text.

KCSI data. The widths from the fit should be considered lower limits since P(ΔE) does not include ΔE_{rot} for pyrazine(E). The α values from fitting to our data are nearly a factor of 2 larger than the estimated KCSI value and a factor of 3 larger than the IRF results. Values of α from IRF studies are often smaller than values from KCSI experiments. Data from IRF studies are sensitive to calibration of the IR signals, and Luther has suggested that the difference in their results is caused by relatively small errors in the IR calibration.[64]

It is not surprising that P(ΔE) is broader than P(E′,E). This feature highlights an important difference between nascent energy transfer distributions from transient IR absorption measurements and those that result from multiple, sequential collisions in KCSI and IRF studies. A P(ΔE) profile based on nascent energy profiles of collision products describes just the first step in a collisional cascade that eventually brings highly excited molecules into thermal equilibrium. On the other hand, multicollision measurements monitor energy loss from hot donor molecules as they not only undergo collisions with molecules at 300 K but also interact with molecules containing additional rotational and translational energy obtained by prior collisions. From the two types of measurements, a clear picture emerges. The first set of collisions leads to a broad distribution of product states as donor molecules lose relatively large chunks of vibrational energy. Then the energy transfer distribution narrows as subsequent collisions continue to dissipate the vibrational energy of the highly excited molecules. The narrowing of the distribution results in part from the reduced vibrational energy of the hot donor molecules as they are quenched. Additional narrowing comes from the smaller energy gaps that are involeved in the rotation-to-rotation energy transfer that

occurs in the collisional cascade.

It is worth noting that substantial rotational energy gain in highly excited pyrazine molecules has been seen in trajectory studies of CO_2 and this behavior is likely to be a general phenomenon for relatively stiff bath molecules such as CO_2. The situation is much different for floppy bath molecules, such as propane and aromatic molecules. Simulations by Luther,[64] Oref,[147-149] and others[150,151] indicate that quenching collisions with floppier bath species are dominated by vibration-to-vibration energy transfer and that the V–RT pathway is almost negligible.

4.5 Conclusions

This Chapter describes studies on the complete energy transfer profiles for quenching collisions between highly vibrationally excited pyrazine molecules (λ = 266 nm) and CO_2 measured using high-resolution transient IR spectroscopy. By measuring the time dependence of nascent changes for population appearance and depletion, the branching ratio for inelastic collisions is quantified. The experimental results indicate that 85% of pyrazine(E)/CO_2 collisions involve V–RT energy transfer and that, within this pathway, two distinct rotational populations exist. 78% of V–RT collisions are weak collisions that are elastic or nearly inelastic and only impart minor changes in rotational angular momentum to CO_2. The remaining 22% of V–RT collisions are strong collisions that impart large changes in CO_2 angular momentum. Nascent recoil velocity measurements establish the impulsive nature of the quenching collisions, even for small values of CO_2 rotation. Measurements of this type lay the groundwork for the development of future models to describe molecular collisions and the exchange of energy.

Chapter 5: Internal Energy Effects on Full Energy Transfer Distribution for CO_2 through Collisions with Highly Vibrationally Excited Pyrazine(E = 32700 and 37900 cm^{-1})

5.1 Introduction

This Chapter addresses the question of how collisional quenching is affected by the internal energy of a highly excited donor molecule. The full outcome of collisions between highly vibrationally excited pyrazine(E = 32700 cm^{-1}) with CO_2 are reported in this Chapter. The effect of internal energy on the collision dynamics is explored by comparing the energy transfer dynamics of CO_2/pyrazine(E) collisions where E = 32700 cm^{-1} or 37900 cm^{-1} (Chapter 4).

Techniques such as UV absorption (UVA),[48,152-155] IR fluorescence (IRF),[156-158] kinetically controlled selective ionization (KCSI)[29,64-66,68,159] and a crossed-beam time-sliced velocity map ion imaging[160-163] have been used to study energy-dependent effects. Using the UVA technique, Troe and co-workers found that the average transfer energy $\langle\Delta E\rangle$ is proportional to the internal energy of excited molecules. They also found that the energy dependence of $\langle\Delta E\rangle$ decreases with increasing excitation energy. Using the IFR method, Barker and co-workers found that $\langle\Delta E\rangle$ depends strongly on internal energy of excited molecules and there is a near-linear correlation between E and $\langle\Delta E\rangle$ at low internal energy (E < 35000 cm^{-1}). Luther and co-workers observed in KCSI studies that $\langle\Delta E\rangle$ is nearly directly proportional to the internal energy of the excited donors at E = 30000 cm^{-1} and less. On the other hand, the molecular beam results of Ni and co-workers suggest that energy transfer probabilities and total collision cross sections are

independent of the internal energy of the hot donor molecules. The discrepancies among these results illustrate the challenges associated with characterizing the collision behavior of high energy molecules.

Using high-resolution transient IR absorption spectroscopy, our group has previously studied the energy-dependent behavior of strong collisions of CO_2 with pyrazine(E)[77] and pyridine(E)[85] where the initial energy was varied by up to 25%. This work measured the appearance of the J = 60–80 states of CO_2. These studies showed that for collisions of pyrazine(E) and pyridine(E) with CO_2, the amount of energy transferred via V−RT collisions does not change much for different internal energies. However, for these collision systems the state-resolved energy transfer rate constants increase with increasing internal energy of the donors.

This Chapter reports the outcome of weak collisions for the CO_2 low states (J = 2–54) through collisions with vibrationally hot pyrazine(E = 32700 cm^{-1}) using high-resolution transient IR absorption spectroscopy. The full distribution for E = 32700 cm^{-1} is obtained by combining low-J data with the previously reported high-J data.[77] The results are compared with the results at E = 37900 cm^{-1} that were presented in Chapter 4. For the two different donor internal energies, our results show that the translational energy distributions are roughly independent of the CO_2 rotational energy for low J states, but increase sharply for higher J states. Our results show that the CO_2 energy gain profiles are affected by the pyrazine energy. The translational energy of the scattered molecules increases as a function of pyrazine energy. CO_2 gains of approximately twice the amount of translational energy from pyrazine(E = 37900 cm^{-1}) as it does from pyrazine(E = 32700 cm^{-1}). The rotational distributions of the scattered CO_2 are double-

exponential for both donor energies, but include larger ΔJ values at the higher donor energy. The full energy transfer probability distribution and average transfer energy during a single pyrazine(E)/CO_2 collision with two different pyrazine internal energies are compared.

5.2 Experimental Methods

This Chapter reports the collision dynamics for vibrationally excited pyrazine(E = 32700 cm^{-1}) with CO_2 by measuring the population changes in CO_2 low-J states (J = 2–54) using the same approach as described in Chapter 4.

Pyrazine(Aldrich, 99%) was degassed by several freeze-pump-thaw cycles. Pyrazine molecules in the gas-phase were excited by at λ = 308.8 nm with the doubled output of a Nd:YAG-pumped dye laser that uses the dye Rhodamine 640. The intensity of the 308.8 nm laser beam was kept below 4.6 MW/cm^2 in order to prevent multiphoton absorption by the pyrazine and to ensure that <15% of the pyrazine molecules are excited.

Tunable single cavity mode IR light at $\lambda \sim 2.7$ μm from a F-center laser was used to probe the population changes of scattered CO_2 (Matheson Tri-gas, 99.995% purity) molecules from collisions with vibrationally excited pyrazine. The collimated, overlapping IR and UV beams were propagated collinearly through a 3 m collision cell. A 1:1 mixture gas of pyrazine and CO_2 with a total pressure ~ 20 mTorr flowed through the cell. The populations of specific CO_2 states were measured using transient IR absorption at t = 1 μs after UV pulse in order to obtain nascent information resulting from single collisions of pyrazine(E) and CO_2.

5.3 Results

5.3.1 Transient IR Absorption Measurement of CO_2 (00^00) State

Transient IR absorption signals for individual CO_2 rotational states were collected immediately following the UV pulse. Two types of IR transient absorption signals for CO_2 (J = 26) from collisions with pyrazine(E = 32700 cm^{-1}) are shown in Figure 5.1: negative-going depletion signals are observed at line center of the IR transition (Figure 5.1a) and positive-going appearance signals are observed in the Doppler broadened wings (Figure 5.1b). For CO_2 low-J states (J < 38), the thermal populations of CO_2 are large enough to be observed prior to collisions with pyrazine(E = 32700 cm^{-1}) and the signals at ν_0 show a decrease in the IR absorption, corresponding to a net flow of CO_2 molecules out of individual J-states due to collisions with pyrazine(E). The depletion process for an initial J-state is shown in Eq 5.1.

$$\text{Pyrazine (E)}+CO_2\left(00^00, \text{J}\right) \xrightarrow{k_{dep}} \text{Pyrazine(E}-\Delta\text{E)}+CO_2\left(00^00, \text{J'}\right) \qquad (5.1)$$

The appearance of CO_2 population due to collisions in Eq 5.2:

$$\text{Pyrazine (E)}+ CO_2(300\ \text{K}) \xrightarrow{k_{app}^{J}} \text{Pyrazine (E}-\Delta\text{E)}+ CO_2(00^00, \text{J}) \qquad (5.2)$$

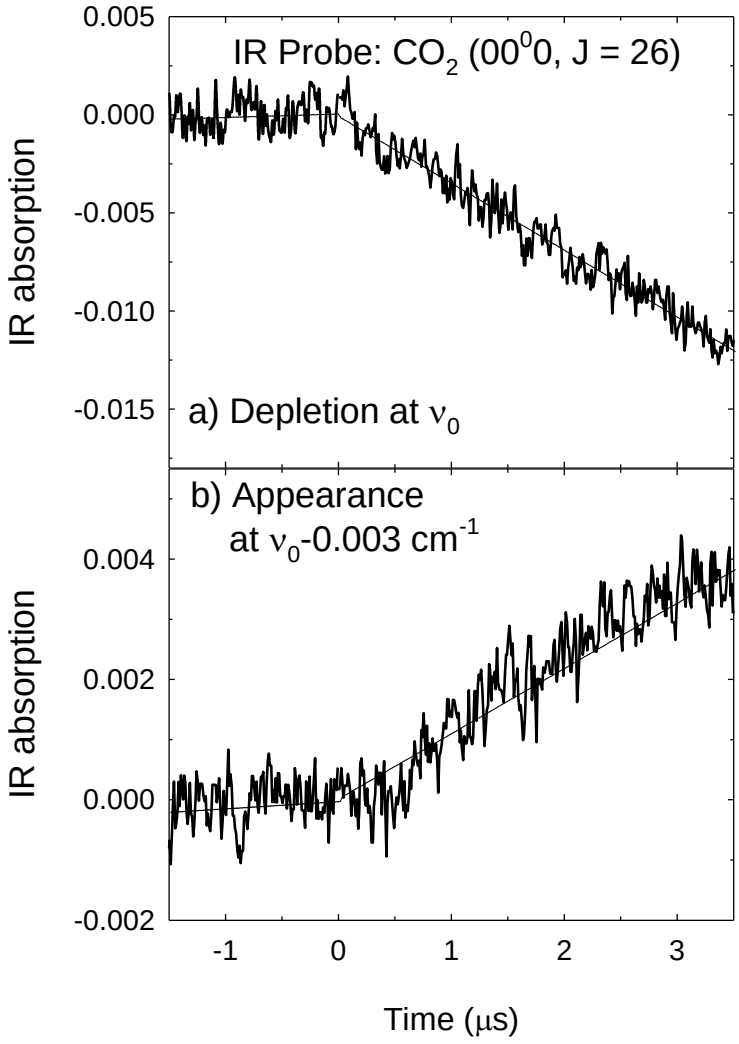

Figure 5.1 Transient absorption signals for scattered CO_2 ($00^0 0$) in the J = 26 state following collisions with highly vibrationally excited pyrazine(E = 32700 cm^{-1}) at two different IR frequencies. The vibrationally hot pyrazine was prepared using 308.8 nm excitation. The total cell pressure is 20 mTorr at 298 K. (a) Depletion of initial population in the J = 26 state at line center ν_0. (b) The appearance signal of CO_2 molecules scattered into J = 26 when the IR probe is tuned to the wings of the Doppler-broadened line profile at a frequency of $\nu_0 - 0.003$ cm^{-1}.

States with J > 38 have negligible population at 300 K, so these states only have appearance signals.

Doppler-broadened transient absorption profiles were measured at t = 1 μs following collisions with vibrationally hot pyrazine, as shown in Figure 5.2. The grey circles in Figure 5.2 are the IR absorption signal at t = 1 μs for CO_2 (J = 26). The transient absorption profile was fitted using a double-Gaussian function as shown in Eq 5.3. The fit results are shown as a solid line.

$$F(\nu)=I_{app}\exp\left[-4\ln 2\left(\frac{\nu-\nu_0}{\Delta\nu_{app}}\right)^2\right]-I_{dep}\exp\left[-4\ln 2\left(\frac{\nu-\nu_0}{\Delta\nu_{dep}}\right)^2\right]+F_0 \qquad (5.3)$$

In Eq 5.3, I_{app} and $\Delta\nu_{app}$ are the intensity and full width at half-maximum (FWHM) describing the appearance population. The depletion process also has intensity I_{dep} and a linewidth $\Delta\nu_{dep}$. F_0 is a minor base line correction that adjusts for instrumental noise, and ν_0 is the transition line center.

Figure 5.2 shows the results of the double-Gaussian fit as the black solid line. In Figure 5.3, the red and blue curves are the appearance and depletion components, respectively, based on the fitting results. T_{app} and T_{dep} are the lab-frame translational temperatures for the appearance and depletion processes calculated from the linewidth parameters $\Delta\nu_{app}$ and $\Delta\nu_{dep}$. The transient absorption profiles for CO_2 states with J > 38 are fitted by a single-Gaussian function that results from setting $I_{dep} = 0$ in Eq 5.3.

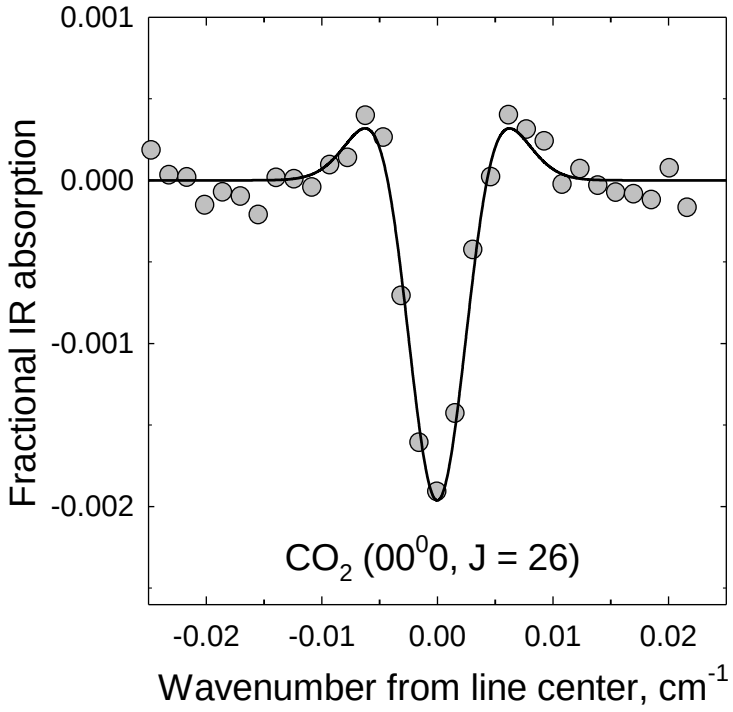

Figure 5.2 The transient absorption line shape for CO_2 (00^00) J = 26 resulting from collisions with highly vibrationally excited pyrazine(E = 32700 cm^{-1}). The circles are measured at t = 1 μs after the UV pulse. The solid curve is the result of fitting a double-Gaussian function to the data.

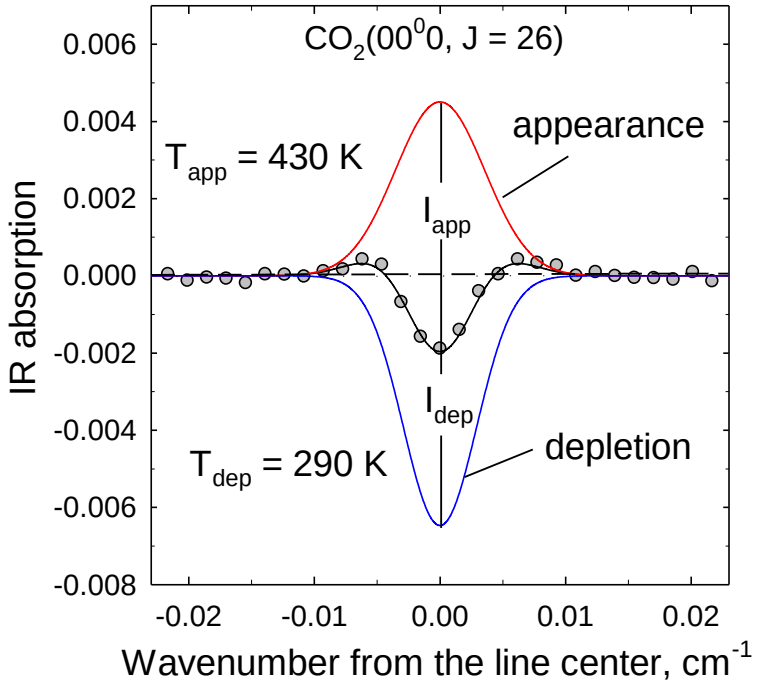

Figure 5.3 Transient absorption line profile for the J = 26 rotational state of CO_2 (00^00). Circles are transient IR absorption data and the black line is a double-Gaussian fit. The double-Gaussian parameters separate appearance process (the red line) and depletion process (the blue line) are from the Double-Gaussian fitting parameters. The appearance curve yields a FWHM linewidth of $\Delta\nu_{app} = 0.0078 \pm 0.001$ cm^{-1} and $T_{app}(lab) = 370 \pm 70$ K. For depletion $\Delta\nu_{dep} = 0.0068 \pm 0.001$ cm^{-1} and $T_{dep,lab} = 290 \pm 60$ K.

5.3.2 Appearance Profile for CO_2 High-J States (J = 56–78)

The work reported in this Chapter used λ = 308.8 nm as an excitation source because this wavelength is at the peak of the wavelength range of dye laser output. Previously the Mullin group investigated the strong collisions of pyrazine(E) with CO_2 by measuring the appearance profiles for high-J states of CO_2 (J = 56–78) at different UV weavelengths (λ = 302, 306.5, 310.1, 317.9, and 323.9 nm) as shown in Figure 5.4.[76] The previous study did not measure the collision dynamics exactly at λ = 308.8 nm, so the scattering results at this wavelength are estimated based on the previous results.

Figure 5.4a shows the J-dependent FWHM linewidths $\Delta\nu_{app}$ for a number of CO_2 states (J = 56–78) as a function of UV wavelength for λ = 286 to 323.9 nm. The values of $\Delta\nu_{app}$ for J = 56–78 at λ = 308.8 nm (black points) are established based on a linear fit to the data. The estimated linewidths $\Delta\nu_{app}$ translational temperatures T_{app} and T_{rel} at λ = 308.8 nm are listed in Table 5.1 for CO_2 J = 56, 62, 68 and 72.

Figure 5.4b shows that the rotational energy distributions of the high-J scattered CO_2 molecules are independent pyrazine internal energy for λ = 302–323.9 nm. We estimate that T_{rot} = 918 ± 100 K for CO_2 J = 56–78 at λ = 308.8 nm. Figure 5.4c shows appearance rate constants k_{app}^{J} for 3 high-J states of CO_2 as a function of UV wavelengths. The k_{app}^{J} values for λ = 308.8 nm are estimated from fitting the data to linear functions.

To combine the low and high J data sets, we repeated measurements of three high-J states (J = 70–74) that overlapped with the previous measurements. Figure 5.5 is a semilog plot of the J = 70–74 measurements and the estimated high J results at 308.8 nm from the previous study. The rotational distribution of scattered CO_2 (J = 70–74) has a

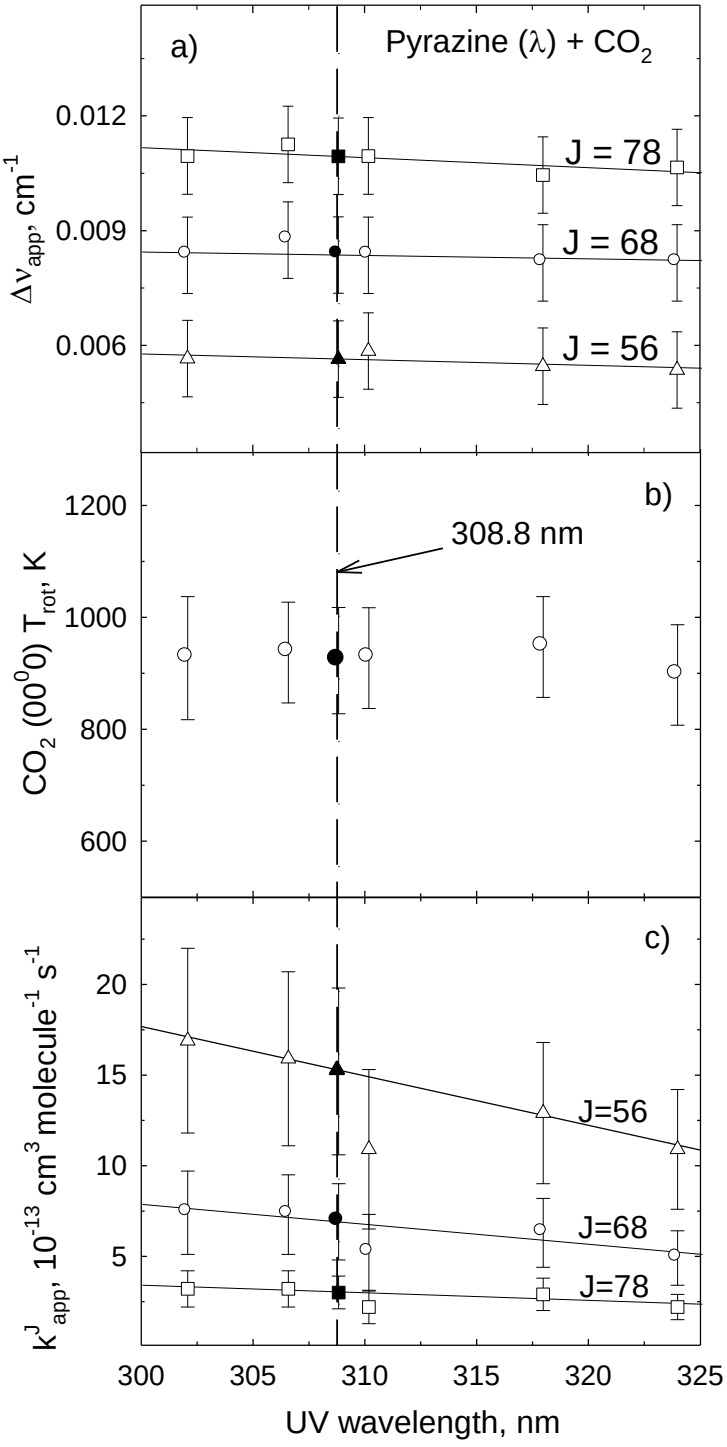

Figure 5.4 Energy transfer data for CO_2 (J = 56–78) that result from collisions with hot pyrazine excited at different UV wavelengths. Data for λ = 308.8 nm (dark symbols) are estimated from previous wavelength-dependent data (open symbols).

Table 5.1 State-specific nascent Doppler-broadened linewidths, translational temperatures and average translational energy gain for appearance of CO_2 (00^00, J) at t = 1 μs following collisions with vibrationally excited pyrazine(E = 32700 cm^{-1}).

CO_2 J	ν_0, cm^{-1a}	$\Delta\nu_{app}$, cm^{-1b}	T_{app}, K[c]	T_{rel}, K[d]	$\langle\Delta E_{rel}\rangle$[e]
2	3717.085	0.0080	400 ± 80	460 ± 90	169
8	3721.522	0.0072	320 ± 70	330 ± 70	34
22	3730.989	0.0071	310 ± 70	320 ± 70	23
26	3733.468	0.0078	370 ± 70	410 ± 80	117
36	3739.232	0.0088	480 ± 90	580 ± 100	294
38	3740.311	0.0098	600 ± 100	760 ± 110	482
44	3743.404	0.0105	680 ± 100	890 ± 120	617
52	3747.195	0.0096	560 ± 90	710 ± 110	430
54	3748.084	0.0102	640 ± 1000	820 ± 120	545
56[f]	2296.056	0.0057	527 ± 131	652 ± 162	370
62[f]	2289.248	0.0071	816 ± 163	1100 ± 220	837
68[f]	2282.227	0.0084	1164 ± 196	1640 ± 276	1400
78[f]	2270.050	0.0110	2009 ± 259	2950 ± 380	2767

[a]ν_0 is the IR transition frequency of CO_2 molecule.

[b]Full width at half-maximum (FWHM) linewidths $\Delta\nu_{app}$ in cm^{-1} for appearance of CO_2 rotational states at 1 μs through highly vibrationally excited pyrazine(E = 32700 cm^{-1}). The uncertainty in linewidths $\Delta\nu_{obs}$ is ± 0.001 cm^{-1}.

[c]The lab-frame translational temperatures $T_{trans,lab}$ (K) for CO_2 rotational states is determined using $T_{trans,lab} = (mc^2/8k_B ln2)(\Delta\nu_{app}/\nu_0)^2$, where m is the mass of CO_2, c is the speed of light, k_B is Boltzmann's constant, ν_0 is the IR transition frequency, and ν_{app} is the nascent Doppler broadened line width.

[d]The center-of-mass frame translational temperature, T_{rel} (K), for appearance of scattered CO_2 through collisions with excited pyrazine(E = 32700 cm^{-1}) is obtained from the equation: $T_{rel} = T_{trans,lab} + (T_{trans,lab} - T_0) \times (m_{CO_2}/m_{pyrazine})$, where m_{CO_2} and $m_{pyrazine}$ are the mass of CO_2 and pyrazine molecules respectively; T_0 = 298 K.

[e] $\langle\Delta E_{rel}\rangle$ in cm^{-1} is the average change in translational energy of pyrazine(E = 32700 cm^{-1})/CO_2 system, which is calculated by $\langle\Delta E_{rel}\rangle = {}^3/_2\, k_B(T_{rel} - T_0)$, where k_B is the Boltzmann constant and T_0 = 298 K.

[f]Estimated values for CO_2 high-J states from the previous paper(Ref. 77) are based on Figure 5.4.

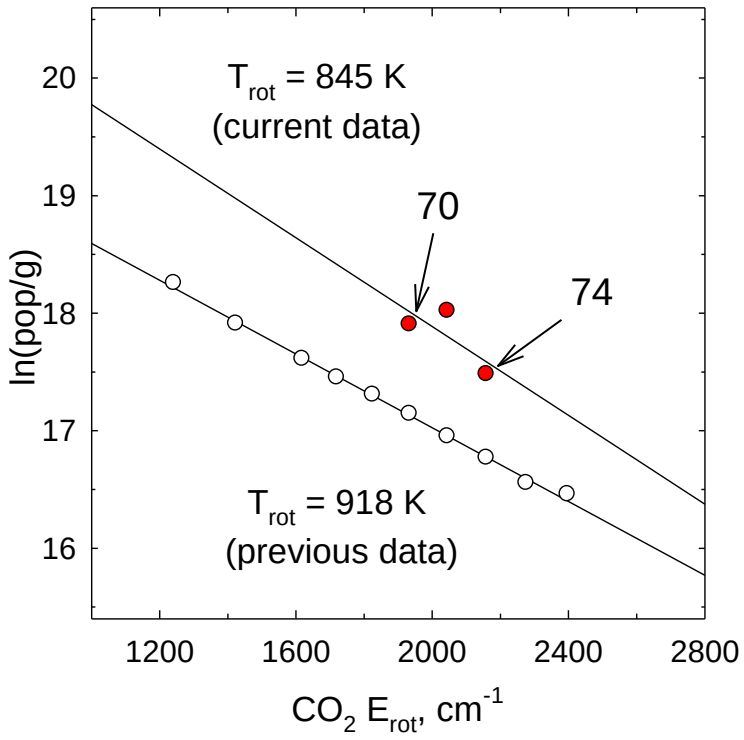

Figure 5.5 The current and previous data for scattered CO_2 molecules at high-J states after collisions with excited pyrazine are compared. Within the error, the rotational distribution of current data (T_{rot} = 845 K) is in agreement with the previous results (T_{rot} = 918 ± 100 K). The absolute populations for CO_2 J = 72–74 in this work are larger than the values for the same states in previous study.[77]

temperature of T_{rot} = 845 K, which is in good agreement with the previous data. However, the current results yield populations that are larger by a factor of 2 than in the previous study. This result indicates that the rate constants k^J_{app} are a factor of two larger than those measured previously. A number of factors may account for this difference, including poorly defined beam overlap profiles, slightly divergent UV and/or IR beams, and errors in the "pressure" reading of highly excited donors and CO_2. We note that the current study was performed using a new transient IR spectrometer with a number of improvements that should yield more accurate absolute population results. We have scaled the previous distribution to our current results for the J = 70–74 states.

5.3.3 Translational and Rotational Energy Gain of Scattered CO_2 (J = 2–78)

Translational energy gain of CO_2 (00^00) from collisions with pyrazine(E = 32700 cm^{-1}) was obtained by measuring transient absorption line profiles for individual CO_2 states. The appearance linewidths $\Delta\nu_{app}$ for scattered CO_2 (J = 2–54) were obtained by fitting the double-Gaussian function in Eq 5.3 to transient line profiles. The lab-frame translational temperatures T_{app} for appearance of scattered CO_2 molecules and the center-of-mass translational temperatures T_{rel} for pyrazine(E)/CO_2 collisions were determined based on $\Delta\nu_{app}$ measurements. The values of $\Delta\nu_{app}$, T_{app} and T_{rel} for CO_2 (J = 2–54) are listed in Table 5.1, along with data for J = 56–78.

The upper plot of Figure 5.6 shows the relative translational temperatures T_{rel} associated with CO_2 J-states (2–78) after single collisions with pyrazine at E =37900 cm^{-1} (circles) and E = 32700 cm^{-1} (triangles). At both energies, the amount of translational energy in the products has a similar J-dependence. For low-J states (J < 36) of CO_2, the

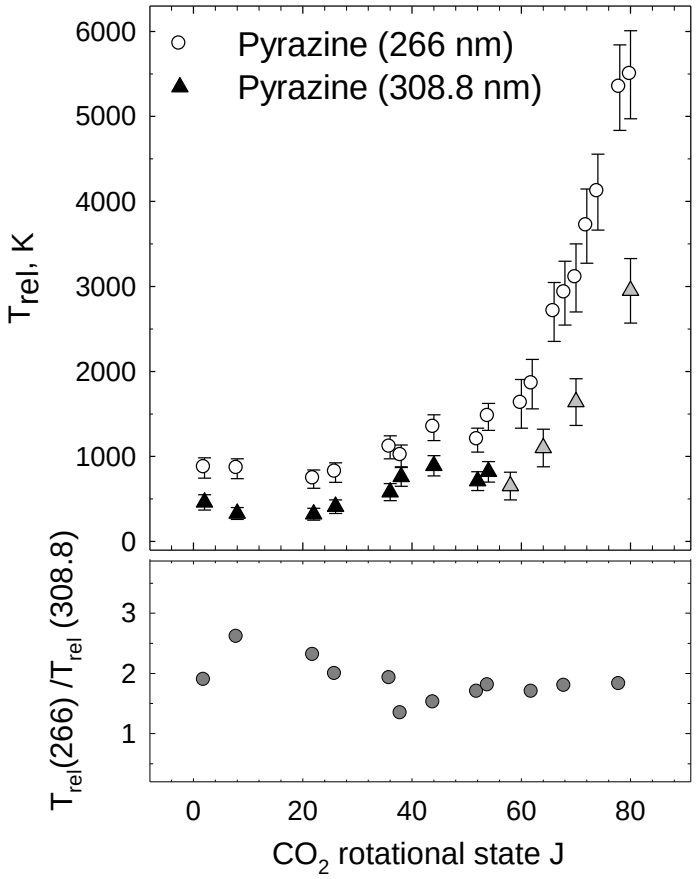

Figure 5.6 Nascent center-of-mass translational temperatures for individual rotational states of scattered CO_2 (00^00) molecule resulting from collisions with highly vibrationally excited pyrazine(E). The open circles show the relative temperatures for appearance of CO_2 states through collisions with vibrationally excited pyrazine(λ = 266 nm) and the black triangles are the relative translational data following collisions with pyrazine(λ = 308.8 nm). The data for CO_2 state J = 66–80 of pyrazine(E = 37900 cm^{-1}):CO_2 system (open circles) are from Ref. 77. The data at CO_2 high-J states (J = 62–78) of pyrazine(λ = 308.8 nm)/CO_2 which are shown by grey triangles are from Ref. 56. The lower plot illustrates the ratio of T_{rel} values for the two different donor energies. also 20% higher than for E = 32700 cm^{-1}.

pyrazine/CO_2 pair with two energies has low T_{rel} values. The values of T_{rel} at high-J states of CO_2 increase sharply as a function of J. The amount of translational energy gain of CO_2 is different at the two pyrazine energies, as shown in the lower plot in Figure 5.6, where the ratio of T_{rel} values is roughly a factor of 2 for the range J = 2–78. Thus, a 14% increase in donor vibrational energy doubles the translational energy of the collision products.

The nascent rotational distribution of scattered CO_2 molecules following collisions with pyrazine(E) where E = 32700 cm^{-1} is shown in Figure 5.7. The rotational distribution of scattered CO_2 is biexponential. The distribution has two sub-distributions that cross near E_{rot} = 1100 ± 100 cm^{-1}. The rotational temperature for the low rotational states is T_{rot} = 359 ± 50 K. For CO_2 E_{rot} > 1100 cm^{-1}, the distribution for scattered CO_2 is characterized by T_{rot} = 918 ± 100 K.

The CO_2 rotational distribution for pyrazine/CO_2 at E = 37900 cm^{-1} also showed biexponential behavior, as discussed in Chapter 4. In that case, the two individual distributions apparently cross at ~ 1100 cm^{-1}. The low CO_2 rotational states have T_{rot} = 439 K for E = 37900 cm^{-1} which is 20% higher than the rotational temperature for E = 32700 cm^{-1}. The high CO_2 rotational states have T_{rot} = 1160 K, also 20% higher than for E = 32700 cm^{-1}.

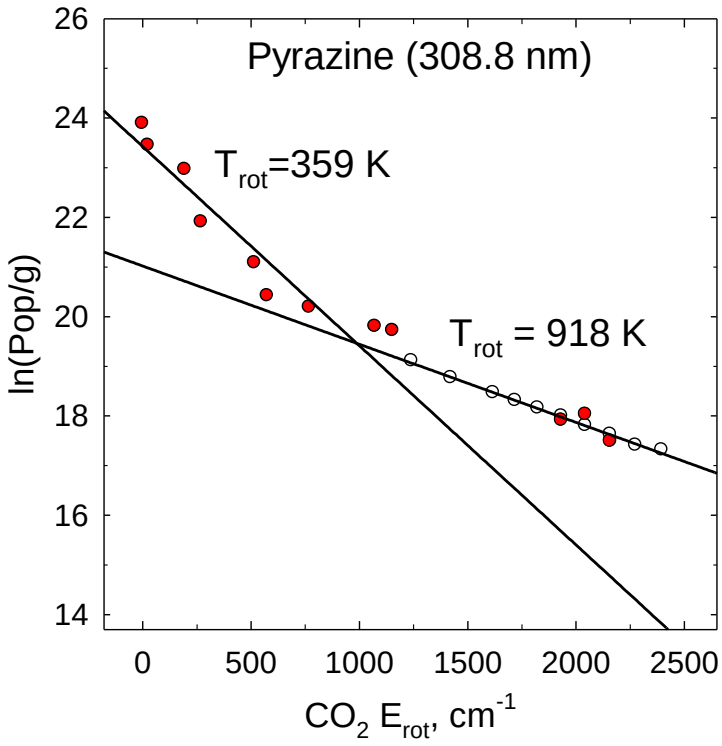

Figure 5.7 Nascent rotational distribution of scattered CO_2 (00^00) following collisions with vibrationally excited pyrazine(λ = 308.8 nm). The current experimental data for CO_2 (J = 2–74) are shown as red circles. The open circles are based on previous measurements for J = 56–80.[56] The distribution for the low-J states is characterized by $T_{rot} = 359 \pm 40$ K. For high-J states, $T_{rot} = 918 \pm 90$ K.

5.3.4 Appearance Energy Transfer Rates for CO_2 /pyrazine system

Rates for the appearance of scattered CO_2 molecules were measured following collisions with pyrazine(E = 32700 cm^{-1}), as described in Eq 5.2. The rate-constant k_{app}^{J} for energy transfer between pyrazine(E) and CO_2 was obtained using Eq 5.4:

$$\Delta\left[CO_2\left(00^00, J\right)\right] = k_{app}^{J}[pyz(E)]_0[CO_2]_0\Delta t \qquad (5.4)$$

where $[pyz(E)]_0$ and $[CO_2]_0$ are the initial concentrations of vibrationally excited pyrazine and CO_2, respectively. The appearance rate constants for individual CO_2 rotational states are listed in Table 5.2. The values of rate constants for CO_2 high-J states (J = 56–78) are obtained are scaled from previous measurements[77] as explained in Section 5.3.2.

The total appearance rate constant k_{app} = (7.7 ± 2.3) × 10^{-10} cm^3·$molecule^{-1}$·s^{-1} for the V–RT channel of pyrazine(E = 32700 cm^{-1})/CO_2 collisions is the sum of k_{app}^{J} for CO_2 (J = 0–100) based on data in Table 5.2 and Figure 5.7. This result is in good agreement with the Lennard-Jones collision rate of k_{LJ} = 5.6 × 10^{-10} cm^3·$molecule^{-1}$·s^{-1}. The appearance rate for pyrazine(E = 37900 cm^{-1})/CO_2 is k_{app} = (4.8 ± 1.4) ×10^{-10} cm^3·$molecule^{-1}$·s^{-1}. k_{app} for pyrazine(E = 37900 cm^{-1}) is 85% k_{LJ}. For E = 32700 cm^{-1}, k_{app} is 38% higher than k_{LJ}. The two appearance rates at different internal energies are reasonably consistent with k_{LJ}. It is interesting that the collision rate is somewhat larger for the higher donor energy. It may be that the two rates are within experimental uncertainty, or the branching ratio of the V–RT and the V–V pathways are sensitive to the changes in donor energy.

Table 5.2 State-resolved energy transfer rate constants k_{app}^{J} for pyrazine(E = 32700 cm^{-1}) /CO_2 collision pair.

J	E_{rot}, cm^{-1}	k_{app}^{J}, $\times 10^{-12a}$	J	E_{rot}, cm^{-1}	k_{app}^{J}, $\times 10^{-12}$
2	2.3413	18.2 ± 5.5	56	1244.22	3.6 ± 1.1
8	28.095	39.7 ± 11.9	60	1426.415	2.8 ± 0.8
22	197.4	64.6 ± 19.4	62	1522.1611	2.4 ± 0.7
26	273.9	26.5 ± 7.9	64	1621.0037	2.1 ± 6.4
36	519.5	16.0 ± 4.8	66	1722.9413	1.9 ± 0.6
38	578.0	8.7 ± 2.6	68	1827.9724	1.6 ± 0.5
44	772.1	8.0 ± 2.4	70	1936.0953	1.4 ± 0.4
52	1074.4	6.4 ± 1.9	72	2047.3081	1.2 ±0.4
54	1157.8	6.1 ± 1.8	74	2162.6090	1.0 ± 0.3
70	1936.0953	1.3 ± 0.4	76	2278.9962	0.9 ± 0.3
72	2047.3081	1.4 ± 0.5	78	2399.4677	0.7 ± 0.3
74	2162.6090	0.9 ± 0.3			
k_{app}, $cm^3 \cdot molecule^{-1} \cdot s^{-1}$[b]			$7.7(\pm 2.3) \times 10^{-10}$		
k_{LJ}, $cm^3 \cdot molecule^{-1} \cdot s^{-1}$			5.6×10^{-10}		

[a]The state-resolved rate constant k_{app}^{J} in $cm^3 \cdot molecule^{-1} \cdot s^{-1}$ at CO_2 low-J states (2–54) is experimental data in this Chapter.

[c]The integrated rate constant k_{app} for V–RT energy transfer channel between vibrationally hot pyrazine(E = 32700 cm^{-1}) and CO_2. k_{app} is the sum of measured by an k_{app}^{J} for CO_2 J = 0–100.

5.3.5 Depletion Collision Process

The depletion of population in CO_2 (00^00, J) due to collisions with pyrazine(E) is described by Eq 5.1. The state-resolved population changes and velocity distributions associated with depletion are measured from the Doppler-broadened transient line profiles of CO_2 low-J states at J < 40. The translational temperatures T_{dep} describing CO_2 molecules scattered out of the low J-states are obtained from the linewidths of depletion curve (Figure 5.4). All values of T_{dep} for CO_2 low J-states are approximately 300 K. The experimental linewidth data and values of T_{dep} for CO_2 (J = 2–38) are listed in Table 5.3.

The depletion rate for a given CO_2 state is described by Eq 5.5.

$$\text{rate}_{dep}(J) = -\frac{d[CO_2(J)]}{dt} = k_{dep} f(J) [CO_2]_0 [pyz(E)]_0 \tag{5.5}$$

Here f(J) is the fractional population in individual J-states of CO_2 at 300K, k_{dep} is the depletion rate constant, $[CO_2]_0$ is the total number density of the CO_2 bath gas, and $[pyz(E)]_0$ is the initial number density of pyrazine(E). To first order, we assume that the depletion rate constant is J-independent at room temperature.

Table 5.3 lists the depletion rates measured for CO_2 low rotational states (J = 2–38). The average depletion rate of low J-states is $\langle k_{dep} \rangle = (7.8 \pm 4.0) \times 10^{-10}$ $cm^3 \cdot molecule^{-1} \cdot s^{-1}$. This result is in good agreement with the depletion rate for pyrazine(E = 37900 cm^{-1}), where $\langle k_{dep} \rangle = (6.0 \pm 1.8) \times 10^{-10} cm^3 \cdot molecule^{-1} \cdot s^{-1}$. This result suggests that the collision rate of the pyrazine(E)/CO_2 system is independent of the internal energy in pyrazine.

Table 5.3 Depletion process Doppler-broadened linewidths, translational temperatures and depletion collision rates.

CO_2 J	ν_0, cm^{-1}	$\Delta\nu_{dep}$, cm^{-1}[a]	T_{dep}, K[b]	k_{dep}, $\times 10^{-10}$ $cm^3 \cdot molecule^{-1} \cdot s^{-1}$
2	3717.085	0.0067	280 ± 60	13.3 ± 3.9
8	3721.522	0.0063	250 ± 55	10.6 ± 3.3
22	3730.989	0.0063	250 ± 55	11.3 ± 3.3
26	3733.468	0.0068	290 ± 60	5.5 ± 1.8
36	3739.232	0.0070	300 ± 60	4.7 ±1.5
38	3740.311	0.0073	340 ± 65	1.6 ±0.6
$\langle k_{dep} \rangle$, $\times 10^{-10}$ $cm^3 \cdot molecule^{-1} \cdot s^{-1}$[c]				7.8 ± 4.0

[a]Full width at half-maximum (FWHM) linewidths $\Delta\nu_{dep}$ for depletion process at CO_2 J-states. The uncertainty of linewidths is reported to ± 0.001 cm^{-1}.

[b]The depletion lab-frame translational temperatures $T_{dep,lab}$ in K for CO_2 rotational states, is determined by the equation: $T_{dep} = (mc^2/8k_B \ln 2)\left(\Delta\nu_{dep}/\nu_0\right)^2$, where m is the mass of CO_2, c is the speed of light, k_B is Boltzmann's constant, ν_0 is the IR transition frequency, and ν_{dep} is the nascent Doppler broadened line width.

[c]$\langle k_{dep} \rangle$ the average of the rate constants k_{dep} at CO_2 low-J states.

5.4 Discussion

This Section considers the effect of the internal energy in pyrazine on the collision dynamics with CO_2 by comparing the V–RT energy transfer pathway at E = 32700 and 37900 cm^{-1}.

5.4.1 Angular Momentum Changes in V–RT Energy Transfer

The studies presented in Chapters 3 and 4 illustrated how angular momentum of bath molecules is correlated with the translational energy of collision products. Here we consider this for the pyrazine(E = 32700 cm^{-1})/CO_2 system.

Table 5.4 lists the average changes in CO_2 angular momentum $\langle \Delta J_{bath} \rangle$ and recoil velocity $\langle \Delta v_{rel} \rangle$ determined from the state-resolved translational temperatures T_{app} (Table 5.1). The initial rotational state of CO_2 bath molecule is taken to be $\langle J_{bath} \rangle$ = 22 at 298 K. The correlation of $\langle \Delta v_{rel} \rangle$ and $\langle \Delta J_{bath} \rangle$ for CO_2 J = 2–78 at E =32700 cm^{-1} are shown as triangles in Figure 5.8. Figure 5.8 shows that $\langle \Delta v_{rel} \rangle$ is a function of $\langle \Delta J_{bath} \rangle$ with smaller values of $\langle \Delta J_{bath} \rangle$ correlating to smaller $\langle \Delta v_{rel} \rangle$ of CO_2 molecules. The smallest $\langle \Delta v_{rel} \rangle$ is at $\langle \Delta J_{bath} \rangle \sim 0$. For $\langle \Delta J_{bath} \rangle > 40$ part, $\langle \Delta v_{rel} \rangle$ values more substantial increases in recoil velocity changes.

Figure 5.8 illustrates the similar correlations of $\langle \Delta v_{rel} \rangle$ and $\langle \Delta J_{rel} \rangle$ for pyrazine(E)/CO_2 pair at two different internal energies. For both each internal energies of pyrazine in Figure 5.8, smaller values of $\langle \Delta J_{bath} \rangle$ correlate to smaller $\langle \Delta v_{rel} \rangle$ of CO_2 molecules, and smallest $\langle \Delta v_{rel} \rangle$ is at $\langle \Delta J_{bath} \rangle \sim 0$, but the values of $\langle \Delta v_{rel} \rangle$ are smaller for the lower donor energy. The same range of much different at different internal energies.

Table 5.4 Angular momentum and recoil velocities for individual states of CO_2 J = 2–78 through collisions with highly vibrationally excited pyrazine(E = 32700 cm^{-1}).

Final J State	$\langle \Delta J_{bath} \rangle^a$	$\langle v_{lab} \rangle^b$	$\langle v_{rel} \rangle^c$	$\langle \Delta v_{rel} \rangle^d$
2	-21.9	476	633	121
8	-20.5	426	540	28
22	0.0	419	527	16
26	13.9	458	560	88
36	28.5	521	713	202
38	31.0	583	820	308
44	38.1	621	884	372
52	47.1	563	786	275
54	49.3	602	852	341
56	51.5	546	757	246
62	58.0	680	983	471
68	64.3	812	1200	688
78	74.8	1067	1609	1097

[a]The average angular momentum changes $\langle \Delta J_{bath} \rangle$ in units of $\hbar$ of CO_2 through collisions with vibrationally excited pyrazine. $\langle \Delta J_{bath} \rangle$ for CO_2 is calculated due to the equation: $\langle \Delta J_{bath} \rangle^2 = \left| \langle J'_{bath} \rangle^2 - \langle J_{bath} \rangle^2 \right|$. $\langle J'_{bath} \rangle$ is average final angular momentum vector of CO_2 bath molecule. The average initial angular momentum vector of CO_2 at 300K is $\langle J_{bath} \rangle \sim 22$.

[b]The average lab-frame velocity $\langle v_{lab} \rangle$ in m s^{-1} of scattered CO_2 at CO_2 states (J = 2 – 78) following collisions with vibrationally excited pyrazine, are determined from

$\langle v_{lab} \rangle = \left(\frac{3k_B T_{app}}{m_{CO_2}} \right)^{1/2}$, where k_B is the Boltzmann constant, T_{app} is the state-specific appearance lab-frame translational temperature listed in Table 5.2, and m_{CO_2} is the mass of CO_2.

[c]$\langle v_{rel} \rangle$, the average center-of-mass frame velocity in m s^{-1} for scattered pyrazine and CO_2 molecules, is determined from the equation: $\langle v_{rel} \rangle = \frac{M}{m_{pyz}} \cdot \left(\langle v_{lab} \rangle^2 - \frac{3k_B T}{M} \right)^{1/2}$ where M is the total mass of pyrazine and CO_2, m_{pyz} is the mass of pyrazine and T = 298 K.

[d]The average change in relative velocity $\langle \Delta v_{rel} \rangle$ in m s^{-1} is determined using an equation: $\langle \Delta v_{rel} \rangle = \langle v_{rel} \rangle - \left(\frac{3k_B T}{\mu} \right)^{1/2}$ where μ is the reduced mass for pyrazine/CO_2.

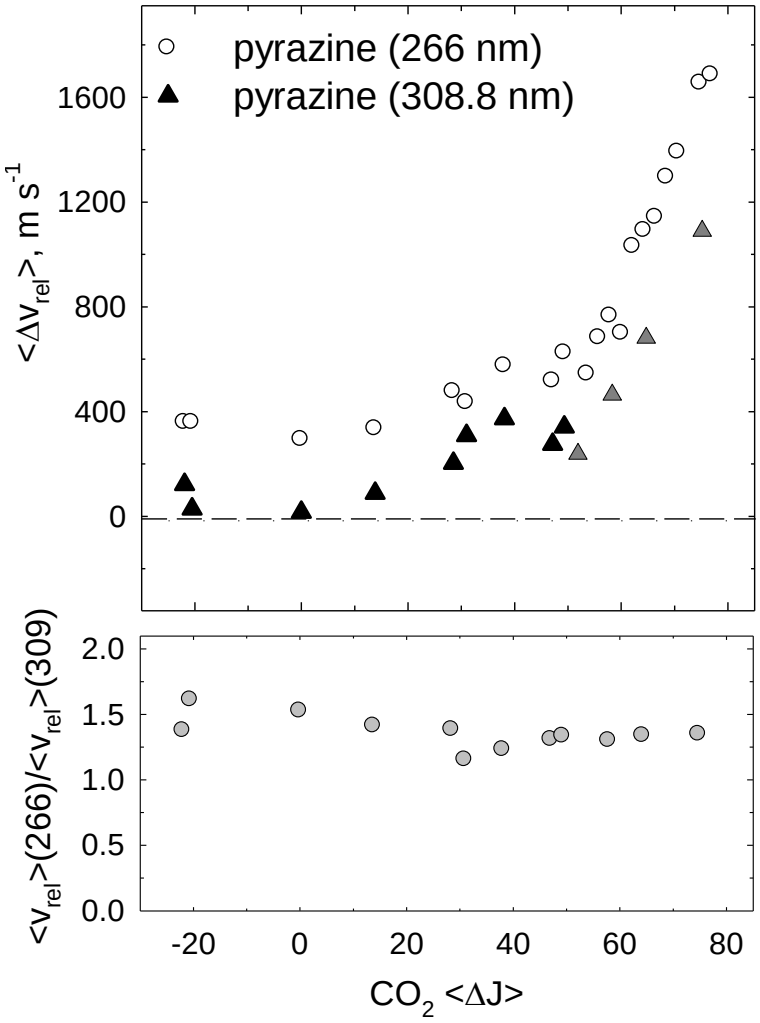

Figure 5.8 The upper plot shows the correlation between the average change in angular momentum $\langle \Delta J_{bath} \rangle$ of CO_2 molecule and the average change of recoil velocity $\langle \Delta v_{rel} \rangle$ for CO_2:pyrazine(E) collisions, where E = 32700 cm^{-1} (grey triangles) and E = 37900 cm^{-1}(open circles). Data for E = 37900 cm^{-1} are from Chapter 4. The open circles in the lower plot illustrate the ratios of $\langle \Delta v_{rel} \rangle$ of two internal energies of pyrazine.

For the same $\langle \Delta J \rangle$ values are observed. For E = 37900 cm^{-1}, the minimum value $\langle \Delta v_{rel} \rangle$ ~ 300 m s^{-1} while for E = 32700 cm^{-1}.

The ratio of the average recoil velocity is shown in the lower plot of Figure 5.8 as a function of $\langle \Delta J \rangle$. In general, the recoil velocities at 266 nm are ~ 1.5 times larger than at 308.8 nm excitation. By increasing the donor energy by 14%, the recoil velocities increase by ~ 50%.

5.4.2 Branching Ratio of Weak and Strong Collisions

The rotational distribution of scattered CO_2 molecules through collisions with pyrazine(E = 37900 cm^{-1}) was analyzed with a two-component model in Chapter 4. This model describes the population changes in each CO_2 rotational state using the sum of two Boltzmann distributions, as in Eq 5.6.

$$Pop_J = g_J \left[I_a \exp\left(\frac{-E_J}{k_B T_a}\right) + I_b \exp\left(\frac{-E_J}{k_B T_b}\right) \right] \tag{5.6}$$

Here g_J is the rotational degeneracy, E_J is the rotational energy, T_a and T_b are rotational temperatures, and I_a and I_b are the intensity parameters. A two-component model is used to describe the population distribution of scattered CO_2 molecules after collisions with pyrazine(E = 32700 cm^{-1}) as shown in Figure 5.9a. The grey circles in Figure 5.9a are the J-specific populations of scattered CO_2 from collisions with pyrazine(E = 32700 cm^{-1}). The solid line is the nonlinear least squares fitting of Eq 5.6 to the data with no initial constraints. The results of the fit have small residuals, as shown in Figure 5.9b.

The four fitting parameters I_a, I_b, T_a and T_b are used to describe the two sub-populations of scattered CO_2 molecules, as, shown in Figure 5.10. CO_2 low-J rotational states are described mostly by the cooler distribution with T_a= 214 K while high-J rotational states are mostly from the hotter population with a rotational temperature of T_b = 909 K. The cooler distribution corresponds to the outcome of weak collisions that are elastic or nearly elastic. The cooler population represents 76% of the observed population. The hotter population results from strong collisions between CO_2 and hot pyrazine and represents 24% of the entire population of scattered CO_2. In comparison, for the pyrazine(E = 37900 cm^{-1}) /CO_2 system, the ratio of cool and hot populations is 78% : 22%. The similar ratios of weak and strong collisions for the two different internal energies shows that the contributions of strong and weak collisions for the whole population distribution of scattered CO_2 bath molecules are not affected by this change in donor energy. We do note that the strong component is diminished in strength for the lower initial energy, as seen in the reduced T_b value at E = 32700 cm^{-1}. This observation suggests that as the internal energy in the donor is reduced, T_b will drop as well and eventually become indistinguishable from T_a. It is likely that some point, the donor energy will be low enough that a single distribution of scattered molecules will be observed.

5.4.3 The Full Energy Transfer Distribution P(ΔE)

The state-resolved energy gain data is used to generate an energy transfer probability distribution function P(ΔE) for the pyrazine(E)/CO_2 collision pair at E = 32700 cm^{-1}. P(ΔE) is generated directly from Doppler-broadened linewidths and energy-transfer rate constants using the method described by Michaels *et al*.[89] The ΔE includes

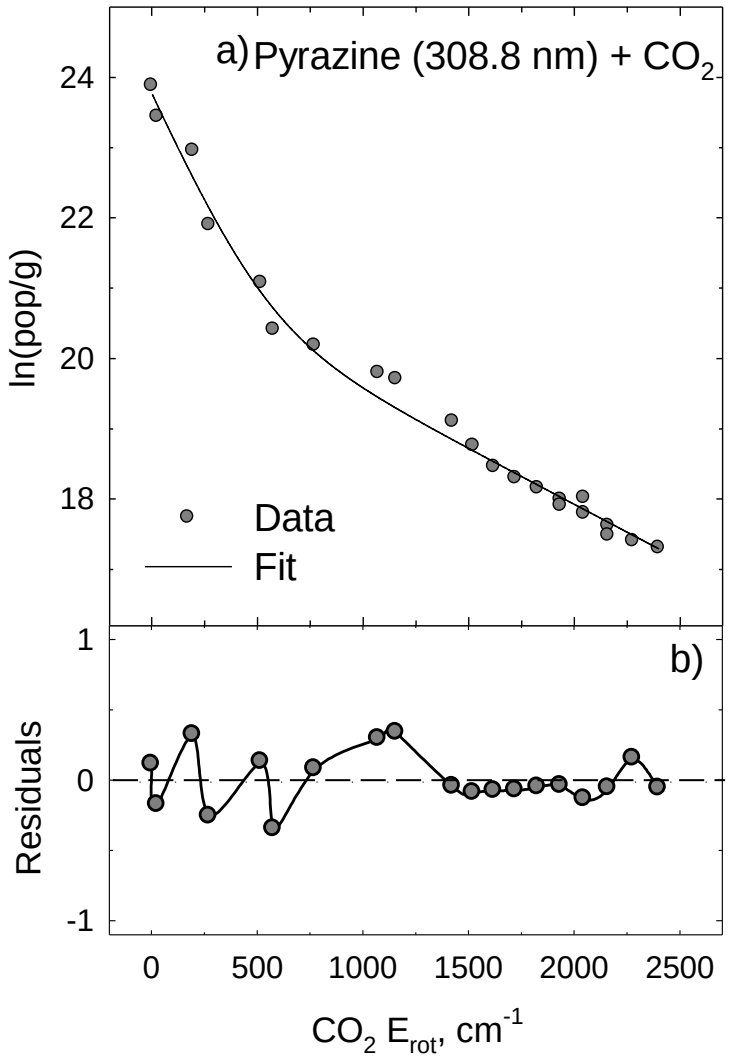

Figure 5.9 (a) A two-component biexponential function fitting curve (Eq 5.6) of the nascent rotational distribution (grey circles) of scattered CO_2 through collisions with pyrazine(E = 32700 cm^{-1}); (b) the results of fitting residuals at CO_2 rotational states are shown as the circles.

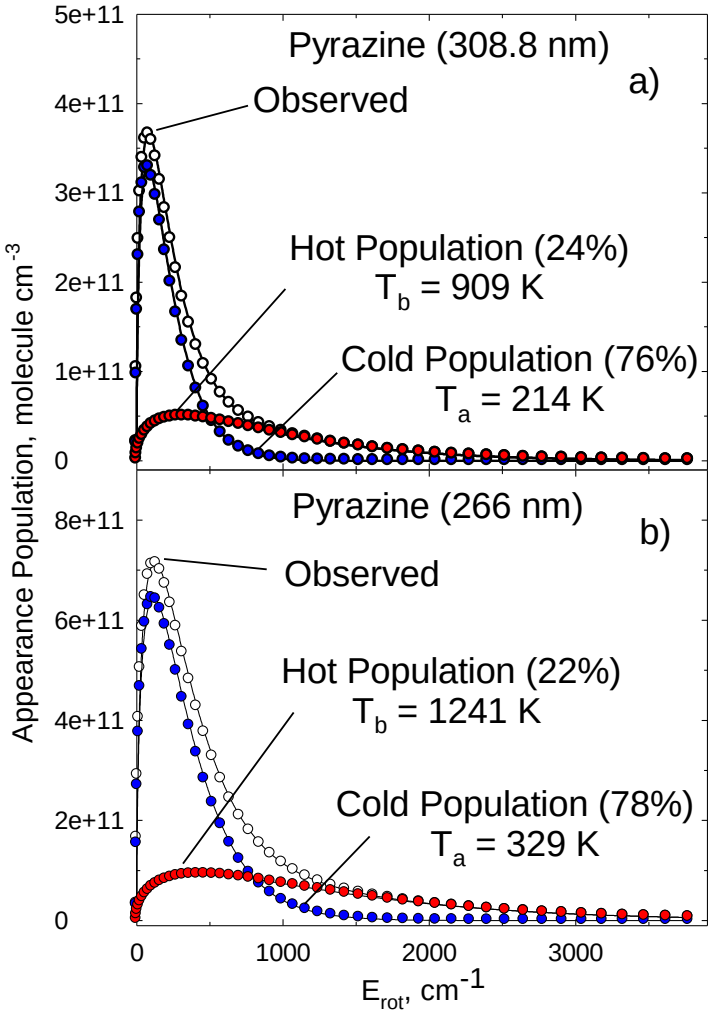

Figure 5.10 Population distributions of scattered CO_2 at t = 1 μs after weak or strong collisions with pyrazine(E). (a) Populations of CO_2 through collisions with pyrazine(E = 32700 cm^{-1}). 76% of the observed CO_2 populations (open circles) are from the cold population with T_{rot} = 214 K which is the product of weak collisions. The hot population with T_{rot} = 909 K from the strong collisions is 24% of the whole observed population. (b) Strong and weak collisions contribute similar percent populations for pyrazine(E = 37900 cm^{-1}). However, T_{rot} = 1241 K of hot population is 300 K bigger than E = 32700 cm^{-1} and T_{rot} = 329 K of cold population for pyrazine(E = 37900 cm^{-1}) is close to room temperature.

the change in CO_2 rotation energy plus the change in translational energy of pyrazine(E) and CO_2.

The P(ΔE) curves for the two pyrazine energies are shown in Figure 5.11. Figure 5.11a shows P(ΔE) distributions relative to k_{LJ} while Figure 5.11b shows P(ΔE) curves relative to k_{app}. 95% of the energy transfer between the pyrazine(E = 32700 cm^{-1})/CO_2 pair happens at ΔE < 1650 cm^{-1}. The maximum intensity of P(ΔE) curve is at ΔE ~ 0 which illustrates that the most collisions between hot pyrazine(E = 32700cm^{-1}) with CO_2 elastic are the most probable occurrence.

Figure 5.11 compares two P(ΔE) functions for CO_2/pyrazine(E) at E = 32700 cm^{-1} and 37900 cm^{-1}. 95% of the energy transfer between the pyrazine(E = 37900 cm^{-1}) and CO_2 pair happens at ΔE < 3100 cm^{-1}, which is almost twice as high as for E = 32700 cm^{-1}. This result illustrates that CO_2 molecules are more likely to gain large amounts of energy from pyrazine with higher vibrational energy and the probability of weak collision decreases between CO_2 and hot pyrazine with higher internal energy. The work in Chapter 4 that illustrates the maximum intensity of P(ΔE) curve of pyrazine(E = 37900cm^{-1})/CO_2 pair is at ΔE ~ 240 cm^{-1}. Base on this P(ΔE) curve, the average energy transfer $\langle\Delta E\rangle$ = 950 cm^{-1}, which is 2 times bigger than the value for E = 32700 cm^{-1}. Chapter 4 explains that there are several reasons why P(ΔE) for E = 37900 cm^{-1} has a maximum value at ΔE > 0. If we shift ΔE by 240 cm^{-1} to let the peak intensity of P(ΔE) occur at ΔE ~ 0, the average energy transfer drops to $\langle\Delta E\rangle$ = 670 cm^{-1} which is ~20 % higher than $\langle\Delta E\rangle$ = 525 cm^{-1} for E = 32700 cm^{-1}.

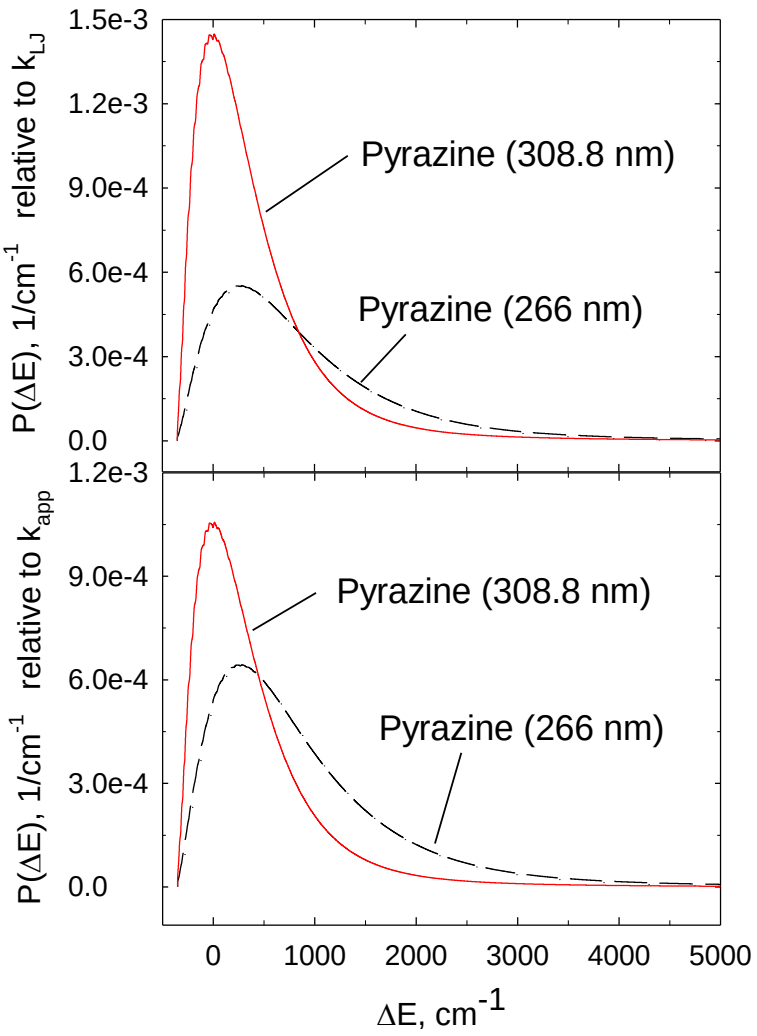

Figure 5.11 Energy-dependent full energy transfer probability distribution function P(ΔE) for pyrazine(E)/CO_2. The red solid line is P(ΔE) of E = 32700 cm^{-1} and the dash line is the one of E = 37900 cm^{-1}. Both of the distribution functions are normalized to the Lennard-Jones collision rate in the upper plot, while they are normalized to the appearance collision rate in the lower plot.

Barker and co-workers measured the collisional deactivation of pyrazine(E = 24000 cm^{-1}) with CO_2 using the IRF technique.[56] They reported that the average energy $\langle\Delta E\rangle$ of CO_2/pyrazine(E = 24000 cm^{-1}) is ~ 180 cm^{-1}. In addition, they found that $\langle\Delta E\rangle$ is approximately linearly dependent on the vibrational energy of pyrazine at low internal energy range (E = 5000 – 35000 cm^{-1}) and they proposed a near-linear equation to model this correlation. If we estimate the average transfer energy using their near-linear equation for pyrazine(E = 32700 cm^{-1}), the value of $\langle\Delta E\rangle$ is ~258 cm^{-1} which is half of our result. Given the differences in the experimental approaches, it is encouraging that the $\langle\Delta E\rangle$ values are in the same order of magnitude. Luther and co-workers also obtained the higher average transfer energies than the data of IRF methods for pyrazine(E)/Ar and pyrazine(E)/Ne pairs at high internal energy (E > 35000 cm^{-1}).[64] For example, at E = 32700 cm^{-1}, Luther's $\langle\Delta E\rangle$ value for pyrazine:Ne system is three times bigger than the result of IRF for the same collision system. For pyrazine/Ar system, the value of $\langle\Delta E\rangle$ from the KCSI technique is four times bigger than the result of IRF. Therefore, Barker's near-linear model might underestimates by a factor of 2-4.

The Luther group studied the collisional energy transfer from pyrazine with internal energies 32700 and 37900 cm^{-1} through collisions with Ar and Ne atoms. For both collision systems, the ratio of $\langle\Delta E\rangle$ for pyrazine(E = 32700 cm^{-1}) is ~ 70% of the value from pyrazine(E = 37900 cm^{-1}). This result shows $\langle\Delta E\rangle$ to have a near-linear dependence on donor internal energy. The results from KCSI, IRF and high IR resolution probing all illustrate that the average energy transfer $\langle\Delta E\rangle$ is sensitive to the internal energy of highly excited donor molecules and has a near-linear correlation to the internal energy.

5.5 Conclusions

This Chapter has investigated the effects of internal energy of donor molecules on collision energy transfer dynamics. The V-RT channel is observed to be the main energy transfer pathway between CO_2 and pyrazine with E= 32700 cm^{-1} and E = 37900 cm^{-1}. CO_2 bath molecules are scattered with twice the relative translational energy from pyrazine (E = 37900 cm^{-1}) as from pyrazine(E = 32700 cm^{-1}). Biexponential rotational distributions of scattered CO_2 from collision with the hot pyrazine at both internal energies are observed. The extent of CO_2 rotational energy is reduced for the lower donor energy. The ratio of the hot/cold populations is independent of internal energy. Internal energies do not influence the collision rate of pyrazine(E)/CO_2 system either. The full energy transfer distribution P(ΔE) confirms that collisions between molecules of lower internal energy transfer less energy than do collisions between hotter molecules. The data showed that the average collision energy $\langle\Delta E\rangle$ is near-linear dependent on the internal energy of pyrazine.

Chapter 6: Full Collisional Energy Gain Profiles of $CO_2(00^00)$ from Collisions with Highly Vibrationally Excited Molecules: 2-Methylpyridine, 2,6-Dimethylpyridine and 3,5-Dimethylpyridine ($E \sim 38500\ cm^{-1}$)

6.1 Introduction

The ability to measure the full product state distribution from collisions of high energy molecules opens up exciting new possibilities for understanding the role of collisional relaxation and chemical reactivity. The work presented in this Chapter focuses on how the molecular structure of the energy donor affects the energy transfer dynamics. A series of methylated pyridines are used as energy donors and the full energy gain profiles in energy-accepting CO_2 molecules are measured with high resolution transient IR absorption. The addition of methyl groups increases the number of vibrational modes in the donor molecules, adds low frequency modes in the form of methyl rotors and lowers the average energy per mode when the excitation energy is held constant. By characterizing the distribution of weak and strong collisions that come from methylated donors, we gain insight into how different types of molecular motion impact overall energy transfer profiles.

A number of techniques have been used to study the role of donor methylation in collisional quenching under multi-collision conditions. Using the IRF technique for donors with $E = 24000\ cm^{-1}$, Miller and Barker found that the average energy loss from toluene ($C_6H_5CH_3$) is larger than for benzene (C_6H_6).[55,59] In collisions with rare gases, toluene(E) loses 3-4 times more energy on average per collision than does benzene. In UVA studies on cycloheptatriennes with $E = 41900\ cm^{-1}$, Troe and coworkers showed

that average energy transfer values increased as a function of the donor size in collisions with a given bath gas.[47-49,52,152-155,164-167]

Previous studies in the Mullin group have used high resolution transient IR absorption to measure the outcome of strong collisions for a series of highly excited azabenzenes (pyrazine,[77,106] pyridine,[85] 2-methylpyridine and 2,6-dimethylpyridine[86]) with H_2O and CO_2 as collision partners. These studies found that the rotational and translational energy distributions of the scattered bath molecules were substantially reduced for the methylated donors. For CO_2 collisions, only the states with J = 60–80 were investigated. To understand more fully how donor methylation impacts the energy transfer dynamics, the work in this Chapter focuses on the appearance of low-J CO_2 states that come primarily from weak collisions.

This Chapter reports the scattering profiles for CO_2 (00^00) in low-J states (J = 2-64) that result from weak collisions with highly vibrationally excited methylpyridine donors: 2-methylpyridine (2MP), 2,6-dimethylpyridine (2,6MP) and 3,5-dimethylpyridine (3,5MP). The structures of the three methylpyridine molecules are shown in Figure 6.1. For 2MP and 2,6MP, strong collision data are combined with the current measurements to generate the full energy transfer profiles for scattered CO_2 molecules. The energy transfer profiles for the three methylated donors are compared and discussed in light of the results presented in Chapters 3-5.

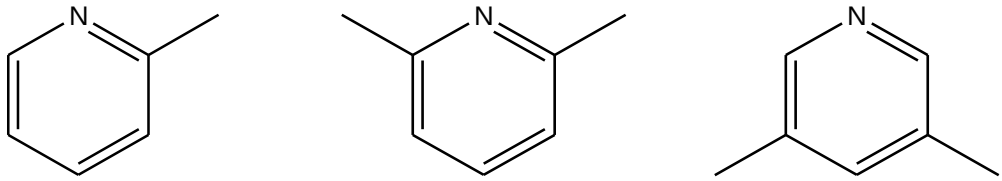

2-methylpyridine (2MP)

2,6-dimethylpyridine (2,6MP)

3,5-dimethylpyridine (3,5MP)

Figure 6.1 The molecular structures of the three methylated pyridine donors.

6.2 Experimental Methods

The work reported in this Chapter was performed using the high-resolution F-center transient IR absorption spectrometer at λ = 2.7 μm. The three highly vibrationally excited donor molecules (2MP, 2,6MP and 3,5MP) were prepared with λ = 266 nm light from a Nd:YAG laser. To minimize multiphoton absorption, the UV power density was kept below 4.9 MW/cm^2. The fraction of excited donors was lower than 15%. Through collisions with excited donors, the number densities of scattered CO_2 at low states (J = 2-64) were probed by IR absorption.

The overlapped IR/UV beams passed through a 3 m collision sample cell. A 1:1 mixture of donor and CO_2 gases at a total pressure of approximately 20 mTorr flowed through the cell. The average collision time in these studies was approximately 4 μs. The transient IR absorption intensities obtained at t = 1 μs ensures that the signals result from single collisions of CO_2 with vibrationally excited donors.

Three donors, 2MP (Aldrich, 98%), 2,6MP (Sigma-Aldrich 99+%) and 3,5MP (Aldrich, 98+%) were degassed by the freeze-pump-thaw method before use and CO_2 (Matheson Tri-gas, 99.995% purity) was used directly.

6.3 Results and Discussion

The V-RT energy transfer dynamics of three highly vibrationally excited alkylpyridine donors with CO_2 are reported here for CO_2 rotational states J = 2–80. The rotational and translational energy profiles for CO_2 are reported. Collision rates and full energy transfer distributions P(ΔE) are also reported. The effect of donor structure on collisional quenching is discussed by comparing the results for the methylated donors with those for pyrazine(E).

6.3.1 Transient IR Absorption of Scattered CO_2 ($00^0 0$) at J= 2-64

For a given CO_2 J-state, two processes are responsible for the transient signals observed through collisions with highly vibrationally excited donors(E) as described in Chapters 3–5. Following collisions with vibrationally hot donors, appearance signals correspond to CO_2 molecules scattering into a specific J-sate while depletion signals show CO_2 population leaving the state. Figure 6.2 shows the transient IR absorption for the CO_2 J = 26 state following collisions with the three donors at two different probe wavelengths. Depletion is seen at the center absorption frequency ν_0 in the three plots on the left in Figure 6.2. Appearance on the other hand is seen in the Doppler-broadened wings, as shown in the right side of Figure 6.2.

CO_2 states have appreciable population up to J = 38 and depletion signals are observed at ν_0 for J ≤ 38. For higher J states, only appearance signals are observed in our measurements. Figure 6.3 shows Doppler-broadened transient line profiles for CO_2 J = 26 at t = 1 μs after excitation of the donors: 2MP (circles), 2,6MP (triangles) and 3,5MP (squares). The black solid curves are the fitting result for the Doppler-broadened line using a double-Gaussian function (Eq 6.1).

$$F(\nu)=I_{app}\exp\left[-4\ln 2\left(\frac{\nu-\nu_0}{\Delta\nu_{app}}\right)^2\right]-I_{dep}\exp\left[-4\ln 2\left(\frac{\nu-\nu_0}{\Delta\nu_{dep}}\right)^2\right]+F_0 \qquad (6.1)$$

Here, I_{app} and I_{dep} are the intensities for appearance and depletion at the center frequency ν_0; $\Delta\nu_{app}$ and $\Delta\nu_{dep}$ are the full widths at half maximum (FWHM) for the appearance and

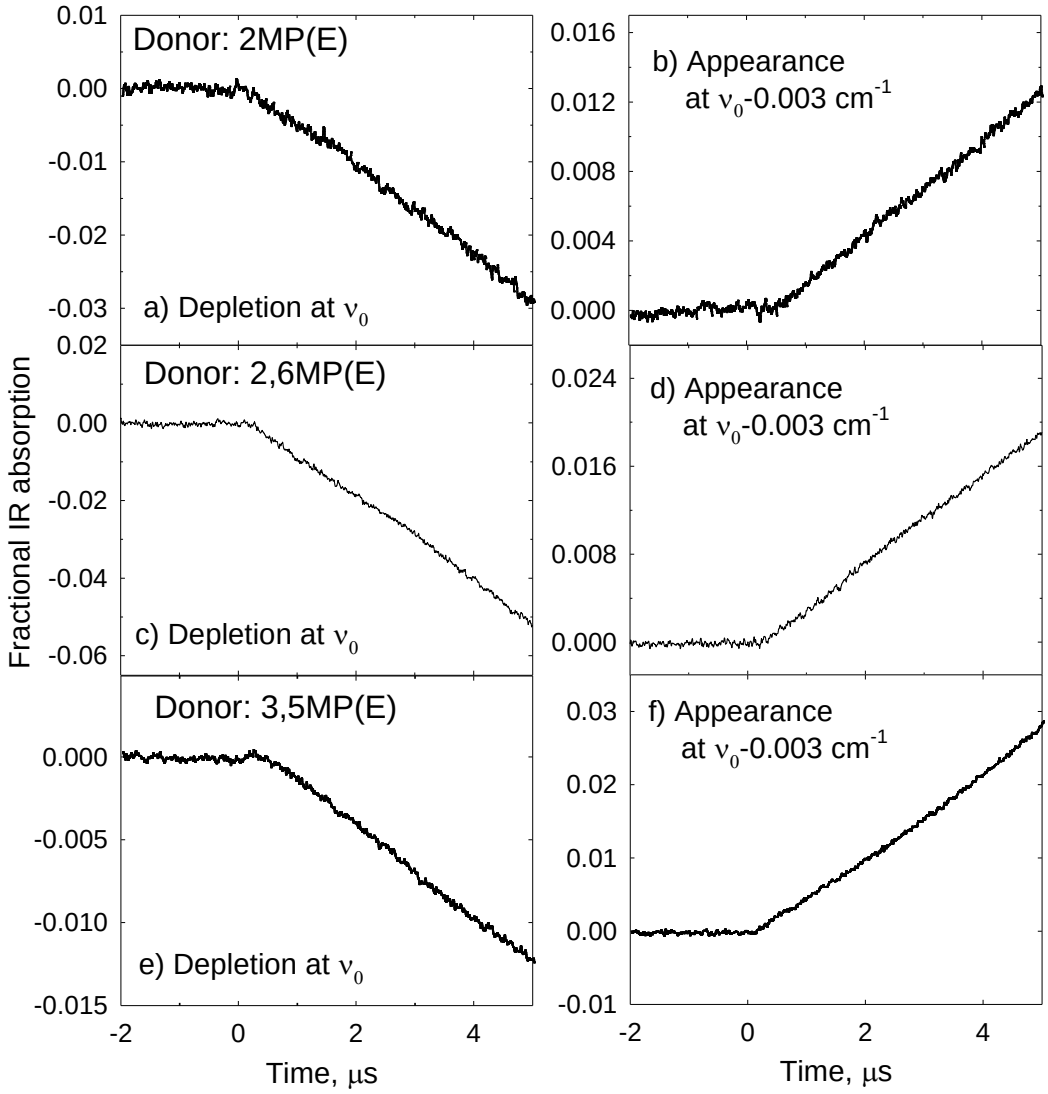

Figure 6.2 Transient absorption signals for scattered CO_2 (00^00) in the J = 26 state after collisions with highly vibrationally excited 2MP (E = 37900 cm^{-1}), 2,6MP (E = 38500 cm^{-1}) and 3,5MP (E = 38500 cm^{-1}) which were prepared by 266 nm. The three plots on the left show depletion signals at line center ν_0. The right-hand plots show CO_2's appearance signals measured at the wings of the Doppler-broadened line profile at a frequency of $\nu_0 - 0.003$ cm^{-1}.

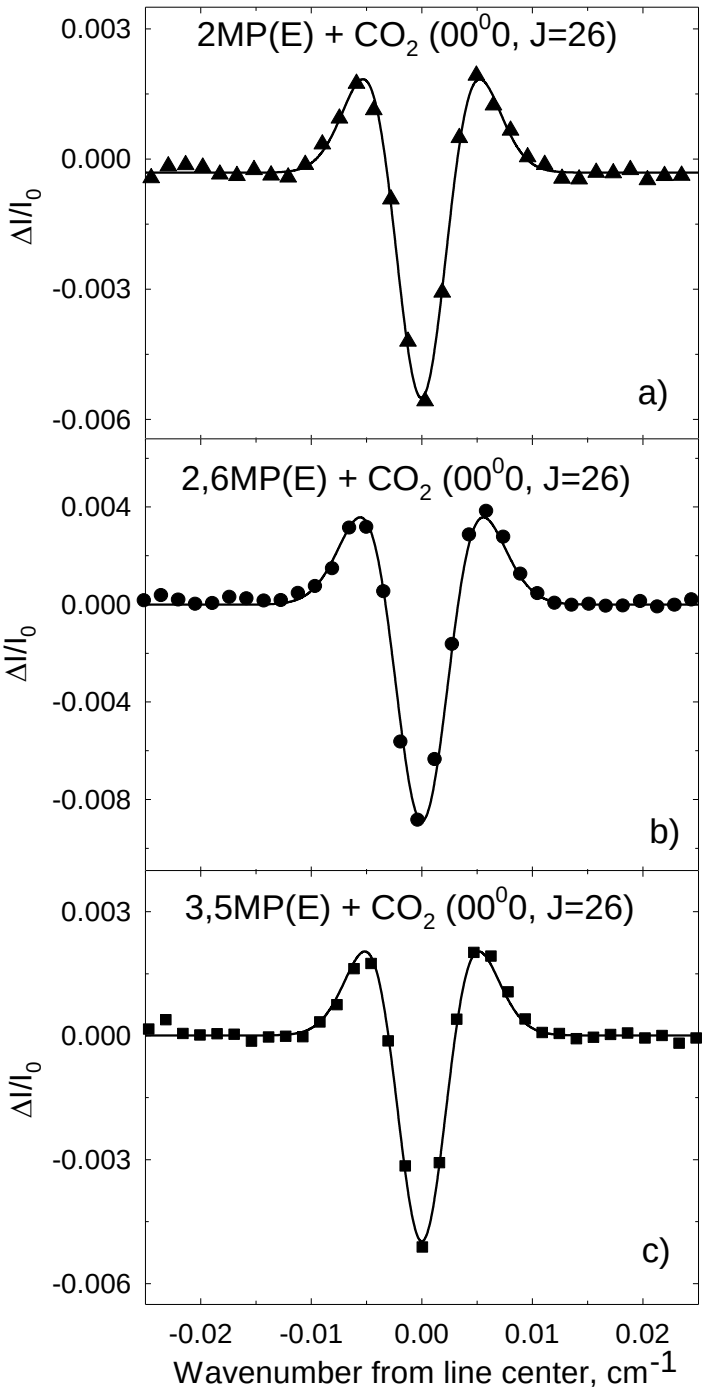

Figure 6.3 The transient IR absorption line shape for CO_2 ($00^0$0) J = 26 at t = 1 μs after single collisions with three highly vibrationally excited donor molecules: (a) 2MP, (b) 2,6MP and (c) 3,5MP. The solid curves are the double-Gaussian fitting results.

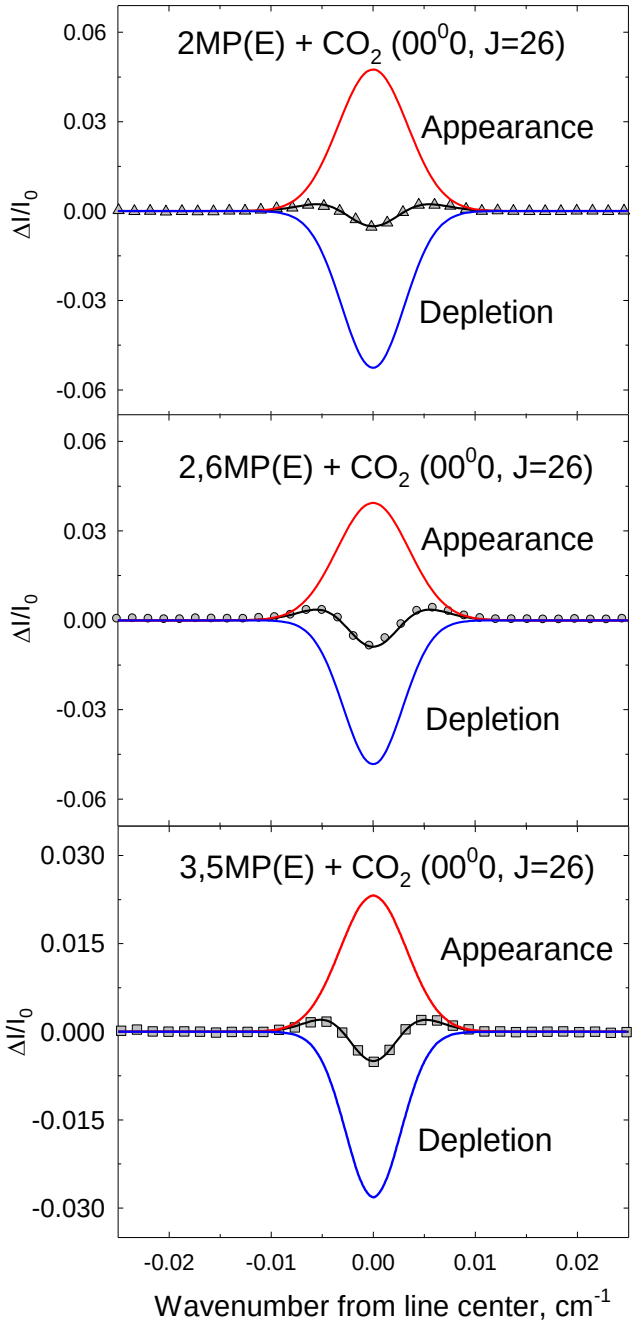

Figure 6.4 Transient absorption line profile for the J = 26 rotational state of CO_2 ($00^0$0) at t = 1 μs following excitation of vibrationally hot 2MP (triangles), 2,6MP (circles) and 3,5MP (squares). The black lines are the double-Gaussian fitting results. Red lines illustrated the appearance process and blue lines show the depletion process.

depletion. From the intensity and line width parameters, the appearance (in red) and depletion (in blue) profiles are shown in Figure 6.4.

6.3.2 Translational Excitation of Scattered CO_2 (00^00) with Three Donor Molecules

The appearance line widths $\Delta\nu_{app}$ of the Doppler-broadened transient line profiles are obtained from the double-Gaussian fitting function Eq 6.1. The values for state-specific $\Delta\nu_{app}$ and the lab-frame and center-of-mass translational temperatures for individual CO_2 states after are listed in Table 6.1.

The full translational energy profiles are plotted in Figure 6.5 for the three donors. The current results for 2MP and 2,6MP are combined with previous high-J results from Ref. 56. The translational distributions of CO_2 with 2,6MP and 3,5MP are very similar. For CO_2 low J-states ($J < 60$), the values of T_{rel} are CO_2 J-independent and have values at approximately 500 K. For CO_2 high rotational states with $J > 60$, the values of T_{rel} increase as a function of the CO_2 J-state.

Chapter 4 reported the translational energy profiles collisions of pyrazine(E) with CO_2 when $E = 37900$ cm^{-1}. Here the effects of donor methylation are explored by comparing results for 2MP, 2,6MP and 3,5MP collisions with pyrazine collisions. The overall trends of J-dependent product translational energies of the four donors are similar. However, compared to pyrazine collisions, the translational energy profiles from the methylated donors are much smaller.

The correlation of changes in angular momentum and recoil velocity was determined for pyrazine(E)-DCl in Chapter 3 and for pyrazine(E)-CO_2 in Chapter 4. Based on the state-specific T_{app} values for J = 2–78, the average changes in CO_2 angular momentum $\langle\Delta J_{bath}\rangle$ and recoil velocity $\langle\Delta v_{rel}\rangle$ for three methylpyridine donors were

Table 6.1 (a) Nascent appearance Doppler-broadened line widths and translational temperatures for 2MP/CO_2 collision pairs.

2MP (E = 38500 cm^{-1}) + CO_2 (00^00)				
J	ν_0, cm^{-1}	$\Delta\nu_{app}$, cm^{-1}[a]	$T_{app,lab}$,K[b]	T_{rel}, K[c]
2	3717.0853	0.0087	477 ± 78	561 ± 91
8	3721.5215	0.0087	471 ± 77	553 ± 90
22	3730.9893	0.0080	396 ± 70	443 ± 78
26	3733.4684	0.0085	459 ± 76	535 ± 88
36	3739.2323	0.0088	472 ± 76	554 ± 89
38	3740.3115	0.0081	403 ± 70	452 ± 79
44	3743.4040	0.0097	581 ± 84	715 ± 104
54	3748.08398	0.0100	613 ± 87	762 ± 108
58	3659.40288	0.0093	553 ± 84	673 ± 102

[a]State-resolved full width at half-maximum (FWHM) line widths, $\Delta\nu_{app}$, for appearance process of CO_2 at 1 μs after collisions with highly vibrationally excited 2MP, 2,6MP or 3,5MP. The uncertainty of $\Delta\nu_{app}$ is ± 0.001 cm^{-1}.

[b]The lab-frame translational temperatures $T_{trans,lab}$ for CO_2 rotational states are calculated from the formula $T_{trans,lab}=(mc^2/(8Rln2))(\Delta\nu_{obs}/\nu_0)^2$, where m is the mass of CO_2, c is the speed of light, R is the gas constant and ν_0 is the center frequency of the absorption line.

[c]The center of mass translational temperature T_{rel} in K for an isotropic distribution of scattered CO_2 molecules is obtained from the equation:

$T_{rel} = T_{trans,lab} + \left(T_{trans,lab} - T_0\right) \times \left(m_{CO_2} / m_{donor}\right)$, where T_0 = 298 K and three donors are 2MP, 2,6MP and 3,5MP.

(b) Nascent appearance Doppler-broadened line widths and translational temperatures for 2,6MP/CO_2 collision pairs.

2,6MP (E = 38500 cm^{-1}) + CO_2 (00^00)				
J	ν_0, cm^{-1}	$\Delta\nu_{app}$, cm^{-1a}	$T_{app,lab}$,K^b	T_{rel}, K^c
2	3717.0853	0.0086	446 ± 75	506 ± 85
8	3721.5215	0.0079	387 ± 69	424 ± 76
22	3730.9893	0.0082	410 ± 71	456 ± 79
26	3733.4684	0.0085	444 ± 74	504 ± 84
36	3739.2323	0.0090	494 ± 78	574 ± 91
38	3740.3115	0.0094	546 ± 82	649 ± 97
44	3743.4040	0.0091	510 ± 79	598 ± 93
52	3747.1946	0.0097	577 ± 84	691 ± 101
54	3748.08398	0.0093	537 ± 81	635 ± 96
58	3659.40288	0.0102	671 ± 93	824 ± 114

(c) Nascent appearance Doppler-broadened line widths and translational temperatures for 3,5MP/CO_2 collision pairs.

3,5MP (E = 38500 cm^{-1}) + CO_2 (00^00)				
J	ν_0, cm^{-1}	$\Delta\nu_{app}$, cm^{-1a}	$T_{app,lab}$,K[b]	T_{rel}, K[c]
2	3717.0853	0.0074	340 ± 65	358 ± 69
8	3721.5215	0.0078	381 ± 69	415 ± 75
22	3730.9893	0.0087	466 ± 76	535 ± 87
26	3733.4684	0.0084	442 ± 74	500 ± 84
36	3739.2323	0.0104	663 ± 90	812 ± 111
38	3740.3115	0.0093	529 ± 81	623 ± 95
44	3743.4040	0.0086	455 ± 74	519 ± 85
52	3747.1946	0.0097	577 ± 84	692 ± 101
66	2387.2578	0.0072	871 ± 162	983 ± 193
70	2388.64	0.0076	783 ± 154	1106 ± 206

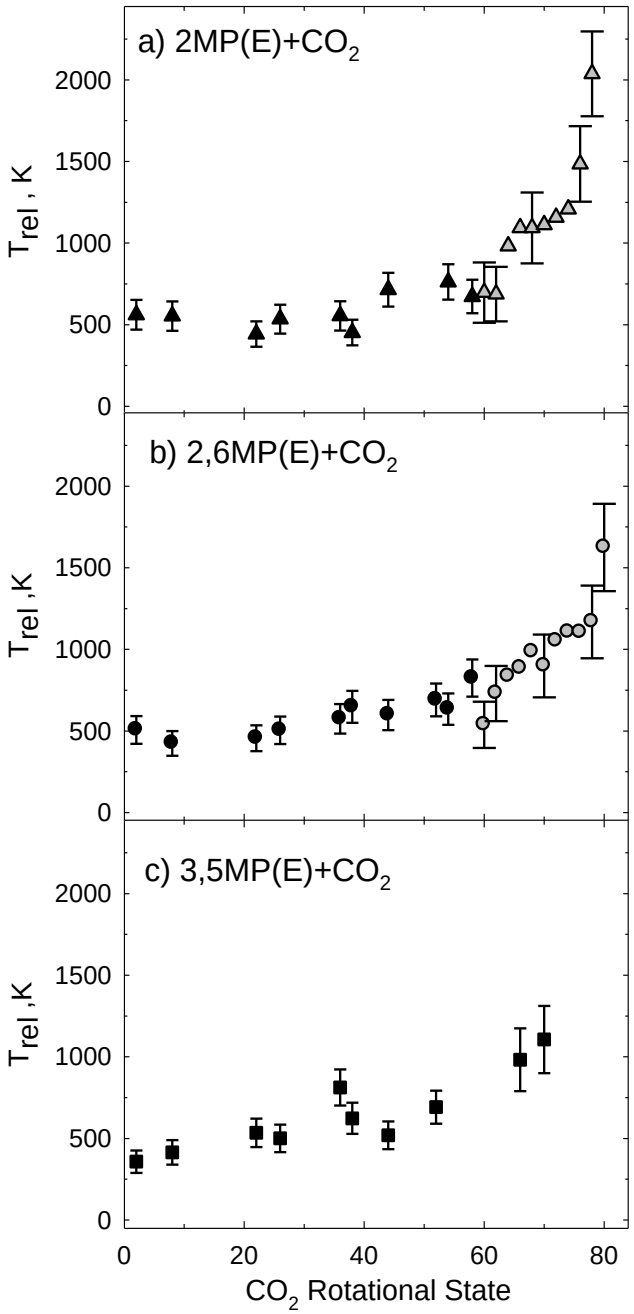

Figure 6.5 Nascent center-of-mass translational temperatures for individual rotational states of scattered CO_2 (00^00) molecule resulting from collisions with highly vibrationally excited 2MP (triangles), 2,6MP (circles) and 3,5MP (squares). The grey symbols are state-resolved translational temperatures at CO_2 high-J states from the previous paper (Ref. 86).

determined and are listed in Table 6.2. The initial average rotational state for CO_2 at 300 K is $\langle J_{ini} \rangle = 22$. The correlation of $\langle \Delta v_{rel} \rangle$ and $\langle \Delta J_{bath} \rangle$ for CO_2 with four donors (pyrazine, 2MP, 2,6MP and 3,5MP) is shown in Figure 6.6. For each donor, Figure 6.6 shows that $\langle \Delta v_{rel} \rangle$ is a function of $\langle \Delta J_{bath} \rangle$ for the J = 2–80 states of CO_2. The smallest values of $\langle \Delta v_{rel} \rangle$ are approximately 100 ms^{-1} for three alkylpyridine-CO_2 pairs which is approximately 200 $m \cdot s^{-1}$ smaller than the value of pyrazine/CO_2. For $\langle \Delta J_{bath} \rangle > 40$, larger changes in recoil velocity $\langle \Delta v_{rel} \rangle$ are seen for each CO_2/donor system. The values of $\langle \Delta v_{rel} \rangle$ for CO_2/pyrazine are larger than for the methylated pyridine donors. The correlation of $\langle \Delta J_{bath} \rangle$ and $\langle \Delta v_{rel} \rangle$ is similar for the methylpyridine/CO_2 systems. Methylation slightly reduces the initial velocity of collision pairs which could lead to collisions that are less impulsive and recoil velocities that are smaller for a given J state. It is likely however that the most important source of the reduction in recoil velocity is that addition of methyl groups increases the low-frequency motions of the high energy molecules and pulls energy out of the high frequency modes.

6.3.3 Rotational Energy Gain of Scattered CO_2 (00^00)

The rotational distributions of scattered CO_2 molecules (J = 2–80) are reported here from collisions with 2MP(E), 2,6MP(E) and 3,5MP(E). Semilog plots of transient populations are shown in Figure 6.7. Two models are used for fitting to the data. A single-exponential population model is fit to the data in the left-hand plots. The values of rotational temperatures for three distributions are T_{rot}=476 K for 2MP, T_{rot} = 472 K for 2,6MP and T_{rot} = 417 K for 3,5MP. There is evidence, particularly in the 2MP and 2,6MP data, that the rotational distributions have two components, one for the low-J data and a hotter distribution for the high-J data. The plots on the right side of Figure 6.7 show

Table 6.2 (a) Angular momentum and recoil velocities for individual states of CO_2 J = 2–78 through collisions with highly vibrationally excited 2MP molecule(E = 38500 cm^{-1}).

2MP (E = 38500 cm^{-1}) + CO_2				
Final J State	$\langle \Delta J_{bath} \rangle^a$	$\langle v_{lab} \rangle^b$	$\langle v_{rel} \rangle^c$	$\langle \Delta v_{rel} \rangle^d$
2	-21.9	519.6	684.0	185.4
8	-20.5	516.7	679.3	180.7
22	0.0	473.8	607.7	109.2
26	13.9	509.7	667.7	169.1
36	28.5	517.2	680.0	181.5
38	31.0	477.5	614.0	115.5
44	38.1	573.7	772.1	273.5
54	49.3	589.3	797.3	298.7
58	53.7	559.5	749.2	250.6
60	55.8	567.7	762.5	263.9
62	58.0	564.7	757.6	259.1
64	60.1	657.4	905.4	406.8
66	62.2	689.0	954.9	456.3
68	64.3	689.0	954.9	456.3
70	66.5	694.3	963.2	464.6
72	68.6	706.8	982.8	484.2
74	70.7	720.3	1003.8	505.2
76	72.7	790.8	1112.9	614.3
78	74.8	915.3	1303.5	804.9

[a]The average angular momentum changes $\langle \Delta J_{bath} \rangle$ in units of $\hbar$ of CO_2 through collisions with vibrationally excited 2MP, 2,6MP and 3,5MP. $\langle \Delta J_{bath} \rangle$ for CO_2 is calculated due to the equation: $\langle \Delta J_{bath} \rangle^2 = \left| \langle J'_{bath} \rangle^2 - \langle J_{bath} \rangle^2 \right|$. $\langle J'_{bath} \rangle$ is average final angular momentum vector of CO_2 bath molecule. The average initial angular momentum vector of CO_2 at 300K is $\langle J_{bath} \rangle \sim 22$.

[b]The average lab-frame velocity $\langle v_{lab} \rangle$ in m s^{-1} of scattered CO_2 at rotational states (J = 2–78) following collisions with vibrationally excited 2MP, 2,6MP or 3,5MP, is calculated from $\langle v_{lab} \rangle = \left(\frac{3k_B T_{app}}{m_{CO_2}} \right)^{1/2}$, where k_B is the Boltzmann constant; T_{app} is the state-specific appearance lab-frame translational temperature listed in Table 6.1; m_{CO_2} is the mass of CO_2.

[c]$\langle v_{rel} \rangle$, the average center-of-mass frame velocity in $m \cdot s^{-1}$ for hot donors (2MP, 2,6MP or 3,5MP) and CO_2 molecules, is determined from the equation: $\langle v_{rel} \rangle = \frac{M}{m_{donor}} \cdot \left(\langle v_{lab} \rangle^2 - \frac{3k_B T}{M} \right)^{1/2}$ where M is the total mass of donors (2MP, 2,6MP or 3,5MP) and CO_2, m_{donor} is the mass of two donors and T = 298 K.

[d]The average change in relative velocity $\langle \Delta v_{rel} \rangle$ in $m \cdot s^{-1}$, is obtained from an equation: $\langle \Delta v_{rel} \rangle = \langle v_{rel} \rangle - \left(\frac{3k_B T}{\mu} \right)^{1/2}$ where μ is the reduced mass for donor/CO_2 collisions system (donor: 2MP, 2,6MP or 3,5MP).

(b) Angular momentum and recoil velocities for individual states of CO_2 J = 2–78 through collisions with 2,6MP molecule (E = 38500 cm^{-1}).

2,6MP (E = 38500 cm^{-1}) + CO_2				
Final J State	$\langle \Delta J_{bath} \rangle^a$	$\langle v_{lab} \rangle^b$	$\langle v_{rel} \rangle^c$	$\langle \Delta v_{rel} \rangle^d$
2	-21.9	502.4	636.0	148.1
8	-20.5	468.4	582.1	94.1
22	0.0	481.9	603.6	115.6
26	13.9	501.5	634.6	146.6
36	28.5	528.8	677.3	189.3
38	31.0	556.3	719.7	231.8
44	38.1	537.8	691.3	203.3
52	47.1	571.5	743.0	255.0
54	49.3	551.4	712.1	224.2
58	53.7	616.5	811.5	323.5
60	55.8	514.9	655.5	167.6
62	58.0	584.9	763.6	275.6
64	60.1	620.2	817.1	329.1
66	62.2	636.4	841.5	353.5
68	64.3	666.8	887.2	399.2
70	66.5	640.4	847.5	359.5
72	68.6	686.5	916.5	428.6
74	70.7	702.0	939.6	451.6
76	72.7	701.6	939.0	451.0
78	74.8	719.9	966.2	478.2

(c) Angular momentum and recoil velocities for individual states of CO_2 J = 2–70 through collisions with highly excited 3,5MP molecule (E = 38500 cm^{-1}).

3,5MP (E = 38500 cm^{-1}) + CO_2				
Final J State	$\langle \Delta J_{bath} \rangle^a$	$\langle v_{lab} \rangle^b$	$\langle v_{rel} \rangle^c$	$\langle \Delta v_{rel} \rangle^d$
2	-21.9	439.2	534.9	46.9
8	-20.5	464.7	576.3	88.2
22	0.0	513.6	653.8	165.7
26	13.9	500.1	632.5	144.5
36	28.5	612.6	805.9	317.8
38	31.0	547.2	705.9	217.8
44	38.1	507.6	644.4	156.3
52	47.1	571.7	743.6	255.6
66	62.2	666.1	886.4	398.3
70	66.5	702.4	940.6	452.5

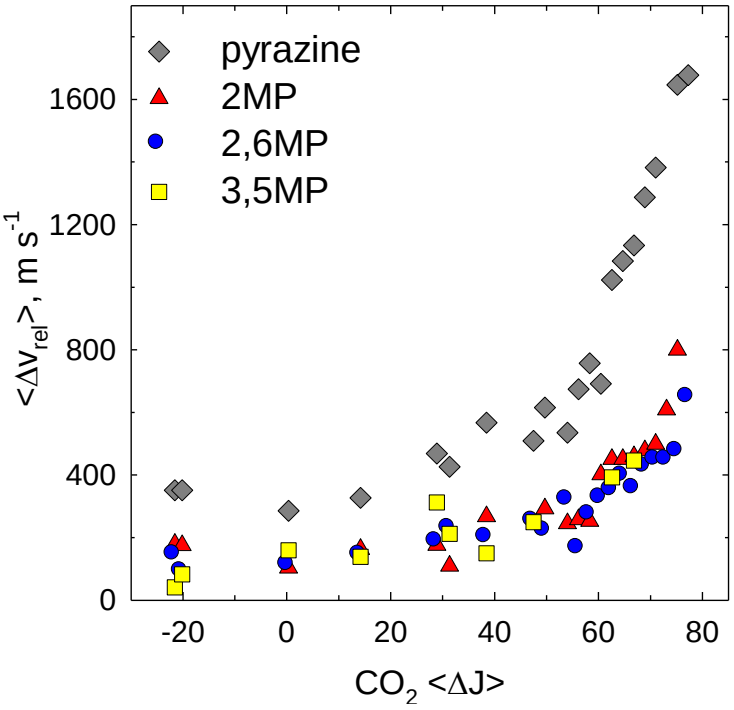

Figure 6.6 The average velocity changes for CO_2 (J = 2–80) through collisions with highly vibrationally excited pyrazine (diamonds), 2MP (triangles), 2,6MP (circles) and 3,5MP (squares). The data for pyrazine/CO_2 were reported in Chapter 4. The data at CO_2 high-J states (J = 56–80) following collisions with 2MP and 2,6MP are obtained from Ref. 86.

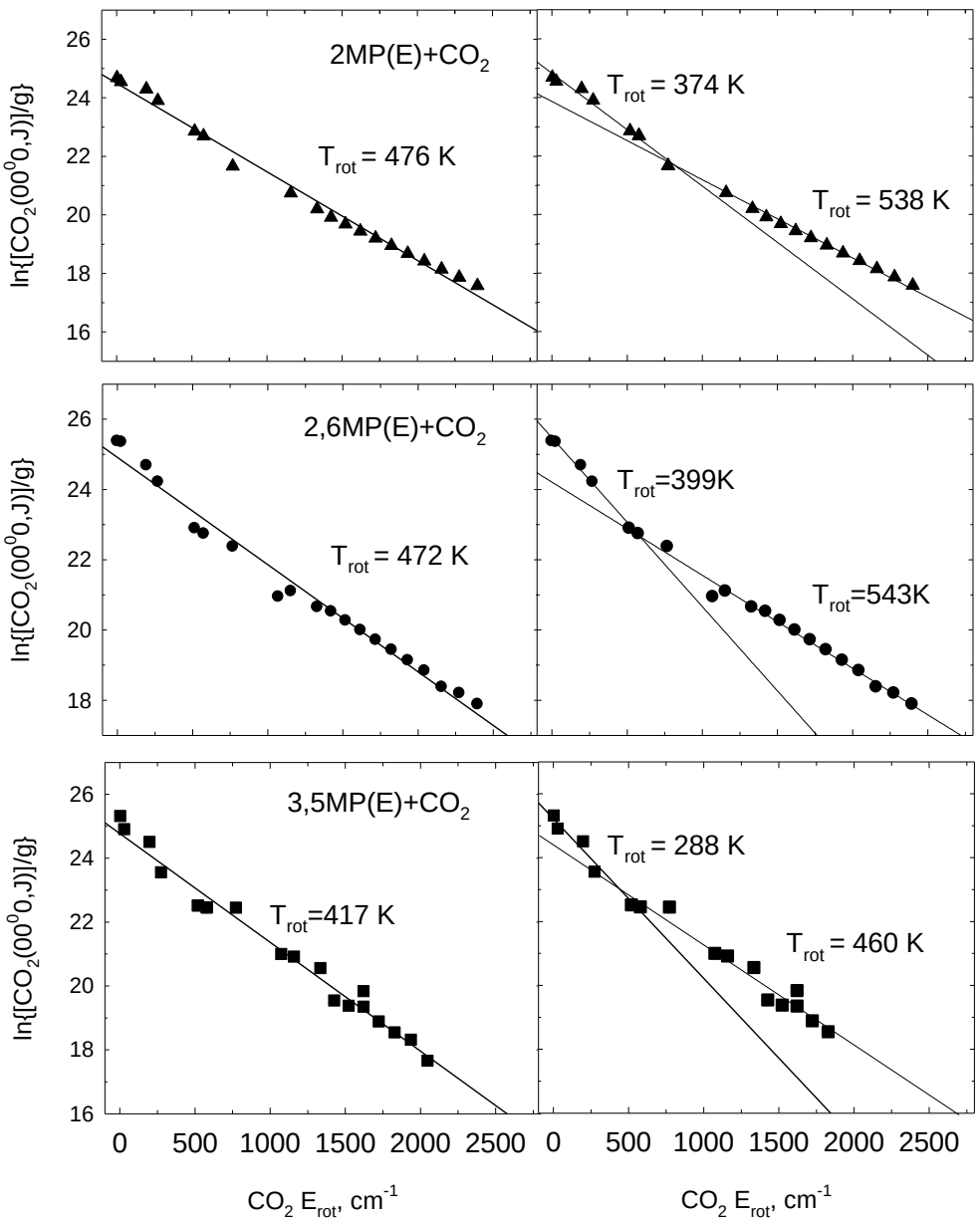

Figure 6.7 Nascent rotational distribution for the J = 2–80 states of CO_2 due to collisions with three highly vibrationally excited donors, 2MP (triangles), 2,6MP (circles) and 3,5MP (squares). The populations of scattered CO_2 after collisions with three donors are fitted by two methods. The three left plots show the single-exponential modes for the rotational distributions while the bi-exponential model is used to fit the three experimental results in the right plots.

the results of fitting the low and high-J regions separately. The crossing points of the two distributions is near E_{rot} = 750 cm^{-1} for 2MP, E_{rot} = 550 cm^{-1} for 2,6MP and E_{rot} = 400 cm^{-1} for 3,5MP. The low energy rotational distributions have temperatures near 300–400 K while the distributions for the higher J states have temperatures near 500 K.

The methylated pyridine donors at E near 38500 cm^{-1} impart substantially less rotational energy to CO_2 than does pyrazine with E=37900 cm^{-1}. For pyrazine(E)/CO_2 collisions, the scattered CO_2 molecules also have two rotational temperatures (as discussed in Chapter 4), and the low energy component is near room temperature. However, the crossing point of the two distributions for pyrazine/CO_2 collisions occurs at a much higher rotational energy of approximately 1160 cm^{-1}. The rotational temperature of the high energy component (T_{rot} = 1164 ± 110 K) is substantially larger than that seen for the methylated donors. It is clear from Figure 6.7 that the methylated donors impart less rotational energy transfer to CO_2 than pyrazine.

Here the rotational distributions for CO_2 J=2–80 are characterized by a two component model. This model treats the total population in a given J state as the sum of two sub-populations using Eq. 6.2.

$$Pop_J = g_J \left[I_a \exp\left(\frac{-E_J}{k_B T_a}\right) + I_b \exp\left(\frac{-E_J}{k_B T_b}\right) \right] \qquad (6.2)$$

Here g_J is the rotational degeneracy; E_J is the rotational energy; T_a and T_b are rotational temperatures; and I_a and I_b are the intensity parameters. The fitting results are shown as solid lines in Figure 6.8 for collisions of CO_2 with 2MP, 2,6MP and 3,5MP. The residuals from the fit are shown in the plots on the right in Figure 6.8.

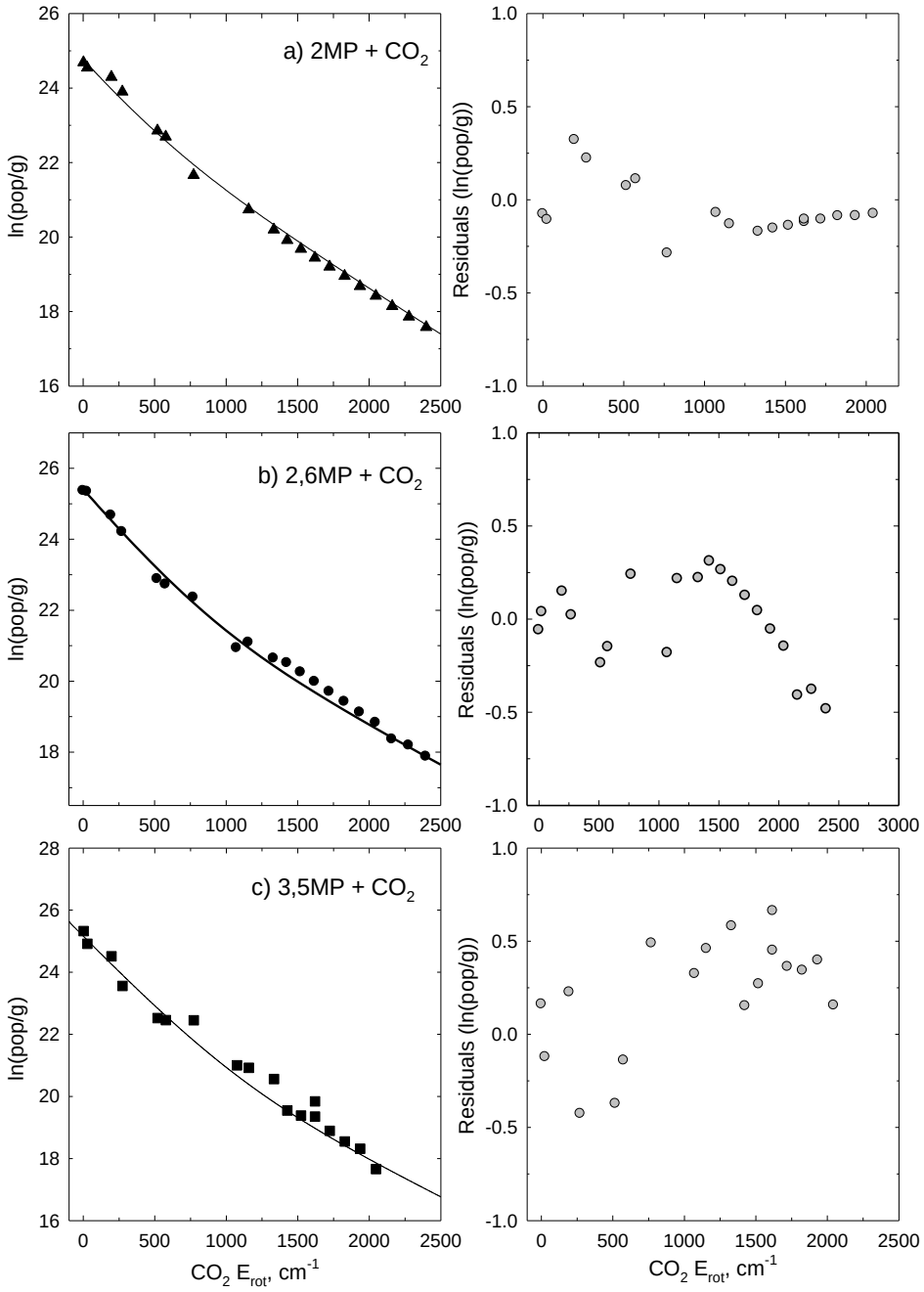

Figure 6.8 A two-component biexponential function fitting curve (Eq 6.4) of the nascent rotational distributions of scattered CO_2 through collisions with excited 2MP, 2,6MP and 3,5MP. (a) The fitting curve for 2MP/CO_2 data (triangles). (b) The fitting curve for 2,6MP data (circles). (c) The fitting curve for 3,5MP/CO_2 data (squares). The plots to the right are the residuals for the fitting results.

The two-component model fits the experimental data of CO_2/2,6MP pair without any constraints. However, the model cannot uniquely fit the CO_2/2MP and CO_2/3,5MP data sets without imposing initial constraints on the fitting parameters. These data sets were fit by setting T_a at 300 K and varying the relative values of I_a and I_b until the residuals were minimized. This process is described in more detail in Appendix D.

The two sub-populations that result from donor/CO_2 collisions are shown in Figure 6.9, based on fitting the data with Eq. 6.4. The cold populations of CO_2 molecules have T_a is near 300 K, indicating that these are elastic or weakly inelastic collisions. The temperatures for the high energy tail are T_b =592 K for 2MP, 852 K for 2,6MP and 600 K for 3,5MP. The elevated rotational temperatures indicate that the collisions are impulsive and involve non-zero ΔJ values for CO_2. The ratios of the number densities for the cold and hot populations are 88:22 for 2,6MP and 85:15 for 3,5MP-CO_2. The population ratio for 2MP is 58:42. It is interesting that the donors with two methyl groups have comparable population ratios. However, given the experimental uncertainties, the spread in the data and the constraints that were imposed in the fitting procedure, it is best not to compare these ratios quantitatively. Instead, a clear qualitative picture of the energy transfer emerges. When CO_2 is the collision partner, two distinct types of collisions are involved in quenching high energy molecules: elastic and nearly elastic collisions dominate the CO_2 populations in low-J states while the higher rotational states have population from more impulsive collisions that involve larger ΔJ values.

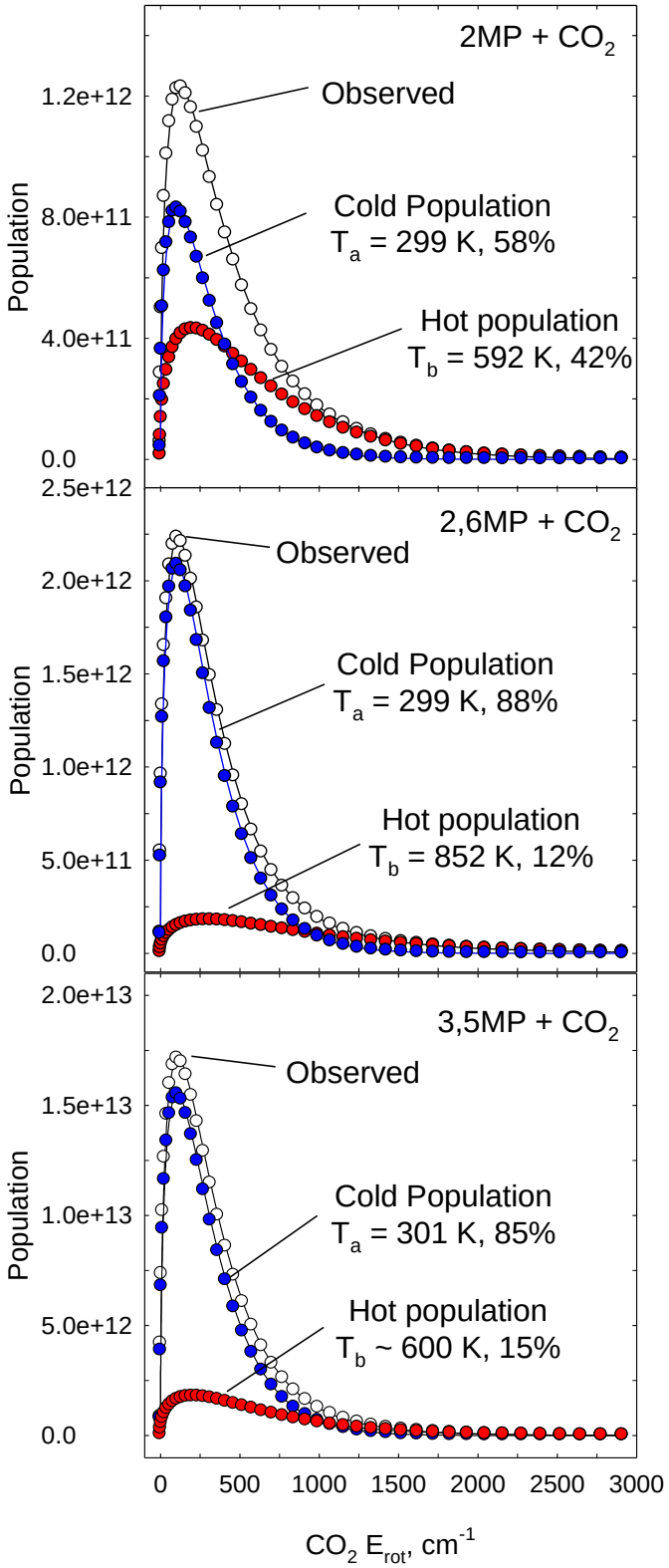
2MP + CO2
Observed
Cold Population
Ta = 299 K, 58%
Hot population
Tb = 592 K, 42%
Population
1.2e+12
8.0e+11
4.0e+11
0.0
2,6MP + CO2
Observed
Cold Population
Ta = 299 K, 88%
Hot population
Tb = 852 K, 12%
2.5e+12
2.0e+12
1.5e+12
1.0e+12
5.0e+11
3,5MP + CO2
Observed
Cold Population
Ta = 301 K, 85%
Hot population
Tb ~ 600 K, 15%
2.0e+13
1.5e+13
1.0e+13
5.0e+12
0
500
1000
1500
2000
2500
3000
CO2 Erot, cm-1

Figure 6.9 Two energy sub-distributions are separated by the two-component model. The cold population distribution with T_a ~ 300 K is associated with weak collisions which shown as three alkylpyridine molecules with CO_2. The hot populations of scattered CO_2 from the strong collisions with three alkylpyrdine molecules are 592 K for 2MP, 852 K for 2,6MP, and 600 K for 3,5MP. The contributions of cold and hot populations for the observed populations are 88:22 for 2,6MP/CO_2, 58:42 for 2MP/CO_2 and 85:15 for 3,5MP/CO_2.

6.3.4 Appearance Collision Rate k_{app} for CO_2 with 2MP, 2,6MP and 3,5MP

The appearance of CO_2 molecules in specific J states due to collisions with 2MP(E), 2,6MP(E) and 3,5MP(E) is described by Eq 6.1. The state-resolved rate constant k^J_{app} for individual J states is obtained using Eq 6.3:

$$\frac{\Delta[CO_2^J]}{\Delta t} = k^J_{app}[\text{donor(E)}]_0[CO_2]_0 \qquad (6.3)$$

Here, $[\text{donor(E)}]_0$ and $[CO_2]_0$ are the initial concentrations for donors (2MP, 2,6MP and 3,5MP) and CO_2; $\Delta[CO_2^J]$ is the change in CO_2 J-specific number density at Δt=1 μs after UV pulse. The state-specific rate constant k^J_{app} for CO_2 states J = 2–58 with three methylated pyridine donors are listed in Table 6.3.

The appearance collision rate constant k_{app} in Table 6.3 is the sum of state-resolved rate-constants for CO_2 J = 0–98, based on $k_{app} = \sum_{J=0-98} k^J_{app}$. Since the V- RT channel to which k_{app} corresponds is one pathway for collisions between donor and bath molecules, k_{app} is a lower limit to the total collision rate constant. The values of k_{app} are (8.1±2.4) × 10^{-10} cm^3 $molecule^{-1}$ s^{-1} for 2MP, (1.2±0.4) × 10^{-9} cm^3 $molecule^{-1}$ s^{-1} for 2,6MP and (9.8±3.0) × 10^{-10} cm^3 $molecule^{-1}$ s^{-1} for 3,5MP.

In Table 6.3, values of the Lennard-Jones collision rates k_{LJ} are listed for 2MP, 2,6MP and 3,5MP with CO_2 at 300 K. The ratio of k_{app} to k_{LJ} is greater than unity for each of these donors: 1.4 for 2MP, 2.0 for 2,6MP and 1.6 for 3,5MP. In comparison, the ratios for pyrazine are 0.85 at E = 37900 cm^{-1} (Chapter 4) and 1.2 at E = 32700 cm^{-1} (Chapter 5). These ratios are illustrated in Figure 6.10. This comparison gives some

Table 6.3. State-specific energy transfer rate constants.

	E_{rot}, cm^{-1}	$k^J_{app} \times 10^{-11}$ $cm^3 \cdot molecule^{-1} \cdot s^{-1}$[a]		
		2MP	2,6MP	3,5MP
2	2.3413	1.1 ± 0.3	1.9 ± 0.6	2.0 ± 0.6
8	28.0951	3.1 ± 0.9	6.3 ± 1.9	4.4 ± 1.3
22	197.4	6.4 ± 1.9	8.5 ± 2.6	8.7 ± 2.6
26	273.9	5.1 ± 1.5	6.2 ± 1.9	4.0 ± 1.2
36	519.5	2.5 ± 0.8	2.3 ± 0.7	1.7 ± 0.5
38	578.0	2.2 ± 0.7	2.1 ± 0.6	1.7 ± 0.5
44	772.1	0.8 ± 0.2	1.7 ± 0.5	2.0 ± 0.6
52	1074.4	—	0.5 ± 0.2	0.5 ± 0.2
54	1157.8	0.4 ± 0.1	0.6 ± 0.2	—
58	1333.8	0.3 ± 0.1	0.4 ± 0.1	—
66	1722.9	—	—	0.10 ± 0.03
68	1828.0	—	—	0.07 ± 0.02
k_{app}, $cm^3 \cdot molecule^{-1} \cdot s^{-1}$[b]		$(8.1 \pm 2.4) \times 10^{-10}$	$(1.2 \pm 0.4) \times 10^{-9}$	$(9.8 \pm 3.0) \times 10^{-10}$
k_{LJ}, $cm^3 \cdot molecule^{-1} \cdot s^{-1}$[c]		5.8×10^{-10}	6.1×10^{-10}	5.8×10^{-10}
$\frac{k_{app}}{k_{LJ}}$		~1.4	~2	~1.6

[a]The state-specific rate constant k_{app}^{J} for appearance of CO_2 (00^00, J = 2–70) through collisions with 2MP, 2,6 MP or 3,5 MP are determined from appearance data at t = 1 μs after UV pulse.

[b]k_{app} is the overall rate for V–RT energy transfer. It is obtained by summing appearance state-resolved rate constants k_{app}^{J} for CO_2 product states (J = 0–98) shown an equation: $k_{app} = \sum_{J=0-98} k_{app}^{J}$.

[c]The Lennard-Jones collision rate constant k_{LJ} is determined as described in Appendix B with following Lennard-Jones parameters:

$\sigma_{CO_2}=4.5\times10^{-10}$m, $(\epsilon/k_B)_{CO_2}=190$ K;

$\sigma_{2MP}=5.6\times10^{-10}$m, $(\epsilon/k_B)_{2MP}=466$ K;

$\sigma_{2,6MP}=5.9\times10^{-10}$m, $(\epsilon/k_B)_{2,6MP}=468$ K (same as 3,5MP).

insight into the collisions of high energy molecules. First of all, we see again that the V–RT channel is the dominant pathway in the collision quenching process for these donors with CO_2. This feature appears to be general for CO_2 collisions with high energy molecules of this type. Secondly, the fact that the energy transfer for methylated donors is greater than the Lennard-Jones collision rate shows that the model collision rate undershoots the actual collision rate by an amount that is not insubstantial.

It would be very interesting to measure the branching ratios for the V–V pathways of these donors with CO_2 to determine the actual total collision rates. The V–V pathways for pyrazine(E)/CO_2 collisions account for about 10–15% of all collisional energy transfer, as reported elsewhere.[74] For 2MP, 2,6MP and 3,5MP, initial attempts to characterize the V–V pathways were not successful due to small signal levels. This channel would be worth revisiting in the future.

It may also be that the internal energy content of the high energy methylated donors increases the collision cross section. Energy dependent measurements may reveal that the collision rates are enhanced for the highly excited methylated donors, but not for pyrazine, because of large amplitude low frequency motions of the methyl groups. Other quenching studies with HOD as the energy acceptor also find that methylated donors have V–RT energy transfer rates that are larger than the Lennard-Jones collision rate and that increase with the extent of methylation, as shown in Figure 6.10. One difference in the HOD collisions is that k_{LJ} does a rather poor job at accounting for H-bonding interactions so that it underestimates the rate for HOD with pyrazine as well.

6.3.5 The Full V−RT Energy Transfer Distribution P(ΔE) for CO_2 with Vibrationally excited 2MP , 2,6MP and 3,5MP.

The state-resolved CO_2 energy gain profiles and rate constants are used to determine J-specific energy gain distribution functions $P_J(\Delta E)$ that are indexed by ΔE. The full energy transfer distribution P(ΔE) is the sum of $P_J(\Delta E)$, shown as $P(\Delta E)= \sum_{i=0}^{98} P_J(\Delta E)$. P(ΔE) curves describe the whole V−RT collision process between hot donors (pyrazine, 2MP, 2,6MP and 3,5MP) and CO_2 molecules in Figure 6.11. Figure 6.11a shows P(ΔE) distributions relative to k_{LJ} and Figure 6.11b shows P(ΔE) curves relative to k_{app}. For ΔE > 0, the P(ΔE) curves correspond to the probability of high energy donor molecules losing their internal energy in collisions with CO_2. For ΔE > 0, the P(ΔE) curves correspond to the probability that donor molecules gain energy in collisions with CO_2. The maximum probability of energy transfer for pyrazine(E) collisions is at ΔE = 240 cm^{-1}. For donors with one or two methyl groups (2MP, 2,6MP or 3,5MP), the maximum P(ΔE) shifts slightly to ΔE = 120 cm^{-1}. Figure 6.11b shows that the P(ΔE) curves for 2,6MP and 3,5MP are similar after being normalized to k_{app}. In addition, Figure 6.11b shows that the presence of at least one methyl group decreases the probability of large transfer energy (ΔE >800 cm^{-1}).

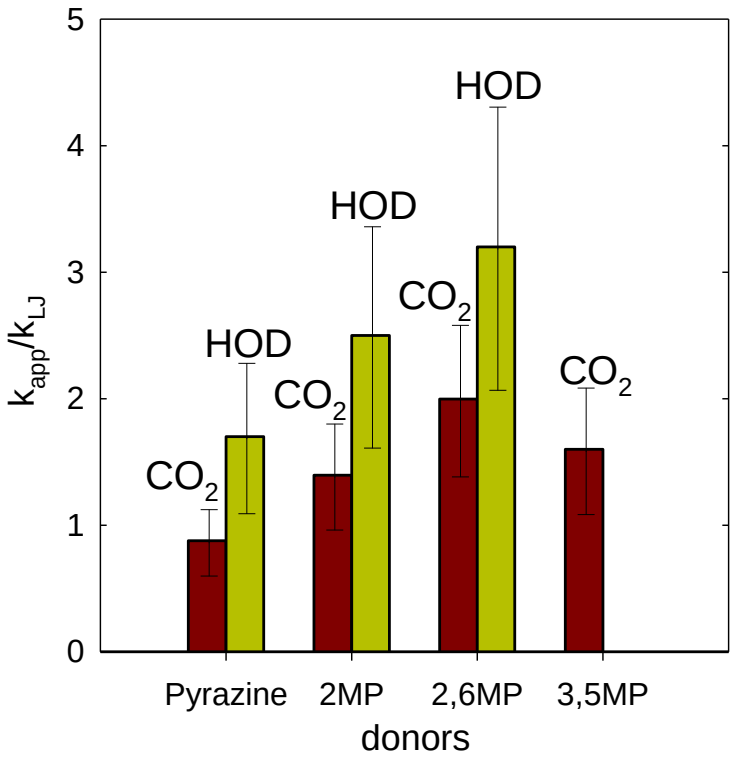

Figure 6.10 The ratios of experimental appearance collision rate k_{app} with Lennard-Jones collision rate k_{LJ} for different collision systems. The red bars show ratio data for CO_2 with vibrationally hot pyrazine, 2MP, 2,6MP and 3,5MP. The ratios of HOD with the first three excited donor species are shown by the green bars.

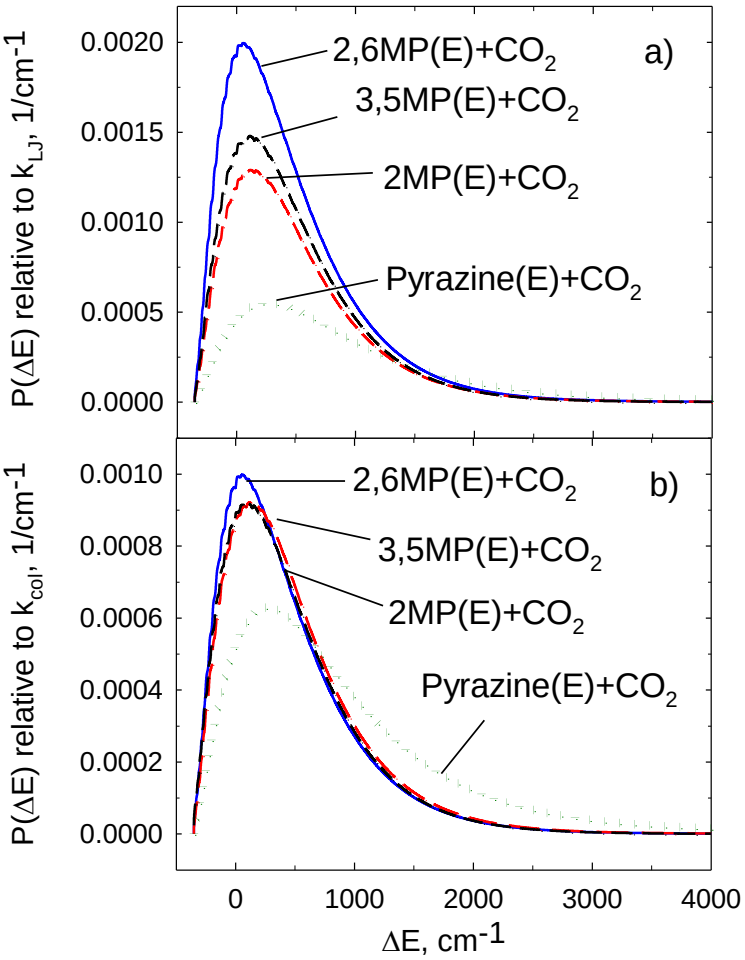

Figure 6.11 The full energy transfer distribution function P(ΔE) curves for CO_2 with four highly vibrationally excited donors: 2MP (long dash line), 2,6MP (solid line), 3,5MP (short dash line) and pyrazine(green dot line). (a) P(ΔE) curves normalized to the Lennard-Jones collision rate k_{LJ} and (b) P(ΔE) curves normalized to the experimental appearance collision rates k_{app}.

6.4 Conclusions

This Chapter reported the complete V–RT collision dynamics of 2MP/CO_2, 2,6MP/CO_2 and 3,5MP/CO_2 systems. In comparison with pyrazine(E) quenching studies, this work shows how the presence of methyl groups in the high energy molecules affects the energy transfer dynamics. The state-resolved measurements show the presence of both strong and weak collisions for three collision systems. The translational energy partitioning at J = 2–80 for scattered CO_2 from the methylated pyridine donors is dependent on CO_2 J-state. It minimizes near the peak of the 300 K thermal distribution of CO_2 and increases significantly as J increases for J > 60. The product translational energies from collisions of 2MP, 2,6MP and 3,5MP are about half as large as those seen for collisions with pyrazine(E). Weak and strong collisions result in two sub-populations for CO_2 rotational energy. The collision rates and the full energy transfer distributions for three donors with CO_2 were measured. The appearance collision rates of three collision systems are 1.4~2 times higher than Lennard-Jones models. This result shows that V–RT energy transfer is the dominant process for these collision systems.

Chapter 7: Energy Dependence of Strong Collision dynamics for Highly Vibrationally Excited Azulene(E = 20390 and 38580 cm^{-1}) with CO_2

7.1 Introduction

Collisional energy transfer of high energy molecules is a key step in many chemical processes but fundamental questions remain unanswered. One such question is how the amount of vibrational energy in the highly excited molecules affects the energy transfer dynamics in terms of product energy partitioning and energy transfer rates. Strong collisions remove large amounts of internal energy in single encounters and effectively compete with unimolecular decomposition when the molecule's internal energy approaches the dissociation limit. Currently, there are no first principles models for predicting how large vibrationally excited molecules lose their energy through strong collisions. The dynamics of strong collisions of highly excited molecules with CO_2 has been well documented for a number of highly excited donor molecules using high-resolution IR probing.[75-77,85,86,90,91,94,96,102,103,106,168-170] The energy dependence of strong collisions of high energy donor molecules, pyridine (E)[85] and pyrazine(E)[75-77,106] with CO_2 has been investigated with state-resolved probing. Chapter 5 reported the energy dependence of full energy transfer of pyrazine(E)/CO_2. These studies were able to vary the donor energy by 10−30%. This Chapter reports on the dynamics of strong collisions of vibrationally excited azulene(E) with CO_2 where E = 20390 and 38580 cm^{-1}. Azulene is an ideal target molecule for this type of study since it can be prepared with internal energy that can be varied by a factor of 2.

The collisional relaxation of azulene(E) has been the subject of a large body of work at energies as high as E = 40000 cm^{-1}.[38,41,50,51,65-67,69-73,92,148,149,155,156,171-174] Azulene has five electronic states from which highly vibrationally excited molecules are readily prepared.[65] The states are accessed by visible or UV light that converts azulene to highly vibrationally excited states in S_0 by rapid radiationless decay with near unity quantum yield.[171,175] UVA and IRF studies on azulene(E) relaxation have reported that average energy transfer values for a number of azulene(E)/bath systems depend roughly linearly on the internal energy.[50,51,155,156,171,172] These studies showed that $\langle\Delta E\rangle$ levels off near E ~ 30000 cm^{-1}. More recent KCSI studies indicate that the linear energy dependence continues to E = 40000 cm^{-1}.[29,65] In other experiments, Flynn and co-workers studied vibration-to-vibration energy transfer in azulene(E)/CO_2 collisions for E = 30600 and 40980 cm^{-1} and report a slight negative energy dependence for the energy transfer rates.[92,174]

The work presented in this Chapter focuses on in establishing how the dynamics of strong collisions is affected when the azulene energy is increased from E = 20390 to 38580 cm^{-1}. By doubling the internal energy of the hot azulene molecule, the strong collision dynamics can be investigated over a much broader range than in earlier state-resolved studies. Previously, our group investigated the energy dependence of strong collisions of CO_2 with pyridine (E = 37000–41000 cm^{-1}) and with pyrazine(E = 32000–41000 cm^{-1}).[75-77,85,86,106] These studies showed that the energy dependence of large-ΔE energy transfer is donor dependent but is not particularly sensitive to these changes in donor energy. The distribution and rates for large-ΔE collisions of pyridine/CO_2 are essentially constant for an approximately 10% increase in donor energy. For pyrazine,

the distribution of large-ΔE collisions does not vary uniformly over an ~30% increase in donor energy. Instead, this component is nearly constant until the internal energy reaches E = 38000 cm^{-1}, where a stepwise increase in the energy transfer is observed. It is known that pyrazine(E) undergoes dissociation at E = 38000 cm^{-1} with a lifetime (τ~70 μs) that is much longer than the energy transfer measurement time of t = 1 μs.[93] Dissociation has not been observed at lower energies. At vibrational energies above this threshold, the energy gain distribution broadens and the energy transfer rate increases monotonically as a function of donor energy. It is interesting that for both pyrazine and pyridine, there are energy ranges where the dynamics of large-ΔE collisions are invariant to the donor energy. In the limit of small internal energies, the probability of large-ΔE collisions must diminish due to energy conservation. This Chapter explores this issue by examining a broader range of internal energy for azulene(E)/CO_2 collisions.

Energy-dependent studies of this kind provide an opportunity to test the role of state density in strong collisions of high energy molecules. Statistical treatments of collisional energy transfer inherently describe energy redistribution in terms of the state density. UVA, IRF, and KCSI experiments have shown that increasing donor state density tends to enhance energy transfer probabilities. The role of the state density energy dependence in controlling the curvature of the energy transfer probability distribution function has been established by experiments on large-ΔE collisions of other donor molecules with CO_2.[86] The GRETCHEN (Golden Rule Modeling of Excitation Transfer in Collisions of High ENergy molecules) model for strong collisions, based on Fermi's Golden Rule, outlines the state density dependence for different donors.[83,86] This model predicts that the distribution of energy transfer of large-ΔE collisions will be

sensitive also to changes in the donor energy, provided that the energy changes are large enough to influence the energy dependence of the state density in Figure 7.1.

In this Chapter, the nascent state-resolved rotational and translational energy distributions and rate constants for scattered CO_2 (00^00) in high rotational states through collisions with azulene(E = 20390 and 38580 cm^{-1}) are presented. Energy transfer distributions were obtained at both azulene energies. Rotational and translational distributions of scattered CO_2 bath are broadened with increasing azulene's energy. The rate for energy transfer via strong collisions with $\Delta E > 3000$ cm^{-1} increases by a factor of 4 when the internal energy of the azulene molecule is doubled. The large-ΔE energy transfer distribution functions agree well with predictions from the GRETCHEN model.

7.2 Experimental Methods

The high resolution diode-laser transient IR absorption spectrometer described in Chapter 2 was used to probe the energy-dependent relaxation experiments. A brief outline is given here. The frequency-doubled or quadrupled pulsed output of a Nd:YAG laser (λ = 532 or 266 nm, respectively) was used to excite azulene with different internal energies as Eq 7.1.

$$\text{Azulene}+h\nu(\lambda=532 \text{ or } 266 \text{ nm}) \rightarrow \text{Azulene}(E=20390 \text{ or } 38500 \text{ cm}^{-1}) \qquad (7.1)$$

The laser power at λ = 532 and 266 nm was kept under 2 MW/cm^2 to minimize multiphoton absorption. Experiments at λ = 266 nm were performed at T = 300 K. Due to the much lower absorption strength of azulene at λ = 532 nm, the experiments at this

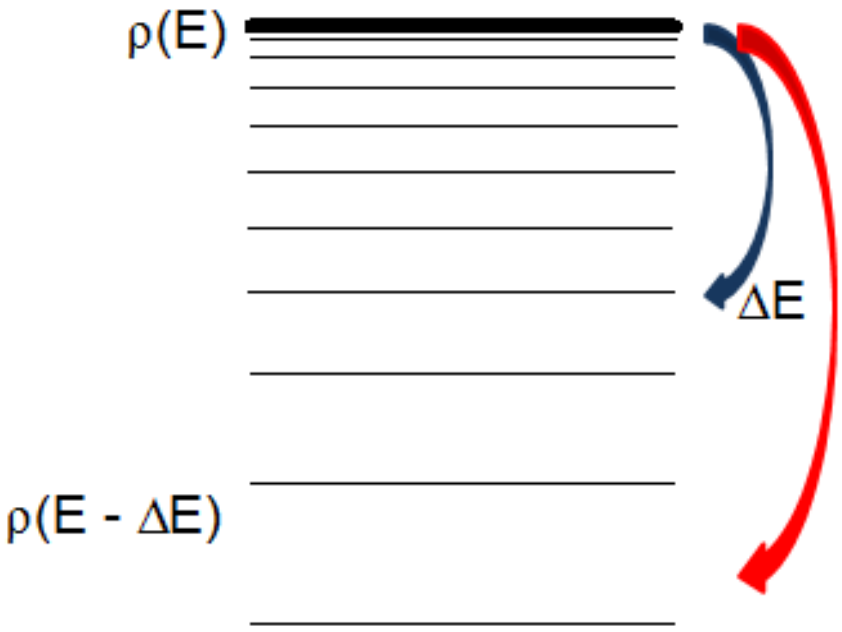

Figure 7.1 The GRETCHEN model is based on Fermi's golden rule. The key idea is that collisions of a highly excited molecule provide time-dependent perturbations that induce energy transfer between molecules. The probability for an energy exchange of the amount ΔE is predicted to be proportional to the final state density ρ(E-ΔE).

excitation wavelength were performed at 360 K to increase the azulene's vapor pressure. For the elevated temperature studies, the collision cell and gas inlet system were wrapped in copper foil, heating tape, and insulation[176,177] and the ambient cell temperature was determined by IR absorption of well-populated CO_2 states. Roughly 5% of the azulene molecules are excited to azulene(E = 20390 or 38500 cm^{-1}).

A 1:1 mixture of azulene and CO_2 with a total pressure of about 15 mTorr was flowed through a 3-m flowing-gas collision cell. The average time between collisions is $t_{col} \sim 4$ μs. The diode laser(λ = 4.3 μm) with a resolution of 0.0003 cm^{-1} probed the populations of scattered CO_2 (00^00) molecules at high rotational states J = 60–78. The nascent transient IR absorption signals are collected at t = 1 μs after the UV pulse. Doppler-broadened transient absorption line profiles were collected by locking the diode laser to a fringe of a scanning Fabry-Perot etalon.

Azulene (Aldrich, >99%) was degassed by the freeze-pump-thaw method before use. Research-grade CO_2 (Matheson, 99.995% purity) was used directly without further purification.

7.3 Results and Discussion

This Section reports on the dynamics of strong collisions of CO_2 with azulene(E) for two initial energies, E =20390 and 38580 cm^{-1}. The appearance rates and nascent rotational and translational energy distributions of scattered CO_2 molecules with J = 60–78 were measured using high-resolution transient IR absorption at λ = 4.3 μm. Both the average rotational energy of the scattered CO_2 molecules with $J \geq 60$ and the average translational energy of the scattered molecules double when the azulene energy increases

by a factor of 2. The energy transfer rates also depend on the azulene internal energy, increasing by a factor of about 4 for a doubling of the initial azulene energy.

7.3.1 CO_2 Rotational Energy Gain from Azulene(E)-CO_2 Strong Collisions

The IR probe transitions involve excitation of one quantum of the CO_2 ν_3 antisymmetric stretch mode for either the P or R branch,

$$CO_2\left(00^00, J, V\right) + h\nu\ (\lambda \sim 4.3\ \mu m) \rightarrow CO_2(00^01, J \pm 1, V) \qquad (7.2)$$

In Eq 7.2, 00^00 represents the CO_2 ground vibrationless state, 00^01 corresponds to one quantum in the ν_3 stretch, J is the rotational angular momentum quantum number, and V is the component of the velocity along the diode laser propagation axis. Figure 7.2 shows the transient IR absorption signals for the J = 66 state of CO_2 (00^00) resulting from collisions with excited azulene at 532 and 266 nm. The appearance signals correspond to population increases in the J = 66 state of CO_2 (00^00) as a function of time. Population data collected at t = 1 μs following the UV pulse result essentially from single collisions between highly excited azulene and CO_2 since the average collision time is t_{col} = 4 μs. Differences in the signal intensities in Figure 7.2 are due to differences in the number density of photoexcited azulene molecules and in the energy transfer cross sections at the two excitation wavelengths.

The nascent rotational distributions of scattered CO_2 in high-J states were determined from fractional absorption measurements at t = 1 μs for both azulene excitation wavelengths. Absorption signals were converted to nascent CO_2 populations using IR absorption coefficients[178] and the transient Doppler-broadened linewidths

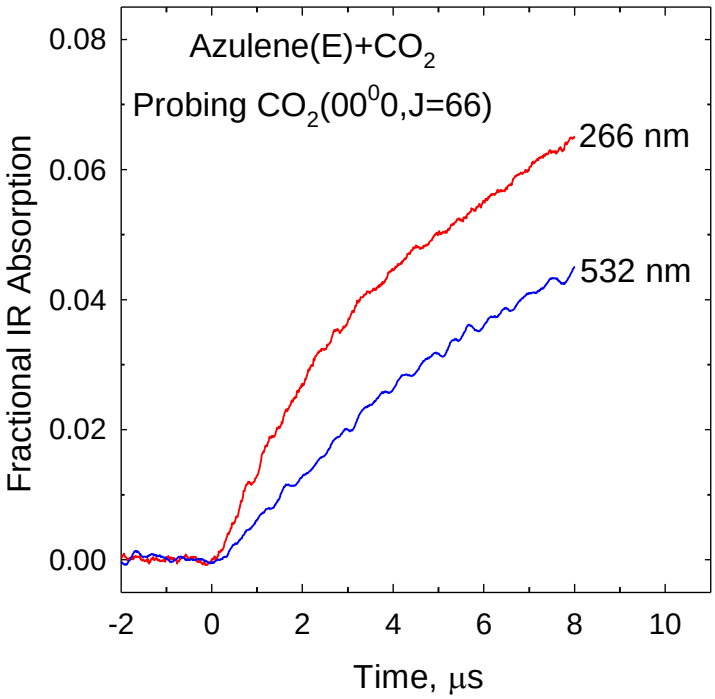

Figure 7.2 Transient IR absorption for CO_2 (00^00) J = 66 following excitation of azulene at λ = 266 (red line) and 532 nm (blue line). The appearance signals of specific CO_2 rotational high-states result from collisions with highly vibrationally excited azulene with different internal energies. The population data were collected at t = 1 μs after UV/visible pulse.

described in the next Section. The nascent CO_2 rotational distributions are broader for the higher donor energy, as shown in Figure 7.3. Each data set in Figure 7.3 is an average of six individual measurements of the rotational distribution which is then fitted using a Boltzmann distribution. For azulene excited at λ = 532 nm, the scattered CO_2 molecules (with $J \geq 60$) have a rotational temperature of T_{rot} = 470 ± 100 K. For excitation at λ = 266 nm, the CO_2 rotational temperature is T_{rot} = 805 ± 80 K. Based on the rotational temperatures, the average rotational energy of CO_2 molecules (with $J \geq 60$) increases by nearly a factor of 2 when the azulene internal energy is doubled. The average *change* in the CO_2 rotational energy $\langle \Delta E_{rot} \rangle$ has a stronger dependence on the azulene initial energy. $\langle \Delta E_{rot} \rangle$ is determined from $\langle \Delta E_{rot} \rangle = k_B (T_{rot} - T_0)$, where T_0 describes the initial rotational distribution. Using the ambient cell temperature for T_0, $\langle \Delta E_{rot} \rangle_{266}$ is around ~4.5 times bigger than $\langle \Delta E_{rot} \rangle_{532}$ for the set of strong collisions under investigation.

7.3.2 Translational Energy Release from Azulene(E)/CO_2 Large-ΔE Collisions

The nascent distributions of recoil velocities for strong collisions were determined from transient absorption line profiles of individual CO_2 rotational states (J = 62–78) measured at t = 1 μs following azulene excitation at λ = 532 and 266 nm. The transient linewidths for a number of individual CO_2 states are listed in the Table 7.1 along with the nascent translational temperatures. The transient CO_2 line profiles are broadened relative to those at the ambient cell temperature and they increase in width as a function of azulene excitation energy. Transient absorption line shapes for the CO_2 (00^00) J = 68 state following azulene excitation at 532 and 266 nm are shown in Figure 7.4. The 1 μs population data have isotropic velocity distributions that are each fit with a Gaussian

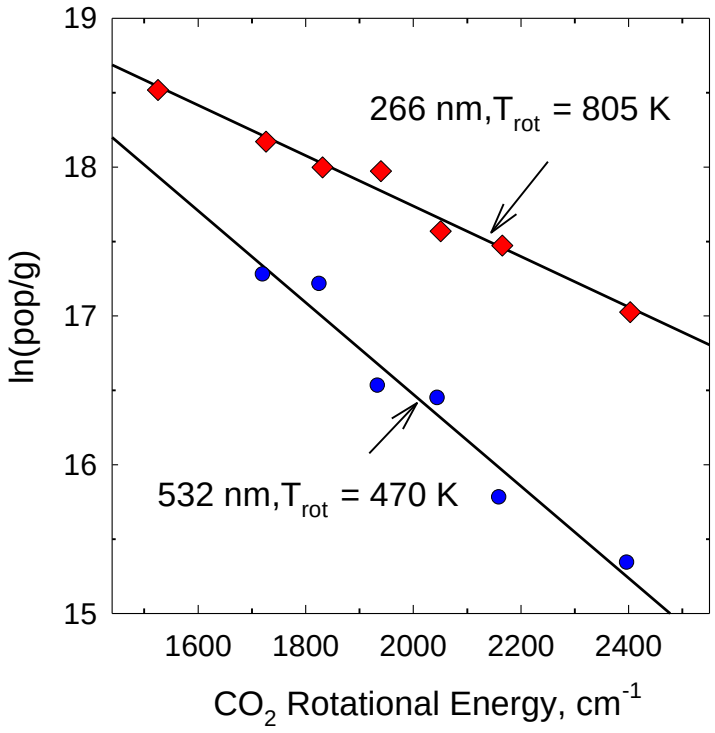

Figure 7.3 Nascent population distributions of CO_2 (00^00) in high-J states (62–78) through from collisions with highly vibrationally excited azulene that was prepared with λ = 532 (blue circles) and 266 nm (red diamonds).

Table 7.1 Doppler-broadened linewidths and translational temperatures for strong collisions of CO_2 with highly vibrationally excited azulene(E=20100 or 38500 cm^{-1}).

	CO_2 (00^00) J	$\Delta\nu_{app}$, cm^{-1}[a]	T_{app}, K[b]	T_{rel}, K[c]
λ_{exc} =532 nm E = 20100 cm^{-1}	66	0.0051	430±80	454±84
	68	0.0055	500±85	548±93
	70	0.0054	475±95	515±103
	72	–	630±150[d]	723±172[d]
	74	0.0060	605±100	689±113
	76	–	657±130[d]	759±151[d]
	78	0.0069	690±110	803±186
λ_{exc} =266 nm E =38500 cm^{-1}	62	0.0067	740±159	891±214
	64	–	854±186[d]	1045±251[d]
	66	0.0078	1015±225	1261±302
	68	0.0073	893±196	1097±263
	70	0.0081	1073±184	1339±248
	72	0.0071	876±190	1074±255
	74	0.0080	1058±235	1319±316
	76	–	1067±213[d]	1331±221[d]
	78	0.0081	1103±245	1379±330

[a]Full width at half maximum linewidths $\Delta\nu_{app}$ of transient absorption line profiles at 1 μs following azulene excitation. Each $\Delta\nu_{app}$ value is the average of three experimental line profile measurements. The 1σ uncertainty in experimental linewidths is ± 0.001 cm^{-1}.

[b]Laboratory frame translational temperatures for scattered CO_2 molecules determined using $T_{app} = (mc^2/8k_B \ln 2)\left(\Delta v_{app}/v^2\right)^2$ in units of K where m is the mass of CO_2, k_B is Boltzmann's constant, c is the speed of light, and ν_0 is the rovibrational transition frequency at line center.

[c]Center-of-mass translational temperatures determined using

$T_{rel} = T_{app} + m_{CO_2}/m_{azulene}\left(T_{app} - T_0\right)$, where T_0 is taken to be the cell temperature of 360 K for 532 nm experiments or 300 K for 266 nm experiments.

[d]For states with low signal to noise levels, the translational energy distributions were interpolated from the data in Figure 7.5.

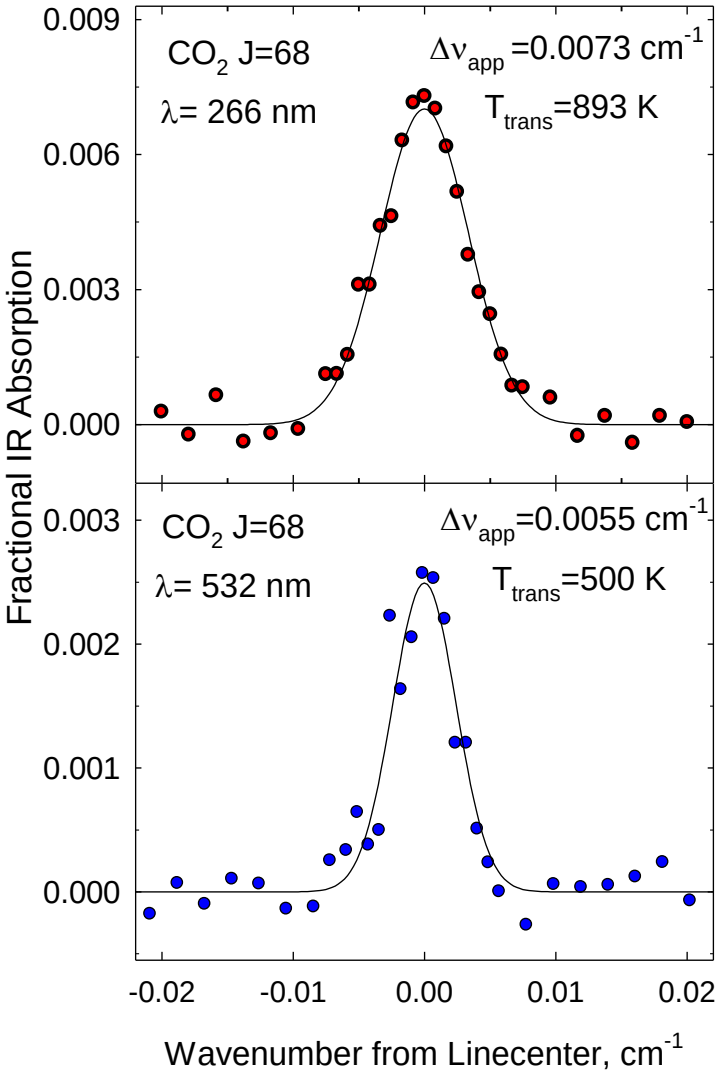

Figure 7.4 Doppler-broadened transient absorption line profile for CO_2 (00^00) J = 68 collected at t = 1 μs following laser excitation of azulene at λ = 266 (red circles) and 532 nm (blue circles). Transient absorption data are fit by a Gaussian function shown as solid lines.

profile. For azulene with E = 20390 cm^{-1}, the full width at half maximum linewidth of the J = 68 state is $\Delta\nu_{app}$ = 0.0055 cm^{-1}, which corresponds to a laboratory-frame velocity distribution with a temperature of T_{app} = 500 ± 85 K. For azulene with E = 38580 cm^{-1}, the nascent velocity distribution for the CO_2 J = 68 state is broadened and has T_{app} = 893 ± 196 K.

The distribution of relative recoil energies for scattered azulene and CO_2 is obtained by converting into the center of mass frame and is a measure of the amount of azulene internal energy that goes into translation of the scattered molecules. For excitation at λ = 532 nm, the relative translational energy distribution for the CO_2 J = 68 state has a temperature of T_{rel} = 548 ± 93 K corresponding to an average translational energy of $\langle E_{rel} \rangle = 1.5 k_B T_{rel} = 571 \pm 101$ cm^{-1}, based on an isotropic velocity distribution. For excitation at λ = 266 nm, the values increase to T_{rel}= 1097 ± 263 K and $\langle E_{rel} \rangle$ = 1144 ± 272 cm^{-1}. For the CO_2 J = 68 state, the average product translational energy increases by a nearly a factor of 2 when the azulene energy is doubled.

Figure 7.5 shows post-collision $\langle E_{rel} \rangle$ values as a function of final CO_2 rotational state for quenching collisions of azulene with E = 20390 and 38580 cm^{-1}. For both initial energies, the translational energy in the scattered molecules increases roughly linearly as a function of CO_2 J state for J > 60. The increase in translational energy with CO_2 J state shows that the relative velocity changes are accompanied by angular momentum increases as expected for impulsive collisional energy transfer.

Linear fits to both data sets in Figure 7.5 have roughly the same slope but are offset from one another by about 20 units of J. The higher energy donor imparts roughly

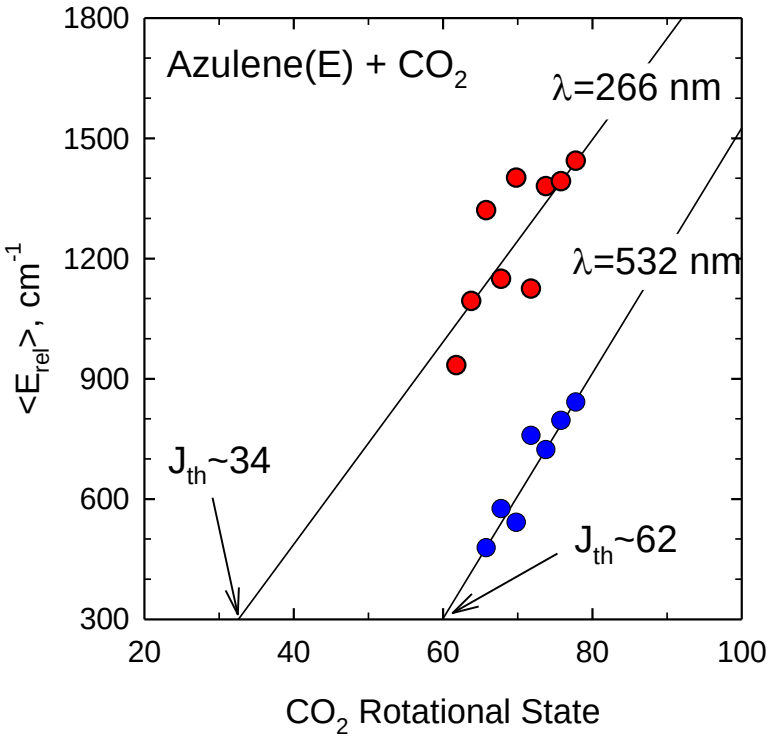

Figure 7.5 CO_2 rotational state dependence of the average relative translational energy distribution through collisions with highly vibrationally excited azulene at λ = 532 (blue) and 266 nm (red).

700 cm^{-1} more translational energy to individual CO_2 product states than the lower energy donor in large-ΔE collisions. For low energy azulene, scattered CO_2 molecules with J = 64–78 have center of mass translational energies of $\langle E_{rel} \rangle$ = 473–837 cm^{-1}. For azulene with E = 38580 cm^{-1}, the J = 62–78 states of CO_2 have larger velocity distributions with $\langle E_{rel} \rangle$ = 930–1440 cm^{-1}.

Average changes in translational energy $\langle \Delta E_{rel} \rangle$ for the scattered molecules are dependent on donor energy. Values of $\langle \Delta E_{rel} \rangle$ for these states are determined using $\langle \Delta E_{rel} \rangle = 1.5 k_B (T_{rel} - T_0)$. For azulene with E = 20390 cm^{-1}, $\langle \Delta E_{rel} \rangle$ = 98–460 cm^{-1}. Substantially larger average changes in translational energy are seen for azulene with E = 38580 cm^{-1}, which has $\langle \Delta E_{rel} \rangle$ = 616–1124 cm^{-1}, indicating that the strong collisions are more impulsive for the higher energy donor.

The data in Figure 7.5 also provide some insight into the product translational energy from low-ΔE collisions (i.e., those producing low-J CO_2 states). Based on propensity rules for collisions that favor small changes in energy and angular momentum, it is reasonable that low-J CO_2 states will have lower translational energies than the high-J states. Figure 7.5 shows that for azulene excited at λ = 532 nm, the low-J CO_2 states are likely to have translational energy distributions that lie within a fairly narrow range with $\langle E_{rel} \rangle$ between 300 and 500 cm^{-1}. There also appears to be a threshold for the onset of $\langle E_{rel} \rangle$ values that increase strongly with J. Extrapolating the 532 nm data to the initial relative translational energy of E_0 = 320 cm^{-1} gives an estimate of the threshold state near J_{th} = 62. For the 266 nm data, the low-J states of CO_2 have a larger range of likely translational energies with values between $\langle E_{rel} \rangle$ of 300 and 900 cm^{-1}. Extrapolation to the initial translational energy of E_0 = 270 cm^{-1} suggests that the minimum threshold J-

state for the high energy azulene is near J_{th} ~ 34. Of course, it is possible that a linear extrapolation to low-J states is not valid and that the J-state dependence of $\langle E_{rel} \rangle$ is a smoothly varying function of J. If this is the case, the onset of large $\langle E_{rel} \rangle$ is likely to occur at J states that are larger than J_{th}. Energy gain measurements for low-ΔE collisions would shed light on this behavior.

7.3.3 Sate-Resolved Rate Constants of Azulene(E)-CO_2 large-ΔE Energy Transfer

State-resolved energy transfer rate constants for large-ΔE collisions between azulene(E) and CO_2 with E = 20390 and 38580 cm^{-1} have been measured. Collisions of azulene(E) with CO_2 lead to the appearance of individual CO_2 (00^00, J) states with energy transfer rate constants k_{app}^J, as shown in Eq 7.3.

$$\text{Azulene(E)} + CO_2(00^00) \xrightarrow{k_{app}^J} \text{Azulene}(E-\Delta E) + CO_2(00^00, J) \tag{7.3}$$

Under single-collision conditions, the initial appearance rate of CO_2 (00^00, J) is due solely to collisions of azulene(E) with CO_2 and is determined using Eq 7.4,

$$\frac{\Delta[CO_2(00^00, J)]}{\Delta t} = k_{app}^J [\text{Azulene(E)}]_0 [CO_2]_0 \tag{7.4}$$

where $[\text{Azulene(E)}]_0$ is the number density of excited azulene initially prepared from the pulsed excitation and $[CO_2]_0$ is the number density of bulk CO_2. The energy transfer rate for production of an individual CO_2 state is measured directly as $\Delta[CO_2(00^00, J)]/\Delta t$,

based on transient absorption data collected at $\Delta t = 1$ μs following the azulene excitation pulse (e.g., Figures 7.2 and 7.3).

Rate constants k_{app}^{J} increase as a function of azulene's internal energy and are listed in Table 7.2. For azulene excited at $\lambda = 532$ nm, the appearance rate constant for CO_2 J = 68 is $k_{app}^{J=68} = (3.1 \pm 0.9) \times 10^{-13}$ cm^3 molecule^{-1} s^{-1}. At $\lambda = 266$ nm, the J = 68 appearance rate increases by a factor of 3 to $k_{app}^{J=68} = (1.1 \pm 0.3) \times 10^{-12}$cm^3 molecule^{-1} s^{-1}. Rate constants for the appearance of other high-J CO_2 states show comparable energy dependencies, with rates of individual CO_2 states that increase by a factor of 3–6 when the azulene energy is doubled.

The large-ΔE component for energy transfer is described by the appearance of the high-J CO_2 states. One way to compare the 532 and 266 nm data is to compare the integrated rate for appearance of high-J CO_2 states. Here, the integrated rate constant k_{int} is the sum of k_{app}^{J} values for CO_2 J = 62–78 states. For excitation at $\lambda = 532$ nm, $k_{int} = (2.2 \pm 0.6) \times 10^{-12}$ cm^3 molecule^{-1} s^{-1}. At $\lambda = 266$ nm excitation, the integrated rate is nearly four times larger with $k_{int} = (8.5 \pm 2.8) \times 10^{-12}$ cm^3 molecule^{-1} s^{-1}. Relative to the Lennard-Jones collision rate of $k_{LJ} = 6.4 \times 10^{-10}$ cm^3 molecule^{-1} s^{-1}, appearance of scattered CO_2 (00^00) with J ≥ 62 due to collisions with azulene($\lambda = 532$ nm) results from one in 290 collisions. When the azulene vibrational energy is increased by a factor of 2, the strong collisions occur roughly once in 75 collisions. Thus, the probability of energy transfer between azulene(E) and CO_2 due to large-ΔE collisions increases by a factor of 4 when the azulene energy is doubled, based on appearance of CO_2 states with J ≥ 62.

Table 7.2 State-specific energy transfer rate constants for collisions of highly excited azulene with CO_2: Azulene(E)+ CO_2 → Azulene(E−ΔE)+ CO_2 ($00^0$0, J, V)

Excitation wavelength λ	532 nm	266 nm
Thermal vibrational energy	1303 cm^{-1}	906 cm^{-1}
Azulene internal energy	20390 cm^{-1}	38580 cm^{-1}
CO_2 ($00^0$0) J state	k^J_{app} (× 10^{-13} cm^3 $molecule^{-1}$ s^{-1})	
62	6.0 ± 1.9	15.8 ± 4.7
64	4.5 ± 1.4	14.0 ± 4.2
66	3.2 ± 1.0	11.8 ± 3.5
68	3.1 ± 0.9	10.9 ± 3.3
70	1.6 ± 0.5	9.8 ± 2.9
72	1.5 ± 0.4	6.6 ± 2.0
74	0.8 ± 0.2	6.3 ± 1.9
76	0.7 ± 0.2	5.1 ± 1.5
78	0.6 ± 0.1	4.2 ± 1.3
k_{int} [a]	(2.2 ± 0.6) × 10^{-12}	(8.5 ± 2.5) ×10^{-12}
$\frac{k_{int}}{k_{LJ}}$ [b]	$\frac{1}{290}$	$\frac{1}{75}$

[a]Integrated bimolecular rate constants k_{int} in $cm^3 molecule^{-1} s^{-1}$ for collisions of azulene(E) that result in CO_2 ($00^0$0) with J = 62–78.

[b]The collision number is the ratio of the integrated rate constant k_{int} to Lennard-Jones collision rate constant k_{LJ}. Lennard-Jones collision rate is k_{LJ} = 6.4 × 10^{-10} cm^3 $molecule^{-}$

^{1} s^{-1} which was calculated in Appendix B. The Lennard-Jones parameters σ and ε for mixed systems are:

azulene [$\sigma_{azulene}$ = 6.61 Å, $\varepsilon_{azulene}/k_B$ = 523 K][50] and CO_2 [σ_{CO_2} = 3.94 Å, ε_{CO_2}/k_B = 201 K][65].

7.3.4 P(ΔE) Curves for Large-ΔE Collisions of Azulene(E) and CO_2

The energy dependence of large-ΔE collisions from the point of view of energy loss from azulene(E) is described by transforming the state-resolved CO_2 scattering data into an energy transfer distribution function. Maxwell-Boltzmann translational energy distributions in the center-of-mass frame are obtained from J-specific Doppler widths (Table 7.1) and appearance rates for individual J states of CO_2 (Table 7.2). The probability distribution function P(ΔE) for energy loss from azulene(E) is obtained by summing energy gain distributions for individual CO_2 J states with $J \geq 60$ as a function of ΔE.[94] The P(ΔE) curve for each donor energy is based on thermal averages for the initial CO_2 rotational and translational energies. The index ΔE corresponds to the amount of internal energy lost from azulene(E) in single collisions with CO_2 and does not include changes in azulene rotational energy. The data reported here are for the high-J CO_2 states and P(ΔE) curves are complete for $\Delta E > 3000$ cm^{-1}. Contributions to P(ΔE) from collisions with $\Delta E < 3000$ cm^{-1} are not known without appearance measurements for lower J states of CO_2. Figure 7.5 shows that the translational energy spread narrows for decreasing J, so that the low-J states should not contribute much to P(ΔE) for $\Delta E > 3000$ cm^{-1}.

Figure 7.6 shows the P(ΔE) probability functions with $\Delta E > 4000$ cm^{-1} for both initial azulene energies. The large-ΔE collisions of the higher energy azulene occur with greater probability and the probability diminishes more slowly as a function of ΔE than for the lower energy donor in Figure 7.6. Both distribution curves in Figure 7.6 are fitted well using a single exponential decay function Eq 7.5.

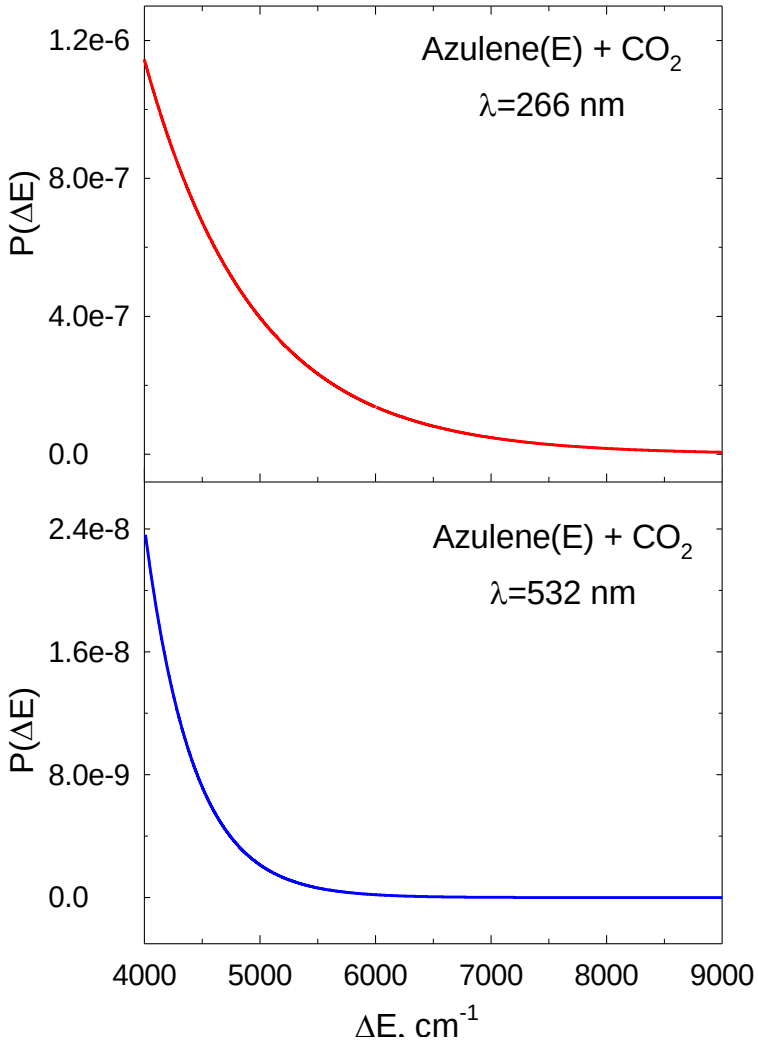

Figure 7.6 Energy transfer distributions P (ΔE) for strong collisions between highly vibrationally excited azulene(E = 38580 and 20390 cm^{-1}) with CO_2. P (ΔE) curves are obtained in terms of the energy transfer rates and rotational/translational gain.

$$P(\Delta E) = \alpha_{obs} \exp\left(-\beta_{obs}\Delta E\right) \quad (7.5)$$

A semilog plot of the P(ΔE) curves is shown in Figure 7.7. A fit of the 266 nm data yields a shape parameter of $\beta_{obs} = 1.05 \times 10^{-3}$ per cm^{-1} and an intensity parameter of $\alpha_{obs} = 7.5 \times 10^{-5}$ per cm^{-1}. The 532 nm data is fitted with $\beta_{obs} = 2.45 \times 10^{-3}$ per cm^{-1} and $\alpha_{obs} = 4.5 \times 10^{-4}$ per cm^{-1}.

The full probability distribution for azulene(E)/CO_2 collisions has been measured with KCSI and calculated independently with PECT.[29,65] Figure 7.7 compares our strong collision results (for $\Delta E > 3000$ cm^{-1}) with those from KCSI and PECT studies. There is fairly good agreement at E = 38580 cm^{-1}, both in the curvature of the distribution function and the order of magnitude of the probability. The IR and KCSI results at E = 38580 cm^{-1} have a similar ΔE dependence, which is seen by the parallel semilog plots in Figure 7.7. At $\Delta E = 3000$ cm^{-1}, the probabilities are approximately 10^{-5} /cm^{-1} but the KCSI value is about 4 times larger than the IR value. The PECT probability curve agrees very well with the KCSI results at $\Delta E = 3000$ cm^{-1} but shows a ΔE dependence that is not as strong as that from either the IR or KCSI results. The weaker ΔE dependence of the PECT results somewhat overestimates the large-ΔE component relative to both KCSI and IR studies, suggesting that a smaller subspace of active degrees of freedom may be involved.

The comparison of IR data with the KCSI and PECT data results is less favorable for azulene with E = 20390 cm^{-1}. The KCSI and PECT results are in relatively good agreement with each other, but the IR data indicate that large-ΔE collisions are greatly diminished by the reduction in donor energy. All three methods find that the probabilities

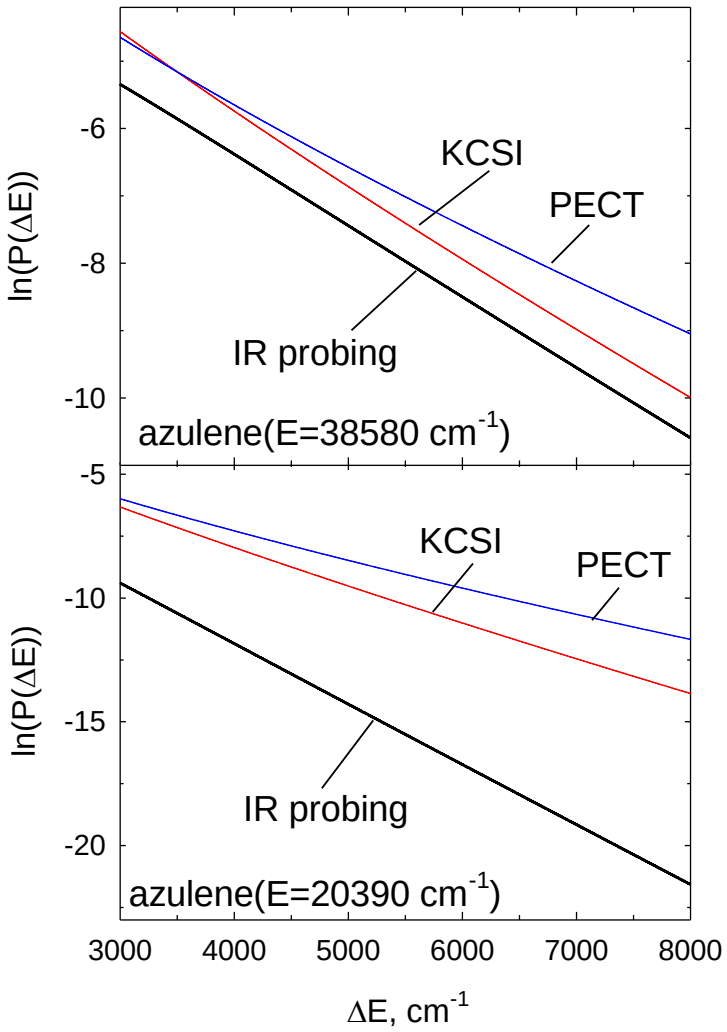

Figure 7.7 Energy transfer probability for strong collisions of azulene (E = 38580 and 20390 cm^{-1}) with CO_2. For each azulene internal energy in two plots, the transient IR probing data (black solid) is compared with the results from KCSI experiment (red) and PECT calculation (blue).

at E = 20390 cm^{-1} are lower than those at E = 38580 cm^{-1}, but the energy dependence is more pronounced for the IR data. For ΔE=3000 cm^{-1}, the KCSI results indicate a probability ratio of 4 between high- and low-energy azulene. The PECT results find a probability ratio of 3 for high- and low-energy donors. The IR data show a difference of a factor of 14.

The large-ΔE data from IR and KCSI studies can also compared by modeling the shape of the distribution functions. Luther and co-workers use a stretched exponential function to describe P (E', E) from KCSI studies. The IR data for $\Delta E > 3000$ cm^{-1} are fitted using an exponential decay function (Eq 7.5) with a shape parameter β_{obs}. The P (E', E) curve for $\Delta E > 3000$ cm^{-1} from the KCSI study are fitted well by Eq 7.5 with a value of β_{obs} (KCSI) = 1.05×10^{-3} per cm^{-1} for E = 38580 cm^{-1}. This result is in exact agreement with our result of β_{obs} (IR) = 1.05×10^{-3} per cm^{-1} at 266 nm excitation. For azulene with E = 20390 cm^{-1}, however, the agreement is not as good. The KCSI data are fitted best with β_{obs} (KCSI) =1.46×10^{-3} per cm^{-1} for azulene with 20390 cm^{-1}, while the IR results indicate that β_{obs} (IR) = 2.45×10^{-3} per cm^{-1} for azulene excited at 532 nm.

The agreement between the IR and KCSI results is less than satisfactory, particularly for the low-energy donor. One source of the discrepancy may come from uncertainty in the high-energy tail of the IR data at E = 20390 cm^{-1} since only high-J states of CO_2 have been measured. It is possible that the lower-J states of CO_2 (J < 60) contribute to collisions with $\Delta E > 3000$ cm^{-1}. This explanation is not likely, however, given that the energy gain distributions at E = 20390 cm^{-1} are substantially compressed compared to the higher energy data. It is possible that for low-energy azulene, the ΔE distribution is so compressed that quantitative information about collisions with $\Delta E >$

3000 cm^{-1} pushes our experimental limits. Future measurements of energy gain into CO_2 states with $J < 60$ should address this issue.

Another consideration is that differences in experimental methods lead to a slightly different definition of energy change. In the KCSI and PECT distributions, E–E' is the change of donor vibrational energy due to collisions. In the IR measurements, ΔE corresponds to the amount of donor vibrational energy that is deposited into rotation and vibration of CO_2 and into recoil velocity of the pair. Any donor vibrational energy that is converted into donor rotational energy is not accounted for in ΔE.

Another difference between the transient IR and KCSI results is that the transient IR data correspond to single collisions between donor and acceptor molecules in which vibrational energy in the donor is the only nonthermal energy. In the KCSI experiments, data are collected over multiple collisions through which the rotational and translational energy distributions of both donor and acceptor molecules are broadened. It is currently not known how this difference impacts the distribution function without additional IR data on the small-ΔE collisions.

The $P(\Delta E)$ curves in Figure 7.6 provide an excellent test of the GRETCHEN model for predicting how large-ΔE collisions depend on the internal energy of the donor molecule. The GRETCHEN model is based on Fermi's Golden Rule and the idea that collisions of a highly-excited molecule provide time-dependent perturbations that induce energy transfer between molecules. The probability for an energy exchange of the amount ΔE is predicted to be proportional to the final state density $\rho(E-\Delta E)$. By changing the initial state density of azulene, the curvature in the energy transfer

distribution function can be expected to scale with the energy dependence of the state density.

In this study, the initial internal energy of the donor molecule is changed by a factor of 2 leading to initial state densities that differ by nearly eight orders of magnitude. The state densities of azulene are $\rho = 2 \times 10^{22}$ states per cm^{-1} at $\lambda = 266$ nm and $\rho = 5 \times 10^{14}$ states per cm^{-1} at $\lambda = 532$ nm, based on a direct count of harmonic states.[179,180] A semilogarithmic plot of the state density of azulene is shown in Figure 7.8 for both initial energies as a function of ΔE for $\Delta E = 0–10000$ cm^{-1}. The bulk of large-ΔE collisions between azulene(E) and CO_2 induce transitions to azulene state densities that are one to two orders of magnitude lower than the initial state density. For the energy range of these experiments, the energy dependence of the state density for each donor is well described by an exponential function of the form

$$\rho(E-\Delta E)=\alpha_\rho \exp\left(-\beta_\rho \Delta E\right) \tag{7.6}$$

where α_ρ and β_ρ are intensity and shape parameters for the state density. A fit of the two data sets gives shape parameters of $\beta_\rho = 7.4 \times 10^{-4}$ per cm^{-1} at $\lambda = 266$ nm and $\beta_\rho = 1.21 \times 10^{-3}$ per cm^{-1} at $\lambda = 532$ nm. The experimental shape parameters β_{obs} are shown in Figure 7.9 as a function of the state density parameters β_ρ for azulene, along with data from previous collisional studies of other donors with CO_2. Azulene data are in excellent agreement with the linear correlation seen for large-ΔE collisions of other donor molecules in collisions with CO_2. This result is an important one that expands the observed correlation of strong collision probability and state density by more than eight

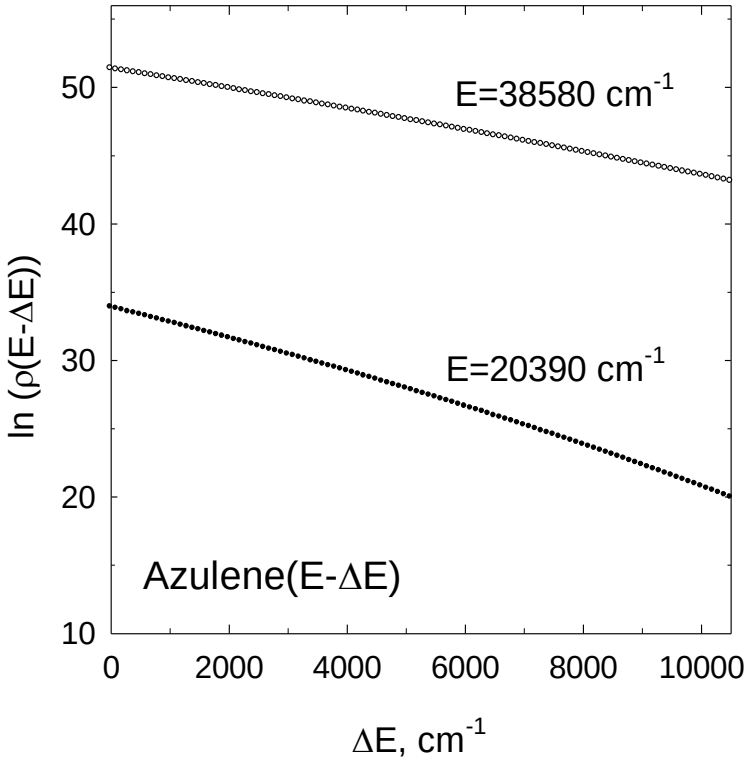

Figure 7.8 Semilogarithmic plot for azulene vibrational state density ρ (E−ΔE) as a function of internal energy for initial E = 38580 and 20390 cm^{-1}.

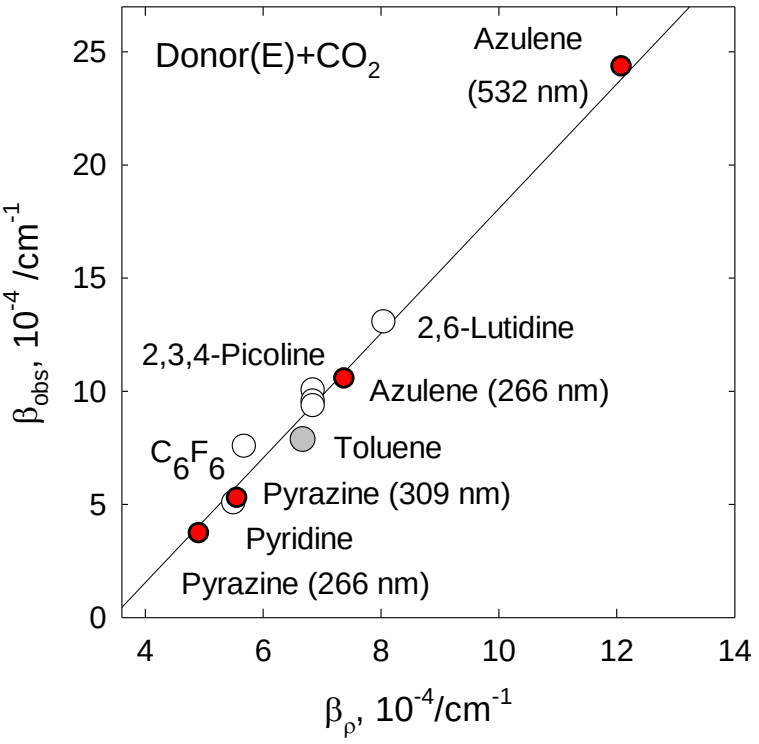

Figure 7.9 The linear correlation of the experimental shape parameter β_{obs} and the state density shape parameter β_ρ for strong collisional quenching of CO_2 with a series of highly vibrationally excited donor molecules: azulene, 2,6-lutidine[86], picoline isomers[88], pyrazine[86], pyridine[85], C_6F_6[94] and toluene[67].

orders of magnitude in state density for a single donor molecule.

The observation that large-ΔE azulene/CO_2 collisions exhibit significant energy-dependent behavior is likely a result of the ability to change the donor energy by a factor of 2. Previous energy-dependent experiments on pyrazine and pyridine relaxation with a CO_2 bath were carried out over smaller ranges of donor vibrational energy and showed very little dependence on E. The pyridine experiments covered only a 10% increase in donor energy and the pyrazine study covered a 30% increase. However the energy dependent results presented here are consistent with the GRETCHEN model. While state density is quite sensitive to changes in the donor energy, the shape parameters that describe $P(\Delta E)$ vary only slightly for relatively small changes in donor energy. This small variation is true especially at higher donor energies. Figure 8.8 shows that for azulene excited at 266 nm, a semilogarithmic plot of $\rho(E-\Delta E)$ is nearly linear for ΔE = 0–10000 cm^{-1}. According to GRETCHEN, this observation means that a single value of β_{obs} will describe the strong collisions for this entire range of donor energies. This behavior is not found at lower donor energies where the state density drops more strongly as a function of ΔE. In the pyrazine and pyridine relaxation studies, the variations in donor energy are small enough that β_{obs} is essentially constant.

It is interesting that the correlation of the shape parameters (Figure 7.9) is best for aromatic donor molecules that have relatively stiff structures. We have found that aromatic donors containing ethyl or propyl groups deviate from the predictions of GRETCHEN.[118] It is the topic of Chapter 8 that strong collisions for ethylpyridine are less significant than predicted while those for propylpyridine are more pronounced. It is possible that donor molecules containing long chain alkyl groups exist in multiple-ring

configurations, at least temporarily, and that the state densities are different substantially from those of molecules with the alkyl group in an extended configuration. It may also be that the aromatic and aliphatic regions of these molecules do not share the vibrational energy statistically on the time scale of collisional energy transfer.

7.4 Conclusion

We have used high resolution transient IR absorption to investigate the strong collisions of azulene(E) with CO_2 at E = 20390 and 38580 cm^{-1} in order to learn how large-ΔE collisional energy transfer is affected by nearly doubling the internal energy of the donor molecule. The energy gain in scattered CO_2 molecules that come from collisions with $\Delta E > 3000$ cm^{-1} has been measured as a function of donor energy. Large-ΔE collisions with higher energy azulene produce scattered CO_2 molecules that have roughly twice the average rotational and translational energies when compared to collisions with the lower energy azulene. The probability for large-ΔE collisions is roughly four times larger for the higher energy donor. The energy transfer distribution functions for collisions with $\Delta E > 3000$ cm^{-1} have probabilities that decay exponentially with ΔE, and this decay is stronger for the lower energy azulene. The distribution function for the 266 nm data agrees reasonably well with KCSI and PECT results although the absolute probability based on IR data is lower by a constant amount. The agreement is not as good at 532 nm. The decay parameters for the energy-dependent distribution functions correlate extremely well with the energy dependence of the azulene state density, as predicted by the GRETCHEN model of energy transfer. The bulk of large-ΔE collisions involve transitions to azulene state densities that are approximately

10–100 times lower than the state density at the initial vibrational energy. These observations provide important information about the influence of state density in the relaxation of highly excited molecules. The work reported here represents a significant step toward a more fundamental understanding of how energy is exchanged in molecular collisions.

Chapter 8: Alkylation Effects on Strong Collisions of Highly Vibrationally Excited Alkylated Pyridines with CO_2

8.1 Introduction

The weak and strong collision dynamics of CO_2 with three different methylated pyridine species were reported in Chapter 6. The study showed that the molecular structure of the donor affects the energy transfer distribution from highly vibrationally excited molecules. This Chapter considers how the strong collisions of highly vibrationally excited molecules are affected by more extensive alkylation of the donor. The strong collision component of the energy transfer distribution function is likely to be most sensitive to the dynamics of energy transfer.

The chemistry and collisional properties of alkenes are often a function of chain length.[181,182] Walker and Morley reported that the product branching ratio in the reaction of alkyl radicals + O_2 at T = 753 K depends on the size of the alkyl reactant. The alkene + HO_2 product channel accounts for 99% for ethyl reactants, 80% for propyl reactants, and 50% for *n*-pentyl reactants.[183] Tardy and Song used time-resolved optoacoustic spectroscopy to measure energy transfer from a series of vibrationally excited fluorinated alkenes in collisions with argon.[184] For fluorinated propane through octane with E_{vib} = 15000–40000 cm^{-1}, they measured a decrease of 30% in energy transfer rates as the number of modes in the donor was increased by a factor of 2.7. They attributed this behavior to the presence of low-frequency vibrational gateway modes that remain well populated through rapid intramolecular vibrational redistribution (IVR). Molecules with

longer chain lengths have a lower average energy per mode as the number of effective vibrational modes increases for a given total energy.

The flexibility of alkylated molecules has also been recognized for enhancing collisional energy transfer. Using the IRF technique, Toselli and Barker found that toluene initially excited with 248-nm light has larger average energy transfer values than does benzene for a number of atomic and molecular collision partners.[55] Using the UVA method, Troe and co-workers report that the collisional deactivation of substituted cycloheptatrienes (E = 41900 cm^{-1}) with rare gases is 30 to 40% more efficient on average for the isopropyl donor than for the ethyl donor.[152,153] For molecular collision partners, though, the dependence of the average energy loss on alkyl substitution is less pronounced. Linhananta and Lim showed in quasiclassical trajectory calculations of collisions of vibrationally hot ethane or propane with rare gases that methyl rotors act as gateway modes and can introduce additional pathways that enhance collisional relaxation.[150,151] Hindered rotors at low energy act like normal vibrations, but torsional rotors can enhance collisional energy transfer in two ways. For a free rotor, internal torsion acts like internal rotation and converts vibrational energy to external rotation in vibrationally hot molecules. This mechanism serves as a gateway for V $\rightarrow$ (R, torsion) energy transfer. At high energies, hindered rotors act like nearly free rotors, again enhancing vibrational relaxation. Collisional relaxation of vibrationally hot propane is more effective than that of ethane because propane has more torsional degrees of freedom and a higher vibrational state density.

Not all studies agree that methyl rotors enhance collisional energy transfer. Bernshtein and Oref compared the collisional relaxation of vibrationally excited benzene,

toluene, *p*-xylene, and azulene by collisions with argon and with cold benzene. The structures of these donor molecules are shown in Figure 8.1.[148,149] When the donor molecules are prepared with the same initial vibrational energy (E ≈ 41000 cm^{-1}), the average vibrational energy loss in collisions with cold benzene is smaller for the methylated donors than for benzene or azulene. The fact that azulene has more efficient energy transfer on average than *p*-xylene even though they have the same number of modes suggests that the low-frequency methyl rotors of toluene and *p*-xylene actually inhibit energy transfer by pulling energy away from the rest of the molecule. However, the energy transfer values for the alkylated donors in collisions with argon are larger than those for benzene. This result suggests that the presence of methyl rotors does not inhibit collisional energy transfer. For both the atomic and polyatomic collision partners, large energy transfer values correlate with the presence of low-frequency gateway modes in the aromatic ring.

This Chapter considers the energy partitioning resulting from strong collisions of CO_2 with a series of alkylated donor species: 2-ethyl pyridine (2EP) at E = 38570 cm^{-1}, 2-propylpyridine (2PP) at E = 38870 cm^{-1} and 2-t-butylpyridine (2tBP) at E = 39123 cm^{-1}. The structures of the alkylated pyridines are shown in Figure 8.1.

The goal of this study is to develop a better understanding of how longer chain alkyl groups impact collisional energy transfer. The experimental data show that the probability for strong collisional energy transfer is reduced for 2EP and 2tBP relative to 2MP. The propylated donor 2PP, however, exhibits more strong collisions than does 2EP. The curvature of the energy transfer distribution functions is compared to the state density energy dependence for a series of donor molecules. Differences are observed for

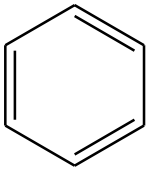

benzene

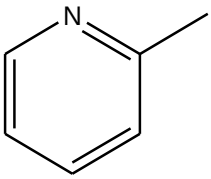

2MP

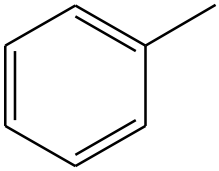

toluene

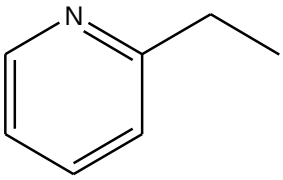

2EP

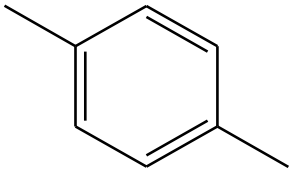

p-xylene

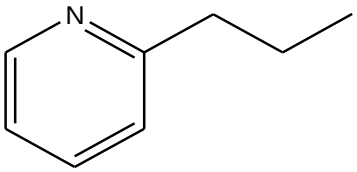

2PP

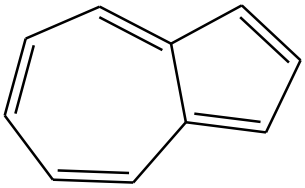

azulene

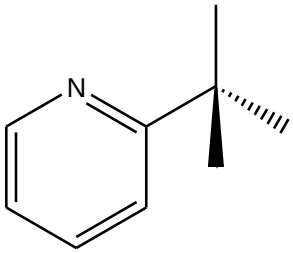

2tBP

Figure 8.1 The structures of the aromatic donor species discussed in this Chapter.

the alkylated species relative to non-alkylated species. How the alkylation affects on strong collision dynamics is discussed in terms of the competing roles of internal energy content, vibrational mode frequencies, and larger amplitude motion that results from the increased flexibility of longer alkyl chains.

8.2 Experimental Methods

This Chapter reports the state-resolved energy transfer to CO_2 from three alkylpyridine donors measured using a high-resolution transient IR diode laser spectrometer. The highly vibrationally excited donor molecules (2EP, 2PP and 2tBP) were prepared by 5 ns pulsed UV excitation at λ=266 nm from a Nd:YAG laser. The UV power was kept at less than 1 MW/cm^2 to minimize the multiphoton absorption. A 1:1 mixture of donor and CO_2 gases was flowed into a 3 meter flowing collision cell with 20 mTorr total pressure. The average collision time was about 4 μs. State-resolved energy gain in individual CO_2 rotational states was probed after the UV pulse using a single mode diode laser operating near λ=4.3 μm. The transient IR probing signal was collected at t = 1 μs after the UV pulse. The amount of translational energy gained in the scattered molecules was determined from transient Doppler broadened line profiles. Line profiles for individual J-states of CO_2 were measured by locking the IR laser to a scanning Fabry-Perot etalon and frequency tuning over a CO_2 rotational line.

The donor molecules used in this study are 2EP (C_7H_9N, ACROS 98+% purity), 2PP ($C_8H_{11}N$, Alfa Aesar 98% purity), 2tBP ($C_9H_{13}N$, Sigma-Aldrich) which were degassed by the freeze-pump-thaw method before use. CO_2 (Matheson, 99.995% purify) is used directly.

8.3 Results and Discussion

This Section reports on the rotational and translational energy gain distributions and rate constants of scattered CO_2 molecules in high-J states (J = 62–78) from strong collisions with three alkyl-pyridine donors. Converting lab-frame translational energy distributions into the center-of-mass frame yields the amount of donor vibrational energy that goes into translation of the two collision partners. The rotational and translational energy gain profiles are combined with absolute energy transfer rate measurements to produce energy transfer distribution functions for strong collisions with $\Delta E > 3000$ cm^{-1}.[89] The probability distributions account for all transferred energy for the V→RT pathway except the amount that goes into rotation of the donor. There is currently not a definitive way to measure the donor rotational energy after collisions. Here I present the nascent energy gain results for CO_2 and the resulting distribution functions. Results for 2EP, 2PP, and 2tBP collisions are compared throughout with those from earlier studies on pyridine (Pyr) and 2-methylpyridine (2MP).[86]

8.3.1 Transient Absorption Signals for CO_2 (00^00) From Collisions with Three Highly Vibrationally Excited Alkyl-Pyridines (2EP, 2PP, and 2tBP)

The collisional quenching of excited donor molecules with CO_2 is given by Eq 8.1.

$$\text{donor}\ (E) + CO_2\left(00^00\right) \xrightarrow{k_{app}^J} \text{donor}\ (E-\Delta E) + CO_2\ (00^00,J,V) \qquad (8.1)$$

where, donor = 2EP, 2PP, 2tBP. The high-resolution transient IR diode laser probes the appearance of scattered CO_2 in high-J states (J = 62–78) using P-branch transitions of the

anti-symmetric stretch mode at $\nu_3 = 2349\ cm^{-1}$. Figure 8.2 shows the transient absorption signals for CO_2 (00^00, J = 62) that result from collisions with 2EP(E), 2PP(E) and 2tBP(E). The fractional absorption signals are converted to the state–specific number density of scattered CO_2 molecules using known IR transition line strengths.[124,185]

8.3.2 Translational Energy Distributions of Scattered CO_2 (J = 62-78) From Collisions with Vibrationally Excited Donors

Doppler broadened line profiles of scattered CO_2 in high-J states (J = 62–78) were collected at t = 1 μs after UV excitation. The three plots in Figure 8.3 show the Doppler-broadened profiles of scattered CO_2 (J = 74) following collisions with the vibrationally excited donors (2EP, 2PP, 2tBP). In Figure 8.3, the sets of fractional IR absorption signals (circles) are fitted by a single-Gaussian function (solid lines). The observed line widths $\Delta\nu_{app}$ are broader than the initial values at T = 300 K (dashed lines) and increase with CO_2 J state. These values are listed in Table 8.1. The data indicate that the large ΔE energy transfer occurs via impulsive collisions. The lab-frame translational temperature T_{app} of scattered CO_2 and the center-of-mass translational temperature T_{rel} for the collision pairs are also reported in Table 8.1.

Figure 8.4 compares the J-dependent center-of-mass translational temperatures T_{rel} for collisions of CO_2 with 5 different alkylated pyridine donors: Pyr, 2MP, 2EP, 2PP and 2tBP. The effect of alkylation is clear from the top plot: pyridine releases much more energy as translation in collisions than do the alkylated donors. However, when the data for the four alkylated donors are compared together in the lower plot of Figure 8.4, it is seen that 2MP consistently results in more product translational energy than do 2EP, 2PP and 2tBP. This observation is consistent with what one would expect for impulsive

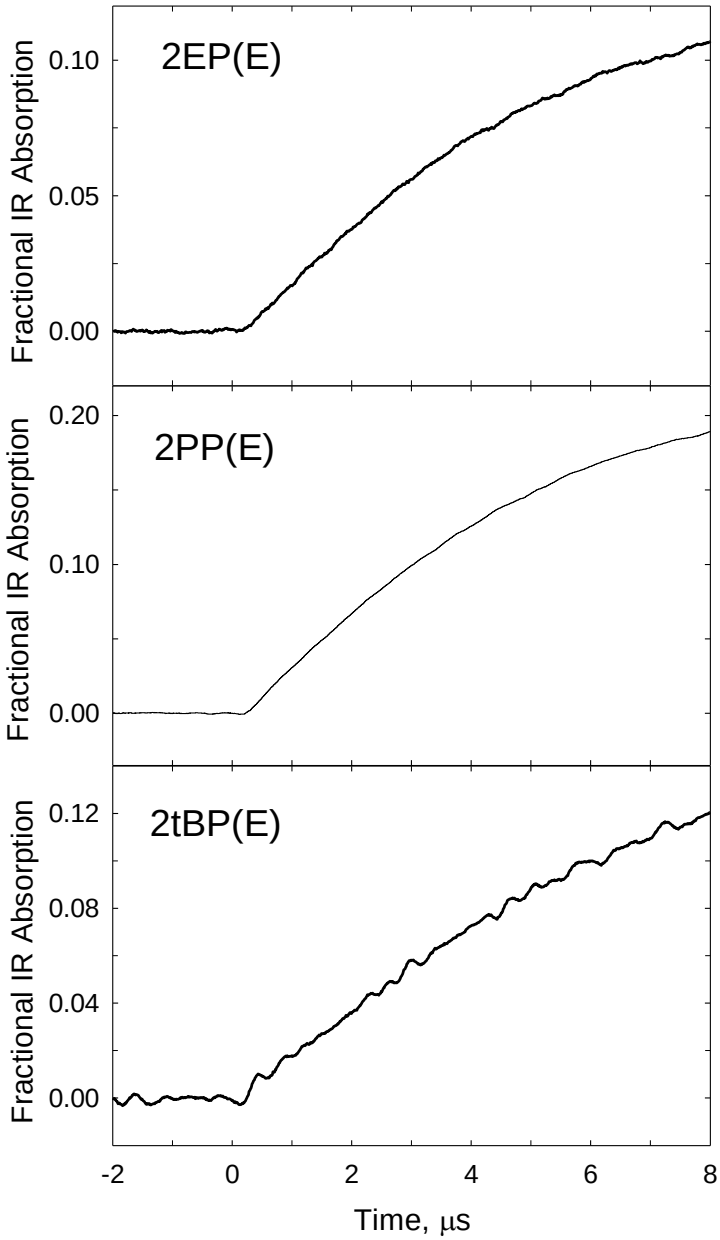

Figure 8.2 Transient IR absorption signals for appearance of CO_2 (00^00, J = 62) through collisions with three donors, 2EP, 2PP, and 2tBP, initially excited with λ = 266 nm. The populations of scattered CO_2 are collected at t=1 μs after UV pulse from the single collision which average collision times are 4–5 μs.

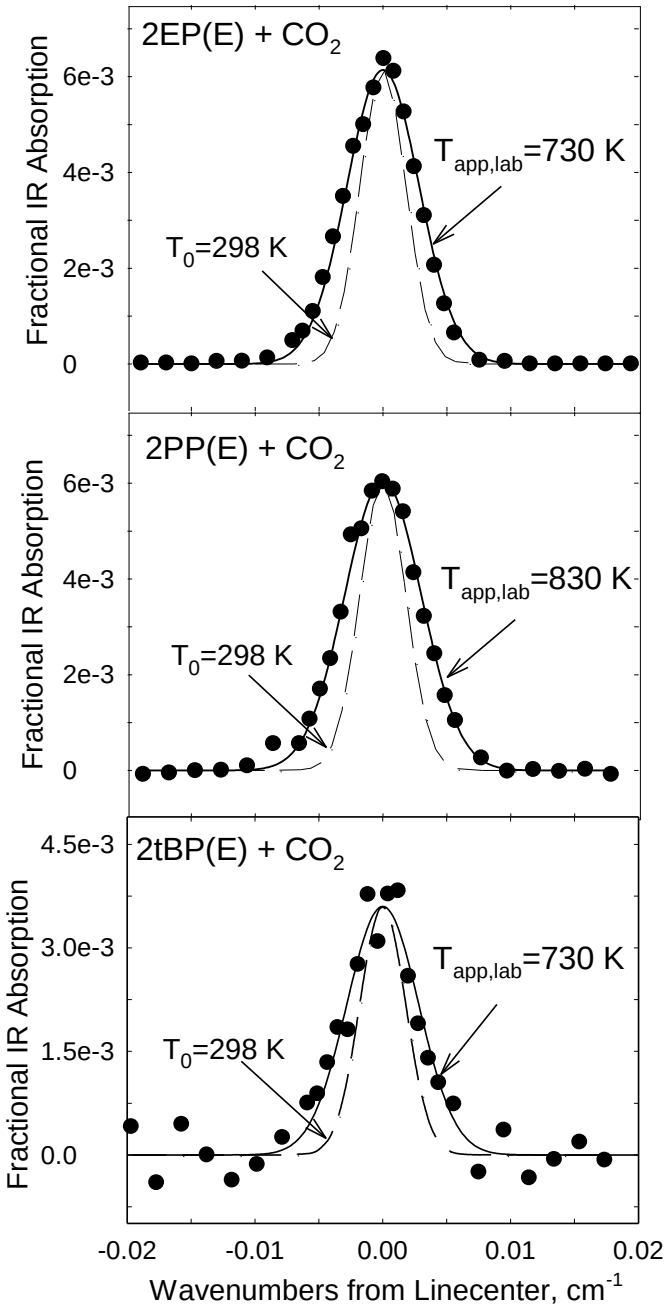

Figure 8.3 Nascent Doppler-broadened line profiles for CO_2 (00^00, J = 72) following collisions with vibrationally excited (a) 2EP, (b) 2PP and 2tBP (c). The solid circles are the transient IR absorption signals at 1 μs after the UV pulse. The line profiles are Gaussian fits shown as the solid curves. The full width at half-maximum of scattered CO_2 through collisions with the vibrationally excited donors is broader than 298 K (dashed lines).

Table 8.1 (a)Doppler broadened linewidth for scattered CO_2 (00^00) for strong collisions with vibrationally excited 2EP molecules.

2EP (E = 38570 cm^{-1}) + CO_2 (00^00)				
J	E_{rot}, cm^{-1}	$\Delta\nu_{app}$, cm^{-1a}	T_{app}, K[b]	T_{rel}, K[c]
62	1522.1611	0.0058	560 ± 168	669 ± 201
66	1722.9413	0.0062	640 ± 192	781 ± 234
68	1827.9724	0.0063	650 ± 195	796 ± 239
70	1936.0953	0.0067	730 ± 219	908 ± 273
72	2047.3081	0.0066	720 ± 216	894 ± 268
74	2162.6090	0.0066	730 ± 219	908 ± 273
78	2399.4677	0.0066	730 ± 219	908 ± 273

[a]The full-width half-maximum line width, $\Delta\nu_{app}$, from fitting the t = 1 μs transient line profile to a Gaussian function. The uncertainty in linewidths is ± 0.001 cm^{-1}.

[b]The lab frame translational temperature, T_{app} in K, is determined using $T_{app} = (mc^2/8k_B \ln 2)(\Delta\nu_{app}/\nu_0)^2$, where m is the mass of CO_2, c is the speed of light, k_B is Boltzmann's constant, ν_0 is the IR transition frequency, and νapp is the nascent Doppler broadened line width.

[c]The center of mass translational temperature T_{rel} for an isotropic distribution of scattered CO_2 molecules is obtained from the equation:

$T_{rel} = T_{app} + (T_{app} - T_0) \times (m_{CO_2}/m_{donor})$, where T_0 = 298 K and three donors are 2EP, 2PP and 2tBP.

(b)Doppler broadened linewidth for scattered CO_2 (00^00) for strong collisions with excited 2PP molecules.

2PP (E = 38870 cm^{-1}) + CO_2 (00^00)				
J	E_{rot}, cm^{-1}	$\Delta\nu_{app}$, cm^{-1a}	T_{app}, K[b]	T_{rel}, K[c]
62	1522.1611	0.0063	645 ± 194	772 ± 232
66	1722.9413	0.0068	760 ± 228	928 ± 279
68	1827.9724	0.0071	833 ± 250	1028 ± 308
70	1936.0953	0.0071	830 ± 249	1024 ± 307
72	2047.3081	0.0071	830 ± 249	1024 ± 307
74	2162.6090	0.0071	843 ± 253	1042 ± 313
76	2278.9962	0.0074	910 ± 273	1133 ± 340

(c)Doppler broadened linewidth for scattered CO_2 (00^00) for strong collisions with the highly vibrationally excited 2tBP molecules.

2tBP (E = 39123 cm^{-1}) + CO_2 (00^00)				
J	E_{rot}, cm^{-1}	$\Delta\nu_{app}$, cm^{-1a}	T_{app}, K^b	T_{rel}, K^c
62	1522.1611	0.0062	620 ± 186	730 ± 219
66	1722.9413	0.0068	760 ± 228	910 ± 273
68	1827.9724	0.0078	910 ± 273	890 ±267
70	1936.0953	0.0067	800 ± 240	970 ± 291
72	2047.3081	0.0065	720 ± 216	860 ± 258
74	2162.6090	0.0071	810 ± 243	980 ± 294
76	2399.4677	0.0071	840 ± 252	1110 ± 333
78	2278.9962	0.0079	1050 ± 315	1290 ± 387

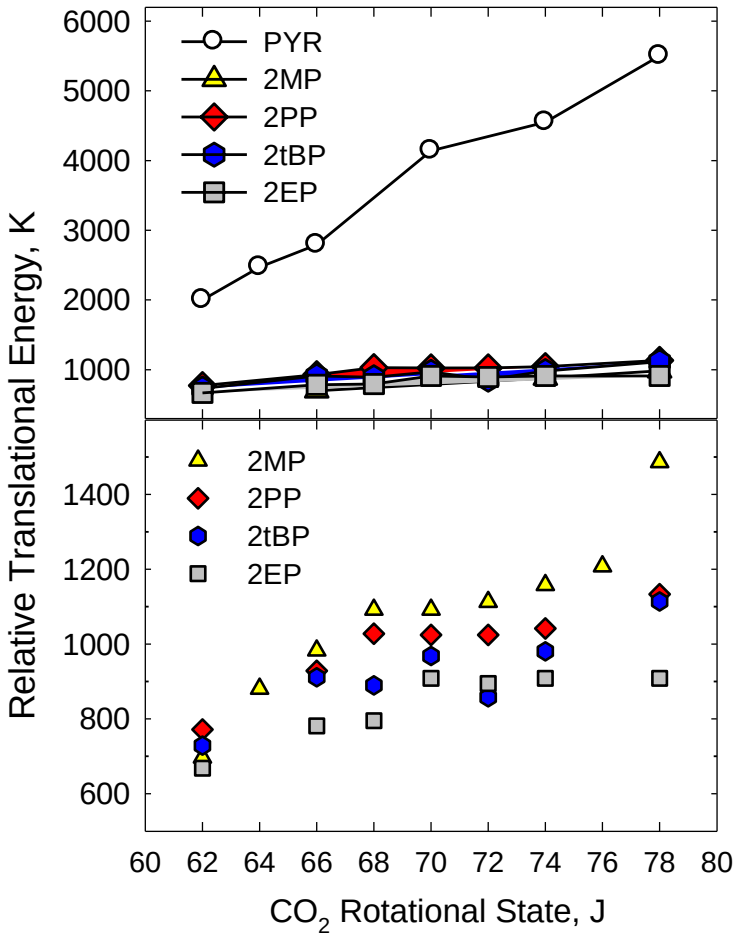

Figure 8.4 The relative translational temperatures T_{rel} that describe the translational energy distributions between recoiling donors and CO_2 (00^00, J = 62–78) are shown in two plots. The upper plot compares the translational energy distributions of the alkylated-pyridines with that for pyridine. Donor alkylation reduces the translational energy of the scattered CO_2 molecules. The lower plot compares T_{rel} for different alkylated donors. The increase in T_{rel} with CO_2 J-state is consistent with an impulsive energy transfer mechanism. For a given J-state, T_{rel} generally follows the ordering of 2MP > 2PP > 2tBP > 2EP.

collisions of different-sized donor molecules containing nearly the same internal energy. The internal energy is spread among more degrees of freedom as the number of vibrational modes increases and less energy is imparted through collisions. The addition of longer chain alkyl groups in particular introduces low frequency torsions and hindered or nearly free rotors that are preferentially populated by IVR.

For 2EP, 2PP and 2tBP, the amount of energy released into translation via strong collisions does not correlate directly with the number of carbons in the alkyl group. The observed trend in energy transfer via strong collisions as a function of alkyl group length is propyl > t-butyl > ethyl. This observation suggests that chain length is an important factor in strong collisional energy transfer. In this way, the translational energy of products from strong collisions increases due to the larger amplitude motion that comes from increased chain length. We note that the differences in the translational energies for strong collisions of three alkyl pyridines are relatively small and that the translational temperatures from three donors are within experimental error, as listed in Table 8.1. Nonetheless, the recoil velocities from the propylpyridine are consistently larger than those for 2tBP and 2EP. We estimated that the chain length for the propyl substituent is ~ 50% larger than for 2tBP and 2EP.

8.3.3 Rotational Energy Gain of Scattered CO_2 from Donors (2EP, 2PP and 2tBP)

The nascent rotational energy gained by scattered CO_2 (00^00) in J = 62–78 was measured for collisions with vibrationally excited 2EP, 2tBP and 2PP. Figure 8.5 shows the rotational distributions of scattered CO_2 in high-J states. The high-J populations are single-exponential distributions with rotational temperatures T_{rot} that are determined from the slope of the semi-log plot. The scattered CO_2 rotational distributions for collisions

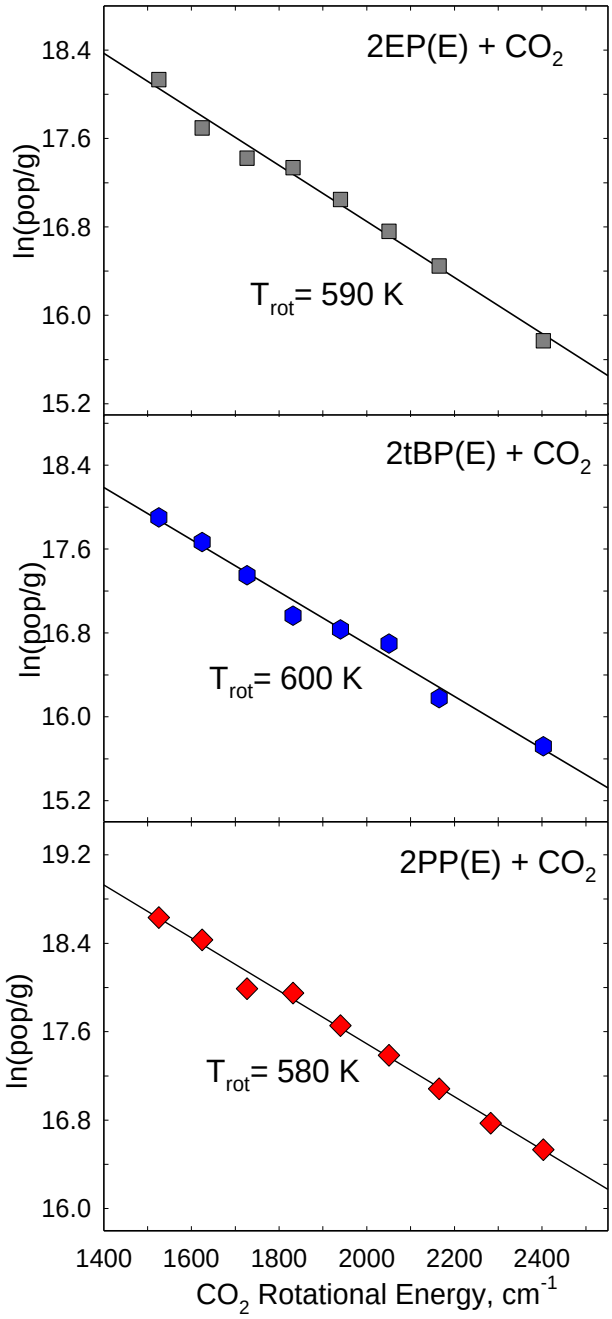

Figure 8.5 Nascent rotational distributions of scattered CO_2 (00^00, J = 62–78) at t = 1 μs following collisions with highly vibrationally excited three alkylated pyridine: 2EP, 2tBP, and 2PP. The rotational distributions of scattered CO_2 through collisions with three donors are similar T_{rot}~ 590 ± 60 K.

with the three donors are nearly the same: T_{rot} = 590 ± 60 K for 2EP, T_{rot} = 580 ± 60 K for 2PP and T_{rot} = 600 ± 60 K for 2tBP.

Within the error, the values of T_{rot} for strong collisions of the alkylated donors are similar to the values for methylated donors: T_{rot} = 610 ± 60 K for 2MP and T_{rot} = 540 ± 60 K for 2,6MP. For the large-ΔE component, the average rotational energy gained for scattered CO_2 from each alkylated pyridine donors is $\langle \Delta E_{rot} \rangle = k_B (T_{rot} - T_0) \sim 210$ cm^{-1} where k_B is Boltzmann constant and T_0 = 298 K. In contrast, when pyridine is the energy donor, the scattered high-J CO_2 molecules have a rotational temperature of T_{rot} = 835 K. Pyridine collisions result in a larger average increase in CO_2 rotational energy of $\langle \Delta E_{rot} \rangle$ = 370 ± 60 cm^{-1}. Donor alkylation reduces the amount of energy that goes into CO_2 rotation and this effect is same for methyl, ethyl, t-butyl, and propyl substituents.

The experimental results presented here and in previous several Chapters show that angular momentum changes in collisions correlate with changes in recoil velocity. The change in total angular momentum vector $\Delta\vec{J}_{total}$ is the product of the impact parameter b, the reduced mass μ, and the change in recoil velocity, as shown in Eq 8.2.

$$\Delta\vec{J}_{total} = \Delta\left(\vec{L}+\vec{J}_{rot}\right) = \Delta\left(\vec{L}+\vec{J}_{bath}+\vec{J}_{donor}\right) = \mu b \Delta\vec{v}_{rel} \qquad (8.2)$$

Here $\Delta\vec{J}_{total}$ is the sum of changes in orbital angular momentum $\vec{L}$ and rotational angular momentum $\vec{J}_{rot}$ for both collision partners. Currently there is no direct way to measure the product rotational states of the hot donor molecule. However, we take final $\vec{J}_{bath}$ as a lower limit to final $\vec{J}_{rot}$ based on Lawrence and Waclawik's study.[131] In Table 8.2, the values of $\langle \Delta J_{bath} \rangle$ and $\langle \Delta v_{rel} \rangle$ for CO_2 are listed.

Table 8.2 (a) The average changes in angular and linear momentum in CO_2 from collisions with highly vibrationally excited 2EP molecules.

2EP (E = 38570 cm^{-1}) + CO_2					
CO_2 J	$\langle\Delta J\rangle$, $\hbar$[a]	$\langle v_{lab}\rangle$, m/s[b]	$\langle v_{rel}\rangle$, m/s[c]	$\langle\Delta v_{rel}\rangle$, m/s[d]	b_{min}, Å[e]
62	55.3	560	726	238	4.7
66	59.8	600	787	299	4.1
68	62.0	611	803	314	4.0
70	64.2	650	862	374	3.5
72	66.3	641	848	360	3.7
74	68.5	642	849	361	3.9
78	72.8	643	851	363	4.1

[a]$\langle\Delta J\rangle$ in $\hbar$ is the average change of CO_2 angular momentum which is determined using $\langle\Delta J_{bath}\rangle=\sqrt{J_{final}^2-J_{initial}^2}$, where $J_{initial}$~22.

[a]Average velocity in the lab frame of scattered CO_2 molecules determined using $\langle v_{lab}\rangle = \left(\frac{3k_BT_{app}}{m_{CO_2}}\right)^{\frac{1}{2}}$, where k_B is the Boltzmann constant, $m_{CO_2}$is the mass of CO_2 molecule. The values of T_{app} are listed in Table 7.1.

[c]$\langle v_{rel}\rangle$, the average velocities in the center-of-mass of donor (E)/CO_2 systems are calculated by using $\langle v_{rel}\rangle = (M/m_{donor}) \cdot [\langle v_{lab}\rangle^2 - (3k_BT/M)]^{1/2}$, where the sum of mass $M= m_{donor}+ m_{CO_2}$ and m_{donor} is the mass of alkylated pyridine (2EP, 2PP and 2tBP).

[d]Average change in center-of-mass velocity $\langle \Delta v_{rel} \rangle$ in m s^{-1} is calculated by an equation: $\langle \Delta v_{rel} \rangle = \langle v_{rel} \rangle - \left(\frac{3k_B T_0}{\mu}\right)^{\frac{1}{2}}$, where μ is the reduced mass for pyrazine/CO_2 pair and $T_0 = 298$ K.

[e]b_{eff}, effective impact parameter for donor (E)/CO_2 system is from $\langle \Delta J_{bath} \rangle \leq \mu \langle \Delta v_{rel} \rangle b_{eff}$ while donors are 2EP, 2PP and 2tBP.

(b) The average changes in angular and linear momentum in CO_2 from collisions with highly vibrationally excited 2PP molecules.

2PP (E = 38870 cm^{-1}) + CO_2					
CO_2 J	$\langle \Delta J \rangle$, $\hbar$[a]	$\langle v_{lab} \rangle$, m/s[b]	$\langle v_{rel} \rangle$, m/s[c]	$\langle \Delta v_{rel} \rangle$, m/s[d]	b_{min}, Å[e]
62	55.3	609	778	298	3.7
66	59.8	658	850	370	3.2
68	62.0	688	892	413	3.0
70	64.2	689	893	414	3.1
72.	66.3	690	894	415	3.1
74	68.5	690	895	416	3.2
76	70.7	721	939	460	3.0

(c) The average changes in angular and linear momentum in CO_2 from collisions with highly vibrationally excited 2tBP molecules.

2tBP (E = 39123 cm^{-1}) + CO_2					
CO_2 J	$\langle \Delta J \rangle$, $\hbar$[a]	$\langle v_{lab} \rangle$, m/s[b]	$\langle v_{rel} \rangle$, m/s[c]	$\langle \Delta v_{rel} \rangle$, m/s[d]	b_{min}, Å[e]
62	55.3	599	747	274	3.9
66	59.8	658	830	357	3.2
68	62.0	756	965	492	2.4
70	64.2	650	818	345	3.6
72.	66.3	631	792	319	4.0
74	68.5	690	874	401	3.3
76	70.7	691	875	402	3.4
78	72.8	770	984	511	2.7

An effective impact parameter b_{eff} for each donor/CO_2 pair was determined by the average change of CO_2 angular momentum $\langle \Delta J_{bath} \rangle$ shown $\langle \Delta J_{bath} \rangle \leq \mu b_{eff} \langle \Delta v_{rel} \rangle$. The correlation between b_{eff} and $\langle \Delta J_{bath} \rangle$ for each donor is in Figure 8.6. The strong collisions of the alkylated pyridine donors (2EP, 2PP and 2tBP) with CO_2 are characterized by b_{eff} = 4.0, 3.3 and 3.3 Å, respectively. From previous studies, pyridine and 2MP with CO_2 have the impact parameters of b_{eff} = 1.4 and 2.9 Å respectively.[87,91] This result indicates that the alkylated donors undergo strong collisions at larger impact parameters than do nonalkylated donors. This result suggests that large amplitude motion of the alkyl groups is involved in strong collisions.

The ratio of b_{eff} to the Lennard-Jones σ parameter provides some information about the region of the donor/CO_2 interaction potential that is probed in these studies. The Lennard-Jones σ parameters for the donor/CO_2 pairs are σ = 4.87 Å (pyridine), 5.04 Å (2MP), 5.28 Å (2EP), 5.45 Å (2PP) and 5.58 Å (2tBP). The ratio of b_{eff}/σ is 29% for pyridine, while for the alkylated 2MP, 2EP, 2PP and 2tBP donors, b_{eff}/σ = 57, 75, 60 and 59%, respectively. This result shows that the collisions studied here probe different regions of the intermolecular potential and are sensitive to donor alkylation. In each case, the collisions have b_{eff} values that are less than σ, showing that the repulsive part of the potential is involved in the strong collision relaxation, but collisions of the alkylated donors are apparently less repulsive than the pyridine collisions. This effect is most likely due to the lower average energy per mode in the alkylated donors. Other factors could also contribute, including structural and electrostatic differences that are affected by high levels of vibrational excitation. For example, the similarity of b_{eff}/σ for 2MP and 2PP may suggest that the propyl group in 2PP is not fully extended during collisions with CO_2.

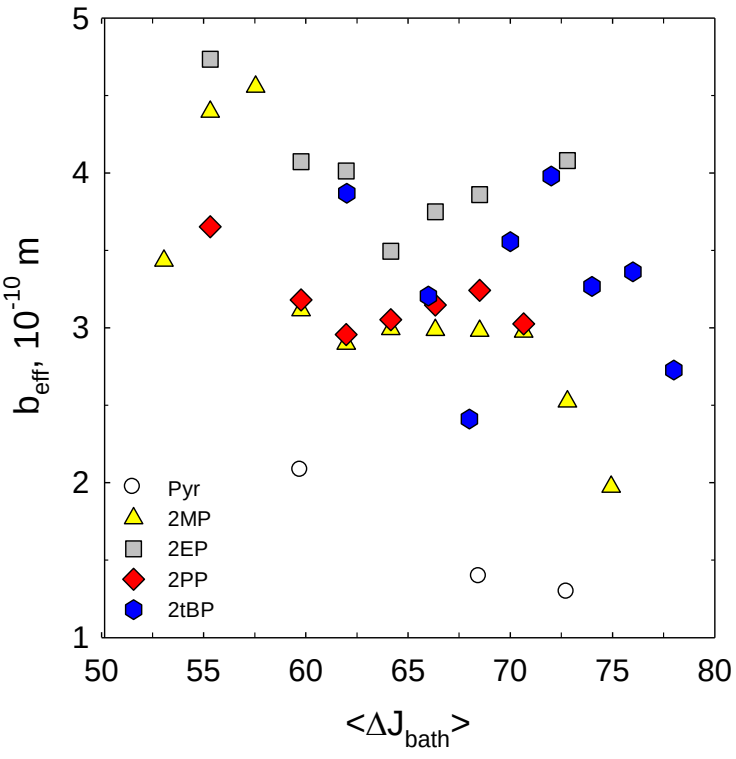

Figure 8.6 The effective impact parameter b_{eff} is a function of the average change of CO_2 angular momentum $\langle \Delta J_{bath} \rangle$. Values of b_{eff} for CO_2 with pyridine and alkylated pyridine pairs are compared.

8.3.4 State-Resolved Energy Transfer Rate Constants k_{app}^{J} for 2EP, 2tBP, and 2PP with CO_2

State-resolved rate constants k_{app}^{J} for energy transfer from 2EP, 2tBP and 2PP to CO_2 via strong collisions were determined by measuring the early time appearance of CO_2 in high-J states, as described in Eq 8.1. CO_2 populations were measured at t = 1 μs after donor excitation where the donor and CO_2 bath concentrations are essentially given by their respective values at t = 0. Under these early time conditions, rate constants were determined for known initial donor and CO_2 bath concentrations using Eq 8.3.

$$k_{app}^{J} = \frac{\Delta[CO_2(00^0 0, J)]}{[Donor(E)]_0[CO_2]_0 \Delta t} \tag{8.3}$$

The scattered CO_2 populations include contributions from the Doppler-broadened line widths. The rate constants for the strong collisions that quench 2EP, 2tBP and 2PP are listed in Table 8.3.

Figure 8.7 compares the energy transfer rates for strong collisions of pyridine, 2MP, 2EP, 2PP and 2tBP with CO_2. Generally, the ordering of rates goes as 2PP > 2MP > 2EP ~ 2tBP > Pyr. To account for differences in the collision rates for the different donors, it is useful to compare the energy transfer on a per-collision basis by normalizing the energy transfer rate to the Lennard-Jones collision rate. The collision rate depends on the collisional cross section reduced mass and translational temperature. The Lennard-Jones collision rates for 2EP, 2PP and 2tBP with CO_2 are listed in Table 8.3. Values of collision rates for pyridine/ CO_2 and 2MP/CO_2 are $k_{LJ} = 5.58 \times 10^{-10}$ cm^3 molecule^{-1} s^{-1}

Table 8.3 Appearance energy transfer rate constants of scattered CO_2 (00^00, J) through collisions with highly vibrationally excited donors: 2EP, 2PP, 2tBP.

CO_2 (00^00)		k^J_{app}, 10^{-13} cm^3 molecule^{-1} s^{-1}		
J state	E_{rot}, cm^{-1}	2EP	2PP	2tBP
		E = 38570 cm^{-1}	E = 38870 cm^{-1}	E= 39123 cm^{-1}
62	1522.1611	15.7 ± 4.7	20.0 ± 6.0	15.4 ± 4.6
64	1621.0037	11.3 ± 3.4	17.0 ± 5.1	11.8 ± 3.5
66	1722.9413	8.7 ± 2.6	11.1 ± 3.3	8.8 ± 2.6
68	1827.9724	7.6 ± 2.3	11.1 ± 3.3	5.7 ± 1.7
70	1936.3081	6.2 ± 1.9	8.5 ± 2.6	5.2 ± 1.6
72	2047.3081	4.5 ± 1.4	6.7 ± 2.0	4.8 ± 1.4
74	2162.6090	3.5 ± 1.1	5.1 ± 1.5	2.5 ± 0.8
76	2278.9962		3.8 ± 1.1	
78	2399.4677	2.0 ± 0.6	3.1 ± 0.9	1.4 ± 0.4
k_{int}, 10^{-12} cm^3 molecule^{-1} s^{-1} for J = 62–78 [a]		6.2 ± 1.9	8.6 ± 2.6	5.8 ± 1.7
k_{LJ}, 10^{-10} cm^3 molecule^{-1} s^{-1} [b]		6.39	6.76	7.05

[a]Integrated collision constant, k_{int} in cm^3 molecule^{-1} s^{-1} is the sum of state-specific collision rates of CO_2 at J = 62–78 through collisions with three alkylpyridine donors.

[b]The Lennard-Jones collision rate constant k_{LJ} for three alkylpyridine donors with CO_2 molecules are determined in Appendix B. The Lennard-Jones parameters are also described there.

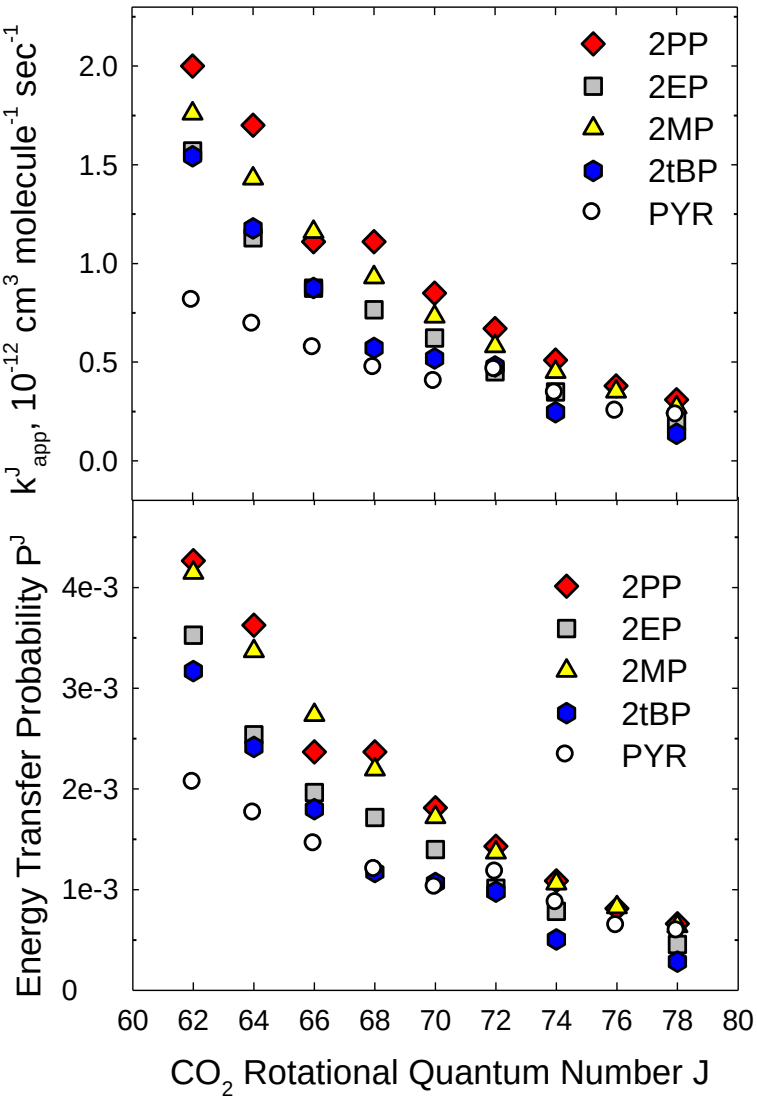

Figure 8.7 Absolute state-specific rate constants k^J_{app} and energy transfer probabilities $P_J(\Delta E)$ for initial appearance of scattered CO_2 (00^00, J = 62–78) following collisions with five donors: Pyr, 2MP, 2EP, 2tBP, and 2PP. Probabilities are based on the Lennard-Jones collision rate. The ordering of rates for appearance of a given CO_2 state is 2PP > 2MP > 2EP ~ 2tBP > Pyr; the ordering of probabilities for CO_2 states is 2PP ~ 2MP > 2EP > 2tBP > Pyr.

and 5.86×10^{-10} cm^3 $molecule^{-1}$ s^{-1}, respectively.

Energy transfer probabilities P_J were calculated by $P_J = k^J_{app}/k_{LJ}$ and are shown in Figure 8.7 for the five donor-CO_2 pairs. Compared on a per-collision basis, the ordering of the energy transfer probability goes as 2PP ~ 2MP > 2EP > 2tBP > Pyr with the J-specific probabilities for 2PP relaxation being about twice those of pyridine. The observed ordering of energy transfer probabilities may be a result of increasing state density in the larger donor molecules. However, comparison with the other donors shows that 2MP has larger rates and probabilities than 2EP, which is not predicted on the basis of donor size.

8.3.5 Energy Transfer Distribution P(ΔE) for Strong Collisions of Donors with CO_2.

Energy transfer distribution functions for strong collisions of 2EP, 2tBP and 2PP with CO_2 were determined from measurements of rate constants and CO_2 energy gain by considering the combined distribution of rotational and translational energy for the scattered CO_2 molecules. The procedure for this transformation has been presented previously and the essential points are discussed here.[89] The key idea is to convert from state- and velocity- indexed data to a ΔE-indexed probability. Each J state of CO_2 has a velocity distribution whose width is specified by the spectral Doppler-broadening and a probability that is determined by the ratio of the rate constant to the collision rate. The probability distribution for the change in energy ΔE is obtained by subtracting the average initial rotational and translational energies. The overall energy transfer probability distribution function P(ΔE) results from summing over the distribution functions of individual CO_2 J states. The only assumptions in this transformation are the values of the precollision energies and the collision rate. Scattered CO_2 molecules in low

J states have not been characterized in these studies so the P(ΔE) curves are complete for $\Delta E > 3000$ cm^{-1}. Contributions to ΔE from donor rotation are not accounted for in the probability distributions. Simulations indicate that donor molecules can gain rotational energy through quenching collisions, but this effect is most pronounced in collisions with rare gas atoms.[186] The extent of rotational energy gain in the donors is expected to be less than for CO_2 based on the conservation of angular momentum and the relatively small rotational constants for the donor molecules.

The energy transfer distribution functions P(ΔE) for the strong collisions of Pyr, 2MP, 2EP, 2tBP and 2PP with CO_2 are shown in Figure 8.8 based on Lennard-Jones collision rates. Pyridine has the largest probability for strong collisions with $\Delta E > 3000$ cm^{-1}. Among the alkylated donors, 2MP and 2PP have similar P(ΔE) curves while 2EP and 2tBP have the lowest probabilities for strong collisions.

Figure 8.8 highlights several important features for strong collisions with CO_2. Strong collisional energy transfer is favored for smaller donor molecules that on average have more energy per mode than do the larger donor molecules for the same initial energies. The alkylated donors have less energy per mode on average than do non-alkylated donors and in general the likelihood of strong collisions for these former donors is reduced. For the alkylated donors, the probability of strong collisions is ordered as 2MP~2PP>2EP~2tBP. It is interesting that P(ΔE) curves for 2EP and 2tBP are very similar. The ethyl and t-butyl groups are believed to extend some distance from the ring, suggesting that the alkyl chain is important in the collision dynamics. However, 2PP, which has the longest propyl chain, imparts substantially more energy to the rotational and translational degrees of freedom of CO_2 in single collisions with $\Delta E > 3000$ cm^{-1} than

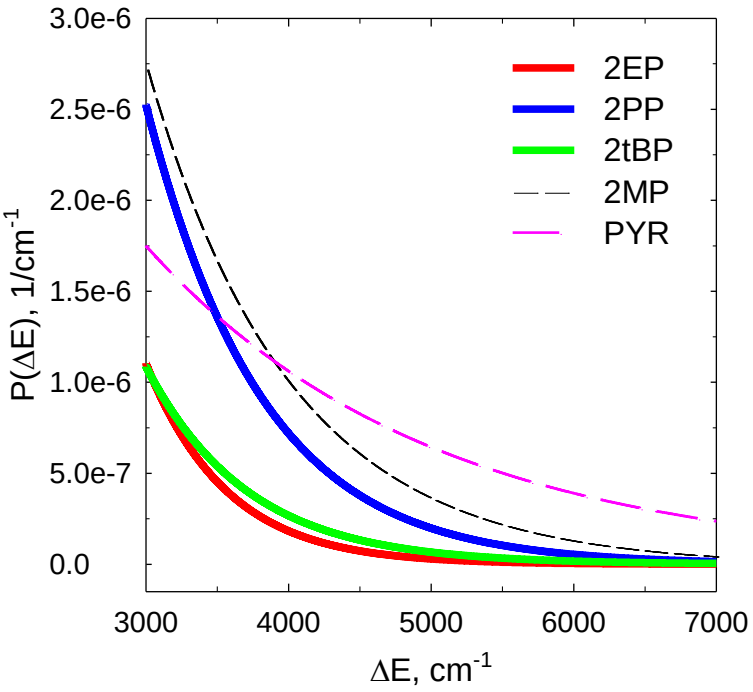

Figure 8.8 Energy transfer distribution function P(ΔE) for strong collisions with ΔE > 4000 cm^{-1} of CO_2 with five vibrationally excited donors. The ordering of energy transfer probabilities is 2MP > 2PP > 2tBP ~ 2EP.

does 2EP and 2tBP. This result is not consistent with the lower average energy per mode of 2PP. It is possible that differences in the potentials of the torsional and methyl rotor vibrations of the various donors contribute to the observed differences in P(ΔE) curves. Simulations on smaller molecules such as ethane and propane have already provided important clues as to how methyl and ethyl torsional motion can enhance vibrational relaxation, and future theoretical studies on mixed alkyl aromatic molecules may provide additional insight.[150,151]

It may be that the longer alkyl chain in 2PP introduces new dynamical effects that are not present in aromatic and methylated aromatic species. Longer-chain alkyl groups can undergo larger-amplitude motion, and whiplike motions of the propyl chain may account for the enhanced strong collisions in 2PP. The possibility for such interactions would be enhanced by chattering collisions in which the donor and bath molecules undergo multiple impulsive encounters during a single "collision." Trajectory calculations of the strong collisions between pyrazine(E = 37900 cm^{-1}) with CO_2 find that nearly 50% of strong collisions have multiple direct encounters.[45] The simulations show that typical chattering collisions involve low relative translational energies and correspondingly small increases in internal rotation of the collision pair. Linhananta and Lim observed chattering collisions for propane (E = 41000 cm^{-1}) with argon and found that collisional energy transfer increased with the number of encounters.[36] The presence of this type of long-lived collision complex could help facilitate energy transfer that involves large amplitude motion of the propyl chain.

It is also possible that the longer chain length of 2PP introduces new possibilities for constrained configurations that increase the mode frequencies of the propyl group.

Models based on simple geometric considerations indicate that the propyl group in 2PP is long enough to form a secondary ringlike structure adjacent to the pyridine ring. Constraining the propyl group configuration would actually increase the energy content of the aromatic ring, which in turn could enhance the strong collisions. This scenario is in agreement with the simulation results of Bernshtein and Oref showing that collisional energy transfer from azulene(E) to benzene is larger than that for *p*-xylene(E).[149] Even though the two donors have the same number of modes, the stiffer ring system has higher mode frequencies and more vibrational energy transfer. It is not clear, however, why the simulations do not show a similar effect when argon is the quencher.

8.3.6 The Effect of State Density on Large-ΔE Energy Transfer

The role of donor state densities in the collisional relaxation of vibrationally excited azabenzenes with bath molecules has been discussed previously for non-alkylated aromatic molecules. This Chapter explores the relationship between donor state density and energy transfer for the alkylated pyridines.

Earlier studies in our laboratories and Chapter 7 have shown that the curvature of the probability distribution function for strong collisions of highly excited azabenzenes and methylated azabenzenes correlates with the energy dependence of the vibrational state density, as shown in Figure 8.9. Figure 8.9 shows that there is a linear correlation between the curvature of the probability distribution function (β_{obs}) and the curvature of the vibrational state density (β_{ρ}). Such a correlation is also seen for collisions of these donors with H_2O.[83]

Based on Fermi's Golden Rule, Mullin and co-workers proposed a model called GRETCHEN (Golden Rule Excitation Transfer in Collisions of High Energy Molecules),

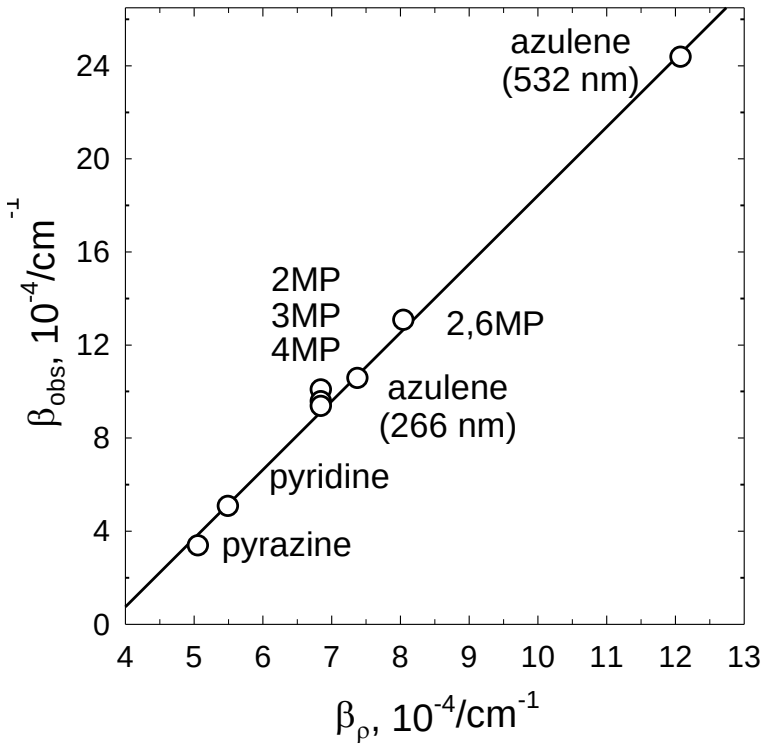

Figure 8.9 The relationship between β_{obs} for strong collisions and the vibrational state density energy dependence parameter β_{ρ} for collisions of CO_2 with highly vibrationally excited donors: pyrazine, pyridine, methylpyridine isomers (2MP, 3MP, 4MP), 2,6MP from the previous studies[83,86,88] and azulene with different internal energies (Chapter 7). For these donor-CO_2 pairs, there is a linear correlation between the parameters β_{ρ} and β_{obs}.

which describes the collisional quenching of highly vibrationally excited molecules. At the initial internal energies for three alkylated pyridine molecules, $\rho(E = 38570\ cm^{-1}) = 4.8 \times 10^{19}$ states/cm^{-1} for 2EP, $\rho(E = 38870\ cm^{-1}) = 5.2 \times 10^{25}$ states/cm^{-1} for 2PP and $\rho(E = 39123\ cm^{-1}) = 1.6 \times 10^{28}$ states/cm^{-1} for 2tBP as shown in Figure 8.10a.

The state densities for 2EP, 2tBP and 2PP molecules were determined as a function of the internal energy decrease E–ΔE in Figure 8.10a using donor vibrational frequencies and performing a direct count of states with the Beyer-Swinehart algorithm.[187] The vibrational modes of 2EP with frequencies above 200 cm^{-1} were measured by Green and Barnard.[188] However, the low-frequency modes that correspond to torsional motions of the 2t-butyl and ethyl groups were not reported. The normal modes of 2EP, 2tBP and 2PP were estimated using Hartree-Fock calculations at the 6-311G** level. At this level of theory, the calculated frequencies for normal modes do not exactly reproduce the experimental results and were adjusted using established scaling factors.[189]

Figure 8.10b shows that the state density of three donors decays nearly exponentially as a function of the loss of internal energy ΔE at ΔE = 3000 – 10000 cm^{-1}. Therefore, the state density curves in this ΔE range can be fitted by an exponential decay function as Eq 8.4.

$$\rho(E - \Delta E) = \alpha_\rho \exp\left(-\beta_\rho \Delta E\right) \tag{8.4}$$

where α_ρ is the intensity parameter and β_ρ is the shape parameter obtained by the slope of Figure 8.10b. The state density shape parameters for 2EP, 2tBP and 2PP are characterized

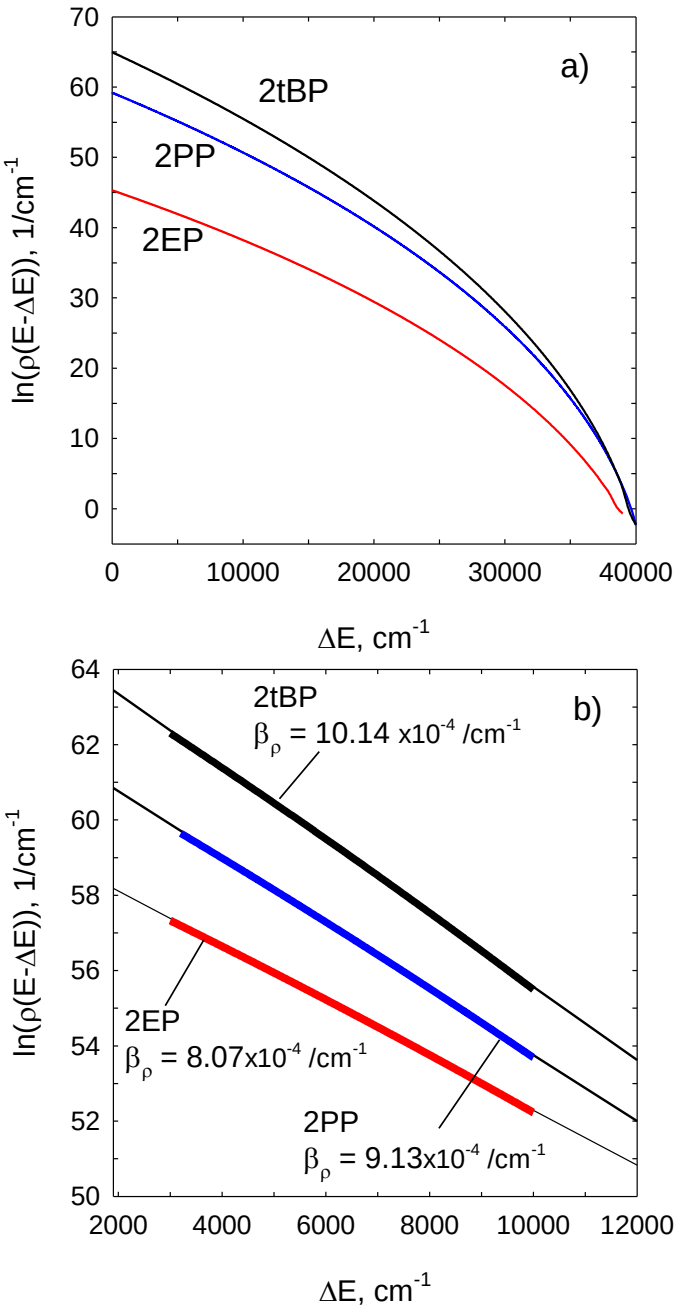

Figure 8.10 (a)The vibrational state density ρ (E–ΔE) of three alkylated pyridine molecules shown as a semilog plot. The donor molecules are initially excited to E = 38570 cm^{-1} for 2EP, E = 38870 cm^{-1} for 2PP and E= 39123 cm^{-1} for 2tBP. (b) The values of shape parameter β_ρ are from the slope of the semilog plot of ρ(E–ΔE) curves.

by β_ρ = 8.07×10^{-4}/cm^{-1} for 2EP, β_ρ = 10.14×10^{-4}/cm^{-1} for 2tBP,and β_ρ = 9.13×10^{-4}/cm^{-1} for 2PP. The ordering of the three β_ρ is 2tBP > 2PP > 2EP.

P(ΔE) curves such as those shown in Figure 8.8 characterize the probability that a vibrationally hot molecule will lose an amount of energy ΔE through collisions with CO_2. The curve for each donor is fit using a single-exponential decay with Eq 8.5.

$$(\Delta E) = \alpha_{obs}\exp(-\beta_{obs}\Delta E) \tag{8.5}$$

where α_{obs} and β_{obs} are fitting parameters. β_{obs} describes the relative weighting of weak to strong collisions for a given donor. Figure 8.11 is the semilog plot of P(ΔE) curves for three alkylpyridine/CO_2 pairs. The values of the slope are the shape parameters β_{obs}: β_{obs} = 1.53×10^{-3} /cm^{-1} for 2EP, β_{obs} = 1.29×10^{-3} /cm^{-1} for 2PP and β_{obs} = 1.32×10^{-3} /cm^{-1} for 2tBP. The ordering of β_{obs} for the three donors is 2tBP~2PP>2EP.

Figure 8.12 shows the β_{obs} values for 2EP, 2PP and 2tBP along with a number of other donor molecules: pyrazine, pyridine, azulene, methylpyridine isomers (2MP, 3MP, and 4MP), and 2,6-dimethylpyridine (2,6MP). In general, the data show that the larger donor molecules have larger values of both β_{obs} and β_ρ. For a given energy loss transition of ΔE, larger donor molecules have greater mismatches in their state densities before and after the collision. This mismatch correlates with a reduction in the likelihood of energy transfer relative to smaller ΔE values and leads to a steeper slope in lnP(ΔE) for the larger donor molecules, hence a larger β_ρ value. This behavior is evident from data for the non-alkylated and methylated donors in Figure 8.9. It is important to clarify that the data in

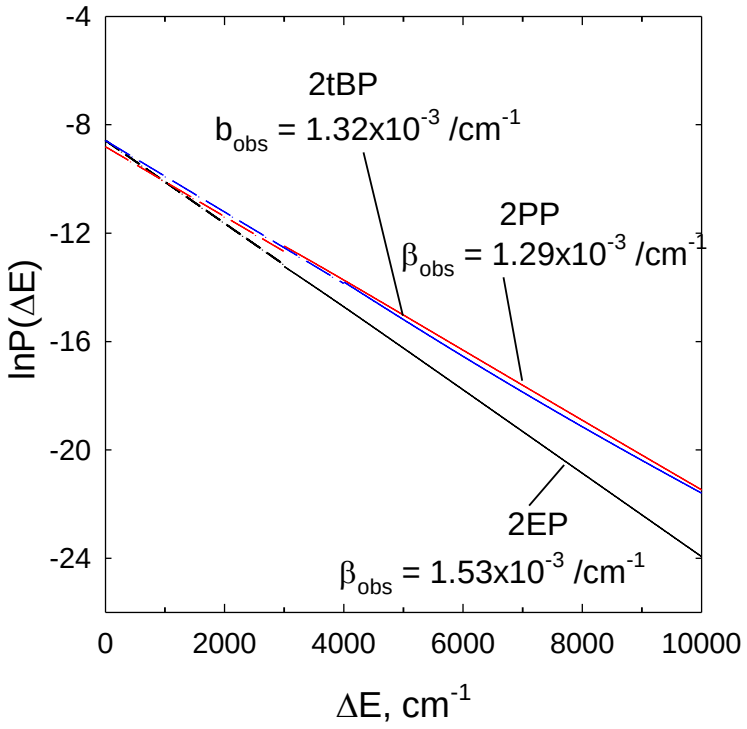

Figure 8.11 Semilog plot of P(ΔE) curve with ΔE > 3000 cm^{-1} for strong collisions of vibrationally excited 2EP, 2tBP and 2PP with CO_2. The slope of the curve is the shape parameter β_{obs}.

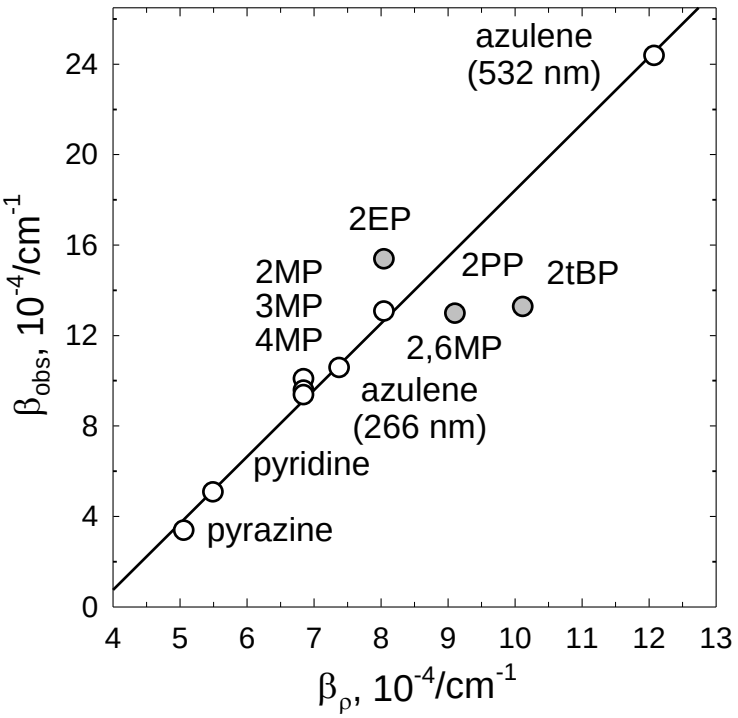

Figure 8.12 The relationship between β_{obs} for strong collisions and the vibrational state density energy dependence parameter β_ρ for collisions of CO_2 with highly vibrationally excited donors: pyrazine, pyridine, azulene with two internal energies, methylpyridine isomers (2MP, 3MP, 4MP), 2,6MP, 2EP, 2PP, and 2tBP. A linear correlation between two parameters is shown for non-alkylated donors and donors containing methyl groups. For donors with larger alkyl groups, β_{obs} no longer correlates with changes in state density associated with ΔE.

Figure 8.9 consider the *curvature* of the energy transfer distribution functions, not the absolute probability itself. At a given internal energy, larger donor molecules have high state densities and are predicted by Fermi's Golden Rule to have larger energy transfer probabilities. The experimental data in this Chapter are generally in agreement with this prediction, but more specific correlation of the energy transfer probability with the donor state density cannot be made without additional knowledge of the matrix elements that couple the initial and final states.

The correlation of β_{obs} and β_ρ for 2EP, 2PP and 2tBP in Figure 8.12 show deviations from the linear correlation seen for the non-alkylated and methylated donors. Collisions with $\Delta E > 3000$ cm^{-1} for 2EP are not as strong as predicted by the state density energy dependence and for 2PP and 2tBP the collisions are stronger than predicted. It is possible that the correlation of the probability distribution curvature (β_{obs}) correlates with state density energy dependence (β_ρ) only holds for aromatic systems with hydrogen or methyl substituents. It is also possible that dynamical effects such as large amplitude motion of longer chain alkyl groups and ring closing mechanisms are responsible for the observed deviations. Such effects are not accounted for by statistical state densities. The effect of anharmonicity was not included in the state density calculations but it is unlikely that anharmonicity would lead to the observed shifts in the β_{obs} values for 2EP, 2tBP and 2PP.

8.4 Conclusion

The effect of alkylation on the strong collisional energy transfer between CO_2 and a series of highly vibrationally excited alkylpyridines ($E \sim 38400$ cm^{-1}) where alkyl = methyl, ethyl, and propyl have been investigated. The nascent rotational and translational

energy distributions for scattered CO_2 molecules were measured under single collision conditions using high-resolution transient IR absorption. Strong collisions between pyridine and CO_2 lead to substantially more rotational and translational energy in the scattered molecules than for the alkylated donors. Differences are also seen in the distribution functions for the strong collisions of the alkylated donors. The ordering of strong collision probabilities with CO_2 is pyridine > 2MP ≈ 2PP > 2EP ≈ 2tBP. The probability for strong collisions with CO_2 is twice as large for 2PP as for 2EP and 2tBP. The Chapter's results show that longer-chain alkyl groups actually enhance strong collisional energy transfer.

Chapter 9: Conclusion

9.1 Summary and Conclusion

Understanding the collisional relaxation of highly vibrationally excited molecules is important for many situations. In this thesis, the dynamics of collisional energy transfer from vibrationally excited molecules to DCl or CO_2 baths through V→RT pathway were investigated using high-resolution transient IR absorption spectroscopy. The goal of this work was to investigate the influence of molecular structure, vibrational state density and vibrational energy on collisional energy transfer. Using this technique, detailed information about the state-resolved product distributions and rate constants for the energy transfer of the collision pairs was obtained.

Six projects were presented in this thesis. Chapters 3 to 6 studied molecular effects for the full collisional energy transfer dynamics of highly vibrational excited donors with bath molecules. Chapter 7 and Chapter 8 studied the strong collision dynamics for collision pairs.

Chapter 3 explored the full energy transfer distribution for the pyrazine(E = 37900 cm^{-1})/DCl pair. The rotational distribution of scattered DCl has a single-exponential distribution and J-dependent translational distributions are observed for this pair. A direct measurement of the collision rate is close to the predictions of the Lennard-Jones collision model. This result confirms that the V–RT pathway is a dominant channel of collision energy transfer.

Chapters 4 and 5 reported studied the weak collision dynamics of CO_2 with pyrazine(E = 32700 and 37900 cm^{-1}) respectively. The internal energy effect on the

collision dynamics of pyrazine(E)/CO_2 pair was investigated by comparing the experimental results at different internal energies. The distributions of rotational and translational energy gain of scattered CO_2 are sensitive to the internal energy of pyrazine. Increasing the internal energy reduces the probability of weak collision and induces more strong collisions. The collision rates are not sensitive to the internal energies. The average collision energy is reduced when the internal energy decreases by 15%.

The influence of molecular structure for the donor molecules is addressed in Chapter 6. This Chapter reported the weak collision dynamics of 2-methylpyridine (E = 37900cm^{-1})/CO_2, 2,6-dimethylpyridine(E = 38300 cm^{-1})/CO_2 and 3,5-demethylpyridine(E = 38300 cm^{-1})/CO_2 systems. Combined with the previous strong collision results, full energy transfer distributions were obtained. The collision results are affected by the number of methyl groups, but not by the position of the methyl groups. Biexponential rotational distributions of scattered CO_2 through collisions with donors were observed. Donor methylation increased the appearance collision rates for different collision systems.

In Chapter 7, the effect of internal energy on strong collisions was measured for collisions of azulene(E = 20390 and 38580 cm^{-1}) with CO_2. The V−RT channel is such sensitive to the internal energy of azulene molecule. The average rotational and translational energies of the scattered CO_2 molecules double when the azulene energy is increased by a factor of 2. The rate of energy transfer into strong collisions increases by nearly a factor of 4 when the azulene energy is doubled. The curvatures of the energy transfer probability distribution functions for $\Delta E > 3000$ cm^{-1} at different initial energies correlate with the energy dependence of the state density, in excellent agreement with

predictions from GRETCHEN theory for describing collisional quenching of highly excited molecules.

The effect of alkylation on strong collisions was studied in Chapter 8. The experimental data for 2-ethylpyridine(E = 38570 cm^{-1})/CO_2, 2-propylpyridine(E = 38870 cm^{-1})/CO_2 and 2-t-butylpyridine(E = 39123 cm^{-1})/CO_2 pairs are compared pyridine (E_{vib}=37920 cm^{-1}) and 2-methylpyridine data from our group's previous projects. Alkylation of donors decreases the rotational and translational energy of scattered CO_2 molecules. Strong collisions are reduced for donors with alkyl chains by lowering the average energy per mode but longer alkyl chain have increased flexibility and higher state densities that enhance energy loss via strong collisions.

9.2 Future Directions

This thesis has presented new insights into the dynamics of collisional quenching of highly vibrationally excited molecules. This thesis helped us to understand how the properties of excited molecules play roles in the collision quenching. These properties include the internal energy, state density, and structure. This thesis also suggests new areas for future research.

The Chapters about the influence of donor structure for the collision quenching of collision system studied the effect of alkylation. How the isotopic substitution of donor molecules affects the collision energy transfer is another interesting topic. Before this project, our group measured the collision dynamics of pyridine-h_5, d_5 and f_5 with HOD as the bath molecule. Due to H-bonding interactions between donor and bath molecules, the experimental collision rates for these systems are several times larger than the Lennard-Jones collision rates. It will be interesting to measure the collisional dynamics of highly

vibrationally excited pyridine-h_5, d_5 and f_5 with CO_2, where hydrogen bonding interactions are not present.

The project on strong collisions of azulene/CO_2 pairs with different internal energies shows us that state-resolved translational energy gain of CO_2 is dependent on the internal energy and that there should be a threshold for this translational distribution. The thresholds at different CO_2 rotational energies were estimated at J_{et} = 62 for azulene(E = 20390 cm^{-1}) and J_{et} = 34 for azulene(E = 38580 cm^{-1}). Due to the experimental full energy transfer results for pyrazine and alkylpyridine (E)/CO_2 pairs, two translational energy distributions for scattered CO_2 through collisions with donor molecules were obtained and the crossing points were found to be in the range J = 50–60. An interesting question is why the two thresholds for CO_2/azulene collisions are different for different azulene energies. In addition, the appearance collision rate for the azulene/CO_2 pair with different internal energies still has not been measured because of the lack of weak collision measurements at CO_2 low-J states. It will be very important to measure the weak collision dynamics for CO_2/azulene pair.

Appendix A: Absorption Frequencies, Rotational Energies, and Transition Intensities for the R Branch of the IR Fundamental of $D^{35}Cl$ and $D^{37}Cl$

The DCl bath molecule was probed following collisions with highly excited pyrazine molecules using high-resolution transient IR absorption spectroscopy in Chapter 3. DCl has two isotopes: $D^{35}Cl$ and $D^{37}Cl$. For IR probing of DCl molecules in specific rotational states, this Appendix collects the information on IR frequencies ν_0, rotational energies E_{rot} and absorption intensities S_J for the two isotopes.

The IR absorption frequencies ν_0 for DCl molecules were determined by Parekunnel and co-workers.[123] Rotational energies of DCl (v = 0) are determined using Eq A.1.

$$E_{rot} = B_0[J(J+1)] - D_0[J(J+1)]^2 + H_0[J(J+1)]^3 + L_0[J(J+1)]^4 \quad (A.1)$$

For the ^{35}Cl isotope, B_0 = 5.39227196(40) cm^{-1}, D_0 = 1.39955(3) × 10^{-4} cm^{-1}, H_0 = 2.282(8) × 10^{-9} cm^{-1}, and L_0 = –5.8(5) × 10^{-14} cm^{-1}. For the ^{37}Cl isotope, B_0 = 5.3764904(2) cm^{-1}, D_0 = 1.31341(21) × 10^{-4} cm^{-1}, H_0 = 2.2646(65) × 10^{-9} cm^{-1}, and L_0 = –6.0(5)×10^{-14} cm^{-1}.[123] The absorption line strength S_J of the DCl molecule is a function of the line strength S_{ji}, which is the absorption from a lower state j to an upper state i. The line strength S_{ji} is related to the Einstein coefficient B_{ji} for spontaneous emission as Eq A.2.[124,178]

$$S_{ji} = \frac{8\pi^3}{3hc} \cdot v_0 \cdot \frac{I_a g_i e^{-E_i/kT}}{Q} \cdot \left(1 - e^{-v_0/kT}\right) \cdot \frac{3h^2}{8\pi^3} B_{ji} \qquad \text{(A.2)}$$

Eq A2 is taken from Ref 124. Here I_a is the naturally-occurring isotopic abundance for chlorine (0.754 for $D^{35}Cl$ and 0.246 for $D^{37}Cl$); g_i is the degeneracy of the upper state; E_j is the energy of the lower state; c is the speed of light; and Q is the partition function. The Einstein B_{ji} coefficient is related to the A_{ij} coefficient spontaneous emission as shown in Eq A.3:

$$B_{ji} = \frac{g_i}{g_j} \cdot \frac{A_{ij}\lambda^3}{8\pi h} \qquad \text{(A.3)}$$

Values for the A_{ij} were determined by Setser and co-workers.[122,178] The R-branch probe transition for rotational states of DCl are listed in Table A.1.

Table A.1 IR probe transients for rotational states of DCl. DCl (v = 0, J) + hν (λ ~ 4.3 μm) → DCl (v = 1, J+1)

	$D^{35}Cl$ (0–1)			$D^{35}Cl$ (0–1)		
J	ν_0 ,cm^{-1}	E_{rot} ,cm^{-1}	S_J, cm $molecule^{-1}$	ν_0 ,cm^{-1}	E_{rot} ,cm^{-1}	S_J, cm $molecule^{-1}$
0	2101.6178	0.0000	6.4880×10^{-20}	2098.5880	0.0000	2.1136×10^{-20}
1	2111.9488	10.7840	1.2150×10^{-19}	2108.8890	10.7524	3.9587×10^{-20}
2	2122.0483	32.3486	1.6190×10^{-19}	2118.9600	32.2539	5.2784×10^{-20}
3	2131.9131	64.6871	1.8210×10^{-19}	2128.7980	64.4979	5.9385×10^{-20}
4	2141.5398	107.7895	1.8220×10^{-19}	2138.3980	107.4742	5.9459×10^{-20}
5	2150.9255	161.6423	1.6620×10^{-19}	2147.7580	161.1696	5.4257×10^{-20}
6	2160.0668	226.2287	1.3980×10^{-19}	2156.8750	225.5673	4.5699×10^{-20}
7	2168.9608	301.5287	1.0940×10^{-19}	2165.7460	300.6475	3.5802×10^{-20}
8	2177.6042	387.5189	8.0040×10^{-20}	2174.3680	386.3869	2.6218×10^{-20}
9	2185.9942	484.1725	5.4910×10^{-20}	2182.7370	482.7588	1.8009×10^{-20}
10	2194.1277	591.4595	3.5410×10^{-20}	2190.8510	589.7334	1.1633×10^{-20}
11	2202.0018	709.3466	2.1510×10^{-20}	2198.7060	707.2777	7.0792×10^{-21}
12	2209.6136	837.7971	1.2330×10^{-20}	2206.3010	835.3551	4.0649×10^{-21}
13	2216.9602	976.7713	6.6760×10^{-21}	2213.6310	973.9262	2.2051×10^{-21}
14	2224.0389	1126.2261	3.4180×10^{-21}	2220.6950	1122.9480	1.1312×10^{-21}
15	2230.8468	1286.1152	1.6560×10^{-21}			
16	2237.3819	1456.3891	7.5970×10^{-22}			
17	2243.6368	1636.9953	3.3040×10^{-22}			
18	2249.6208	1827.8778	1.3620×10^{-22}			

19	2255.3204	2028.9779	5.3320×10^{-23}	
20	2260.7348	2240.2334	1.9810×10^{-23}	
21	2265.8624	2461.5795	6.9920×10^{-24}	

Appendix B: Lennard-Jones Collision Model Calculation

There are a number of theories to describe the rate constant of bimolecular collisions. The model used in this thesis is Lennard-Jones model.[190]

The Lennard-Jones model includes long-range attractive forces and short-range repulsive forces using the Lennard-Jones potential (Eq B.1).

$$V(r)=4\varepsilon\left\{\left(\frac{\sigma}{r}\right)^{12}-\left(\frac{\sigma}{r}\right)^{6}\right\} \tag{B.1}$$

This thesis uses the Lennard-Jones model to calculate the collision rate for several collision systems. The Lennard-Jones collision rate includes the collision cross section σ and potential well ε for collision pairs at room temperature, as in Eq B.2.

$$k_{LJ}=\left(\frac{8k_BT}{\pi\mu}\right)^{\frac{1}{2}}\cdot\Omega^{(2,2)^*}\cdot\pi\sigma^2 \tag{B.2}$$

where, $\Omega^{(2,2)^*}$ is the collision integral, k_B is Boltzmann's constant and σ is the Lennard-Jones parameter.

The collision integral $\Omega^{(2,2)^*}$ is a function of the reduced temperature T*, Eq B.3.

$$\Omega^{(2,2)^*}=1.16145\left(T^*\right)^{-0.14874}+0.52487\exp\left\{-0.7732T^*\right\}+2.16178\exp\left\{-2.43787T^*\right\} \tag{B.3}$$

The reduced temperature T* is obtained from Eq B.4.

$$T^{*}= \frac{k_B T}{\varepsilon} \tag{B.4}$$

The Lennard-Jones parameters σ and ε/k_B for the mixed donor/bath systems are obtained using established combining rules, which are shown as Eq B.5 and B.6, respectively.[190]

$$\sigma= \frac{1}{2} (\sigma_{donor}+ \sigma_{bath}) \tag{B.5}$$

$$(\varepsilon/k_B)= \left(\left(\frac{\varepsilon}{k_B}\right)_{donor} \times \left(\frac{\varepsilon}{k_B}\right)_{bath}\right)^{\frac{1}{2}} \tag{B.6}$$

The Lennard-Jones parameters for two bath molecules in thesis are taken from the literature, and are shown in Table B.1.

Two methods are used here to obtain the Lennard-Jones parameters for donor molecules. Parameters for pyridine, 2MP and azulene come from critical temperatures T_c and critical volume V_c.[191] Lennard-Jones parameter values for 2EP, 2PP, 2,6MP and 3,5MP could not be found in the literature, therefore, these values were estimated based other related donors.

Values of σ and ε for 2EP, 2PP, 2,6MP and 2tBP were estimated based on data for pyridine and 2MP values and trends in benzene series[192] and cyclopentane series[192] as shown in Figure B.1. Critical temperatures T_c and critical volume V_c of all molecules are

Table B.1 Lennard-Jones parameters for CO_2 and DCl bath molecules.

	σ, nm	ε/k_B, K
CO_2	0.45[a]	190[a]
DCl	0.34[b]	328[c]

[a]Two Lennard-Jones parameters of CO_2 are from Ref. 187.

[b]The Lennard-Jones parameter σ of DCl is from Ref. 124.

[c]The Lennard-Jones parameter ε/k_B is from Ref. 125.

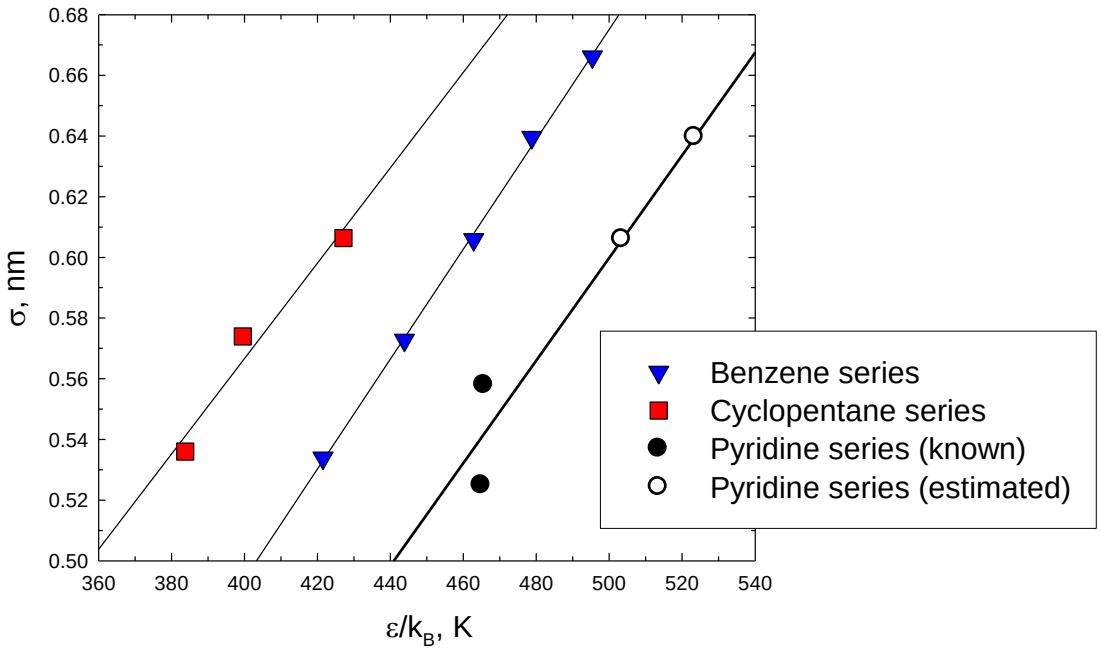

Figure B.1 The linear relationship between σ and ε/k_B for two series of alkylated cyclic molecules (benzene and cyclopentane) is used to estimate parameters for alkylated pyridines with CO_2. Blue triangles are for the benzene series: (in order from lower to higher ε/k_B) benzene, methylbenzene, ethylbenzene, propylbenzene and butylbenzene.[192] Red squares are for the cyclopentane series: (in order from lower to higher ε/k_B) cyclopentane, methyl-cyclopentane and ethyl-cyclopentane.[192]

Black circles are for the pyridine series, with open circles for estimated values for 2EP and 2PP. The pyridine series is assumed to have a similar linear relationship as the other ring molecules and a slope that is the average of the benzene and cyclopentane values. σ values for 2EP and 2PP are assumed to be the same as for the ring molecules with the same alkyl chains.

listed in Table B.2.

Two Lennard-Jones parameters, σ and ε/k_B, for the donor molecules are calculated using Eq B.7 and B.8.[193]

$$\sigma^3 \approx \frac{9}{8}\frac{v_C}{\pi N_A} \tag{B.7}$$

$$\varepsilon \approx \frac{3}{4}\, T_c \tag{B.8}$$

where N_A is Avogadro's number. Lennard-Jones collision rate constants k_{LJ} for collision systems in this thesis are shown in Table B.3.

Table B.2 Critical temperature T_c and critical volume V_c of molecules.

Molecule	T_c, K[a]	V_c, cm^{3a}
Pyridine	620	243
2-methyl-pyridine	621	292
2,6-methyl-pyridine	623.8	343[b]
Benzene	562.16	259
Methyl-benzene	591.8	316
Ethyl-benzene	617.2	374
Propyl-benzene	638.32	440
Butyl-benzene	660.5	497
Cyclopentane	511.7	260
Methyl-cyclopentane	532.73	319
Ethyl-cyclopentane	569.5	375
Azulene	795.8[c]	406[c]

[a]Data are from Ref. 188.

[b]The cristal volume V_c for a,6MP are estimated from extrapolation of V_c for pyridine and 2MP.

[c]Data are Ref. 50.

Table B.3 Lennard-Jones collision rate constants for collision pairs in this thesis.

Collision pair	σ_{donor}, nm	σ_{DB}, nm[a]	$(\varepsilon/k_B)_{donor}$, K	$(\varepsilon/k_B)_{DB}$, K[b]	k_{LJ}, 10^{-10} cm^3 $molecule^{-1}$ s^{-1}[c]
Pyz:DCl	0.535	0.436	435.5	377.9	5.40
Pyz:CO_2	0.535	0.492	435.5	287.7	5.60
Pyr:CO_2	0.523	0.487	465.0	297.2	5.58
2MP:CO_2	0.558	0.504	465.7	297.5	5.86
2EP:CO_2	0.606	0.528	503.5	309.3	6.39
2PP:CO_2	0.640	0.545	523.5	315.4	6.76
2tBP:CO_2	0.670	0.558	539	320.0	7.05
2,6MP:CO_2	0.589	0.520	467.9	298.2	5.80
Azu:CO_2	0.661	0.555	532	317.9	6.40

[a] LJ parameter σ_{DB} for donor/bath pair.

[b] LJ parameter $(\varepsilon/k_B)_{DB}$ for donor/bath pair.

Appendix C: The Residual test for Double-Gaussian Fitting Model

The number density of scattered bath molecules in a given rotational state after collisions with vibrationally excited donors is from two processes, appearance and depletion. The best fitting model for the experimental Doppler broadened line profiles is a double-Gaussian function that is the sum of two Gaussian functions, as shown in Eq C.1.

$$y = a\cdot\exp\left[-4\ln 2\left(\frac{x-x_0}{b}\right)^2\right] - c\cdot\exp\left[-4\ln 2\left(\frac{x-x_0}{d}\right)^2\right] + y_0 \qquad (C.1)$$

where, a and c are the amplitudes and b and d are the linewidths for each Gaussian, y_0 is a base line correction and $x-x_0$ is the deviation from the peak center. The double-Gaussian function includes six parameters: a, b, c, d, x_0 and y_0. In the upper plot of Figure C.1, the experimental data (eg: DCl (J = 5) for pyrazine(E = 37900 cm^{-1})/DCl pair) are fit by the double-Gaussian function without any constraints, as shown by a solid line. The fitting results of six parameters are also shown in upper plot. The lower plot illustrates the residual value for the fit. The residual value is the difference between the experimental data and the fitting data.

The residual value is a useful factor that evaluates the goodness of fit. Here the goodness of the double-Gaussian fit is tested. First, x_0 and y_0 are minor offsets and shifting the data reduces the number of fitting parameters to 4. In this test, one of the other four parameters (a, b, c or d) is constrained to a fixed value and a set of fitting

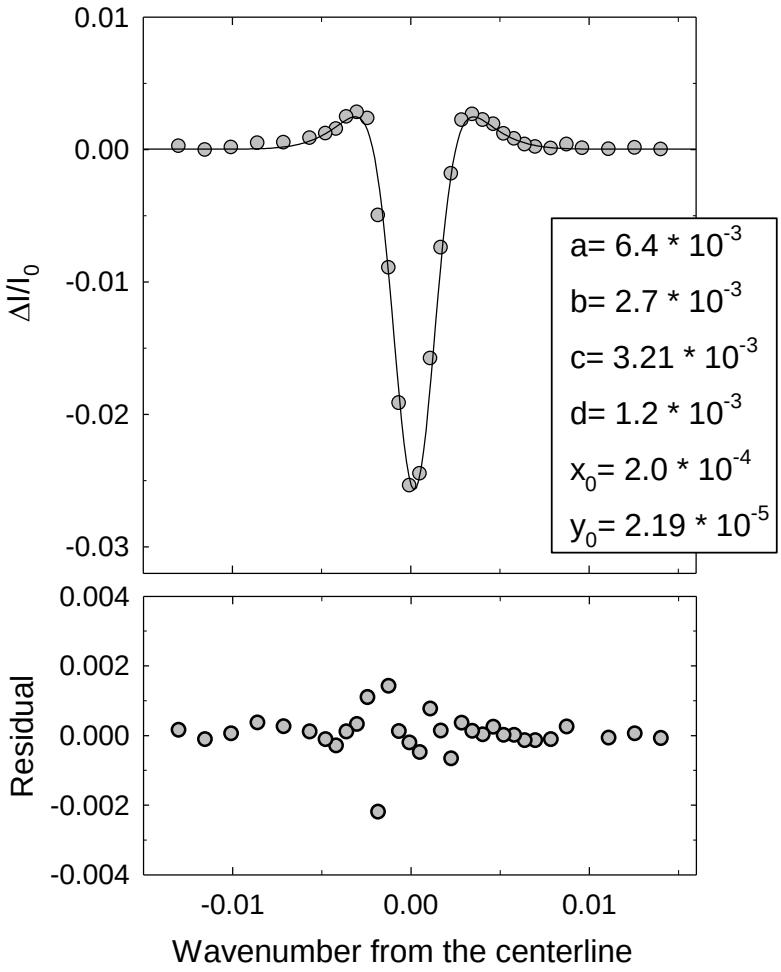

Figure C.1 The experimental data for DCl (J = 5) from collisions with vibrationally excited pyrazine are fitted by a double-Gaussian function. The data are illustrated as grey circles and the fitting result is shown as a solid line. One set of fitting results for six parameters are also shown in the upper plot. The residual value for each point is shown as the grey circles in the lower plot.

of fitting parameters and residuals are obtained for a 3-parameter.

The sum of residual values at different fixed values of parameter a are shown in Figure C.2a. Figure C.2a shows the residual data by scanning the value of parameter a with small steps in a reasonable range. The best fit has the smallest residual. There is a single minimum for the residual sum indicating the best fit for parameter a. In other two plots of Figure C.2, parameters b and c are checked individually. There is only one point with smallest residual for each plot. At the best fitting point for each fixed parameter, the fitting results of four parameters are all similar as the fitting data without any constraints in Figure C.1.

Due to this test, the fit results of the Double-Gaussian function without constraints in Figure C.1 are the best and unique fit values.

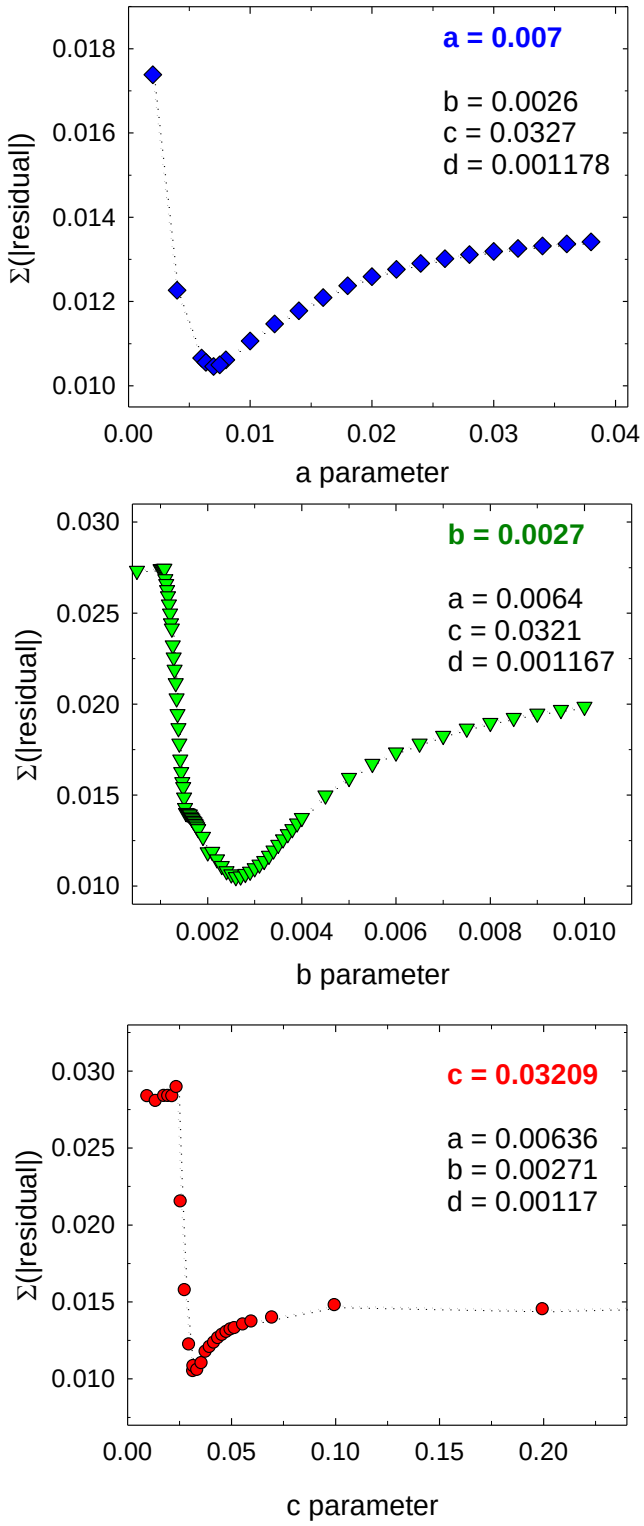

Figure C.2 The sum of residuals based on 3 parameters fitting with one parameter constained.

Appendix D: A Two-Component Fitting Model with Constraints

The weak collision research in Chapter 3 to Chapter 6 helps us to open a new door to understand the collisional quenching dynamics for two molecules. Since the populations in specific J states are the products of weak and strong collisions, we need to find a good model to fit the experimental data and separate the two processes. This thesis chooses a two-component model for fitting the data shown as Eq. D.1.

$$Pop_J = g_J \left[I_a \exp\left(\frac{-E_J}{k_B T_a}\right) + I_b \exp\left(\frac{-E_J}{k_B T_b}\right) \right] \quad \text{(D.1)}$$

where g_J is the rotational degeneracy; E_J is the rotational energy; T_a and T_b are rotational temperatures; I_a and I_b are the intensity parameters. This model successfully fit pyrazine/CO_2 pair and 2,6MP/CO_2 pair (Chapter 4, Chapter 5 and Chapter 6) data without any constraints. However, this model cannot fit 2MP/CO_2 and 3,5MP/CO_2 without constraints. The way to obtain the best fitting results by finding the smallest residual values.

In one limit, weak collisions can be treated as elastic collisions, and the cold population temperature is estimated to be T_a = 300 K. The number of parameter drops to three. Two ways are then used to find the smallest residuals: changing the ratio of two intensity parameters I_a:I_b and tuning the value of the other temperature parameter T_b.

The experimental data for 2MP/CO_2 pair are fitted by Eq D.1 at different ratios of I_a:I_b. The fitting results for four parameters and constraints are listed in Table D.1.

Table D.1 The two-component model fitting constraints and fitting results of CO_2 with donors (2MP and 3,5MP).

Donor	constraints		T_a[a]	T_b	$I_a \times 10^{10}$	$I_b \times 10^{10}$	Cold%[b]	Hot%[c]
	T_b	400	300	400	7.28	1.24	81.5%	18.5%
3,5MP		500	300	500	7.28	1.24	81.5%	18.5%
		550	300	550	7.7	7.48	84.9%	15.1%
		600	300	600	7.82	6.35	86.0%	14.0%
		650	300	650	7.92	5.38	87.2%	12.8%
		700	300	700	8.02	4.58	88.3%	11.7%
		800	300	800	8.17	3.39	90.0%	10.0%
2MP	I_a:I_b	4:1	300	643	4.63	1.16	65.1%	34.9%
		2:1	300	559	3.78	1.89	51.7%	48.3%
		3:1	300	605	4.31	1.44	59.8%	40.2%
		7:3	300	576	3.99	1.71	54.9%	45.1%
		73:27	300	592	4.18	1.55	57.8%	42.2%

[a]The colder temperature Ta in K is fixed at room temperature for the two-component mode.

[b]The percent of cold distribution for the whole observed distribution.

[c]The percent of hot distribution for the observed distribution.

At a given value of I_a:I_b, one set of fitting residuals is obtained in Figure D.1. Figure D.1a shows that smallest residuals are at I_a:I_b = 7.3:2.7. The fitting results of this collision pairs are chosen at this smallest residual place.

For 3,5MP/CO_2 pair, we tune the values of another temperature parameter, T_b. The constraint values of T_b and fitting results are listed in Table D.1. The smallest residual is at T_b = 600 K from Figure D.1b. The smallest residual represents the bet fit for the bi-exponential distribution.

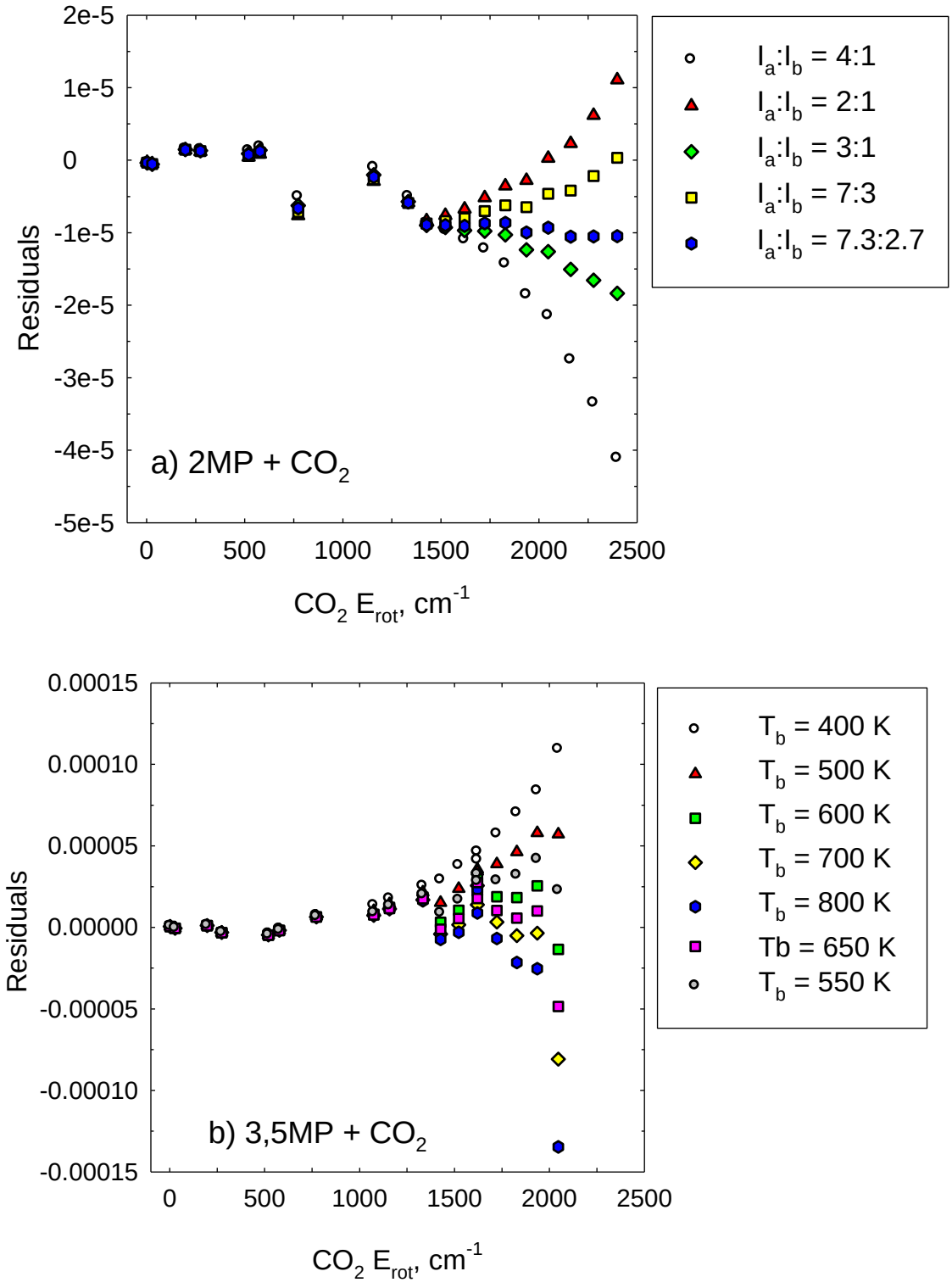

Figure D.1 The residuals for fitting results of the two-component mode at different constraints.

Bibliography

(1) Lindemann, F. A. *Trans. Faraday Soc.* **1922**, *17*, 598.

(2) *Unimolecular Reaction Dynamics: Theory and Experiments*; Baer, T.; Hase, L. M., Eds.; Oxford University Press: New York, 1996.

(3) Barker, J. R.; Yoder, L. M.; King, K. D. *J. Phys. Chem. A* **2001**, *105*, 796.

(4) Flynn, G. W.; Parmenter, C. S.; Wodtke, A. M. *J. Phys. Chem.* **1996**, *100*, 12817.

(5) Oref, I.; Tardy, D. C. *Chem. Rev.* **1990**, *90*, 1407.

(6) Tardy, D. C.; Rabinovitch, B. S. *Chem. Rev.* **1977**, *77*, 369.

(7) Krajnovich, D. J.; Parmenter, C. S.; Catlett, D. L. *Chem. Rev.* **1987**, *87*, 237.

(8) Weston, R. E.; Flynn, G. W. *Annu. Rev. Phys. Chem.* **1992**, *43*, 559.

(9) *Molecular Energy Transfer in Gases*; Cottrell, T. L.; C., M. J., Eds.; Butterworths Scientific: London, 1961.

(10) *Introduction to Molecular Energy Transfer*; Yardley, J. T., Ed.; Academic: New York, 1980.

(11) Keeton, R. G.; Bass, H. E. *J. Acoust. Soc. Am.* **1976**, *60*, 78.

(12) *Unimolecular Reactions*; Robinson, P. J.; Holbrook, K. A., Eds.; Wiley-Interscience: London, 1972.

(13) Troe, J. *J. Chem. Phys.* **1977**, *66*, 4745.

(14) Troe, J. *J. Chem. Phys.* **1977**, *66*, 4758.

(15) Chan, S. C.; Rabinovi.Bs; Bryant, J. T.; Spicer, L. D.; Fujimoto, T.; Lin, Y. N.; Pavlou, S. P. *J. Phys. Chem.* **1970**, *74*, 3160.

(16) Snavely, D. L.; Zare, R. N.; Miller, J. A.; Chandler, D. W. *J. Phys. Chem.* **1986**, *90*, 3544.

(17) Kohlmaier, G. H.; Rabinovitch, B. S. *J. Chem. Phys.* **1963**, *38*, 1692.

(18) Kohlmaier, G. H.; Rabinovitch, B. S. *J. Chem. Phys.* **1963**, *38*, 1709.

(19) Simons, J. W.; Rabinovitch, B. S.; Setser, D. W. *J. Chem. Phys.* **1964**, *41*, 800.

(20) Tardy, D. C.; Rabinovi.Bs; Larson, C. W. *J. Chem. Phys.* **1966**, *45*, 1163.

(21) Serauska.Rv; Schlag, E. W. *J. Chem. Phys.* **1965**, *42*, 3009.

(22) Valance, W. G.; Schlag, E. W. *J. Chem. Phys.* **1966**, *45*, 216.

(23) Weyssenh.Hv; Schlag, E. W. *J. Chem. Phys.* **1973**, *59*, 729.

(24) Nordholm, S.; Freasier, B. C.; Jolly, D. L. *Chem. Phys.* **1977**, *25*, 433.

(25) Freasier, B. C.; Jolly, D. L.; Nordholm, S. *Chem. Phys.* **1978**, *32*, 161.

(26) Schranz, H. W.; Nordholm, S. *Int. J. Chem. Kinet.* **1981**, *13*, 1051.

(27) Nilsson, D.; Nordholm, S. *J. Chem. Phys.* **2002**, *116*, 7040.

(28) Nilsson, D.; Nordholm, S. *J. Chem. Phys.* **2003**, *119*, 11212.

(29) Lenzer, T.; Luther, K.; Nilsson, D.; Nordholm, S. *J. Phys. Chem. B* **2005**, *109*, 8325.

(30) Nilsson, D.; Nordholm, S. *J. Phys. Chem. A* **2006**, *110*, 3289.

(31) Lendvay, G.; Schatz, G. C. *J. Chem. Phys.* **1993**, *98*, 1034.

(32) Lendvay, G.; Schatz, G. C.; Harding, L. B. *Faraday Discuss.* **1995**, *102*, 389.

(33) Clarke, D. L.; Oref, I.; Gilbert, R. G.; Lim, K. F. *J. Chem. Phys.* **1992**, *96*, 5983.

(34) Lim, K. F.; Gilbert, R. G. *J. Phys. Chem.* **1990**, *94*, 77.

(35) Lim, K. F. *J. Chem. Phys.* **1994**, *100*, 7385.

(36) Linhananta, A.; Lim, K. F. *Phys. Chem. Chem. Phys.* **2002**, *4*, 577.

(37) Bernshtein, V.; Oref, I. *J. Phys. Chem. A* **2004**, *108*, 8131.

(38) Bernshtein, V.; Oref, I. *J. Chem. Phys.* **2006**, *125*, 133105.

(39) Lenzer, T.; Luther, K.; Troe, J.; Gilbert, R. G.; Lim, K. F. *J. Chem. Phys.* **1995**, *103*, 626.

(40) Lenzer, T.; Luther, K. *Ber. Bunsen. Phys. Chem.* **1997**, *101*, 581.

(41) Grigoleit, U.; Lenzer, T.; Luther, K. *Z. Phys. Chem.* **2000**, *214*, 1065.

(42) Yoder, L. M.; Barker, J. R. *J. Phys. Chem. A* **2000**, *104*, 10184.

(43) Higgins, C. J.; Chapman, S. *J. Phys. Chem. A* **2004**, *108*, 8009.

(44) Higgins, C.; Ju, Q.; Seiser, N.; Flynn, G. W.; Chapman, S. *J. Phys. Chem. A* **2001**, *105*, 2858.

(45) Li, Z. M.; Sansom, R.; Bonella, S.; Coker, D. F.; Mullin, A. S. *J. Phys. Chem. A* **2005**, *109*, 7657.

(46) Hippler, H.; Troe, J.; Wendelken, H. J. *Chem. Phys. Lett.* **1981**, *84*, 257.

(47) Hippler, H.; Luther, K.; Troe, J.; Wendelken, H. J. *J. Chem. Phys.* **1983**, *79*, 239.

(48) Hippler, H.; Troe, J.; Wendelken, H. J. *J. Chem. Phys.* **1983**, *78*, 5351.

(49) Heymann, M.; Hippler, H.; Troe, J. *J. Chem. Phys.* **1984**, *80*, 1853.

(50) Hippler, H.; Lindemann, L.; Troe, J. *J. Chem. Phys.* **1985**, *83*, 3906.

(51) Hippler, H.; Otto, B.; Troe, J. *Ber. Bunsen. Phys. Chem.* **1989**, *93*, 428.

(52) Troe, J. *J. Chem. Phys.* **1992**, *97*, 288.

(53) Barker, J. R. *J. Phys. Chem.* **1984**, *88*, 11.

(54) Toselli, B. M.; Barker, J. R. *J. Chem. Phys.* **1991**, *95*, 8108.

(55) Toselli, B. M.; Barker, J. R. *J. Chem. Phys.* **1992**, *97*, 1809.

(56) Miller, L. A.; Barker, J. R. *J. Chem. Phys.* **1996**, *105*, 1383.

(57) Miller, L. A.; Cook, C. D.; Barker, J. R. *J. Chem. Phys.* **1996**, *105*, 3012.

(58) Barker, J. R.; Toselli, B. M. *Int. Rev. Phys. Chem.* **1993**, *12*, 305.

(59) Toselli, B. M.; Brenner, J. D.; Yerram, M. L.; Chin, W. E.; King, K. D.; Barker, J. R. *J. Chem. Phys.* **1991**, *95*, 176.

(60) Brenner, J. D.; Erinjeri, J. P.; Barker, J. R. *Chem. Phys.* **1993**, *175*, 99.

(61) Hartland, G. V.; Qin, D.; Dai, H. L. *J. Chem. Phys.* **1994**, *101*, 8554.

(62) Hartland, G. V.; Qin, D.; Dai, H. L. *J. Chem. Phys.* **1994**, *100*, 7832.

(63) Hartland, G. V.; Qin, D.; Dai, H. L. *J. Chem. Phys.* **1995**, *102*, 8677.

(64) Grigoleit, U.; Lenzer, T.; Luther, K.; Mutzel, M.; Takahara, A. *Phys. Chem. Chem. Phys.* **2001**, *3*, 2191.

(65) Hold, U.; Lenzer, T.; Luther, K.; Symonds, A. C. *J. Chem. Phys.* **2003**, *119*, 11192.

(66) Hold, U.; Lenzer, T.; Luther, K.; Reihs, K.; Symonds, A. C. *J. Chem. Phys.* **2000**, *112*, 4076.

(67) Lenzer, T.; Luther, K.; Reihs, K.; Symonds, A. C. *J. Chem. Phys.* **2000**, *112*, 4090.

(68) Frerichs, H.; Hollerbach, M.; Lenzer, T.; Luther, K. *J. Phys. Chem. A* **2006**, *110*, 3179.

(69) Liu, C. L.; Hsu, H. C.; Lyu, J. J.; Ni, C. K. *J. Chem. Phys.* **2006**, *124*, 054302.

(70) Liu, C. L.; Hsu, H. C.; Lyu, J. J.; Ni, C. K. *J. Chem. Phys.* **2006**, *125*, 204309.

(71) Hsu, H. C.; Lyu, J. J.; Liu, C. L.; Huang, C. L.; Ni, C. K. *J. Chem. Phys.* **2006**, *124*, 134303.

(72) Bernshtein, V.; Oref, I.; Liu, C. L.; Hsu, H. C.; Ni, C. K. *Chem. Phys. Lett.* **2006**, *429*, 317.

(73) Liu, C. L.; Hsu, H. C.; Lyu, J. J.; Ni, C. K. *J. Chem. Phys.* **2005**, *123*, 131102.

(74) Michaels, C. A.; Mullin, A. S.; Park, J.; Chou, J. Z.; Flynn, G. W. *J. Chem. Phys.* **1998**, *108*, 2744.

(75) Wall, M. C.; Lemoff, A. S.; Mullin, A. S. *J. Phys. Chem. A* **1998**, *102*, 9101.

(76) Wall, M. C.; Mullin, A. S. *J. Chem. Phys.* **1998**, *108*, 9658.

(77) Wall, M. C.; Lemoff, A. E.; Mullin, A. S. *J. Chem. Phys.* **1999**, *111*, 7373.

(78) Havey, D. K.; Liu, Q. N.; Li, Z. M.; Elioff, M.; Fang, M.; Neudel, J.; Mullin, A. S. *J. Phys. Chem. A* **2007**, *111*, 2458.

(79) Havey, D. K.; Liu, Q. N.; Li, Z. M.; Elioff, M.; Mullin, A. S. *J. Phys. Chem. A* **2007**, *111*, 13321.

(80) Liu, Q. N.; Havey, D. K.; Mullin, A. S. *J. Phys. Chem. A* **2008**, *112*, 9509.

(81) Havey, D. K.; Liu, Q. N.; Li, Z.; Mullin, A. S. *J. Phys. Chem. A* **2009**, *113*, 4387.

(82) Elioff, M. S.; Sansom, R. L.; Mullin, A. S. *J. Phys. Chem. A* **2000**, *104*, 10304.

(83) Elioff, M. S.; Fang, M.; Mullin, A. S. *J. Chem. Phys.* **2001**, *115*, 6990.

(84) Elioff, M. S.; Fang, M.; Mullin, A. S. *J. Chem. Phys.* **2002**, *117*, 6880.

(85) Park, J.; Li, Z. M.; Lemoff, A. S.; Rossi, C.; Elioff, M. S.; Mullin, A. S. *J. Phys. Chem. A* **2002**, *106*, 3642.

(86) Park, J.; Shum, L.; Lemoff, A. S.; Werner, K.; Mullin, A. S. *J. Chem. Phys.* **2002**, *117*, 5221.

(87) Li, Z. M.; Korobkova, E.; Werner, K.; Shum, L.; Mullin, A. S. *J. Chem. Phys.* **2005**, *123*, 174306/1.

(88) Miller, E. M.; Murat, L.; Bennette, N.; Hayes, M.; Mullin, A. S. *J. Phys. Chem. A* **2006**, *110*, 3266.

(89) Michaels, C. A.; Flynn, G. W. *J. Chem. Phys.* **1997**, *106*, 3558.

(90) Mullin, A. S.; Park, J.; Chou, J. Z.; Flynn, G. W.; Weston, R. E. *Chem. Phys.* **1993**, *175*, 53.

(91) Mullin, A. S.; Michaels, C. A.; Flynn, G. W. *J. Chem. Phys.* **1995**, *102*, 6032.

(92) Jalenak, W.; Weston, R. E.; Sears, T. J.; Flynn, G. W. *J. Chem. Phys.* **1988**, *89*, 2015.

(93) Michaels, C. A.; Tapalian, H. C.; Lin, Z.; Sevy, E. T.; Flynn, G. W. *Faraday Discuss.* **1995**, *102*, 405.

(94) Michaels, C. A.; Lin, Z.; Mullin, A. S.; Tapalian, H. C.; Flynn, G. W. *J. Chem. Phys.* **1997**, *106*, 7055.

(95) Michaels, C. A.; Mullin, A. S.; Flynn, G. W. *J. Chem. Phys.* **1995**, *102*, 6682.

(96) Sevy, E. T.; Muyskens, M. A.; Lin, Z.; Flynn, G. W. *J. Phys. Chem. A* **2000**, *104*, 10538.

(97) Sevy, E. T.; Rubin, S. M.; Lin, Z.; Flynn, G. W. *J. Chem. Phys.* **2000**, *113*, 4912.

(98) Eng, J.; Raghavachari, K.; Struck, L. M.; Chabal, Y. J.; Bent, B. E.; Banaszak-Holl, M. M.; McFeely, F. R.; Michaels, A. M.; Flynn, G. W.; Christman, S. B.; Chaban, E. E.; Williams, G. P.; Radermacher, K.; Mantl, S. *J. Chem. Phys.* **1998**, *108*, 8680.

(99) Hewitt, S. A.; Zhu, L.; Flynn, G. W. *J. Chem. Phys.* **1992**, *97*, 6396.

(100) Khan, F. A.; Kreutz, T. G.; Zhu, L.; Flynn, G. W.; Weston, R. E. *J. Phys. Chem.* **1988**, *92*, 6171.

(101) Sevy, E. T.; Michaels, C. A.; Tapalian, H. C.; Flynn, G. W. *J. Chem. Phys.* **2000**, *112*, 5844.

(102) Sevy, E. T.; Muyskens, M. A.; Rubin, S. M.; Flynn, G. W.; Muckerman, J. T. *J. Chem. Phys.* **2000**, *112*, 5829.

(103) Duffin, A. M.; Johnson, J. A.; Muyskens, M. A.; Sevy, E. T. *J. Phys. Chem. A* **2007**, *111*, 13330.

(104) Dietz, T. G.; Duncan, M. A.; Pulu, A. C.; Smalley, R. E. *J. Phys. Chem.* **1982**, *86*, 4026.

(105) Knee, J.; Johnson, P. *J. Phys. Chem.* **1985**, *89*, 948.

(106) Elioff, M. S.; Wall, M. C.; Lemoff, A. S.; Mullin, A. S. *J. Chem. Phys.* **1999**, *110*, 5578.

(107) Bolovinos, A.; Tsekeris, P.; Philis, J.; Pantos, E.; Andritsopoulos, G. *J. Mol. Spectrosc.* **1984**, *103*, 240.

(108) Ruth, A. A.; Kim, E. K.; Hese, A. *Phys. Chem. Chem. Phys.* **1999**, *1*, 5121.

(109) Lin, M. F.; Huang, C. L.; Lee, Y. T.; Ni, C. K. *J. Chem. Phys.* **2003**, *119*, 2032.

(110) Hirata, Y.; Lim, E. C. *J. Chem. Phys.* **1978**, *69*, 3292.

(111) Yamazaki, I.; Murao, T.; Yamanaka, T.; Yoshihara, K. *Faraday Discuss.* **1983**, *75*, 395.

(112) Sushida, K.; Fujita, M.; Yamazaki, I.; Baba, H. *Bull. Chem. Soc. Jpn.* **1983**, *56*, 2228.

(113) Yamazaki, I.; Sushida, K.; Baba, H. *J. Chem. Phys.* **1979**, *71*, 381.

(114) Sevy, E. T.; Flynn, G. W. *Abstr. Paper Am Chem Soc Natl Meet* **1998**, *215*, 318.

(115) Du, J.; Yuan, L. W.; Hsieh, S.; Lin, F.; Mullin, A. S. *J. Phys. Chem. A* **2008**, *112*, 9396.

(116) Havey, D. K.; Du, J.; Liu, Q. N.; Mullin, A. S. *J. Phys. Chem. A* **2010**, *114*, 1569.

(117) Yuan, L. W.; Du, J.; Mullin, A. S. *J. Chem. Phys.* **2008**, *129*, 014303.

(118) Liu, Q. N.; Du, J.; Havey, D. K.; Li, Z. M.; Miller, E. M.; Mullin, A. S. *J. Phys. Chem. A* **2007**, *111*, 4073.

(119) *Operation & Maintenance Manual for the Powerlite 8000 Series Laser*; Continuum Inc., 1996.

(120) Li, Z. M.; Korobkova, E.; Werner, K.; Shum, L.; Mullin, A. S. *J. Chem. Phys.* **2005**, *123*.

(121) Wormald, C. J.; Wurzberger, B. *Phys. Chem. Chem. Phys.* **2000**, *2*, 5133.

(122) Arunan, E.; Setser, D. W.; Ogilvie, J. F. *J. Chem. Phys.* **1992**, *97*, 1734.

(123) Parekunnel, T.; Hirao, T.; Le Roy, R. J.; Bernath, P. F. *J. Mol. Spectrosc.* **1999**, *195*, 185.

(124) Rothman, L. S.; Jacquemart, D.; Barbe, A.; Benner, D. C.; Birk, M.; Brown, L. R.; Carleer, M. R.; Chackerian, C.; Chance, K.; Coudert, L. H.; Dana, V.; Devi, V. M.; Flaud, J. M.; Gamache, R. R.; Goldman, A.; Hartmann, J. M.; Jucks, K. W.; Maki, A. G.; Mandin, J. Y.; Massie, S. T.; Orphal, J.; Perrin, A.; Rinsland, C. P.; Smith, M. A. H.; Tennyson, J.; Tolchenov, R. N.; Toth, R. A.; Vander Auwera, J.; Varanasi, P.; Wagner, G. *J. Quant. Spectrosc. Radiat. Transfer* **2005**, *96*, 139.

(125) Scott, T. P.; Smith, N.; Magill, P. D.; Pritchard, D. E.; Stewart, B. *J. Phys. Chem.* **1996**, *100*, 7981.

(126) Bernstein, R. B. *J. Chem. Phys.* **1962**, *34*, 361.

(127) Clare, S.; Marks, A. J.; McCaffery, A. J. *J. Phys. Chem. A* **2000**, *104*, 7181.

(128) McCaffery, A. J.; Alwahabi, Z. T.; Osborne, M. A.; Williams, C. J. *J. Chem. Phys.* **1993**, *98*, 4586.

(129) McCaffery, A. J.; Osborne, M. A.; Marsh, R. J.; Lawrance, W. D.; Waclawik, E. R. *J. Chem. Phys.* **2004**, *121*, 169.

(130) Osborne, M. A.; McCaffery, A. J. *J. Chem. Phys.* **1994**, *101*, 5604.

(131) Waclawik, E. R.; Lawrance, W. D. *J. Chem. Phys.* **1998**, *109*, 5921.

(132) Zeleznik, F. J.; Dugan, J. V. *J. Chem. Phys.* **1971**, *54*, 4523.

(133) *Molecular Theory of Gases and Liquids*; Hirschfelder, J. O.; Curtis, C. F.; Bird, R. B., Eds. Wiley: New York, 1964.

(134) Bevilacqua, T. J.; Weisman, R. B. *J. Chem. Phys.* **1993**, *98*, 6316.

(135) Cheney, B. V.; Schulz, M. W. *J. Phys. Chem.* **1990**, *94*, 6268.

(136) Cheney, B. V.; Schulz, M. W.; Cheney, J.; Richards, W. G. *J. Am. Chem. Soc.* **1988**, *110*, 4195.

(137) Gotch, A. J.; Zwier, T. S. *J. Chem. Phys.* **1990**, *93*, 6977.

(138) Read, W. G.; Campbell, E. J.; Henderson, G.; Flygare, W. H. *J. Am. Chem. Soc.* **1981**, *103*, 7670.

(139) Zhao, Y.; Tishchenko, O.; Truhlar, D. G. *J. Phys. Chem. B* **2005**, *109*, 19046.

(140) Perkins, B. G.; Haber, T.; Nesbitt, D. J. *J. Phys. Chem. B* **2005**, *109*, 16396.

(141) Perkins, B. G.; Nesbitt, D. J. *Proc. Natl. Acad. Sci. U. S. A.* **2008**, *105*, 12684.

(142) Perkins, B. G.; Nesbitt, D. J. *J. Phys. Chem. A* **2008**, *112*, 9324.

(143) Alwahabi, Z. T.; Besley, N. A.; McCaffery, A. J.; Osborne, M. A.; Rawi, Z. *J. Chem. Phys.* **1995**, *102*, 7945.

(144) McCaffery, A. J.; Marsh, R. J. *J. Phys. B: At. Mol. Opt. Phys.* **2001**, *34*, R131.

(145) Marsh, R. J.; McCaffery, A. J. *J. Phys. B: At. Mol. Opt. Phys.* **2003**, *36*, 1363.

(146) McCaffery, A. J. *Phys. Chem. Chem. Phys.* **2004**, *6*, 1637.

(147) Bernshtein, V.; Oref, I. *J. Phys. Chem. B* **2005**, *109*, 8310.

(148) Bernshtein, V.; Oref, I. *J. Phys. Chem. A* **2006**, *110*, 8477.

(149) Bernshtein, V.; Oref, I. *J. Phys. Chem. A* **2006**, *110*, 1541.

(150) Linhananta, A.; Lim, K. F. *Phys. Chem. Chem. Phys.* **1999**, *1*, 3467.

(151) Linhananta, A.; Lim, K. F. *Phys. Chem. Chem. Phys.* **2000**, *2*, 1385.

(152) Hippler, H.; Troe, J.; Wendelken, H. J. *J. Chem. Phys.* **1983**, *78*, 6709.

(153) Hippler, H.; Troe, J.; Wendelken, H. J. *J. Chem. Phys.* **1983**, *78*, 6718.

(154) Troe, J. *J. Chem. Phys.* **1982**, *77*, 3485.

(155) Damm, M.; Deckert, F.; Hippler, H.; Troe, J. *J. Phys. Chem.* **1991**, *95*, 2005.

(156) Rossi, M. J.; Pladziewicz, J. R.; Barker, J. R. *J. Chem. Phys.* **1983**, *78*, 6695.

(157) Barker, J. R.; Rossi, M. J.; Pladziewicz, J. R. *Chem. Phys. Lett.* **1982**, *90*, 99.

(158) Rossi, M. J.; Barker, J. R. *Chem. Phys. Lett.* **1982**, *85*, 21.

(159) Frerichs, H.; Lenzer, T.; Luther, K.; Schwarzer, D. *Phys. Chem. Chem. Phys.* **2005**, *7*, 620.

(160) Liu, C. L.; Hsu, H. C.; Ni, C. K. *J. Chem. Phys.* **2008**, *128*, 164316.

(161) Liu, C. L.; Hsu, H. C.; Hsu, Y. C.; Ni, C. K. *J. Chem. Phys.* **2008**, *128*, 124320.

(162) Hsu, H. C.; Liu, C. L.; Hsu, Y. C.; Ni, C. K. *J. Chem. Phys.* **2008**, *129*, 044301.

(163) Liu, C. L.; Hsu, H. C.; Hsu, Y. C.; Ni, C. K. *J. Chem. Phys.* **2007**, *127*, 104311.

(164) Dove, J. E.; Hippler, H.; Plach, J.; Troe, J. *J. Chem. Phys.* **1984**, *81*, 1209.

(165) Herzog, B.; Hippler, H.; Kang, L.; Troe, J. *Chem. Phys. Lett.* **1985**, *120*, 124.

(166) Schwarzer, D.; Troe, J.; Votsmeier, M.; Zerezke, M. *Ber. Bunsen. Phys. Chem.* **1997**, *101*, 595.

(167) Schwarzer, D.; Troe, J.; Zerezke, M. *J. Phys. Chem. A* **1998**, *102*, 4207.

(168) Johnson, J. A.; Duffin, A. M.; Hom, B. J.; Jackson, K. E.; Sevy, E. T. *J. Chem. Phys.* **2008**, *128*, 054304.

(169) Johnson, J. A.; Kim, K.; Mayhew, M.; Mitchell, D. G.; Sevy, E. T. *J. Phys. Chem. A* **2008**, *112*, 2543.

(170) Mitchell, D. G.; Johnson, A. M.; Johnson, J. A.; Judd, K. A.; Kim, K.; Mayhew, M.; Powell, A. L.; Sevy, E. T. *J. Phys. Chem. A* **2008**, *112*, 1157.

(171) Barker, J. R.; Golden, R. E. *J. Phys. Chem.* **1984**, *88*, 1012.

(172) Shi, J.; Barker, J. R. *J. Chem. Phys.* **1988**, *88*, 6219.

(173) Damm, M.; Hippler, H.; Troe, J. *J. Chem. Phys.* **1988**, *88*, 3564.

(174) Jalenak, W.; Weston, R. E.; Sears, T. J.; Flynn, G. W. *J. Chem. Phys.* **1985**, *83*, 6049.

(175) Fujii, M.; Ebata, T.; Mikami, N.; Ito, M. *Chem. Phys.* **1983**, *77*, 191.

(176) Burkholder, J. B.; Mills, M.; McKeen, S. *Geophys. Res. Lett.* **2000**, *27*, 2493.

(177) Hintze, P. E.; Feierabend, K. J.; Havey, D. K.; Vaida, V. *Spectrochim. Acta, Part A* **2005**, *61*, 559.

(178) Rothman, L. S.; Rinsland, C. P.; Goldman, A.; Massie, S. T.; Edwards, D. P.; Flaud, J. M.; Perrin, A.; Camy-Peyret, C.; Dana, V.; Mandin, J. Y.; Schroeder, J.; McCann, A.; Gamache, R. R.; Wattson, R. B.; Yoshino, K.; Chance, K. V.; Jucks, K. W.; Brown, L. R.; Nemtchinov, V.; Varanasi, P. *J. Quant. Spectrosc. Radiat. Transfer* **1998**, *60*, 665.

(179) Beyer, T.; Swinehar.Df. *Commun. ACM* **1973**, *16*, 379.

(180) Chao, R. S.; Khanna, R. K. *Spectrochim. Acta, Part A* **1977**, *33*, 53.

(181) DeSain, J. D.; Taatjes, C. A.; Miller, J. A.; Klippenstein, S. J.; Hahn, D. K. *Faraday Discuss.* **2001**, *119*, 101.

(182) DeSain, J. D.; Klippenstein, S. J.; Miller, J. A.; Taatjes, C. A. *J. Phys. Chem. A* **2003**, *107*, 4415.

(183) Walker, R. W.; Morley, C. *Low Temperature Combustion and Autoignition*; Amsterdam, 1997.

(184) Tardy, D. C.; Song, B. H. *J. Phys. Chem.* **1993**, *97*, 5628.

(185) Roney, P. L.; Findlay, F. D.; Buijs, H. L.; Cann, M. W. P.; Nicholls, R. W. *App. Opt.* **1978**, *17*, 2599.

(186) Lenzer, T.; Luther, K. *J. Chem. Phys.* **1996**, *104*, 3391.

(187) Stein, S. E.; Rabinovi.Bs. *J. Chem. Phys.* **1973**, *58*, 2438.

(188) Green, J. H. S.; Barnard, P. W. B. *J. Chem. Soc.* **1963**, 640.

(189) Scott, A. P.; Radom, L. *J. Phys. Chem.* **1996**, *100*, 16502.

(190) Lim, K. F. *Quantum Chem. Program Exchange Bull.* **1994**, *14*, 3.

(191) McQuarrie, D. A. *Statistical Mechanics*; Harper & Row: New York, 1976.

(192) Lide, D. R. *CRC Handbook of Chemistry and Physics*; CRC Press Inc.: New York, 2004-2005.

(193) McQuarrie, D. A. Statistical Mechanics. In *University Science Books* New York, 2000.